Direct cell to cell spread of influenza A viruses

Daniel Weir

Submitted in fulfilment of the requirements for the degree of Doctor of Philosophy

College of Medical, Veterinary and Life Sciences University of Glasgow

September 2025

“A system of cells interlinked, within cells interlinked, within cells interlinked within one stem.

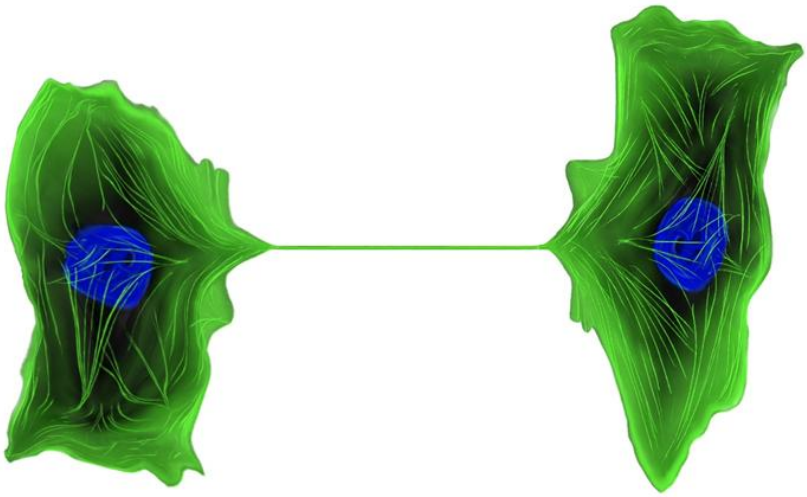

And dreadfully distinct against the dark, a tall white fountain played.”

- Vladimir Nabokov, *Pale Fire* (1962)

Abstract

Influenza A viruses (IAVs) continue to cause widespread morbidity and mortality across the globe, driven by their evolutionary capacity to evade immune responses and adapt to spread between diverse hosts. Despite extensive surveillance of population-level transmission, the mechanisms governing IAV spread between individual cells within infected tissues remain incompletely understood. The intercellular spread of IAVs can either occur by the release of virus particles or by the transfer of viral genomes directly between cells (direct cell to cell spread). Infection by extracellular viruses is well-studied, but the importance and wider implications of direct cell to cell spread during IAV infection is unclear. To investigate this, I first established tissue culture models in which I could quantify the frequency of IAV direct cell to cell spread. I show that, even in the presence of drugs that completely inhibit extracellular virus spread, up to 40% of IAV infected cells are able to infect their neighbours, an effect that was consistent between IAV strains with different virion morphologies. Direct cell to cell spread of IAVs can occur by the induction of intercellular membrane connections known as tunnelling nanotube-like structures (TLSs), which are capable of trafficking the viral genome between cells. I show that TLSs are formed by IAV infected cells *in vivo*, and used *in vitro* models to ask how IAVs induce their formation. I found that TLS formation is not induced by cytokine signalling from infected to uninfected cells, but induction requires intracellular IAV replication. I therefore looked at the intracellular responses to infection and found that the ability of IAVs to drive TLS formation can be modulated by chemically inhibiting, or inducing apoptosis. I then found that inhibiting apoptosis, which prevents IAVs from inducing TLSs, lead to a significant reduction in the ability of IAVs to directly spread between distant cells. Interestingly, I found that direct cell to cell contacts allow uninfected cells to suppress apoptosis of neighbouring infected cells, with data revealing a potential role of uninfected cell mitochondrial transfer to infected cells. The results of this thesis, which suggest that IAVs efficiently perform direct cell to cell spread and control their ability to so through a regulation of host cell apoptosis, identifies a new way in which a virus can manipulate its host to evade antiviral immune responses, ensuring its continued spread even within the restrictive environment of the respiratory tract.

Contents

List of Figures

List of Tables

Publications

Publications obtained from work included in this thesis:

Weir D, Bentley-Abbot C, McCowan J, Loney C, Roberts E, Hutchinson E, (2025) Induction of tunnelling nanotube-like structures by influenza A viruses requires the onset of apoptosis. PLOS Pathogens 21(6): e1013191. https://doi.org/10.1371/journal.ppat.1013191

Publications obtained from work not included in this thesis:

Sims A, Weir D, Cole S, Hutchinson E, (2025) SARS-CoV-2 cellular coinfection is limited by superinfection exclusion. Journal of Virology. Apr 15;99(4):e0207724. doi: 10.1128/jvi.02077-24. https://doi.org/10.1128/jvi.02077-24.

Acknowledgements

Though my science hasn't saved the world, it has made me more a part of it. I have travelled to new places, shared company with the most brilliant people, and uncovered secrets about my greatest passion, influenza. This has only been possible due to the qualities and efforts of the people I had beside me.

Firstly, to my parents, to whom I dedicate this thesis. At every stage of this journey they made my ambitions seem possible. Nothing about my early life suggested to them that my future was academic, and yet they held that door open for me until I was ready. To my mum, your care and belief in me has sharpened my passion that I have for my work. To my dad, you'd make a much better scientist than I'll ever be. Yet I know you'd sacrifice a lot more than what you've already done for me to have this opportunity. Also, to my sister and grandparents, your constant care and support has kept me going. As is only fair, any positive outcome of this work I share with you all.

With everything familiar on the far side of the Irish sea, my treasured friends transformed my time in Glasgow into the best 3 and a half years. Eilidh Rivers, Hollie Jackson Ireland, Emma Davies, Kieran Lamb, Harry Scott, Alex Wilson, Cal Bentley Abbott, Sarah Cole, Sarah Walsh, Lea Meyers, you all mean a great deal to me. I am so grateful to have spent the time I had with you all. To Spyros Lytras and Anna Sims, I have been honoured to see you both achieve so much, and lucky to have been granted such precious friendships. Anna, you had to deal with a lot sitting next to me. But how lucky was I, that for the good part of 3 years, I was greeted everyday by this warm, kind and caring person, who ultimately would allow me to feel at home in places otherwise cold and foreign. The mornings when you'd turn the corner, I'd just knew that day would turn out just fine. Spyros, you are a confident, brilliant scientist with an unmatched personality. My greatest reassurance is knowing that you are always there and able to chat about anything, as well as providing the much needed honest opinion and silver lining to every situation.

To Professor Ed Hutchinson, my supervisor and friend. Thank you. The best decision I ever made was choosing the CVR, and as you would later come to know, this was for the purpose of joining your lab. The story of this PhD would

have been an immediate horror hadn't you given me the guidance you did throughout. What began with a lot of uncertainty, turned into something really special, and I hope you realise that the magic of this can't be explained by luck or a single student. In my humble opinion, your brilliance is the kind that will define an era of virology research. The benefit of being your PhD student will be measured across my career, such is the lasting impact you have made on me. But science aside, thank you for looking after the person underneath the lab coat. There is no other supervisor in the world that could have done what you did for me. This time, I don't need more replicates to know that this n of 1 is significant.

Thanks must also go to the incomparable bioimaging team consisting of two really special individuals, Colin Loney and Deirdre McLachlan. Not only did they know the solution to every technical imaging problem and analysis I had, they always seemed to know what words I needed to hear.

Lastly, I would like to thank Professor Pablo Murcia, Dr Ed Roberts and Dr Chris Boutell. Together, with Professor Hutchinson, they formed an extraordinary supervisory team, offering unique perspectives and ideas. They also supported my progress and development earnestly, and I am touched by their genuine care.

Ultimately, I am an individual shaped by greater people, and I am beyond grateful for them all. My only hope for my efforts, is that they see their contributions reflected in them.

Author Declaration

I declare that, except where explicit reference is made to the contribution of others, that this thesis is the result of my own work and has not been submitted for any other degree at the University of Glasgow or any other institution.

Daniel Weir

September 2025

Abbreviations

Abbreviation	Definition
AcGFP	Aequorea coerulescens Green Fluorescent Protein
AIV	Avian influenza virus
ANP32	Acidic Nuclear Phosphoprotein of size 32 kilodalton
BoHV	Bovine alphaherpesvirus
BSA	Bovine serum albumin
CFR	Case fatality rates
CHIKV	Chikungunya virus
CMAH	Cytidine Monophospho-N-Acetylneuraminic Acid Hydroxylase
CNS	Central nervous system
CPE	Cytopathic effect
cRNP	Complementary ribonucleoprotein complex
DAPI	4′,6-diamidino-2-phenylindole
DC	Dendritic cells
DiD	1,1'-dioctadecyl-3,3,3',3'-tetramethylindodicarbocyanine perchlorate
DiO	3,3'-dioctadecyloxacarbocyanine perchlorate
DMEM	Dulbecco's Modified Eagle Medium
DMSO	Dimethyl sulfoxide
DPI	Days post infection
DTT	Dithiothreitol
DVG	Defective viral genome
EBV	Epstein-Barr virus
eGFP	Enhanced green fluorescent protein
EGFR	Epidermal growth factor receptor
ER	Endoplasmic reticulum
EV	Extracellular vesicle
FACS	Fluorescence-activated cell sorting
FBS	Foetal bovine serum
FFU	Fluorescent forming unit
FI	Fluorescence intensity
GaAsP	Gallium Arsenide Phosphide
GFP	Green fluorescent protein
HA	Hemagglutinin
HCl	Hydrochloric acid
HEF	Hemagglutinin-Esterase-Fusion protein

HEK	Human embryonic kidney
HIV	Human immunodeficiency virus
HMPV	Human metapneumovirus
HPI	Hours post infection
HPT	Hours post treatment
HSV	Herpes simplex virus
HTLV	Human T-lymphotropic virus
IAV	Influenza A virus
IF	Immunofluorescence
IFN	Interferon
JAK	Janus Kinase
KSHV	Kaposi's sarcoma-associated herpesvirus
LVI	Liquid viral inclusion
M1	Matrix 1 protein
M2	Matrix 2 protein
MAPK	Mitogen-activated protein kinase
MDCK	Madin-Darby Canine Kidney
MDM	Monocyte-derived macrophages
MHV	Murine gammaherpesvirus
mRNA	Messenger ribonucleic acid
MSCs	Mesenchymal stem cells
mTOR	Mammalian target of rapamycin
NA	Neuraminidase
NaCl	Sodium Chloride
NDV	Newcastle disease virus
NEP	Nuclear export protein
Neu5Ac	*N*-acetylneuraminic acid
Neu5Gc	*N*-glycolylneuraminic acid
NLS	Nuclear localisation signals
NP	Nucleoprotein
NPC	Nuclear pore complex
NS	Non-structural protein
PA	Polymerase acidic protein
PAGE	Polyacrylamide gel electrophoresis
PAK1	p21-activated kinase 1
PAK2	P21 (RAC1) activated kinase 2
PB1	Polymerase basic 1 protein
PB2	Polymerase basic 2 protein

PBS	Phosphate buffered saline
PBS-T	0.1% Tween-20 in PBS
PFU	Plaque forming units
PI3K	Phosphatidylinositol 3-kinase
PIV	Parainfluenza virus
PRRSV	Porcine reproduction and respiratory syndrome virus
PRV	Pseudorabies virus
pSTAT1	Phosphorylated signal transducer and activator of transcription 1
RdRp	RNA-dependent RNA polymerase
RE	Recycling endosome
RFP	Red fluorescent protein
RFU	Relative fluorescent units
RNA	Ribonucleic acid
ROS	Reactive oxygen species
RPM	Revolutions per minute
SARS-CoV-2	Severe acute respiratory syndrome coronavirus 2
SD	Standard deviation
SDS	Sodium dodecyl sulfate
SFV	Semliki forest virus
SINV	Sindbis virus
STAT	Signal transducer and activator of transcription
SV40	Simian virus 40 large T-antigen
TLS	Tunnelling nanotube-like structure
TNT	Tunnelling nanotube
TPCK	Tosylphenylalanine chloromethyl ketone
UTR	Untranslated region
VACV	Vaccinia virus
vRNA	Viral ribonucleic acid
vRNP	Viral ribonucleoprotein complex
VSV	Vesicular stomatitis virus
WD PHAEC	Well-differentiated primary human airway epithelial cell culture
WT	Wild-type

Chapter 1

1 Introduction

1.1 Influenza

1.1.1 Overview of influenza viruses

The *Orthomyxoviridae* family encompasses several genera of negative-sense, segmented, single stranded RNA viruses, among which the influenza viruses stand out for their clinical and epidemiological significance (1, 2). These viruses are the aetiological agents of influenza, a disease known colloquially as 'the flu'. There are four types of influenza viruses, influenza A, B, C and D, classified in four genera (each containing a single species): alpha-, beta-, gamma-, and delta-influenza virus respectively (1). Whilst influenza D virus (IDV) primarily infects cattle (3), a variety of birds and mammals (including humans) can be infected with influenza A, B and C viruses (2). Influenza A (IAV) and B (IBV) viruses are responsible for the most clinically significant infections of humans, and the two lineages of IBV (Victoria and Yamagata) are predominately human pathogens (2, 4). The close association of IBVs with humans meant that the social distancing measures taken to reduce the spread of severe acute respiratory syndrome coronavirus 2 (SARS-CoV-2) had the indirect consequence of making the IBV Yamagata lineage extinct (5). In contrast, most of the highly diverse IAVs typically infect waterfowl, but IAVs have also been found to infect an expansive range of hosts, including other avian species and mammals (including swine, horses and humans) (6). The ability of IAVs to infect a broad range of hosts is impressive and we are still uncovering susceptible host species of emerging and established IAVs. For example, surveillance has lead to the recent discovery of novel IAVs within bats (7), and the surprising incursion of avian IAVs into cattle (8). It is this flexible host range of IAVs that lies at the heart of their pandemic capability (see 1.1.2), making efforts to understand this particular group of influenza viruses critical.

Influenza virus particles (aka the influenza virion) possess an envelope composed of a host-derived phospholipid bilayer that encloses their segmented RNA genome (Figure 1-1). This envelope also contains the transmembrane matrix 2

(M2) protein and, in the case of IAV and IBV, the viral glycoproteins hemagglutinin (HA) and neuraminidase (NA) (Figure 1-1, (9, 10)). IAVs are classified according to the genetic and antigenic properties of these surface glycoproteins, and to date, 19 HA and 11 NA subtypes have been reported (11, 12). Most of these subtypes are found within aquatic birds, although H17N10 and H18N11 viruses have so far been found exclusively within bats (13, 14). In total, there are 209 possible HA and NA combinations, and whilst over 130 have been found, many are yet to be observed in nature with their sudden emergence remaining a possibility (15). In addition to HA and NA, IBV envelopes contain the NB protein (encoded for by the same gene segment as NA and is unique to IBVs) (16). On the other hand, ICVs and IDVs do not have separate HA and NA proteins, but instead have a single multifunctional surface glycoprotein known as the Hemagglutinin-Esterase-Fusion (HEF) protein (17, 18).

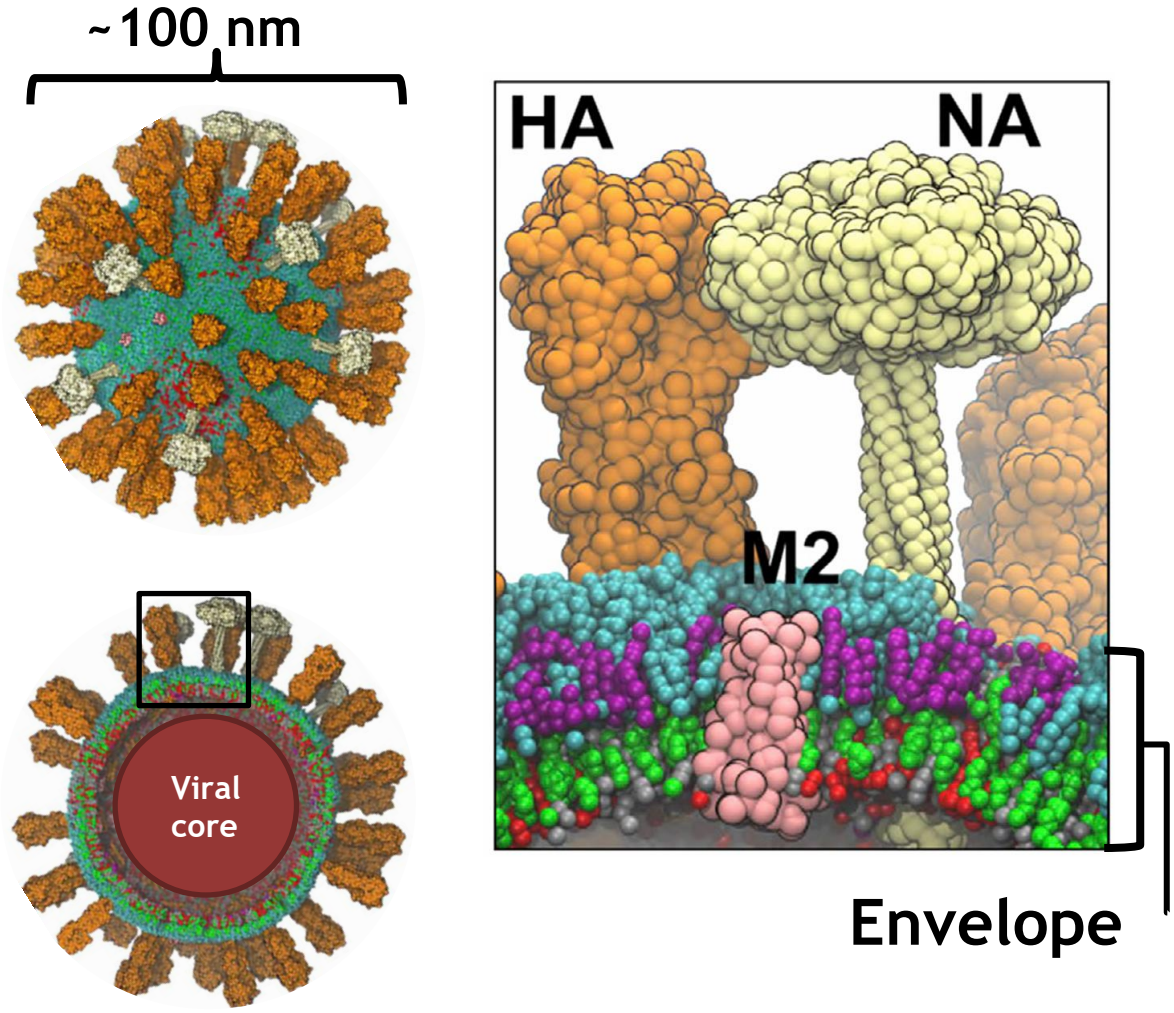

Figure 1-1: The virion structure of IAV. The host derived lipid envelope of influenza viruses establishes the viral core of which is occupied by the segmented viral genome (collectively represented by the red circle). The envelope contains several structural viral proteins, including the glycoproteins (HA and NA) that can be used to distinguish between IAV subtypes. Hemagglutinin (HA), neuraminidase (NA), matrix protein 2 (M2). Figure adapted from Reddy *et al.* (19).

1.1.2 Influenza A virus outbreaks, disease burden and viral evolution

Influenza A viruses are able to rapidly spread, leading to outbreaks that can span geographical regions and host species, often leaving a lasting legacy. With the reservoir of IAVs being aquatic birds, IAVs frequently spread amongst avian populations causing epizootics (6). The movement of infected animals can seed outbreaks in different regions and continents, leading to a panzootic (20). When wild birds have an interface with domesticated birds or mammals, this can quickly lead to human exposure (21). Given the right set of circumstances, humans can become infected with an epizootic IAV (21, 22). It is thought that an intermediate host species, such as pigs, that can be infected with both avian and mammalian IAVs, helps to increases the likelihood of human infection with an avian influenza virus (23). When this occurs it is referred to as a zoonotic event, and if the virus is suitably adapted (see 'epizootic and panzootic IAV' below, and section 1.1.3), these IAVs can quicky spread amongst the human population, causing a pandemic (24). Over the 20th and 21st centuries, influenza pandemics have occurred roughly every 30 years (H1N1 (1918, 1977 and 2009), H2N2 (1957), H3N2 (1968)). Influenza pandemics typically progress through several infection waves, the cumulative scale of which are often significant enough that population immunity brings an end to the pandemic (22, 24). However, these pandemic viruses persist at lower levels and become endemic – mutating to evade antibody neutralisation acquired from previous exposure or vaccination. This results in a legacy of these pandemics, with seasonal outbreaks of infection in temperate regions of each hemisphere during the colder months, and a more complex pattern of outbreaks in the tropics (24). This results in annual epidemics of influenza viruses that requires an updated approach to control. Interestingly, pandemic IAVs have typically replaced epidemic IAVs (H2N2 replaced H1N1 in 1957, and then H3N2 replaced H2N2 in 1968) (25). However, the reemergence of H1N1 in 1977 did not replace H3N2 and both IAV subtypes have cocirculated, increasing the complexity of IAV epidemics (25).

The consequences and effects of IAV outbreaks are complex, with panzootics, pandemics and epidemics presenting shared and unique challenges as outlined below.

Epizootic and panzootic IAV – The first documented record of an influenza epizootic is believed to have been made in 1878 regarding avian influenza virus (AIV) (26), and since then, few parts of the world have remained untouched by these avian viruses (27). The spread of highly pathogenic AIVs of the H5 and H7 subtype, particularly within Asia, Europe and Africa, has resulted in the deaths or destruction of hundreds of millions of birds (27). At the time of writing this thesis, the impact of AIV is in sharp focus due to the ongoing H5N1 clade 2.3.4.4.b panzootic, the expansion of which dates back to 2020 (28). This panzootic has seen the introduction of avian influenza viruses into new territories (29), and has lead to the infection of both wild mammals (aquatic and terrestrial) and domestic animals (e.g. cattle, cats and goats) (8, 20, 30, 31). Such infections have resulted in mass die-offs of both bird and seal populations, with devastating consequences to ecology and diversity (32, 33). Such devastation to animal populations, particularly within domesticated animals used for agriculture, can also incur a massive financial cost (e.g. an estimated $380 million was lost when 17 million birds were culled in British Columbia following an outbreak in 2004) as well as causing food insecurity (34).

The evolution of IAVs accelerates during these panzootics, with the spread of avian influenza viruses (particularly of the H5N1 subtype) to mammalian species resulting in the acquisition of adaptations to non-avian hosts. For example, the characteristic mammalian adaptations - PB2 E627K and HA Q222H have been detected in human and animal H5N1 cases (35). Furthermore, the significant pandemic risk benchmark of mammal-to-mammal transmission is now believed to be possible between seals infected with H5N1 2.3.4.4b, due to mammalian adaptation (e.g. PB2 D701N) of these viruses (30).

Pandemic IAV – Mammalian adaptations of viruses within domesticated animals that interface with humans are of particular concern as they increase the potential for a zoonotic infection - the event that triggers IAV pandemics. Even if the infections are dead-end, individual cases of zoonotic infections, particularly with highly pathogenic avian influenza viruses, can be incredibly serious with staggeringly high case fatality rates (CFR). For example, an investigation in 2017 found that the CFR of highly pathogenic H5N1 zoonotic infections was approximately 66%, but when isolating index cases, this was as high as 100% (36). However, it is worth noting that zoonotic events (especially

those with little to no clinical consequence) are often missed, which inflate such estimates as CFRs.

The greater diversity of IAVs that circulate amongst animal populations relative to those circulating within the human population means that zoonotic infections often introduce an antigenically unique virus, with no established immune protection against it (25). This results in a pandemic, with the virus rapidly spreading amongst the susceptible population, providing that the virus can replicate and transmit between its new human host (37). IAVs can readily acquire these capabilities if coinfection occurs with a seasonal human strain. Coinfection can lead to the generation of progeny viruses with segments of different strain origin, in a process referred to as reassortment (22). Such a scenario can combine the antigenic novelty of epizootic IAVs (such as HA and NA), with the human adapted proteins of seasonal IAVs that drive its replication (38). Under such a scenario, antigenically novel viruses can suddenly emerge from a single infection and spread efficiently within and between humans. This sudden evolution of IAVs through reassortment is referred to as antigenic shift, and has been the manner in which all the major IAV pandemics of the last century have been initiated (22).

Recorded IAV pandemics have caused huge numbers of infections and fatalities, with the 1918 H1N1 pandemic (known colloquially as ‘The Spanish Flu’) being the most significant. The virus, believed to be of avian origin, infected nearly one third of the world’s population (roughly 500 million people), and is estimated to have caused at least 50 million deaths (39). Noticeably during this pandemic, many fatalities involved otherwise healthy young adults (39). Unsurprisingly, a secondary consequence of such devastation on the working population, was a dramatic impact on the global economy (the scale of which was comparable to the great recession of 2008-2009) (40).

Epidemic IAV – Once IAV pandemics have spread sufficiently, a significant proportion of the population will have been exposed and generated an adaptive immune response that suppresses the virus and its onward spread. This establishes selective pressures that drive the emergence of variants that are no longer neutralised by the antibodies generated from prior exposure. IAV genome replication is error prone, with an estimated error rate of 1 per 2,000 to 10,000

nucleotides (41-43). Therefore, mutations within the epitopes of the surface HA and NA antigens can rapidly arise which can evade antibody neutralisation, allowing reinfection of previously infected hosts and increasing the spread of the virus, causing recurrent epidemics (44, 45). This process of nucleotide substitution driving glycoprotein diversification, immune evasion and seasonal outbreaks is referred to as antigenic drift (2).

Seasonal flu epidemics are a major source of strain on healthcare systems every winter with many vulnerable patients falling seriously ill. Current estimates suggest that up to 1 billion infections are caused annually, resulting in 3 to 5 million cases of serious illness, with hundreds of thousands of deaths caused by pneumonia and complications (respiratory and cardiovascular) related to influenza (2, 46).

Overall, the scale and immediate surge of cases and fatalities of panzootics and pandemics are often overwhelming – contributing to food insecurity and stretching health care systems. Similarly, the case fatality rates of zoonotic infections are often extremely high, and annual epidemics eventually cause more deaths than some pandemics (2). Furthermore, the opportunities for IAVs to progress to pandemics is aided by its impressive geographical and host range as well as its ability to reassort with other viruses. The error prone replication of these viruses maintains the burden of IAVs until the next pandemic likely takes its place.

1.1.3 Transmission of influenza A viruses

1.1.3.1 Routes of IAV transmission

The routes of IAV transmission often reflect the tissues the virus infects within avian and mammalian hosts. For example, avian influenza viruses primarily infect the mucosal epithelial cells of the respiratory and gastrointestinal tract (albeit infection with highly pathogenic (HPAIV) AIV is systemic) (47, 48). Therefore, the primary route of transmission between birds is through the consumption of water or food contaminated with faeces, i.e. the faecal-oral route (49). Within mammals, particularly humans, IAVs primarily infect the epithelial cells of the respiratory tract (50, 51). Therefore, the primary route of

mammalian adapted IAV transmission is through respiratory secretions, aerosols and droplets (52, 53). Where exceptions to this are found, this has coincided with findings of IAV infection of atypical tissues. For example, novel bovine H5N1 was found to be present in extremely high titres in mammary tissues of cow udders, with few instances of IAV detected in the respiratory tissue (54). This finding coincided with the reports that transmission between cattle (and cross species infection of humans and cats) is believed to be through exposure of contaminated, unpasteurised milk or milking equipment (55, 56).

More broadly speaking, IAVs can transmit either as a result of close contact , or through indirect exposure through contaminated material (i.e. fomites). In both circumstances, the transmission of IAVs is dependent on a number of interlinking factors including the environment and stability of the virus itself.

1.1.3.2 Factors that influence IAV transmission

The seasonality of IAV epidemics in temperate climates suggests that IAV transmission between humans can be influenced by the changes in weather. Research has found that IAV virion viability is influenced by ambient relative humidity, and that IAV transmission is most supported at colder temperatures (e.g. 5 ℃) and lower relative humidities (between 20-35%) (57). Whilst it is unknown how these conditions favour IAV stability and transmission, recent hypotheses propose that rates of evaporation of IAV containing aerosols and droplets influence the concentration of salts and protons that directly influence the function and properties of the critical surface viral glycoproteins, such as the receptor binding protein HA (22, 58).

If an IAV virion remains viable long enough to reach a new host, successful transmission then requires the virus to encounter susceptible host cells. This is thought to be primarily determined by the presence, and linkages, of terminal sialic acid moieties on glycans and glycolipids, forming the IAV receptors recognised by HA. Firstly, there are two major types of sialic acids that function as IAV receptors, *N*-acetylneuraminic acid (Neu5Ac) and *N*-glycolylneuraminic acid (Neu5Gc) (22). The latter is enzymatically synthesised from the former, by the Cytidine Monophospho-N-Acetylneuraminic Acid Hydroxylase (CMAH) enzyme. Some species, such as humans and ferrets, lack the functional gene

that encodes this enzyme and therefore only contain Neu5Ac sialic acids (59). This contributes to the species specificity of IAVs, with Neu5Gc binding IAVs (e.g. equine influenza viruses) failing to infect cells expressing Neu5Ac (e.g. human epithelial cells) (59, 60). Furthermore, the linkages of these terminal sialic acids, can either be in a α-2,6- or α-2,3- confirmation, which require HA binding of either human or avian adapted IAVs respectively (61). These subtle differences in receptors are so crucial to IAV infection, and transmission, that differences in sialic acid linkages between different species is considered a major host range barrier, and a major influencer of IAV airborne transmission (22).

Following IAV replication within the cell (see 1.2.2), transmission of IAVs requires the virion to be released from the infected host. This must begin at the infected cell surface, through the sialidase function of NA (see 1.2.2.3). This viral glycoprotein cleaves sialic acids so that newly formed viruses can be untethered from the infected cell (62). This cleavage function of NA also extends to the movement of the virion through the mucus that lines the tissues IAVs infect (63). Mucus provides a constitutive immune barrier by sequestering IAVs. Mucus is a rich source of sialic acids and can quickly tether released IAV virions through HA binding (64). The captured virus can be moved through the respiratory tract via mucociliary flow, or via peristalsis through the gastrointestinal tract, and then is eventually inactivated by the acidic environment of the stomach (65, 66). Therefore, the transmission of IAVs requires an efficient NA protein that can cleave through the mucus of its host (63). Interestingly, the stalk of NA of avian IAVs are shorter than their mammalian counterparts, and this short stalk NA was found to reduce airborne transmission between ferrets (the gold standard for modelling the spread of IAVs between humans) (67). It is hypothesised that stalk length of NA directly influences the ability of these viruses the cleave mucus and is likely establishing a host range barrier and an important consideration when assessing IAV transmissibility (22, 67). Additionally, the mucosa of the human respiratory tract has a low pH of around 5.5 (68), which can cause conformational changes of non-human adapted HA proteins, rendering it unable to trigger fusion in a new host (see 1.2.2.1) (68). Therefore, IAVs that transmit between hosts must be adapted to the pH of the mucus found at the natural site of infection.

Whilst it is clear that environmental factors can influence IAV transmission, the influence of these factors depends on wider context. For example, dense housing of poultry and pigs can reduce the time these viruses need to be viable outside of a host, and therefore could prioritise the influence of viral proteins such as HA and NA in receptor binding and mucus clearance in such settings.

1.1.3.3 Reducing IAV disease burden and spread

The management of IAV outbreaks amongst birds, especially poultry, varies between regions but typically involves a combination of surveillance, vaccination and culling of flocks when highly pathogenic AIV is detected (69). In the UK, when cases of HPAIV are detected in an area, those responsible for the care and management of susceptible birds are required to bring them indoors to prevent any interactions with potentially infected wild animals to help minimise risk of infection.

Public health messaging encourages people to avoid contact with diseased animals, and those who are at high risk of bird flu exposure (such as poultry farmers) are reminded of notifiable symptoms and encouraged to wear personal protective equipment. In the UK, public health bodies (such as Public Health Scotland) offer a free annual flu vaccine to certain bird handlers. When zoonotic infections are detected, these individuals are isolated and disease monitored. Close contacts of these individuals are also determined and monitored for the establishment of symptoms and infection. These efforts are in place to curb any sustained chains of transmission before an epizootic or epidemic ensues.

Vaccines are used to reduce the impact of seasonal flu outbreaks and offer protection especially for the most vulnerable individuals. Until recently these vaccines were typically quadrivalent, meaning they encompass four representative strains of IAVs known to circulate amongst humans in recent times (two IAVs of the H1N1 and H3N2 subtypes, and two IBV lineages: Victoria and Yamagata). Due to the aforementioned antigenic drift of IAVs (see 1.1.2), these vaccines are reviewed and updated annually with the intention of improving the recognition of the evolved virus by the adaptive immune response. Recent updates to the vaccine have reflected the extinction of the Yamagata

lineage (see 1.1.1), and the World Health Organisation (WHO) now recommends a trivalent vaccine (70).

Another important strategy to reduce the disease burden of IAVs is through the use of antiviral drugs. Currently used antiviral drugs against IAVs can be categorised as either neuraminidase inhibitors (oseltamivir, zanamivir or peramivir), or polymerase inhibitors (e.g. the polymerase acidic (PA) endonuclease inhibitor Baloxavir or Favipiravir) (71). The neuraminidase inhibitors mimic the sialic substrate of this enzyme, and therefore are competitive inhibitors. The occupation of the active site with the inhibitor prevents the cleavage of sialic acids (see 1.1.3.2), that through binding HA causes the retention of newly formed virions on the infected cell surface, preventing onward infection spread. In contrast, Baloxavir is not a competitive inhibitor, but instead interferes with the enzymatic function of PA by chelating divalent metal ions which are required in the active site (72, 73). The PA endonuclease function is critical during the transcription of viral mRNA (see 1.2.2.2) and inhibition of this prevents the synthesis of viral proteins required for replication. Favipiravir is a recently approved polymerase inhibitor also used to treat SARS-CoV-2 (74). It inhibits IAV polymerase activity by mimicking a purine nucleotide, and upon its incorporation into the active site it causes premature termination of messenger RNA (mRNA) and viral RNA (vRNA) synthesis (see 1.2.2.2) (74). Alternative drugs that inhibited the function of the M2 ion channel (adamantanes) are no longer used due to the acquired resistance by IAVs against these drugs (75).

1.2 Influenza A virus replication and spread within the host

1.2.1 Overview of the IAV genome

Influenza A viruses contain eight genome segments, which are distinct viral RNA (vRNA) templates bound at the 5′ and 3′ end by an RNA-dependent RNA polymerase (RdRp, Figure 1-2) (76). The IAV polymerase is a heterotrimer, consisting of PA and the polymerase basic 1 and 2 (PB1 and PB2) proteins (77). The remainder of the vRNA template associates with nucleoprotein (NP), which oligomerises to form a helix that packages and protects the viral genome (Figure

1-2 a) (78, 79). Collectively, these segmented structures of RNA and protein are referred to as viral ribonucleoprotein (vRNP) complexes, and represent the infectious units of IAVs.

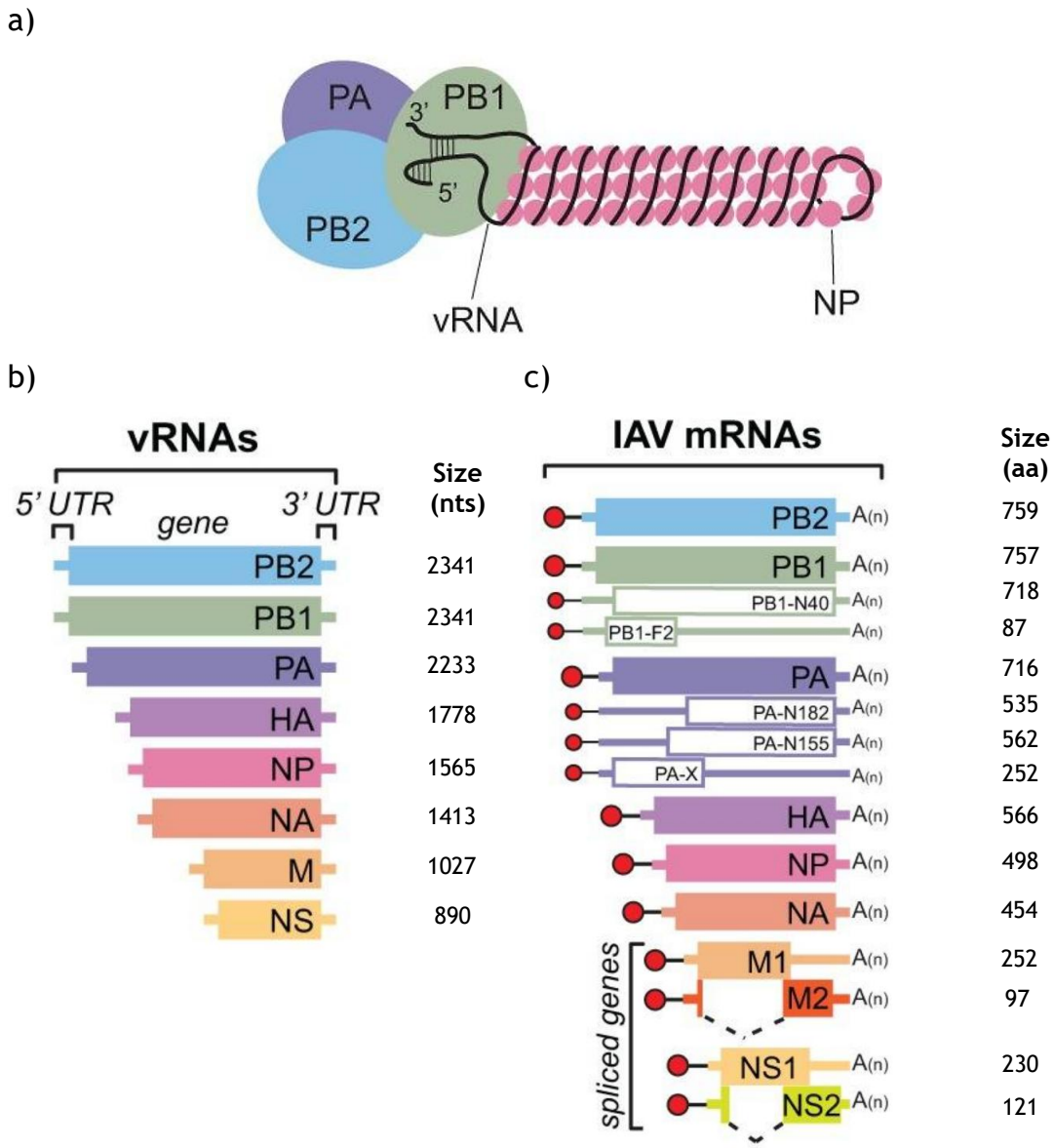

Figure 1-2: The segmented RNA genome of IAV is composed of eight vRNP complexes. (a) Schematic of a vRNP complex which consists of viral RNA in association with a heterotrimeric polymerase head (PB2, PB1 and PA) and NP. (b) The eight viral RNA transcripts that make up the IAV genome. Also shown is the 5' and 3' untranslated regions (UTR), and the size in nucleotides (nts) ot each segment. (c) The mRNA transcripts and gene products (indicated with the boxes) produced from the vRNA templates. The host derived 5′ m^7pppG cap is denoted by the red circle, and the black lines are representative of the 10–13 nucleotides, derived from host mRNAs by the cap-snatching mechanism. The 3′ poly-A tail generated from reiterative stuttering of the polymerase during transcription is abbreviated as A(n). Accessory proteins are shown in the transparent boxes, and the alternatively spliced transcripts of M and NS is show with the dashed lines. Also shown is the size in amino acids (aa) of each protein encoded. Figure adapted from Dou *et al.* (44).

Each vRNA template contains the nucleotide sequence of at least one gene product, that is flanked with 5′ and 3′ untranslated regions (UTRs, Figure 1-2 b). The UTRs are partially complementary, and form the panhandle structure that is

recognised by the RdRp and functions as the viral promoter for transcription (80). Furthermore, the UTRs contain packaging signals for the incorporation of vRNPs into new virions (81). The gene products encoded by each IAV segment are summarised in Table 1-1, and includes the proteins synthesised from the alternatively spliced mRNAs of segment seven and eight (11, 82). Additionally, some IAV segments contain overlapping open reading frames (ORFs), that when translated, produce accessory proteins (proteins that are not required for viral replication but can influence pathogenesis) (83). A notable example of an accessory protein is PB1-F2, which is produced by most IAV strains from a +1 ORF in segment 2 (Figure 1-2 c (84)). PB1-F2 can increase polymerase activity, and induce apoptosis, thereby influencing IAV pathogenesis (84, 85).

Table 1-1: The major IAV gene products and their function.

Segment no.	Gene product	Function	Ref.
1	PB2	Component of the vRNP associated RNA polymerase, and binds to host mRNA during cap snatching.	(86)
2	PB1	Component of the vRNP associated RNA polymerase, and forms the polymerase core.	(80)
3	PA	Component of the vRNP associated RNA polymerase, and has endonuclease activity required for cap snatching.	(87)
4	HA	Binds to host cell receptors and mediates membrane fusion during entry.	(88)
5	NP	Encapsidates viral RNA. Packages and protects RNA and participates in vRNP nuclear trafficking.	(78, 89, 90)
6	NA	Cleaves sialic acids to release virions and prevents aggregation.	(62, 64)
7	M (M1 & M2)	M1 – Lines the inner envelope of virions and is involved in virion assembly and the regulation of virion morphology. M2 - Ion channel that facilitates vRNP uncoating in endosomes.	(91-94)
8	NS (NS1 & NS2/NEP)	NS1 – Interferon antagonist. NS2/NEP – Facilitates vRNP nuclear export. Can support polymerase activity.	(95-97)

1.2.2 IAV replication is dependent on a variety of cellular processes and host factors

The limited number of viral proteins encoded by the IAV genome is indicative of its effectiveness in exploiting the host cell machinery to complete its replication. At each stage of IAV replication (summarised in Figure 1-3), a wide variety of host cell factors and processes are required, and will be discussed in this section.

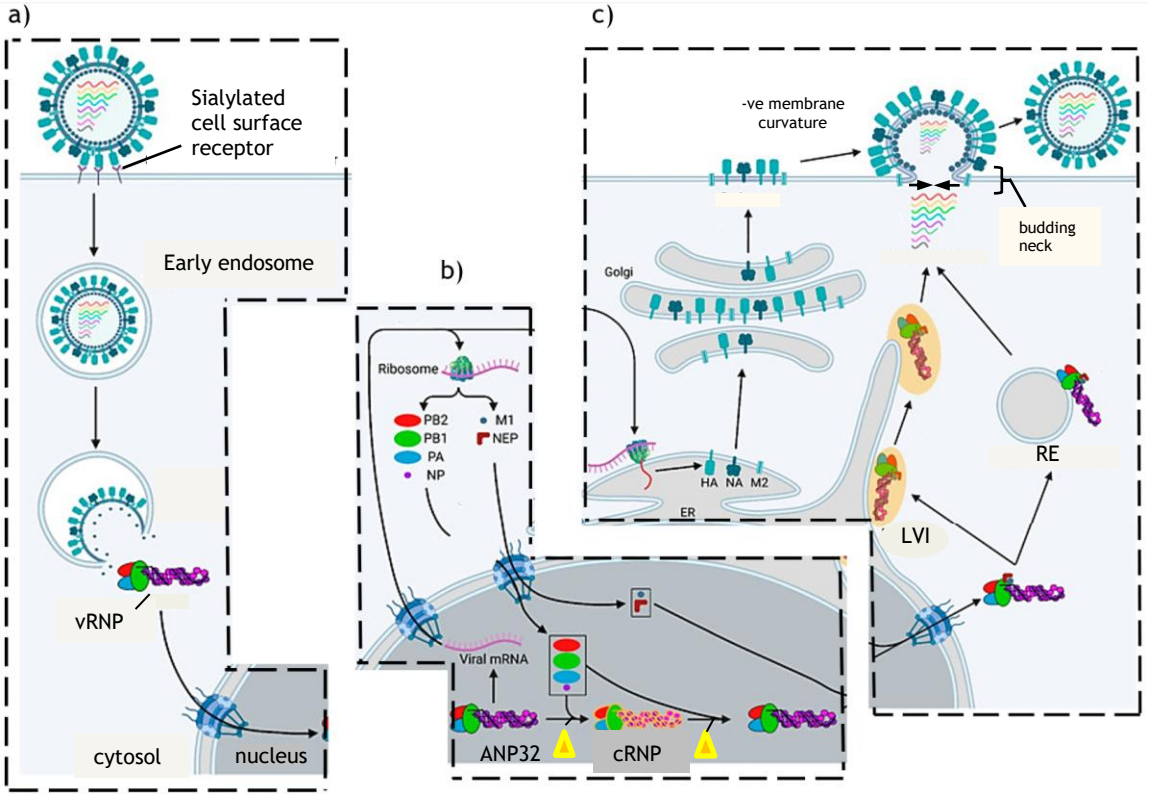

Figure 1-3: The IAV replication cycle. A schematic overview of the general stages of IAV replication, which can be categorised as (a) IAV cellular and nuclear entry (see 1.2.2.1). (b) IAV transcription and replication (see 1.2.2.2) and (c) IAV nuclear export, assembly and release (see 1.2.2.3). vRNP (viral ribonucleoprotein complex), cRNP (complementary ribonucleoprotein complex), ANP32 (Acidic Nuclear Phosphoprotein of size 32 kilodalton, represented by the yellow triangle), mRNA (messenger ribonucleic acid), PB2 (polymerase basic 2 protein), PB1 (polymerase basic 1 protein), PA (polymerase acidic protein), NP (nucleoprotein), M1 (Matrix 1 protein), NEP (nuclear export protein), HA (haemagglutinin), NA (neuraminidase), M2 (matrix 2 protein), ER (endoplasmic reticulum), LVI (Liquid Viral Inclusion) RE (recycling endosome). Figure adapted from Carter *et al.* (11)

1.2.2.1 IAV cellular and nuclear entry

Unusually for an RNA virus, IAVs replicate within the nucleus of the cell. Therefore, the initial stages of the IAV replication cycle are characterised by the entry and movement of the viral genome from the cell surface into the nucleus (Figure 1-3 a). Entry of IAVs requires successful HA binding to specific sialic acid receptors (see 1.1.3.2). The receptor-binding domain of HA resides within the

HA1 subunit (the globular head) and becomes functionally active following proteolytic cleavage of the HA0 precursor by host proteases such as human airway trypsin-like protease (HAT) or transmembrane protease serine 2 (TMPRSS2) (98, 99). Internalisation of IAV virions occurs through receptor mediated endocytosis, and is primarily clathrin-dependent, requiring both dynamin and the adaptor protein Epsin-1 (100, 101). However, endocytosis of IAV virions can also occur through the mechanism of macropinocytosis (102). The internalised virion is first located within an early endosome, that matures into a late endosome characterised by a low luminal pH. This acidic environment causes a conformational change of HA that leads to the exposure of the fusion peptide (located at the N-terminus of the HA2 subunit, the stem of the glycoprotein) (103). The hydrophobic fusion peptide is approximately 20 amino acids long, and is inserted into the endosomal membrane, anchoring the virion. The HA2 proteins then fold back on themselves, and in doing so, brings the membrane of the endosome and virion in close proximity, enabling fusion (104).

The low pH of the late endosome also activates the M2 ion channel which acidifies the virion core and allows the flow of potassium ions, causing vRNPs to dissociate from M1 (105). This exposes nuclear localisation signals (NLS) located on the N-terminus of NP, which is engaged by adaptor protein, importin α (106, 107). The importin α proteins are in turn recognised by the transport receptor, importin ß, via the N-terminal importin ß binding domain (108). The vRNPs in complex with these importins traverses the nuclear pore complex (NPC), where importin α and ß dissociate from vRNPs via separate mechanisms involving the host factors Ran-GTP and CSE1L respectively (109).

1.2.2.2 IAV transcription and replication

IAVs undergo transcription and replication in the nucleus (Figure 1-3 b), where it has access to a number of key host factors required for these processes. First, viral mRNA is transcribed from vRNA templates by the vRNP associated RdRp. Transcription is primed through cap snatching, which refers to the process by which the subunits of the IAV polymerase binds, cleaves and positions 5′m^7pppG caps from host derived mRNA transcripts for viral mRNA elongation and ultimately protein synthesis by ribosomes (110). Specifically, the PB2 subunit contains a cap binding domain that recognises and interacts with 5′ capped host

mRNAs (80). The PA subunit interacts with the phosphorylated (at serine 5) C-terminus of the host RNA polymerase II, encouraging the binding of PB2 with nascent RNA transcripts (111). Additionally, PA contains an endonuclease domain that cleaves these host mRNAs approximately 10 to 13 nucleotides downstream from the 5′ cap (112). The PB2 domain, still bound to the 5′ cap, is thought to rotate 70° to position the capped RNA fragment into the RdRp active site within the PB1 subunit (111). Viral mRNA elongation is terminated when the polymerase encounters a short stretch of uracil bases at the 5′ end of the vRNA template (113). This causes the polymerase to stutter reiteratively, and ultimately polyadenylates the mRNA transcripts (113).

During IAV infection, transcription precedes genomic replication as the formation of more vRNP copies first requires the production of more viral proteins. IAV mRNAs are exported from the nucleus by the nuclear RNA export factor 1 (NXF1) pathway (108, 114), and translation of viral proteins not found within the virion envelope is performed by cytoplasmic ribosomes (Figure 1-3). The nuclear import of newly synthesised PB2 and NP occurs through the typical importin α -ß import pathway, utilising NLSs present in both proteins (115). However, PB1 and PA are imported as a heterodimer, with the NLS of PB1 directly interacting with ß importin-binding protein 5 (RanBP5), and therefore not requiring importin α (116, 117).

The import of NP, PB2, PB1 and PA into the nucleus means that viral genome replication can be supported. In contrast with transcription, the process of vRNA replication occurs through an intermediate complementary RNA (cRNA) transcript, and is primer-independent. The production of the positive-sense cRNA, and negative-sense vRNA, requires the formation of a replication platform (80, 118). This consists of the RNA containing, ribonucleoprotein complex with a replicating polymerase, an RNA free encapsidating polymerase and a host Acidic Nuclear Phosphoprotein of size 32 kilodalton (ANP32) protein. First, the vRNA is used as a template by the replicating polymerase to produce the cRNA strand. The synthesis of cRNA occurs through terminal initiation, with an ApG dinucleotide base pairing with the first two nucleotides of the vRNA 3’ end (80). The encapsidating polymerase forms an asymmetric dimer with the replicating polymerase, optimally positioning the promoter binding site of the empty polymerase to receive the 5’ end of cRNA as it emerges from the replicating

polymerase (119). The ANP32 protein interacts with the encapsidating polymerase of IAVs and contains a low complexity acidic region (LCAR) which interacts with NP (119). Current hypotheses propose that ANP32 increases the local density of IAV NP, enabling its association with RNA and the co-replicative assembly of the ribonucleoprotein complex (80).

The production of vRNPs from cRNPs follows a similar process, requiring pppApG dinucleotide initiation, and the replication platform. However, the difference in positions of the cRNA 3' promoter within the RdRp requires the template to be repositioned within the active site prior to elongation to ensure full length vRNA synthesis (80). This backtracking to the 3' end of vRNA is thought to require conformational changes of the polymerase triggered by the dimerisation of the replicating polymerase with a symmetrical transactivating viral polymerase (120).

1.2.2.3 IAV nuclear export, assembly and release

The formation of IAV progeny requires the trafficking of newly assembled vRNPs out of the nucleus and towards budding sites at the plasma membrane, where they are joined by a number of host and viral proteins (121) (Figure 1-3 c). The IAV membrane proteins (HA, NA and M2) are synthesised by ribosomes associated with the endoplasmic reticulum (ER) where they integrate into membranes, appropriately fold and oligomerise (44). Next, these proteins are delivered to the Golgi where, in the case of HPAI, HA0 is modified and the polybasic cleavage site within this viral protein is proteolytically cleaved (producing the aforementioned HA1 and HA2, see 1.2.2.1). Cleavage of HPAI HA0 can be performed within this subcellular organelle due to the ability of ubiquitously expressed proteases that can catalyse this (122). In contrast, the monobasic cleavage site of LPAI and human IAV stains, restricts HA0 cleavage to cell surface located proteases (123). The virus membrane proteins are then delivered to budding sites in the plasma membrane. The accumulation of HA at the plasma membrane signals (via the Ras-dependent Raf/MEK/ERK mitogen-activated protein (MAP) kinase signalling pathway) that virion formation can commence, and triggers the nuclear export of vRNPs (124). Nuclear export requires both M1 and NEP to be transported to the nucleus. Currently published data has generated the daisy chain model of vRNP nuclear export, where in which M1

directly binds to vRNPs (particularly NP) and functions as an adaptor protein, recruiting the NEP protein and subsequently CRM1, forming the vRNP – M1 – NEP – CRM1 export complex (105, 125-127). CRM1 binds to nuclear export signals and forms a complex with Ran-GTP, which mediates the nuclear export of the substrate (128).

The trafficking of vRNPs through the cytoplasm to the plasma membrane requires interactions of the host GTPase Rab11 with the PB2-627 domain of vRNPs (129, 130). Two models of intracellular trafficking of Rab11 associated vRNPs have been proposed: the recycling endosome model and the modified ER model (Figure 1-3 c). In the recycling endosome model, vRNP - Rab11 are loaded onto recycling endosomes that move along microtubules towards the plasma membrane (131). Conversely, the modified ER model proposes that IAV infection alters the interactions of Rab11, and causes extensive tubulation of the ER that extends throughout the cytoplasm of the cell (132). It is then proposed that vRNPs associate with Rab11 on these modified ER networks to form irregularly coated vesicles that bud towards the plasma membrane (132). More recently, it has been suggested that liquid organelles that are found near the ER exit sites can accumulate Rab11 and vRNPs forming liquid viral inclusions (133). These inclusions can move along the modified ER, merging with each other, encouraging both intersegment interactions and the delivery of different gene segments (133, 134).

IAVs bud from lipid rafts within the plasma membrane that are enriched in cholesterol and sphingolipids (135). These domains must receive the envelope proteins and all eight vRNPs for fully infectious particles to form. Whilst the localisation of NA to lipid rafts is believed to be due to an inherent property of its transmembrane domain, HA is thought to first require the fatty acid modifications that occurs in the Golgi (136-138). The cytoplasmic tails of these glycoproteins is proposed to then recruit M1 to the cytoplasmic side, whilst M2 accumulates at the boundaries of the lipid rafts (139, 140). With the help of packaging signals, the vRNPs are assembled to the budding sites via binding to the recruited M1 (141, 142). However, with many virions (up to 90%) lacking at least one gene segment (with these particles being referred to as semi-infectious), suggest that the packaging of IAV gene segments is inefficient (143).

Budding of IAV progeny virions is induced through the triggering of membrane curvature (Figure 1-3c). IAVs achieve this through membrane crowding of the outer leaflet of the plasma membrane by HA and NA (144, 145), and the oligomerisation of M1 at the cytoplasmic side of the budding site is thought to confer a membrane bending property of this protein (146). Additionally, M2 is a membrane bending protein and due to its accumulation at the lipid raft boundaries, the resulting negative membrane curvature brings the opposite sides of the viral envelope together, facilitating viral bud neck formation and ultimately scission (Figure 1-3c) (139). After scission, the viral envelope is now separate from the plasma membrane, however, it still remains associated with the infected cell surface until NA cleaves the sialic acid receptors (see 1.1.3.2).

1.2.3 The spread and interactions of IAVs within the lung

1.2.3.1 IAV spread within the lung is spatially structured

IAVs released from the apical side of epithelial cells, into the airway lumen, spread to the surrounding epithelia of the lung in a spatially structured way (147, 148). This results in the formation of infected lesions at the approximate site of initial virus deposition, which expand over time (149, 150). From *in vitro* studies, it is estimated that single infected cells can produce several hundred viruses (e.g. seasonal H3N2 can produce approximately 700 viruses on average) (151). This burst size emphasises the potential of the virion to seed many individual cellular infections within the lung. However, the strong spatial structure of IAV infection points to robust ways in which IAV within host spread is governed. Factors that contribute to the patterns of IAV spread *in vivo*, include the extent by which mucins can sequester IAV virions, the interactions between infected regions and the spatial heterogeneity of cell types with different receptor distributions and proteases (that cleave HA0) expressed (reviewed in (148)).

Whilst IAV infection is clearly spatially structured, the distance that progeny IAV virions can spread within the lung is experimentally uncharacterised. Nevertheless, the ability of IAVs to spread between hosts demonstrates that long distance spread of cell-free IAV virions occurs, and should also contribute to long range within host spread. Evidence to this point was presented by Fukuyama *et*

al, when they showed that fluorescent reporter viruses formed infected foci within bronchial epithelial cells by 2 days post infection (152). However, IAV infection was detected at relatively distant sites within alveolar cells by 5 days post infection, suggesting that the flow of air may allow for the occasional delivery of IAV virions to susceptible cells in deeper regions of the lung (152).

1.2.3.2 Spread of infection within the lung shapes IAV population diversity

Intriguingly, as IAV infection progresses, the genetic diversity amongst these viruses was reduced in ways consistent with diversity loss during general spatial expansion of populations (150, 153, 154). It was found that stochastic effects reduced nucleotide variants isolated from an infected individual over several days by 43%, despite consistently high viral titres (154). This suggests that stochastic founder effects and genetic bottlenecks are at play during IAV infection spread in the respiratory tract.

Ferreri *et al*. investigated the impact of barcoded H1N1 IAV dispersal within the respiratory tract (encompassing the nasal cavity, trachea and lung lobes of ferrets) on population diversity (150). The authors found that a high population diversity was maintained as IAV infection (that was initiated in the nasal cavity) moves to the trachea by diffusive dispersal, i.e. gradual expansion of the leading edge of an infected region (150). The spatial continuation of the original population is believed to maintain the genotypes of the founder population, and lowers the impact of genetic drift - with neutral or deleterious mutations simply disappearing or being outcompeted by either similar or adapted progeny (155). Therefore, the high diversity and rapid expansion of infection by diffusive dispersal at these anatomical sites is more conducive to adaptive mutations (150). In contrast, long-distance dispersal to the lungs resulted in a loss of diversity likely due to bottlenecks during seeding and the genetic isolation of those viruses able to seed infection in the lower respiratory tract (150). Under these conditions, characterised by small and isolated populations, viral evolution is governed more strongly by the stochastic process of genetic drift (150).

In addition to the effects on IAV population genetic diversity, the within host spread of IAVs can also drive changes in virion morphology. IAV virions are pleiomorphic (Figure 1-4), with morphologies being categorised as spherical,

bacilliform or filamentous (156, 157). Although the most widely-used laboratory strains of IAVs have lost their ability to form filamentous virions, clinical and veterinary isolates typically produce a variety of virions including long filaments (reviewed in (158)), and natural infections seemingly select for filamentous particles (159-161). This suggests that the filamentous morphology might provide an advantage to the within host spread of IAV infection. In support of this idea, it has recently been shown that filamentous virions can enhance infectivity and fusion even in the presence of neutralising antibodies (162).

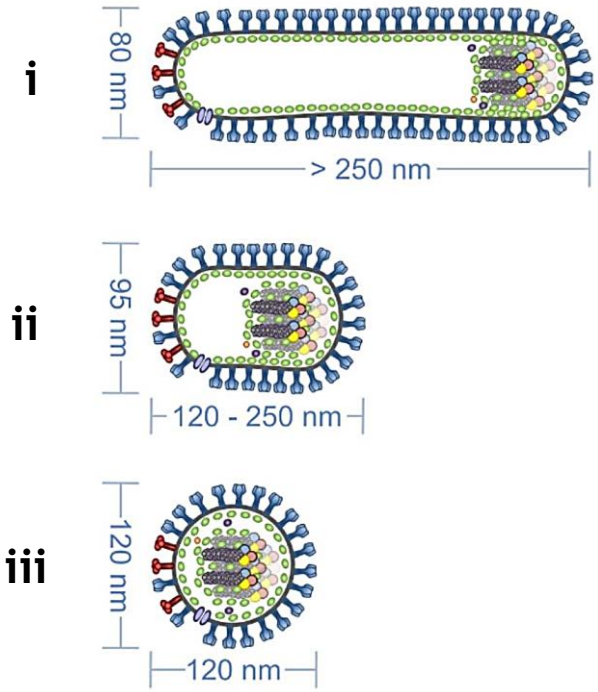

Figure 1-4: IAV virions are pleiomorphic. The morphology of IAVs can be categorised as (i) filamentous, (ii) bacilliform, or (iii) spherical. nm (nanometres). Figure modified from Dadonaite *et al.* (158).

1.2.3.3 Virus-virus interactions in the lung: coinfection and superinfection

During the spread of IAVs within the lung, infected lesions can expand into one another (163). This can bring viruses descended from different progenitors into close proximity with each other. The consequence of this is an increased potential for virus-virus interactions within cells, relative to that achieved during initial infection following natural transmission. That being said, the delivery of multiple IAV genomes into a single cell (resulting in coinfection) can be temporally restricted. If the timings of primary and secondary virus infection are not identical, the cell is said to be superinfected by the second virus, and this is the most likely method of coinfection (163). However, superinfection can

be restricted by superinfection exclusion, which is a time dependent cellular block to secondary virus infection (163). The onset of IAV superinfection exclusion occurs as early as 3 hours post primary infection, and therefore secondary virus infection needs to be rapid for these viruses to interact (163). Whilst best characterised *in vitro*, this effect can also be seen in the lungs of infected mice (163). Sims *et al.* used different fluorescent reporter viruses to intranasally infect mice, and where evidence was found of distinct lesions expanding into each other, coinfection (cells positive for both fluorophores) was only found within a small number of cells (163). Certain anatomical regions, such as the bronchi, had a greater likelihood of containing coinfected lesions and the authors propose that this was a consequence of the simultaneous delivery of large numbers of viruses at this site shortly after experimental intranasal inoculation (163). Indeed, other research has confirmed a high percentage (20%) of coinfected bronchial epithelial cells using similar fluorescent reporter IAVs (152).

If achieved by spreading IAVs, coinfection can have significant consequences. Firstly, the kinetics of IAV replication can be enhanced by coinfection with homologous viruses (164). Additionally, since the majority of IAV virions lack the ability to express genes from at least one genome segment (see 1.2.2.3), coinfection can provide an exogenous source of this missing segment. This complementation, known as multiplicity reactivation, can reestablish the fully infectious parental virus (143). However, if coinfection is achieved by differential parental viruses, this can lead to a unique combination of genome segments, creating a novel strain with pandemic potential (i.e. reassortment, see 1.1.2). Indeed, coinfected cells can efficiently produce reassortant progeny (165), and reassortment can be frequently detected from isolates collected from guinea pigs coinfected as a result of natural transmission from differently infected cagemates (166). Therefore, coinfection resulting in reassortment is very much a real world risk as is evidenced by the high frequency of reassortment amongst avian influenza viruses (167).

Not all consequences of coinfection enhance, or expand, the infectious capabilities of IAVs. For example, the gene segments of IAVs can have large internal deletions that fail to produce the required viral proteins for IAV replication (168). These defective viral genomes (DVGs) require coinfection with

complete, wild type (WT) genomes in order to facilitate their replication. Since DVGs are characteristically shorter in length compared with WT genomes, they are thought to be replicated at an increased rate (169). For example, a genome replication assay using increasingly shorter length PB1 and HA mutants showed that there was an inverse relationship between segment length and the enrichment of them (170). In this way, DVGs could outcompete WT genomes in their acquisition of viral proteins, such as the polymerase complexes. Ultimately, DVGs can package into virions after coinfection. This therefore reduces the proportion of virions produced that contain full length gene segments (i.e. WT virus). However, the aforementioned need DVGs have for coinfection with a WT virus eventually reduces their abundance in the population and an increases in WT virus can be observed (171).

1.3 Direct cell to cell spread

The conventional route of IAV spread within and between hosts is through virions. Although this can be an efficient route for the spread of suitably adapted IAVs within a susceptible host, the extracellular environment often poses a hostile barrier to virions, and limits their within-host dissemination. Whether it is through antibody neutralisation, antiviral drug treatment or the sequestration of virions in mucus, the movement of virions to neighbouring cells can be restricted. These challenges can often be circumvented by virus direct cell to cell spread. Virus direct cell to cell spread refers to the transmission of viral components—such as genomes, proteins, or replication complexes—from an infected cell to adjacent cells via physical contact. This mode of spread bypasses the broader extracellular environment, and some mechanisms occur independently of fully formed viral particles. In this section I will outline these different mechanisms of virus direct cell to cell spread, the proviral consequences of these unconventional (and often overlooked) routes and the current evidence for the direct cell to cell spread of IAVs.

1.3.1 Mechanisms of animal virus direct cell to cell spread

1.3.1.1 Syncytia and membrane pores

Multinucleated giant cells, also known as syncytia, arise from membrane fusion between adjacent cells. This membrane fusion can result from the expression

and stimulated conformational changes of abundant viral fusion proteins on the cell surface. Many viruses, including all enveloped viruses, have viral fusion proteins and numerous studies have shown that these proteins can induce syncytia formation both *in vitro* and *in vivo* (172-174). The result is the complete mixing of the cytoplasm of the fused cells, along with the viral genomes present. This grants the virus immediate access to large quantities of cellular material that can carry out gene expression and replication without ever encountering the extracellular environment (175).

Membrane pores (initially identified in measles virus infected, well-differentiated primary human airway epithelial cell cultures) allow cytoplasmic transfer between cells and with it, ribonucleoprotein complexes of the measles virus (176). In these infected cultures, membrane pores between adjacent cells were found to be approximately 250 nm in diameter, and their formation required afadin, the actin filament binding protein nectin-4 (the measles virus receptor) (176). The measles virus ribonucleoprotein complexes move along the circumapical F-actin rings that are localised near adherens junctions (177). The membrane pores are anchored to circumapical F-actin rings through interactions with afadin, and viral glycoprotein H binding to nectin-4 stabilises the membrane pore, facilitating the delivery and movement of the measles virus ribonucleoprotein complexes through the pore, to the adjacent cell (177).

1.3.1.2 Cell junctions and virological synapses

Cell junctions are composed of several transmembrane proteins that form localised seals (tight junctions, adherens junctions, desmosomes and gap junctions) between polarised epithelial cells. These barriers are not usually penetrated by animal viruses in healthy epithelia (178), but several viruses have now been shown to use these cell junctions to great effect. For example, tight junctions are implicated in the direct cell to cell spread of hepatitis C virus (HCV). It was found that components of tight junctions (claudin-1 and occludin) were required for the direct cell to cell spread of HCV, leading to the proposal that HCV transmission can occur through partially sealed cell junctions (179, 180). In contrast, adherens junctions are involved in the direct cell to cell spread of herpes simplex virus type 1 (HSV-1). Specifically, HSV-1 is preferentially directed to cell junctions by the glycoprotein complex gI/gE (181,

182). It was then found that gI/gE colocalised with ß-catenin - a protein component of adherens junctions - but not with tight junction components such as ZO-1 (182). Indeed the cell to cell spread of HSV-1 is dependent on gI/gE, and is not restricted by the presence of neutralising antibodies that are excluded from cell junctions (181).

The role of desmosomes (cell junctions containing desmosomal cadherins and intermediate filaments such as keratin, (183)) in virus cell to cell spread is less well studied, nevertheless, lymphocytic choriomeningitis virus (LCMV) infection was found to undergo direct cell to cell spread following an increase desmosome formation (184). Mechanistically, LCMV increases desmosome formation via the nucleoprotein binding to, and stabilisation of, keratin 1 - an important desmosome component (184). Lastly, gap junctions are yet to be shown to facilitate the direct cell to cell spread of viruses, and their role in regulating virus transmission is currently limited to their importance in cell communication. For example, pseudorabies virus (PRV) hinders gap junction intercellular communication and with it innate immune response activation, facilitating conventional virus spread (185).

Virological synapses similarly allow the transfer of viruses between a narrow, antibody excluding space between adjacent cell membranes (186). However, unlike existing cell junctions, these specialised contact zones are formed following infection. For example, following contact of a human T-cell leukaemia virus type 1 (HTLV-1) infected lymphocytes with an uninfected T-cell, Env, Gag and viral RNA is rapidly recruited to the contact site (187). Analogous results are seen with HIV-1 infected T cells, and the proposed model of direct cell to cell spread of these viruses is the release of the virus particle into the viral synaptic cleft and fusion with the uninfected cell (187-189).

1.3.1.3 Filopodia and actin tails

Through the polymerisation of cortical F-actin, the plasma membrane can be narrowly extended out to form finger-liker protrusions (0.1 – 0.3 µm in diameter), known as filopodia (190). These extensions are multifunctional, with roles in cell motility, extracellular matrix adhesion and cellular communication (190). The formation of filopodia is driven by the vasodilator-stimulated

phosphoprotein (VASP) which recruits and clusters the Insulin Receptor Substrate of 53 Kilodalton (IRSp53), which functions as a plasma membrane deforming protein (191). IRSp53 is activated following the binding of the Rho GTPase Cdc42, a known regulator of actin polymerisation that works in concert with formin proteins and Myosin X that elongates and stabilises actin bundles (192). This results in the initiation and elongation of the filopodia protrusion.

Even though filopodia are relatively short structures (approximate average length of 3 μm, and rarely exceeding 5 μm) (193), they are able to reduce the distances between cells, enabling the direct cell to cell spread of viruses in different ways. In the case of murine leukaemia virus (MLV) cell to cell transmission, filopodia of different cellular origin can interact through Env - receptor interactions forming a filopodia bridge (a cytoneme) (194). The MLV virions attached to the infected cell was found to "surf" along the filopodia bridge surface towards the uninfected cell body (194). Alternatively, filopodia can be induced from African swine fever virus (ASFV) and alphavirus infection, where direct cell to cell spread is performed respectively from virions localised in the filopodia tip, or virions that assemble and bud from the tip into a protected space, similar to that in a virological synapse (195, 196).

Actin tails, triggered by virus infection, also require actin polymerisation at the rear of a virus particle and at the tip of the structure. However, what has traditionally distinguished these structures from filopodia in the direct cell to cell spread of viruses, is the activation of actin nucleation factors (N-WASP and Arp2/3) by viral proteins, resulting in branched actin polymerisation as opposed to formin-mediated parallel actin bundles (197-199). Viruses that use actin tails to project the virion towards uninfected cells include vaccinia virus (VACV), which induce their formation through the A36 and A33 proteins (200, 201).

1.3.1.4 Tunnelling nanotubes

Tunnelling nanotubes (TNTs) are similar to filopodia, in that they are F-actin rich, thin membrane extensions that connect cells (202). However, what makes TNTs unique is that they connect cells over a much longer distance, they are suspended above the substrate *in vitro* and can mediate fusion to create an open-ended channel between the cytoplasm of cells in connection (193, 202). In

this way, TNTs can facilitate cellular communication through trafficking, and delivery, of various cargos such as ions, proteins, RNA and organelles (202-205). Structures that display most, but not all of these defining features are commonly referred to as TNT-like structures (TLSs) (206-209).

The dimensions of TNTs vary between cell types, and their thicknesses is thought to be influenced primarily by their cytoskeletal components (210). For example, TNTs that contain only F-actin (the essential cytoskeletal component of TNTs) are noticeably thinner than those that also contain microtubules (>0.7 μm) (211, 212). This distinction also influences the cargos that each type of TNT traffics, with microtubules enabling the trafficking of larger cargo, such as entire organelles (211).

TNTs were first reported in 2004 by Rustom *et al*. and their unique biological properties were noted alongside their fragility and transiency (202). The use of TNTs as a mechanism of virus direct cell to cell spread was reported just 4 years later, when Sowinski *et al*. found that HIV exploited TNTs for its spread between distant T cells (213). In this instance, the TNTs were closed-ended, meaning that membrane fusion was not required, and the cytoplasm of the cells remained distinct during transmission (213). Since this discovery, it has since been shown that HIV not only uses TNTs for direct cell to cell spread, but infection actually induces their formation between macrophages (212). Interestingly, these TNTs were open-ended, revealing a cell type influence on the types of TNTs that formed (212). The literature of TNTs in virus direct cell to cell spread has continued to greatly expand, and many viruses have since been shown to induce and exploit these structures for immune evading intercellular transmission, and I will discuss this further in section 1.4.2.1.

1.3.2 Advantages of direct cell to cell spread

Mechanism of direct cell to cell spread deliver virions, or viral genomes, right to the target cell. This can prove to be advantageous for the virus in many different ways. Firstly, this delivery can be much faster than cell free virions, bypassing the rate limiting step of diffusion of extracellular virions (214). Specifically, mechanisms of direct cell to cell spread that proceed membrane fusion, can deliver viral genomes before the stages of virion assembly.

Additionally, the recruitment of receptors of some viruses to cell to cell contact sites can increase the efficiency of virus entry (215). This can result in direct cell to cell spread being the most efficient route of intercellular virus transmission. For example, it is estimated that HIV spreads directly between cells 10-18,000 times more efficiently than with extracellular virions (200, 215, 216).

Direct cell to cell spread can also result in the delivery of multiple viral genomes to a single cell (217). This can increase the likelihood that infection is successfully established, overcoming genetic defects (218). Furthermore, the delivery of multiple viral genomes could influence virus fitness and evolution, alleviating transmission bottlenecks and maintaining heterogeneity in virus populations (218, 219). However, within individual cells, infection is still established by fewer viruses than are delivered (189, 215, 217). Therefore, genetic bottlenecks are likely still a feature of direct cell to cell spread.

Perhaps the best characterised advantage of virus direct cell to cell spread is the evasion of anti-viral and immune barriers. Direct cell to cell spread establishes cell contacts that enables the transfer of infection even in the presence of neutralising antibodies (179, 220, 221). This can be achieved by the formation of tight cell to cell contacts (e.g. cell junctions and virological synapses) that cannot be breached by antibodies (179), or through the transfer of cytoplasmic viral material avoiding the antibody containing extracellular space entirely (e.g. syncytia, membrane pores and open-ended TNTs) (221-223). Additionally, some evidence suggests that direct cell to cell spread of retroviruses is less inhibited by innate immune restriction factors (TRIM5α and tetherin) (224-226), and the transfer of IAV NS1, the interferon antagonist, through TNTs is speculated to suppress the innate immune response in recipient cells, priming them for infection (223).

1.3.3 Direct cell to cell spread of IAVs

The observation of IAV direct cell to cell spread has been reported in numerous studies. Within each, interesting mechanistic insights have been generated. Firstly, Mori *et al*. showed that direct cell to cell spread of the A/WSN/1933 (H1N1) IAV strain occurred on the apical side of cells and was independent of the

function of NA (227). Instead the authors linked the function of HA, and its cleavage, to greater amounts of cell to cell transmission, with exogenous TPCK trypsin facilitating the direct cell to cell transmission of an NA deficient WSN virus (227). Unusually, WSN does not require exogenous TPCK trypsin for HA mediated virus entry (228), suggesting that HA function alone is insufficient, or that IAV direct cell to cell spread requires exogenous proteases. Therefore, Mori *et al.* consistently used exogenous TPCK treated trypsin in further assays and found that the area of Udorn infection was reduced when virion release was inhibited by oseltamivir treatment, but this was reduced even further when amantadine was added in combination. This work therefore suggested that IAVs performed direct cell to cell spread through mechanisms that transfer virions that are associated with cell surfaces, that then undergo canonical entry through receptor mediated endocytosis.

Roberts *et al.* showed that 44% of Udorn NP positive foci consisted of 3 or more adjacent cells (microplaques) when cell free virion spread was inhibited with zanamivir, and that the mean number of cells within a microplaque was approximately 3 (222). To then investigate whether virion entry was required for this efficient direct cell to cell spread, the authors used ammonium chloride in place of zanamivir. Ammonium chloride prevents HA fusion to endosomes by raising the intraluminal pH, as well as inhibiting the M2 ion channel (229). The authors found that when virion entry was inhibited by ammonium chloride, there were comparable microplaque sizes to the zanamivir treated samples (222). This indicated that the direct cell to cell spread of Udorn was not occurring through the transfer of cell associated viruses that required canonical virion entry, contrary to the report by Mori *et al.*(227). The authors then showed that this direct cell to cell spread of Udorn can be significantly reduced when cells are treated with drugs that disrupt the cytoskeleton (222). This result correlated with the observation that these drugs reduced the formation of TNTs, for which they also show contained components of the vRNP complex. This suggested that these structures can incorporate IAV genomes and deliver them to neighbouring cells (222). Therefore, Roberts *et al.* showed that IAV direct cell to cell spread did not require virion entry, but instead occurred primarily through cytoplasmic viral genome transfer, with an implication of TNTs in facilitating this.

Subsequently, Ganti *et al*. confirmed that IAVs spread directly between cells through cytoplasmic viral genome transfer. They did this by showing that microplaques still formed following infection with HA-deficient viruses (230). Furthermore, the authors showed that microplaques could be significantly reduced following treatment with cytochalasin D – a drug that disrupts the F-actin cytoskeleton, and with it TNT formation (222, 230). They also showed a significant reduction in viral titre when cocultures of HA expressing cells and HA-deficient IAV infected WT cells were treated with this drug. This strengthened the suggestion made by Roberts *et al*., that TNTs mediate the direct cell to cell spread of cytoplasmic IAV genomes. Additionally, the authors presented evidence that the cytoplasmic transfer of material (including vRNPs) through TNTs may not be unidirectional. They found that when they infected Rab11a knock out (KO) A549 cells and then cocultured them with uninfected WT A549 cells, Rab11a and NP were found to colocalise within TNTs. This revealed that both cells in a TNT connection can contribute to the contents within a TNT, and therefore, the cargo delivered by it. This suggests that the transfer of cytoplasmic viral genomes during IAV direct cell to cell spread may be bidirectional and could facilitate simultaneous coinfection, or superinfection (see 1.2.3.3), of two cells if the TNT connected separately infected cells.

The cocultures performed by Kongsomros *et al*. also showed that cytochalasin D reduced the direct cell to cell spread of H5N1 and H1N1 viruses in the presence of oseltamivir (231). This effect was greater for the H5N1 virus which correlated with an ability of this strain to cause greater levels of membrane exchange (trogocytosis) (231). The authors propose that trogocytosis is the process by which IAV direct cell to cell spread occurs and establishes this difference between the strains of this study. They also propose that trogocytosis then leads to the formation of TNTs (that they observed H5N1 viruses to induce), which can then continue the direct cell to cell spread of IAV infection (231). This model supports the idea that both mechanisms of IAV direct cell to cell spread—cell-associated virus transfer (made possible through trogocytosis) and cytoplasmic viral genome transfer (made possible through open-ended TNTs)—can operate simultaneously. This also could bridge studies that present evidence for one of the mechanisms over the other. However, because antiviral drugs were absent in assays comparing cell to cell transmission between direct-contact cells (i.e.,

coculture) and transwell-separated cells, as well as in assays measuring trogocytosis levels, it remains unclear whether direct cell to cell spread is responsible for the observed differences. If such processes are involved, the specific mechanism driving these differences are also uncertain. In other words, the contributions of cell associated virus transfer and cytoplasmic viral genome transfer were not deciphered. Furthermore, the data presented does not rule out the possibility that trogocytosis was caused by TNTs that fused with the recipient cells. The mechanistic insights from this study are further confused by the lack of convincing evidence that trogocytosis is actually mediating direct cell to cell spread of IAV infection, as indeed, the timings of IAV direct cell to cell spread presented in this study (3 hours post coculture) poorly correlate with when trogocytosis is observed (1 hour), but do correlate with the induction of TNTs (3 hours) (231). Additionally, without a comparison in TNT induction between the strains of this study, the contribution of TNTs as the mechanism that could be establishing this strain-dependent difference in direct cell to cell spread remains unexplored.

1.4 Tunnelling nanotubes: their formation, induction and role in disease

The majority of the current evidence of IAV direct cell to cell spread has suggested a key role of TNTs in this process (see 1.3.3). This mechanism of direct cell to cell spread is shared with other viruses, and the induction of these structures is a notable feature of this unconventional route of intercellular transmission (see 1.3.1.4). Therefore, an understanding of how TNTs could be used by IAVs for the direct cell to cell spread of infection requires knowledge of how TNTs are formed and induced, as well as their known role in regulating disease and cellular function.

1.4.1 Mechanisms of tunnelling nanotube formation

1.4.1.1 Modes and stages of TNT formation

Currently there are two proposed modes of TNT formation. The first is cell dislodgement, where two initially adjacent cells are in association with each other via plasma membrane interactions. As the cells then move apart, the maintenance of a plasma membrane association creates a TNT (232, 233).

Alternatively, the mode of protrusion extension proposes that a cell produces a TNT precursor structure upon receiving a tubulogenic stimuli, and this protrusion is extended by the modulation of cortical F-actin until it reaches and associates with the plasma membrane of a distant cell, forming a TNT (193, 233).

Within the protrusion extension mechanism of TNT formation, the initial involvement of stimuli produced by different cellular and environmental cues (Figure 1-5 a), has resulted in a greater curiosity and attention for this mechanism. Such focus has aided the differentiation of TNTs from structures such as filopodia. For example, cell micropatterning experiments (preventing cell dislodgement) enabled the characterisation of comparative filopodia and TNT lengths, as well as an impressive dissection of the unique modulation of branched and linear F-actin networks required for TNT initiation (193) (Figure 1-5 b, also see 1.4.1.2). Additionally, the induction of TNTs by different stimuli (see 1.4.2), has led to exciting hypotheses surrounding the directionality of subsequent TNT precursor extension. It is speculated that TNT precursors are frequently directed to chemokine producing cells, extending along a concentration gradient of secreted factors (234). This is referred to as the TNT pathfinding hypothesis (Figure 1-5 c), and is thought to determine which cell pairs become connected and ultimately the downstream consequences of the triggered TNTs (235).

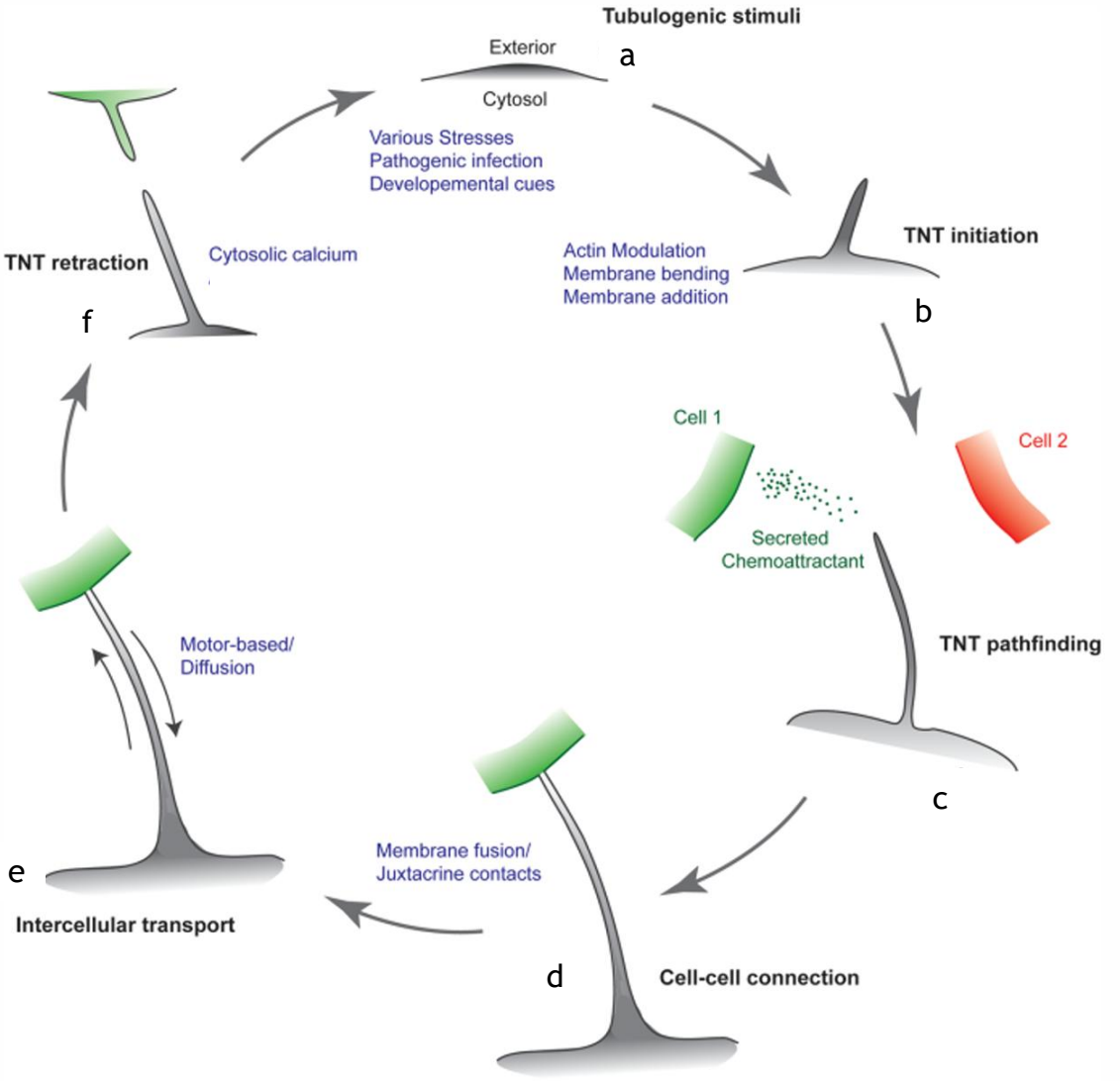

Figure 1-5: Stages of TNT formation during protrusion extension. (a) A tubulogenic stimuli is received by the TNT producing cell. (b) This triggers the initiation of a TNT precursor, requiring actin modulation, membrane bending and elongation. (c) The elongating TNT precursor is believed to be directed to chemokine producing cells in a process referred to as TNT pathfinding. (d) Through interactions between the membranes of TNT producing and recipient cells, the membranes are either fused (forming open-ended TNTs) or maintained by juxtacrine contacts (closed-ended TNTs). (e) Cargo is exchanged between cells through the TNTs, until (f) the TNT structure is eventually retracted. Figure is adapted from Dagar *et al.* (235).

TNT mediated cell connections require close contact with the TNT tip and the recipient cell membrane (Figure 1-5 d). This close association can then form juxtacrine contacts or membrane fusion, forming closed-ended or open-ended TNTs respectively (see 1.3.1.4). The identity of the membrane proteins that enable each of these membrane interactions is currently limited. In neuronal CAD cells, juxtacrine interactions are thought to involve the localized enrichment of membrane adhesion proteins like E-cadherin at TNT tips, where they associate with cortical F-actin through ß-catenin (236). Adhesion proteins are also thought to be involved in TNT membrane fusion, primarily by

maintaining membrane proximity prior to hemifusion of the outer plasma membrane leaflets (237). The eventual fusion of the inner leaflet is then required for a contiguous TNT to form, and myoferlin - the integral membrane protein - is hypothesised to help mediate this cell to cell fusion (235).

The exact mechanism of cytoplasmic cargo trafficking through open-ended TNTs is dependent on the properties and sizes of both the cargo and the TNT, but can be driven by motor proteins (such as myosin) along actin filaments, or by diffusion (Figure 1-5 e) (238). Cargo can also be delivered through closed-ended TNTs, although this is thought to either involve trogocytosis (the engulfment of plasma membrane fragments from cells in direct contact), or by the release of cargo within vesicles that is then taken up by the TNT recipient cell via endocytosis (235).

TNTs that contain microtubules are not only known to traffic larger cargos (such as organelles), but are also known to be more stable than TNTs containing F-actin only (239). The stability, and thus the lifetime of TNTs is thought to be regulated by a number of cytoskeletal interacting proteins. For example, EPS8 bundles F-actin and was found to be important for TNT formation in neuronal CAD cells at the expense of filopodia formation (240). Interestingly, TNTs induced by the US3 protein of pseudorabies virus were found to have elevated stabilities due to post translational modifications of tubulin (acetylated and detyrosinated) (241, 242). Nevertheless, TNTs are still broadly considered to be transient structures (202), but aside from a possible link with increased intracellular calcium ion concentrations, little is known about the mechanisms that mediate the retraction of TNTs (Figure 1-5 f) (243).

1.4.1.2 Modulation of cortical F-actin during TNT initiation

The ability of TNTs to reach distant cells is facilitated by the unique ways in which linear cortical F-actin is polymerised when TNTs are initiated. Therefore, a number of F-actin modulating proteins, and associated pathways, have been implicated in TNT biogenesis (Figure 1-6). However, the same proteins can have opposing effects on TNT formation in different cell types. For example, the actin nucleating Arp2/3 complex, which assembles branched actin filaments, is required for TNT formation within murine RAW/LR5 macrophages (244).

Conversely, in neuronal CAD cells, Arp2/3 activation was found to reduce TNT numbers. Interestingly, Arp2/3 was found to favour filopodia formation at the expense of TNT formation (245). This therefore reveals that TNT formation in neurons requires a shift from branched to linear F-actin dynamics, and further distinguishes filopodia from TNTs (193).

Master regulators of actin, and TNT formation, include the Rho GTPases: CDC42, RhoA and Rac1 (Figure 1-6). These Rho GTPases modulate cofilin phosphorylation through the regulation of LIM kinases (LIMK) (246). In its dephosphorylated form, cofilin binds to actin and depolymerises it. Therefore, via the intermediate effectors such as PAK1 (p21-activated kinase) downstream of CDC42 and RhoA, or ROCK (Rho-associated kinase) downstream of Rac1, Rho GTPases contribute to TNT formation by rendering cofilin inactive (235, 247). Additionally, the effector proteins of CDC42 and Rac1 (WASP and WAVE respectively) promotes actin nucleation through binding to the Arp2/3 complex (248).

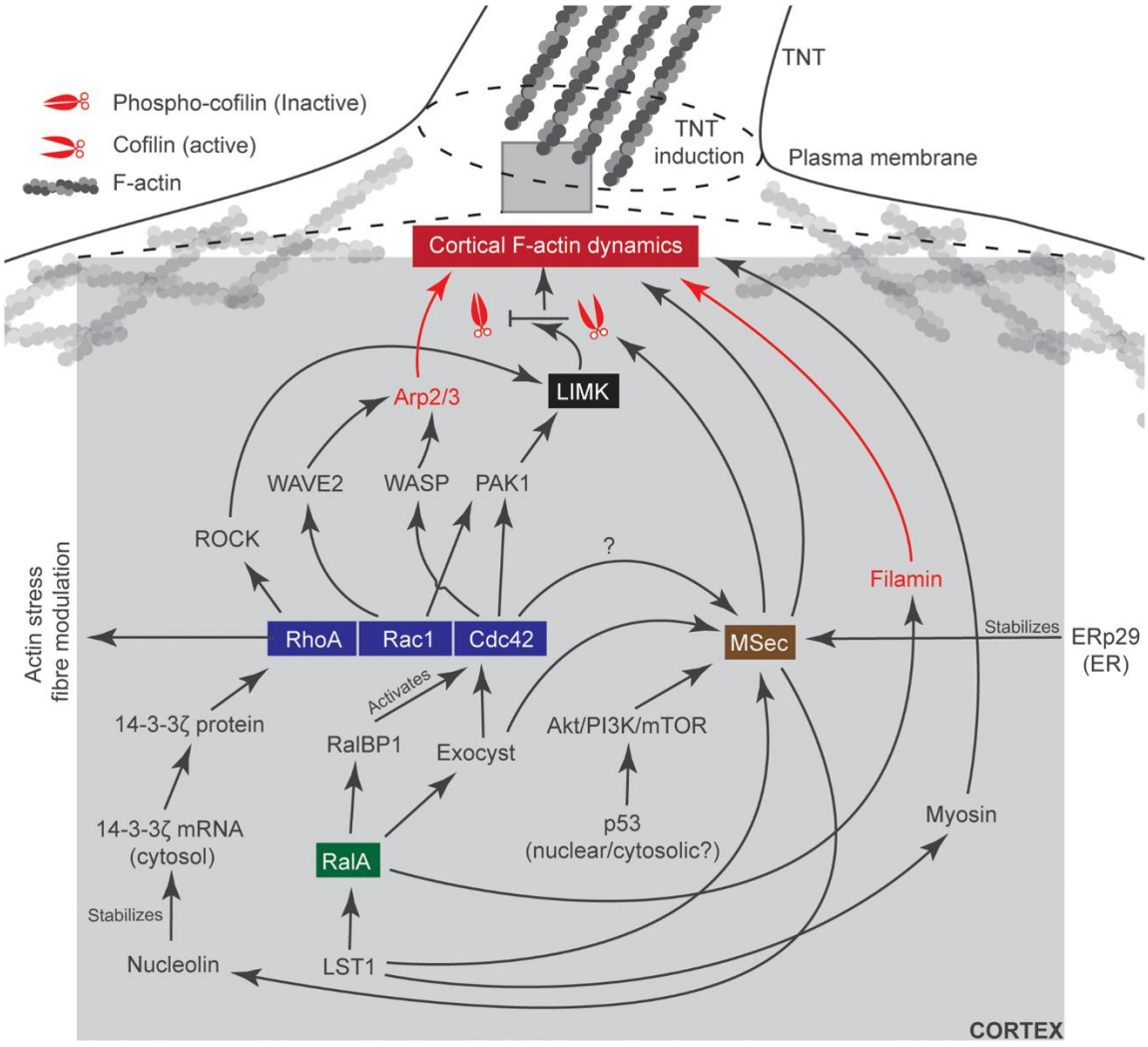

Figure 1-6: The biogenesis of TNTs involves a number of F-actin modulating proteins. Figure adapted from Dagar *et al.* (235). Details of how these F-actin modulating proteins contribute to TNT biogenesis is provided in the main body text,

The Ras-like small GTPase, RalA, interacts with a number of actin modulatory pathways involving either CDC42 or Msec via the exocyst complex (Figure 1-6) (239). The exocyst complex was found to be required for TNT formation in HeLa cells and macrophages, emphasising the role of these pathways (239). MSec is a structural homolog of the exocyst complex subunit Exoc3, and its interaction with the ER-resident chaperone protein (ERp29), was found to be required for TNT formation in several cell types (249). Additional interactions of MSec with nucleolin (an RNA binding protein) also contributes to TNT formation (250). This is thought to be due to the deactivation of cofilin through the activity of 14-3-3ζ protein, the mRNA levels of which is stabilised by MSec recruited nucleolin (250).

Other key players in the modulation of F-actin essential for TNT initiation include actin-based motor proteins and potentially tumour suppressor proteins (Figure 1-6). Myosin-X is a non-muscle motor protein important for linking cortical actin with the plasma membrane. The integral membrane protein, LST1, can help recruit myosin to the plasma membrane, and the FERM domain of myosin-X induces TNTs through mediating an interaction between the cortical F-actin and membrane integrins (208, 251). Importantly, the FERM domain is also found in Ezrin-Radixin-Moesin family proteins, which are also known to aid in TNT-like structure formation by a similar mechanism (252, 253). The role of the p53 tumour suppressor protein in TNT formation is controversial (see 1.4.2.1). Where evidence of an involvement of p53 exists, it is linked with a downstream activation of the Akt/PI3K/mTOR pathway which influences F-actin dynamics, possibly through activating MSec (235, 254).

1.4.2 The formation of tunnelling nanotubes can be induced

1.4.2.1 Tunnelling nanotube induction outside the context of infection

Outside the context of infection, a variety of stimuli and cell culture conditions have been shown to induce the formation of TNTs (summarised in Table 1-2). These conditions are commonly associated with cell stress and therefore, unsurprisingly, can involve cellular proteins that govern cell fate decisions such as the transcription factor p53. However, it is often unclear how cell stress leads

to the induction of TNTs. For example, evidence for the involvement of p53 in TNT induction is conflicting, particularly following hydrogen peroxide (H_2O_2) treatment. TNTs were shown to be induced following oxidative stress triggered by H_2O_2 treatment and that this induction was shown to be regulated when p53 was overexpressed or knocked out/down (255). However, it was later shown that the effect of H_2O_2 treatment on TNT induction was dependent on cell type but not on p53 activation (256). The p53-null human osteosarcoma cell line SAOS-2 did not induce the formation of TNTs following H_2O_2 treatment, whereas isolated primary mesenchymal stromal stem cells (MSCs) from a double knock-out (dKO) (p53−/−) C57BL/6 mouse showed an increase in TNT formation following H_2O_2 treatment (256).

Further nuance in cell stress mediated TNT induction can be seen following hypoxia treatment, which has been shown to regulate the extent of TNT induction between ovarian cancer cell lines (257). Interestingly, the extent of this induction was seemingly dependent on whether these cells were sensitive to chemotherapeutic drugs, with the chemoresistant cell lines (SKOV3 and C200) inducing more TNTs under hypoxic conditions (2% oxygen, 5% carbon dioxide, and 93% nitrogen), whereas the chemosensitive cell line A2780 showed no change in TNT induction between normoxic and hypoxic conditions (257). Such findings suggest an unusual connection between mechanisms of chemotherapeutic resistance and TNT induction, and it is curious to note that resistant cells seemingly induce more TNTs. Interestingly, a link between TNTs and chemoresistance has been established (see 1.4.3.1) (258), and it is possible that the induction of TNTs by these resistant cells may be exacerbating this phenotype, contributing to an even greater resistance to these drugs.

Beyond intracellular responses to cell culture stress that promote TNT formation, secreted factors have also been shown to induce TNT-like structures in recipient cells. For example, IFN-α treatment has been shown to drive TLS induction within Kcl-22 cells (259), and conditioned media from macrophages has been shown to induce TNTs within the breast cancer cell line MCF-7, potentially by the secretion of paracrine cytokines and chemokines (260, 261). However, conditioned media from 7 day serum starved stressed rat primary neurons and astrocytes did not induce TNTs between the recipient cells (255),

suggesting that the effect of conditioned media and secreted factors may be context or cell type dependent.

Table 1-2: The stress conditions that can induce the formation of TNTs between cells *in vitro*.

Stimulus/condition	Cell type(s)	Proposed mechanism	Ref.
Oxidative stress (H_2O_2 treatment)	Primary rat hippocampal astrocytes and neurons. Mouse mesenchymal stem cells (MSCs).	Activation of p53 transcription factor that then upregulates EGFR which activates the Akt/PI3K/mTOR pathway. Induces MSec overexpression, and together with RalA and the exocyst complex triggers F-actin polymerization and TNT formation.	(255, 256)
Serum starvation	Primary rat hippocampal astrocytes and neurons. Mesothelioma cells (VAMT).	Similar to H_2O_2 induction of TNTs. Activation of p53 transcription factor leading to the activation of the Akt/PI3K/mTOR pathway. Also induces MSec overexpression.	(255, 262)
Hypoxia/reoxygenation	Ovarian cancer cells (SKOV3 and C200), Colon cancer cells (SW480 and HCT-116 carcinoma cells and NIH 3T3 fibroblasts). Mesenchymal stem cells (MSCs) and Human umbilical vein endothelial cells (HUVEC).	Dependent on the mammalian target of rapamycin (mTOR) pathway. Dependent on the presentation of phosphatidylserine on the outer leaflet of the plasma membrane.	(257, 263, 264)
Hyperglycemia	Mesothelioma cells (VAMT).	Unknown	(265)

Chemotherapeutic drugs (e.g. doxorubicin)	Pancreatic adenocarcinoma cell lines (MIA PaCa-2 and S2013)	Unknown	(266)
Androgen receptor/pathway blockage	Prostate cancer cell lines (LNCaP and PC3)	Induction of stress chaperone proteins that trigger TNTs through the PI3K/AKT pathway with the help of Eps8.	(267)
Nanomaterials (e.g. cobalt nanoparticles, titanium dioxide nanoparticles, and multi-walled carbon nanotubes)	U251 human glioma cells	Increases reactive oxygen species (ROS), that then induces TNTs through the PI3K/AKT/mTOR pathway.	(254)

1.4.2.2 Tunnelling nanotube induction by infection

A large number of microorganisms have been shown to trigger the formation of TNTs and TNT-like structures (268). In particular, a wide variety of viruses have been shown to induce their formation, and this includes several significant pathogens of humans and other animals (summarised in Table 1-3). It is striking to note from these studies that there is a lack of a common theme for how these viruses induce TNT formation. Some trends, or commonalities, can be seen for closely related viruses. For example, it appears that the conserved US3 protein of the *Alphaherpesevirinae* subfamily is crucial for TNT induction by PRV and bovine herpesvirus (BoHV-1) viruses (220, 241, 269). However, it is clear that TNT induction can be a unique property of specific viruses and that relatedness with a TNT inducing virus does not mean TNT induction is shared. Examples of this can be seen between members of the *Flaviviridae* family, with numerous Zika virus strains inducing TNTs whilst Dengue virus and yellow fever virus failed to have this effect in trophoblast cells (270). Cell type dependency remains a possibility, and HIV-1 infection demonstrates this as TNT-like structure induction is seen in human macrophages but not in T cells (212). Furthermore, the TNT-like structures that formed from infected macrophages contained microtubules and in this way differed to those that existed between T cells (212).

Overall, the induction of TNTs or TNT-like structures by viruses is complex and the differences observed likely reflect their unique evolution of viruses with their specific hosts and the cells they transmit between. This complexity means that the investigation of TNT induction by a virus in each cell type often begins from scratch. However, TNT induction by cell stress known to also be brought about by virus infection could provide a helpful starting point for future investigations. For example, it was shown that the triggering of TNTs by PRRSV infection correlated with an elevated expression of ROS (271), and therefore, it is possible that PRRSV infection induces TNTs much in the same way that general oxidative cell stress does (see 1.4.2.1).

Table 1-3: Viruses that induce TNTs or TNT-like structures.

Virus	Cell type(s)	Proposed mechanism	Notes	Ref.
HIV-1	Macrophages, MDMs, T lymphocytes, B cells, DCs	The viral protein Nef, with the help of MSec, Myo 10 and the exocyst complex, induces F-actin remodelling via the interaction with Vav. Nef also regulates TNT formation by activating PAK2 which regulates the phosphorylation of RalA. Complement opsonised HIV-1 can induce TNTs between DCs through the C5a receptor.	In addition to F-actin, structures between macrophages contained microtubules. T cell nanotubes are closed ended but are not induced by HIV-1 infection. Virus particles "surf" on nanotube surface.	(272-276)
HTLV-1	MT-2, Jurkat, THP-1	TNT-like structures were enhanced through the function of the viral protein p8.	Cytarabine reduces TNT-like structure formation and the direct cell to cell spread of HTLV-1 whilst not affecting p8 expression.	(277, 278)
HMPV	BEAS-2B, A549, Vero,16HBE	Cytoskeleton remodelling requiring Rho GTPases (CDC42, Rac1, and RhoA). The viral phosphoprotein induces membrane extensions and colocalises with actin.	N/A	(221)

NDV	DF-1, BSR-T7/5, Vero	TNT-like structure induction required the viral protein F, and a methyltransferase K-D-K-E motif.	NDV NP protein is found within TNT-like structures containing both F-actin and tubulin.	(279)
Measles virus	Glial cells (GCCM)	N/A	Infected cells appear to fuse with uninfected cells via TNT-like structures.	(172)
PIV5	A549, MDCK, Vero	N/A	N/A	(222)
SARS-CoV-2	Vero E6, SH-SY5Y	Infection upregulates CK2 and p38 MAPK activity that promotes actin polymerisation.	TNTs contained replicative complexes and mature virions. TNT mediated infection spread did not require host cell receptors.	(280, 281)
PRV	ST, RK13	RhoA phosphorylation triggered by the viral protein US3 resulting in actin cytoskeleton reorganisation. US3 can also phosphorylate and activate PAK1/2 leading to the dephosphorylation of cofilin.	TNT-like structures also contained microtubules, with post translational modifications enhancing structure stability. Adhesion molecules (E-cadherin and beta-catenin) are present in the cell connection area.	(241, 269, 282, 283)

HSV-1	HCECs, Vero	F-actin assembly through the Arp2/3 complex was required for TNT formation.	N/A	(284)
BoHV-1	MDBK, KOP, bovine fibroblasts	Cytoskeletal reorganisation through the viral protein US3.	The US3 protein is a conserved serine/threonine kinase that is conserved among the *Alphaherpesvirinae* subfamily	(220, 285, 286)
MHV-68	NIH-3 T3, BHK-21, 293 T	Actin cytoskeleton reorganisation by the viral protein gp48.	Gp48 promotes direct cell to cell spread.	(287, 288)
EBV	293 T, Cos7, HeLa	TNT-like protrusions formed by the viral glycoproteins BMRF2 and BDLF2.	N/A	(289)
CHIKV, SINV, SFV	Vero, HUVEC, MEF	TNT-like structure formation requires the expression and interaction of E2 and capsid proteins.	TNT-like structures were not found to be open ended. CHIKV direct cell to cell spread was found to not require host cell receptors.	(196)
PRRSV	HEK-293T, MARC-145	Speculated to involve the viral GP5 protein that associates with TNTs, and the increase in ROS following infection.	TNTs contained myosin IIA alongside F-actin. Mitochondria, viral proteins and viral RNA can be transported via TNTs. TNT mediated	(271, 290)

			spread of infection did not require host cell receptors.	
VACV	Vero	Speculated to involve the viral protein F11L that blocks RhoA signalling and induces actin rearrangements.	It was found that TNT-like structures elongated with cell migration.	(291-293)
Ebola virus	Vero, HUVECs, Macrophages	Nucleocapsid expression alone can trigger the formation of TNT-like structures that can then traffic this viral protein even in the absence of an infection.	TNT-like structures contain the viral genome and viral proteins (VP40 and GP) alongside F-actin and tubulin.	(294)
Zika virus	Trophoblasts (HTR-8, JEG-3), primary human trophoblasts, A549s	NS1 viral protein expression and presentation in the plasma membrane as membrane-associated dimers is required for TNT formation.	TNTs can deliver virions, dsRNA, proteins and mitochondria. NS1 colocalises with actin and tubulin filaments in TNTs.	(270)
IAV	A549, MDCK, Vero	N/A	Rab11a was shown to be required for NP incorporation within TNTs but had no effect on TNT induction.	(222, 230)

1.4.3 The role of tunnelling nanotubes in health and disease

Beyond the direct cell to cell spread of infection, the induction of TNTs is known to play diverse roles in both health and disease. Additionally, the trafficking of cytoplasmic cargo through open-ended TNTs is believed to be bidirectional (295), possibly expanding the diversity of cargo trafficked, and thus the downstream effects on the recipient cell.

1.4.3.1 TNTs in non-infectious disease

Neurodegenerative diseases such as Alzheimer's and Parkinsons can be caused by misfolded proteins such as tau and α-synuclein respectively. It was found that these misfolded aggregated proteins can spread through TNTs connecting neurons *in vitro* (296, 297). This has implicated TNTs in neurodegenerative disease progression, and strikingly tau increased TNT formation in culture, suggesting that these disease causing proteins are also driving their intercellular spread to healthy neurons (297).

TNTs have also been implicated in the tumour microenvironment. For example, TNT mediated mitochondrial transfer has been shown to restore oxidative phosphorylation in damaged tumour cells, promoting chemoresistance and immune evasion (298). Moreover, TNTs support the dissemination of oncogenic signals and anti-apoptotic factors, contributing to tumour aggressiveness and coordination among malignant cells (299). Their presence in various cancer types underscores their role in shaping tumour behaviour, and recent studies suggest that targeting TNT formation, or function may offer novel therapeutic strategies (298-300).

1.4.3.2 TNTs in maintaining healthy cellular processes

TNT-like structures have been observed during the developmental stages of *Drosophila* and were therefore proposed to be important for embryonic development. However, these structures were later identified as cytonemes, which are filopodia based structures as opposed to legitimate TNTs (see 1.3.1.3). Nevertheless, other organisms such as the unicellular malaria parasite have been shown to form TNT-like structures within the midgut of the *Anopheles* mosquito

during gametogenesis, once again proposing a developmental role of these structures.

The majority of immune cells are known to form TNTs (301), so it is perhaps unsurprising that TNTs have been shown to play a role in normal immune responses. Perhaps the best example of this is the reticulation of polarised dendritic cells by CD40L (302). Zaccard *et al.* reported that CD40L (a key T cell-derived signal) induces the formation of functional TNT networks specifically in dendritic cells that have been polarized by type-1 immunity mediators, such as IFN-γ (302). These TNTs form a reticulated network, enabling direct intercellular transfer of vesicles, and antigens (302). This ultimately aids the function of these cells in supporting the antigen specific adaptive immune response. Interestingly, the authors also found that HIV could take advantage of reticulated DC networks for cell to cell spread, emphasising how well viruses can exploit these structures (302).

TNTs associated with disease may not necessarily be contributing to its progression, but instead may actually be correcting it. For example, with the lysosomal storage disease of cystinosis (the accumulation of cystine within lysosomes), TNTs from hematopoietic stem cell (HSC) derived macrophages traffic healthy lysosomes to cystinotic fibroblasts (303). The trafficking of lysosomes was bidirectional — functional cystinosin loaded lysosomes delivered to the deficient cells, and in return the macrophages received cystine-loaded lysosomes – enabling cross-correction (303). TNT formation was enhanced by contact with diseased cells, and *in vivo*, HSC-derived macrophages extended TNT-like structures across kidney basement membranes to deliver corrective lysosomal cargo to proximal tubular cells (303). This ability of TNTs to correct lysosomal disease has contributed to the exciting therapeutic potential of HSC transplantation.

Given this evidence of TNT bidirectional trafficking, the exploitation of TNTs by viruses during normal cellular function, and the ability of TNTs to correct and contribute to various diseases, suggests that the induction of TNTs by viruses could have greater consequences beyond just the spread of infection. However, our understanding of how virus induced TNT formation regulates cellular

homeostasis, contributes to other disease states and the cellular outcomes of infection is currently very limited.

1.5 Thesis aims

The significant threat of influenza A viruses to the health and wellbeing of so many species makes a comprehensive understanding of how these viruses move within its hosts essential. The focus on the extracellular spread of IAVs (whilst most relevant to interhost spread) has resulted in a large gap in our knowledge of how these viruses move covertly between cells via mechanisms of direct cell to cell spread. Mechanisms of virus direct cell to cell spread are diverse, and clarity into the mechanisms used by IAVs is required. It is also unknown if such mechanisms are shared between different IAVs, and whether these can be broadly targeted by antiviral drugs.

To date, TNTs are the best studied mechanism of IAV direct cell to cell spread, and like many other viruses, IAVs have been shown to induce their formation. Despite growing evidence that TNTs can contribute to the immune evading spread of IAV infection, and possible reassortment, little is known about how IAVs trigger this induction, and their ability to form in the tissues IAVs naturally infect remains unexplored.

Additionally, TNTs have been shown to facilitate bidirectional trafficking of cytoplasmic cargo that influences both health and disease. This bidirectional trafficking has also been seen for IAV infection. However, the consequence of TNT connections between uninfected and IAV infected cells has focused on the unidirectional delivery of viral genomes to the uninfected cell. A significant gap in our knowledge is how the uninfected cell shapes the outcomes of IAV infection through trafficking its cytoplasmic contents in the opposite direction of the incoming viral genomes.

This thesis, structured according to its 4 aims (Table 1-4), explores these gaps in our knowledge of IAV direct cell to cell spread. The expansion of this area of IAV infection biology could provide valuable insights and tools that better prepares us for the inevitable future public health emergencies brought about by the pathogen that is the influenza virus.

Table 1-4: Thesis aims and the corresponding results chapter.

Aim	Results chapter
Aim 1: Characterise the mechanisms and efficiency of IAV direct cell to cell spread.	3
Aim 2: Establish how IAV infection induces the formation of TNT-like structures (TLSs).	4
Aim 3: Assess the contribution of TLSs during IAV direct cell to cell spread *in vitro* and investigate their relevance *in vivo*.	4
Aim 4: Investigate TLS pathfinding during IAV infection and explore how uninfected cell-derived cargo influences cellular outcomes.	5

Chapter 2

2 Materials and Methods

2.1 Materials

2.1.1 General reagents

Table 2.1.1 List of general reagents

Reagent	Source
4′,6-diamidino-2-phenylindole (DAPI)	ThermoFisher Scientific
Coomassie Brilliant Blue	Bio-Rad
Dimethyl Sulfoxide (DMSO) Hybri-Max/anhydrous	Sigma
Formaldehyde (37-41%)	ThermoFisher Scientific
Glycerol	ThermoFisher Scientific
Hydrochloric acid (HCl) (~37%)	ThermoFisher Scientific
PageRuler™ Prestained Protein Ladder (10 - 180 kDa)	ThermoFisher Scientific
Phalloidin-iFluor (488, 555 or 647)	Abcam
ProLong Gold Antifade mounting media	Invitrogen
Sodium Chloride (NaCl)	VWR
Triton X-100	Sigma
Tween 20	Sigma
UltraPure Agarose	ThermoFisher Scientific
Avicel	Sigma

2.1.2 Cell culture reagents

Table 2.1.2 List of cell culture reagents

Reagent	Source
Dulbecco's Modified Eagle Medium (DMEM)	Gibco
Foetal Bovine Serum (FBS)	Bio-Rad
Dulbecco's Phosphate Buffered Saline (PBS)	Gibco
TrypLE Express	Gibco
Tosylphenylalanine chloromethyl ketone (TPCK)-treated trypsin	Sigma
Bovine Serum Albumin (BSA) Fraction V	Sigma
Hoescht 33342	ThermoFisher Scientific
CellEvent™ caspase 3/7 red detection reagent	ThermoFisher Scientific
MitoTracker™ Red CMXRos Dye, for flow cytometry	Invitrogen
MitoTracker™ Deep Red FM	Invitrogen
Vybrant™ DiI/DiD/DiO Cell-Labeling Solution	Invitrogen
Lipofectamine™ 2000 Transfection Reagent	Invitrogen
Opti-MEM	Gibco

2.1.3 Cell lines

Table 2.1.3 Cell lines

Cell line	Details	Culture conditions[a]	Source
Madin-Darby Canine Kidney (MDCK)	Dog Kidney epithelial cells	10% (v/v) FBS	Prof. P Digard (Roslin Institute, University of Edinburgh)
Human Embryonic Kidney (HEK) 293T	HEK cells expressing simian virus 40 (SV40) large T-antigen	10% (v/v) FBS	Prof. S Wilson (MRC-University of Glasgow Centre for Virus Research)
A549	Adenocarcinoma human alveolar epithelial cells	10% (v/v) FBS	Prof. S Wilson (MRC-University of Glasgow Centre for Virus Research)
A549 AcGFP	A549 cells expressing a membrane targeted[b] AcGFP	10% (v/v) FBS and 2 µg/mL Puromycin	Generated from A549 cells in this thesis
MDCK AcGFP	MDCK cells expressing a membrane targeted[b] AcGFP	10% (v/v) FBS and 10 µg/mL Puromycin	Generated from MDCK cells in this thesis

[a] For the culture of all cell lines, DMEM (supplied containing glutamine) was used and supplemented with FBS at the specified concentrations.

[b] The membrane targeting sequence of the modified GFP is a palmitoylation signal within the N-terminal 20 amino acids of neuromodulin (304).

2.1.4 Drugs and other supplements

Table 2.1.4 List of drugs and other supplements

Reagent	Solvent	Concentration range tested	Optimal concentration	Source
Zanamivir	Milli-Q water	0.12 – 0.48 µM	0.36 Mm	Sigma
Amantadine (1-adamantanamine)	Milli-Q water	0.5 – 50 µM	N/A	ThermoFisher Scientific
IPA-3	DMSO	0.25 – 5 µM	3 µM	Sigma
Cytochalasin D	DMSO	10 - 50 µM	20 µM	abcam
Taxol (Paclitaxel)	DMSO	60 - 140 µM	100 µM	Merck
Z-VAD-fmk	N/A	20 - 100 µM	100 µM	Promega
Ruxolitinib	N/A	N/A	2 µM	Stratech
Human Interferon (IFN) Beta 1a	N/A	N/A	1000 U/ mL	Stratech
Cisplatin (cis-Diammineplatinum (II) dichloride)	PBS	10 – 1000 µM	30 µM	Sigma
Puromycin	N/A	2 – 10 µg/mL	2 µg/mL	ThermoFisher Scientific

2.1.5 Viruses

Table 2.1.5 List of viruses

Virus	Strain/variant details	Source
PR8	Influenza A/Puerto Rico/8/1934 (H1N1)	Prof. R Fouchier (Erasmus MC)[a] (305)
Udorn	Influenza A/Udorn 307/1972 (H3N2)	Prof. P Digard (Roslin Institute, University of Edinburgh)[a] (93)
PR8 MUd	Reassortant with Udorn segment 7 (matrix gene) in a PR8 background.	See source for PR8 and Udorn[a]
Udorn MPR8	Reassortant with PR8 segment 7 (matrix gene) in a Udorn background.	See source for PR8 and Udorn[a]
PR8 BrightFlu	Modified PR8 virus encoding a ZsGreen fluorophore within segment 8	Dr S Jasmin & Dr Rute Pinto (MRC University of Glasgow Centre for Virus Research)[b] (149)
PR8 Cre	Modified PR8 virus encoding a Cre recombinase within segment 8.	Prof. B tenOever (New York University)[b] (306)

[a] Virus was provided in the form of reverse genetic system plasmids (see2.2.2 Virus rescue).

[b] Virus was provided as a culture.

2.1.6 Antibodies

Table 2.1.6 List of primary antibodies

Antigen	Species	Working dilution	Source
Haemagglutinin (H3)	Mouse, monoclonal	1:2000	Dr S Wharton (Francis Crick Institute)
Haemagglutinin (H1)	Rabbit, monoclonal	1:100	Prof. P Digard (Roslin Institute, University of Edinburgh)
IAV Nucleoprotein	Sheep, polyclonal	1:1000	Influenza Virus Toolkit (www.influenza.bio)
Phosphorylated STAT1 (pSTAT1)	Rabbit, monoclonal	1:1000	Cell Signalling Technology
α-Tubulin	Mouse, monoclonal	1:1000	Sigma-Aldrich

Table 2.1.7 List of secondary antibodies

Target	Conjugate	Species	Working dilution	Source
anti-Mouse IgG	Alexa Fluor™ 555	Goat	1:500	ThermoFisher Scientific
anti-Rabbit IgG	Alexa Fluor™ 555	Donkey	1:500	ThermoFisher Scientific
anti-Sheep IgG	Alexa Fluor™ 488/555/647	Donkey	1:1000	ThermoFisher Scientific
anti-Rabbit	DyLight™ 800	Goat	1:10,000	Invitrogen
anti-Mouse IgG	DyLight™ 680	Goat	1:10,000	Invitrogen

2.1.7 Buffers and solutions

Table 2.1.8 List of buffers and solutions

Buffer	Components
Coomassie Brilliant Blue cell staining solution	0.2% (w/v) Coomassie Brilliant Blue, 7.5% (v/v) acetic acid and 50% (v/v) ethanol in Milli-Q water.
Immunofluorescence (IF) permeabilisation buffer	0.2% (w/v) Triton-X100 in PBS.
IF blocking and washing buffer	2% (w/v) FBS in PBS.
Phalloidin dilution buffer	1% (w/v) BSA in PBS.
PBA buffer	1% (w/v) BSA, 0.05% (w/v) NaN3 in PBS.
Acid wash (pH 3)	10 mM HCl and 150 mM NaCl in Milli-Q water.
Laemmli Buffer	20% (v/v) glycerol, 2% (w/v) Sodium dodecyl sulfate (SDS), 24 mM Tris pH 6.8, 0.1M Dithiothreitol (DTT), 0.2% (v/v) bromophenol blue, 0.2% (v/v) cyanol in Milli-Q water, supplemented with benzonase (Merck) and protease inhibitor cocktail (ThermoFisher Scientific).
SDS-Polyacrylamide gel electrophoresis (PAGE) running buffer	0.3% (w/v) Tris, 1.44% (w/v) Glycine, and 0.1% (w/v) SDS in Milli-Q water.
Western blot washing buffer	0.1% (v/v) Tween 20 in PBS (PBS-T).
Western blot blocking buffer	5% (w/v) powdered milk in PBS-T.

2.2 Methods

2.2.1 Cell culture

All viruses and cell cultures were handled within microbiological safety cabinets under biosafety containment level 2.

2.2.1.1 Maintaining cells

Cells were cultured in complete media, typically Dulbecco's Modified Eagle Medium (DMEM) with 10% Foetal Bovine Serum (FBS), unless specified otherwise (Table 2.1.3). All cells were maintained in either T75 or T150 flasks (Corning) at 37°C and 5% CO_2 within a humidified incubator. Cells were passaged once they reached confluency, by first washing the cells with PBS, then adding TrypLE Express trypsin (Gibco) to the flask. The cells were then incubated at 37℃ for up to 45 minutes, with occasional agitation, until all cells became detached from the flask surface. The cells in suspension were then diluted appropriately in complete media for either continued passage (cells were transferred to a fresh flask of similar size, typically as a 1:10 dilution), or for seeding at a density required for experiments. Cells were continually passaged until their growth became altered, failing to reach confluency across several passages (typically >40 passages for MDCK cells).

2.2.1.2 Generation of AcGFP membrane labelled cells

The genetically modified MDCK and A549 cell lines constitutively expressing the membrane targeted AcGFP1 fluorophore (MDCK/A549 AcGFP, Table 2.1.3) were generated using prepackaged lentivirus (TakaraBio, rLV.EF1.AcGFP1-Mem-9). Transduction of wild-type (WT) MDCK and A549 cells was performed by seeding a 6 well plate (Corning) with 5×10^5 or 2.5×10^5 cells per well respectively. Following an overnight incubation, a transduction mix was prepared by adding lentivirus to complete media containing polybrene (4 µg/ml, Sigma) to achieve an MOI of 10 transduction units (TU) per cell. A mock transduction mix lacking the lentivirus was also prepared. The transduction mixes were directly added over cells and incubated for 5.5 hours at 37°C. The cells were washed once with PBS and complete media added and incubated for 24 hours. Cells were then trypsinised and reseeded into T75 flasks containing complete media. Following a further 24 hour incubation, the cells were treated and maintained with complete media supplemented with either 10 or 2 µg/ml puromycin (ThermoFisher Scientific) for MDCKs or A549s respectively. Cells were used for experimentation when all the cells in the mock transduced cells had been selected against (i.e. detached and died), and the majority (>90%) of transduced cells were fluorescent. After each passage and prior to all experiments, the retention of

the fluorescence signal was assessed with an EVOS fluorescent microscope (M5000, Invitrogen).

2.2.2 Virus stocks and titration

2.2.2.1 Virus rescue

Wild-type A/Puerto Rico/8/1934 H1N1 (PR8), and A/Udorn/307/1972 H3N2 (Udorn) (Table 2.1.5) viruses were generated through reverse genetic systems as previously described (305, 307). Using Lipofectamine™ 2000 Transfection Reagent (Invitrogen) HEK293T cells were transfected with either the 8 plasmid pDUAL or the 12 plasmid pHH21 reverse genetic systems, for PR8 and Udorn respectively (Table 2.1.5). Segment 7 reassortant viruses containing the matrix gene of PR8 or Udorn within a background of Udorn (Udorn MPR8) or PR8 (PR8 MUd), were prepared by swapping the corresponding vRNA encoding plasmids. For each virus rescue, a negative transfection control lacking the PB2 encoding plasmid was included.

Following overnight incubation at 37℃, the media over cells was replaced with viral growth media (VGM) consisting of 1 µg/mL TPCK trypsin, and 0.14% (w/v) BSA in DMEM. The cells were incubated for a further 48 hours, and the supernatant was harvested and centrifuged (Eppendorf Centrifuge MiniSpin) for 1 minute at 13k rpm. The virus containing supernatant (this is referred to passage zero or P0 virus stock) was aliquoted and stored at -70℃.

2.2.2.2 Virus propagation

All viruses were propagated using MDCK cells. Between 4 and 5 × 10^6 cells were seeded into T25 flasks (Corning) and viruses were propagated from either P0 stocks (2.2.2.1), or from the titred stocks provided by others (see Table 2.1.5), including BrightFlu (PR8 virus encoding the fluorophore ZsGreen in segment 8 of the genome, (149)). Prior to inoculation, the virus stocks were diluted differently depending on their source (P0 or ≥P1), as detailed in Table 2.2.1.

Table 2.2.1 Dilution of inoculum

Virus stock	Dilution
Virus rescue stock (P0)	100 µL diluted in 1 mL VGM
Titred stock (≥P1)	Stock diluted to an MOI of 0.001 in 1 mL VGM.

The 1 mL inoculum was adsorbed onto cells by incubating at 37°C for 45 minutes, with occasional rocking. After this, a further 5 mL of VGM was added to the flask. The virus-containing media were collected between 2 and 3 days post infection (dpi), or when 90% of cells had been lost to cytopathic effect (CPE). Cell debris was removed by centrifuging the harvested media for 5 minutes at 3000 rpm and 4°C, using a benchtop microfuge (Eppendorf). Aliquots were prepared from the supernatant and stored at -70°C.

2.2.2.3 Virus stock titrations

Plaque assay Infectious titres of viruses (as plaque forming units (PFU)/mL) were determined under agarose by conventional plaque assay in MDCK cells (308). Viruses were serially diluted (10-fold) in VGM and used to inoculate confluent MDCKs, seeded into either 12 or 6 well plates two days prior (Table 2.2.2).

Table 2.2.2 Plaque assay plate formats

Plate format (Corning)	MDCK seeding density/well	Inoculum volume/well
12 well	5×10^5	350 µL
6 well	1×10^6	450 µL

Adsorption of virus onto cells was done by incubating the plates at 37°C for 1 hour, rocking the plates every 15 minutes. An agarose overlay was prepared by mixing molten agarose with VGM in a 1:1 ratio, achieving the desired concentration of each overlay component (Table 2.2.3).

Table 2.2.3 Agarose overlay

Overlay component	Contents[a]	Initial concentration	Final concentration
Agarose	UltraPure Agarose	2.4% (w/v) in Milli-Q water	1.2% (w/v)
VGM	TPCK treated trypsin	2 µg/mL	1 µg/mL
	BSA	0.28% (w/v)	0.14% (w/v)
	DMEM	N/A	N/A

[a] For manufacturer information refer to Table 2.1.1 and Table 2.1.2.

The inoculum was removed and the agarose overlay added to the wells. Once the agarose solidified at room temperature the plates were incubated at 37°C and 5% CO_2 for 2 to 3 days, after which the agarose plugs were removed and

cells fixed and stained with Coomassie Brilliant Blue cell staining solution for a minimum of 30 minutes (Table 2.1.8). The stain was then removed and plates washed with water. Countable plaques (up to 300) in two separate dilution wells were counted and used to calculate the plaque titre according to the formula below. The average plaque titre (as PFU/mL) across these two wells was recorded as the plaque titre for the stock.

$$\text{Plaque Titre } \left(^{\text{PFU}}/_{\text{mL}}\right) = \frac{\text{Number of plaques (PFU)}}{\text{Innoculum volume (mL)}} \times \text{dilution factor}$$

Single cell fluorescence assay The infectious titre, in fluorescent forming units (FFU)/mL, of the fluorescent reporter virus BrightFlu was determined by flow cytometry. This was done by performing a 3-fold serial dilution of virus stocks in VGM, and adsorbing 200 µL of each dilution for 45 minutes onto subconfluent MDCK cells (seeded at a density of 6×10^4 cells per well of a 24 well plate, the day before). After this incubation, the inoculum was removed and cells washed twice with PBS and then overlayed with complete media. At 16 hours post infection (hpi), the cells were resuspended into a single-cell suspension with equal volumes of TrypLE Express trypsin and complete media. Cells were fixed by mixing the cell suspension in a 1:1 ratio with 4% (v/v) formaldehyde. The percentage of cells positive for ZsGreen signal was determined by flow cytometry (see 2.2.3) and assuming that infections occurred independently and that every cell was equally susceptible to infection, the ratio of FFU to cells can be calculated from the proportion of infected cells using the Poisson distribution (309). The formulae used for this calculation is shown below:

$$m = -ln\,(1 - P\,)$$

Where m is the MOI (FFU/cell) and P is the proportion of cells that are fluorescent. The infectious titre can then be calculated as follows:

$$\text{Infectious titre } \left(^{\text{FFU}}/_{\text{mL}}\right) = \frac{m\ (\text{FFU/cell})}{\text{Innoculum volume (mL)}} \times \text{total no. of cells} \times \text{dilution factor}$$

2.2.3 Flow cytometry

Sample preparation MDCK cells were seeded into a 24 well plate at a density of 6×10^4 cells per well. BrightFlu virus was diluted in VGM according to experimental needs (see 2.2.2.3 and 2.2.4.2), and adsorbed onto cells in 200 µL inoculum volumes for 45 minutes. The inoculum was removed and cells washed twice with PBS before overlaying with complete media. Infection was carried out for 16 hours, after which the cells were trypsinised with 200 µL TrypLE Express trypsin and mixed with an equal volume of complete media to form a single cell suspension. Cell suspensions were transferred to round bottom 96 well plates (Costar) containing an equal volume of 4% formaldehyde. Each sample was tested in technical triplicate.

Analysis Cells positive for ZsGreen signal were detected and quantified using a Guava easyCyte HT cytometer (Luminex). FlowJo software v10.10 was used to analyze flow cytometry data by implementing a sequential gating strategy to ensure accurate population selection (Figure 2-1). Initially, cell debris was excluded by drawing an elliptical gate based on forward scatter (FSC) and side scatter (SSC), which represent cell size and granularity, respectively (Figure 2-1 a). This step eliminates non-cellular debris and small fragmented cells that exhibit low FSC and SSC values, ensuring that only intact cells are considered for further analysis.

Following debris exclusion, single cells (singlets) were identified and isolated using a polygonal gate based on side scatter area (SSC-A) and side scatter width or length (SSC-W or SSC-L) (Figure 2-1 b). This gating step distinguishes true singlet events from doublets or clumped cells, as singlets maintain a consistent SSC-W to SSC-A ratio, whereas aggregated cells show broader scatter width due to multiple nuclei or larger overall cellular structures.

a)

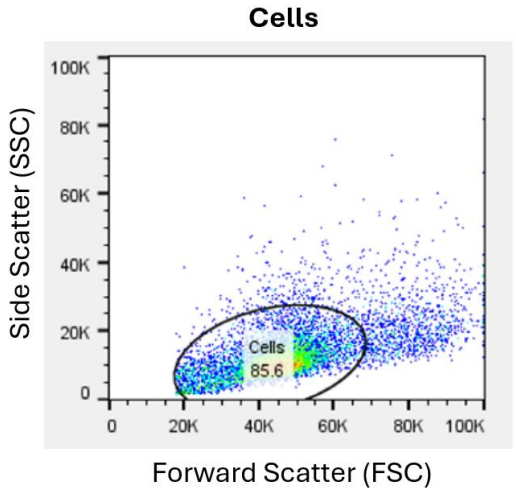

b)

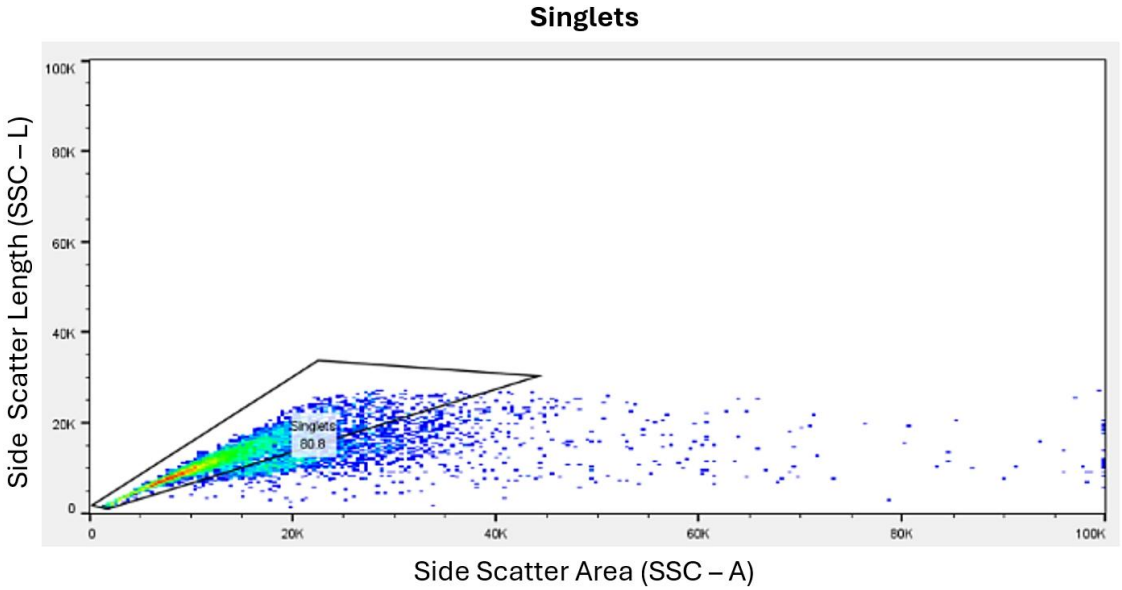

Figure 2-1: Gating strategy for identifying individual cells. (a) An elliptical gate was drawn to exclude cell debris based on forward scatter (FSC) and side scatter (SSC) values. (b) Single cells, or singlets, were then isolated from clumps by drawing a polygonal gate based on side scatter area (SSC-A) and side scatter length (SSC-L) values. Colour gradient reflects event density, with warmer tones indicating higher concentrations of cells.

Once singlets were accurately gated, quadrant gating parameters were adjusted to determine fluorescence intensity levels above background. A mock-infected sample was used as a reference control to set threshold values, ensuring that fluorescence signals were accurately quantified. This allowed for the precise classification of cells collected from infected samples into distinct populations according to the presence or absence of fluorescence signal above background.

2.2.4 Direct cell to cell spread assays

2.2.4.1 Microplaque assay

Confluent MDCK cells, within 12 well plates, were infected with PR8, Udorn, PR8 MUd or Udorn MPR8 at MOIs achieving approximately 1000 non-overlapping nucleoprotein (NP) positive infected foci per well. Following a 2 hour incubation at 37°C, the inoculum was removed, and cells acid washed (Table 2.1.8) for 1 minute to inactivate uninternalised virions. Cells were washed three times with PBS before adding 1 ml overlay unique to the experiment (Table 2.2.4). These experiments can be broadly categorised as either part of assay validation or microplaque assay analysis.

Assay validation (assessment of CPE) Overlay, in formulations 1-4, 7 and 8 (Table 2.2.4) were added to infected cells. At 48 hpi, the overlay was removed by washing with PBS and stained with Coomassie Blue for 30 minutes. The resulting cytopathic effect was visually assessed, comparing the influence of TPCK trypsin (1 µg/mL) on the formation of CPE, in the presence or absence of zanamivir (0.12 mM, overlay formulation 1 verses 2, and 3 verses 4) or amantadine (0.5, 5, or 50 mM, overlay formulation 7 verses 8).

Assay validation (virus release assay) Overlay formulations 5 and 6 (Table 2.2.4) were added to infected cells. At 48 hpi, the overlay was collected and added to 1.5 mL microcentrifuge tubes (Eppendorf). Cell debris was removed by centrifugation at 13000 rpm for 1 minute, and the supernatant transferred to fresh tubes and TPCK trypsin (1 µg/mL) added. Supernatant treated with TPCK trypsin was added to fresh, confluent MDCK cells and incubated for 2 hours at 37°C with occasional rocking. The inoculum was removed and cells washed with PBS, before adding an agarose overlay containing TPCK trypsin (Table 2.2.3). Plates were incubated at 37°C for 3 days, after which the agarose plugs were removed and cells stained with Coomassie Blue for 30 minutes. The resulting cytopathic effect was visually assessed.

Microplaque assay analysis Overlay formulations 1, 4-6, and 9 (Table 2.2.4) were added to infected cells. Zanamivir, where included in the absence of other drugs (i.e. variation 4), was tested at increasing concentrations (0.12,

0.24, 0.36 and 0.48 mM). Amantadine was also titrated (0.5, 5 and 50 mM) when applied in combination with zanamivir (overlay formulation 9), the latter of which was included at a concentration of 0.36 mM. At 48 hpi, the overlay was removed, cells washed with PBS and fixed with 4% formaldehyde for 10 minutes. Fixative was removed and cells washed three times with 2% FBS in PBS (IF blocking buffer), prior to immunostaining (see section 2.2.5.1).

Table 2.2.4 Microplaque assay overlays

	Formulation								
Overlay component	**1[a]**	**2[b]**	**3[b]**	**4[a]**	**5[c]**	**6[c]**	**7[b]**	**8[b]**	**9[d]**
DMEM	Y	Y	Y	Y	Y	Y	Y	Y	Y
BSA	Y	Y	Y	Y	Y	Y	Y	Y	Y
Avicel	Y	Y	Y	Y			Y	Y	Y
TPCK trypsin		Y	Y				Y		
Zanamivir			Y	Y	Y				Y
Amantadine							Y	Y	Y

[a] Overlay used for assay validation (assessment of CPE) and microplaque assay.

[b] Overlay used for assay validation (assessment of CPE).

[c] Overlay used for assay validation (virus release assay) and microplaque assay.

[d] Overlay used for microplaque assay.

Where indicated, cytochalasin D (20 µM, abcam), IPA-3 (3 µM, Sigma), taxol (100 µM, Merck), Z-VAD-fmk (100 µM, Promega) or DMSO was also included in the microplaque assay overlay (overlay variation 4, Table 2.2.4) which lacked TPCK trypsin and contained both avicel and zanamivir (0.36 mM). The overlay was removed by washing with PBS at 48 hpi, unless otherwise stated, and cells fixed with 4% formaldehyde as detailed above.

2.2.4.2 Subconfluent cell assay

Plates (of 24 wells) were seeded with 6×10^4 MDCK cells per well. Following overnight incubation, cells were washed with PBS and infected with BrightFlu virus at an MOI of 0.1 FFU/cell. Following a 1-hour adsorption in VGM at 37°C, the inoculum was removed and cells washed twice with PBS. An overlay consisting of DMEM, with and without 0.36 mM zanamivir was added over cells. Where indicated DMSO, or drug (cytochalasin D (20 µM), IPA-3 (3 µM), taxol (100 µM), or Z-VAD-fmk (100 µM) was included in the cell overlay. Cells were washed, resuspended and fixed as done previously for flow cytometry (see 2.2.3), at

either 8 or 24 hpi. Samples were analysed by flow cytometry in technical triplicate.

2.2.5 Immunostaining

2.2.5.1 Immunocytochemistry

Cells were permeabilised with 0.2% Triton-X100 in PBS for 7 minutes and washed three times with 2% FBS in PBS. Samples were blocked in 2% FBS for 1 h followed by the probing with sheep anti-NP primary antibody (Influenza Virus Toolkit, www.influenza.bio) [1:1000], incubated for 1 hour at room temperature. Cells were washed three times with 2% FBS before secondary antibody incubation for 30 minutes using anti-sheep Alexa Fluor 488, 555 or 647 (ThermoFisher Scientific) alongside 4′,6-diamidino-2-phenylindole (DAPI, Thermo Fisher) [both diluted 1:1000]. For super resolution confocal microscopy, cells were additionally stained with 1X phalloidin-iFluor 488, 555 or 647 (Abcam) in 1% (w/v) BSA in PBS for 30 minutes. Coverslips (13 mm, VWR) were mounted onto slides using ProLong Gold Antifade mounting media (Invitrogen).

2.2.5.2 Immunostaining IAV virions

MDCK cells were infected with P1 PR8, Udorn, PR8 MUd, or Udorn MPR8 virus at an MOI of 0.25 PFU/cell. The supernatant was collected 48 hpi, and cell debris removed by centrifugation at 13,000 rpm for 1 minute. The virus supernatant was then diluted 1:10 in PBS and spun onto sterile coverslips (13 mm, VWR), placed in 24 well plates, by centrifugation at 1000 g for 30 minutes at 4°C. The media was carefully removed from each well and coverslips were fixed for 10 minutes with 200 µL 4% formaldehyde. The fixative was then removed and coverslips washed three times with 2% FBS and blocked in 2% FBS for at least 1 hour. For all viruses, with the exception of PR8 MUd, coverslips were stained with mouse anti-H3 primary antibody [1:2000] (kindly provided by Dr Stephen Wharton, Francis Crick Institute) and goat anti-mouse Alexa-Fluor 555 [1:500] (ThermoFisher Scientific). PR8 MUd was stained using rabbit anti-H1 [1:100] (kindly provided by Prof. Paul Digard, Roslin Institute, University of Edinburgh) and donkey anti-rabbit Alexa-Fluor 555 [1:500] (ThermoFisher Scientific). For HA surface-stained cells, unpermeabilised cells were blocked with 2% FBS for 1 hour with immunostaining performed as above with the inclusion of DAPI [1:1000].

Coverslips were mounted onto slides using ProLong Gold Antifade mounting media (Invitrogen).

2.2.6 Mice infections and thick tissue sectioning

Animal work was done in accordance with the EU Directive 2010/63/eu and Animal (Scientific Procedures) Act 1986, under a project licence P72BA642F. All handling of mice was performed at the Cancer Research UK, Scotland Institute. Infection of mice was performed by Dr Ed Roberts and the culling and dissection of mice was performed by Jack McCowan.

Three mT/mG mice, between 17 and 18 weeks old, were kindly provided by Dr Stephanie May (Cancer Research UK, Scotland Institute). Two mice were intranasally infected with 1000 PFU of PR8-Cre. A naïve mouse was mock infected with PBS in a similar manner. The weight of each mouse was measured daily to ensure that disease progression did not exceed humane limits and ethical guidelines. Six days post infection the mice were euthanised, the lungs harvested and were either inflated with 1.2% agarose or left deflated. Lungs were fixed in a bath of 4% formaldehyde overnight before being transferred to PBA (1% BSA, 0.05% NaN3 in PBS). All lung lobes were separated via dissection, and, with the exception of the larger left lung lobe, were embedded in optimal cutting temperature compound (OCT, VWR) and frozen at -70℃. Tissue sectioning of the left lung lobe was performed with a vibratome (Leica), cutting tissue at 200 µm thicknesses. The OCT embedded lobes were cut at either 100, 50 or 25 µm thicknesses using a CryoStat (CM1950, Leica), which maintained the sample at -20℃. Thick tissue sections embedded and cut in OCT were placed onto slides and stored at -70°C, whereas the 200 µm thick sections were stored in PBA at 4℃. Prior to imaging, samples were brought to room temperature, and samples embedded in OCT were washed by immersing the sections in PBS. A seal-frame incubation chamber (ThermoFisher Scientific) was placed around the tissue section on the glass slide and the chamber filled with Ce3D tissue clearing solution. Coverslips (24 mm, Fisherbrand™ Glass Square Coverslips) were placed on top of the seal-frame incubation chambers.

2.2.7 IAV infection for measuring tunnelling nanotube-like structure induction

MDCK cells were seeded onto sterile 13 mm glass coverslips (VWR) placed within 24 well plates at a density of 6×10^4 cells per well. Following overnight incubation, cells were washed with PBS and infected with WT or reassortant virus at an MOI of 1.5 PFU/cell. Adsorption was performed for 45 minutes at 37°C in VGM, after which the inoculum was removed, and cells washed with PBS to remove any remaining TPCK trypsin. The cells were overlaid with 1 mL Opti-MEM (Gibco), and where indicated, DMSO, IPA-3, cytochalasin D, taxol, or Z-VAD-fmk was also included in this overlay at the specified concentration (Table 2.1.4). Cells were fixed at 16 hpi unless otherwise stated. This was done by gently adding 500 µL 12% formaldehyde directly to the 1 mL Opti-MEM overlay to a final concentration of 4% (v/v). Plates were incubated at 8°C for 2 hours, and the media then gently removed from each well. Coverslips were allowed to air dry for approximately 10 minutes before washing once with 2% (v/v) FBS.

2.2.8 U.V. inactivation of virus

MDCK cells were infected with either PR8 or Udorn and overlaid with 1mL Opti-MEM as done previously (see 2.2.7). Where indicated either DMSO, ruxolitinib or IFN-β (Table 2.1.4) were also added to the Opti-MEM overlay. The overlay was harvested at 16 hpi, flash frozen on dry ice and kept at -70°C until ready to U.V. inactivate. Samples were thawed 8 hours after harvesting and distributed across a 96 well plate (Corning) in 100 µL volumes per well. The plate (with the lid removed) was held on ice and an 8W 254 nm U.V. lamp (UVS-28 EL, UVP) placed approximately 2 inches above the samples. Exposure to U.V. light was performed in three sequential 2 minute bursts, shaking and rotating the plate 180° after each 2 minute increment. Post U.V. treatment, 100 µL samples of the same origin were pooled together and added to coverslips within 24 well plates seeded with 6×10^4 MDCK cells per well 24 hours prior. Cells were either fixed as before (see 2.2.7) or harvested for western blotting (see 2.2.9).

2.2.9 Western blotting

At the specified time points, MDCKs were harvested by scrapping then pelleting the cells by centrifugation at 13,000 rpm for 1 minute. The cells were lysed by

resuspending the cell pellet with 20 µL Laemmli buffer (Table 2.1.8). Lysates were heated at 37°C for 30 minutes, then at 95°C for 5 minutes. AnyKD mini-PROTEAN TGX gels (BioRad) were loaded with 6 µL of each sample, and 5 µL of the PageRuler™ Prestained Protein Ladder (Table 2.1.1), the latter of which was used as a molecular mass reference marker. Proteins were separated by SDS-PAGE by running the loaded gels at 100 volts until the dye front reached the bottom of the gel. Separated proteins were then transferred to a nitrocellulose membrane using the quick transfer protocol on the TransBlot Turbo system (BioRad). Membranes were blocked for 1 hour with 0.1% Tween 20 in PBS (PBS-T)/5% milk, and then washed three times with PBS-T. Membranes were transferred to 50 mL Falcon tubes (Corning) containing primary antibodies (anti-phosphorylated STAT1, Cell Signalling Technology and anti-alpha Tubulin, Merck) diluted 1:1000 in PBS-T/5% milk. Membranes were rocked at 4°C overnight before being washed three times with PBS-T. Membranes were then transferred to 50 mL falcon tubes containing secondary antibodies (anti-rabbit DyLight 800 and anti-Mouse DyLight 680, Invitrogen) diluted 1:10,000 in PBS-T/5% milk and then incubated for 45 minutes at room temperature. Membranes were washed three times with PBS-T, then with PBS and finally with water. Membranes were imaged using the LI-COR CLx-Odyssey Imaging platform. Quantification was performed by measuring band intensities in Image Studio Lite Software (Ver 5.2), with the α-tubulin loading control used for normalisation.

2.2.10 Apoptosis

2.2.10.1 Detection of active caspase 3/7

Plates (24 well, Corning) were seeded with 6×10^4 MDCK cells per well and incubated for 24 hours. Cells were washed with PBS and infected with BrightFlu at the specified MOI (FFU/cell) by diluting the virus in VGM and adsorbing onto cells for 45 minutes at 37°C. The inoculum was removed and cells washed with PBS before adding a 300 µL overlay consisting of 60 µM CellEvent caspase 3/7 red detection reagent (ThermoFisher Scientific), DMSO and 0.36 mM zanamivir in complete media. Where indicated either IPA-3, Taxol or Z-VAD-fmk (Table 2.1.4) was also included in the overlay. Cells were incubated for the specified time points, after which Hoescht 33342 was added directly to the overlay achieving a

final concentration of 5 µg/mL and incubated for 20 minutes at 37°C. Cells were then imaged live using the Nexcelom Celigo image cytometer.

2.2.10.2 Induction of apoptosis with cisplatin

MDCK cells were seeded into either 96 or 24 well plates (Corning) at a density of 2×10^4 or 6×10^4 cells per well respectively. Cells were washed with PBS and overlayed with cisplatin diluted in complete media to the specified concentration. Where the activation of caspase 3/7 was measured, 60 µM CellEvent caspase 3/7 red detection reagent was also included in the overlay and at the specified time points Hoescht 33342 was added directly to the overlay achieving a final concentration of 5 µg/mL and incubated for 20 minutes at 37°C. Cells were then imaged live using the Nexcelom Celigo image cytometer. Alternatively the cells were fixed by adding 12% formaldehyde directly to the overlay to a final concentration of 4%. Plates were incubated at 8°C for 2 hours, and the media then gently removed from each well. Coverslips were allowed to air dry for approximately 10 minutes before washing once with 2% FBS.

2.2.10.3 Transwell experiments

Transwell 12mm polycarbonate membrane inserts with pores 3µm in size (Costar) were soaked in complete medium for 1 hour. The transwell inserts were seeded with 2.92×10^5 MDCK cells in 1 mL and in parallel, 12 well plates were seeded with 1.08×10^5 cells. The cells within the wells were washed with PBS and infected with BrightFlu at an MOI of 1 FFU/cell. The transwell inserts were washed with PBS and mock infected by adding VGM. The inoculum and VGM was removed and cells washed with PBS. Mock infected transwell inserts were placed over the cells seeded in the plates. Zanamivir diluted to 0.36 mM in complete media was then added to each well (1 mL in wells with no insert and 1 mL in both the transwell insert and the well beneath). At 16 hpi the transwell inserts were removed and CellEvent caspase 3/7 red detection reagent was added to the overlay to a final concentration of 60 µM. Cells were incubated at 37°C for 1 hour before adding Hoescht 33342 as done previously. Plates were scanned live using the Nexcelom Celigo image cytometer.

2.2.11 Cocultures

2.2.11.1 Lipophilic dye cocultures

Twelve well plates were seeded with MDCKs at a density of 2.5×10^5 cells per well. Following overnight incubation wells were either stained with 0.5X or 1X Vybrant™ DiO (green), DiI (red) or DiD (far red) (Table 2.1.2). Cells were stained for the duration of time indicated, after which the dye was removed and cells washed three times with pre-warmed complete media, each time incubating the cells for 10 minutes at 37°C. Cells were trypsinised and green and red cells were cocultured in equal parts onto 13 mm sterile coverslips placed in 24 well plates to a total density of 6×10^4 cells per well. Cells were incubated for 16 hours and then infected with PR8 at an MOI of 0.6 (PFU/cell). After 16 hpi cells were fixed with 12% formaldehyde, as previously (see 2.2.7).

2.2.11.2 A549 and A549 AcGFP coculture

Wild type A549 and A549 AcGFP cells were resuspended in complete media as done previously (see 2.2.1.1) and 2.25×10^4 cells of each type was mixed together in 1.5 mL Eppendorf tubes. This cell mixture (totalling 4.5×10^4 cells for each well) was seeded onto sterile 13 mm glass coverslips. Following overnight incubation, cells were infected with PR8 at an MOI of 2.5 PFU/cell with the overlay conditions and fixation method the same as above (see 2.2.7).

2.2.11.3 MitoTracker coculture

Wild type MDCK cells in suspension, post cell passaging, were diluted to 1×10^6 cells per mL of complete media. MitoTracker Red CMXRos (Invitrogen) was diluted 1:1000 in the cell suspension and mixed. A separate cell suspension was treated with 500 µM MitoTracker Deep Red FM (Invitrogen). A cell suspension was mock treated by adding the same volume of anhydrous DMSO (Merck). The MitoTracker cell suspension mix was incubated at 37 °C for 45 minutes, agitating the cells every 15 minutes. The cells were pelleted by centrifuging at 400 xg for 5 minutes and washed by resuspending in complete media and repeating the centrifugation step. Following resuspension in complete media the cells were counted and diluted to 9×10^4 cells/500 µL. For cocultures, cells stained with either Red or Deep Red MitoTracker were mixed at a 1:1 ratio in Eppendorf

tubes by pipetting. Cells were infected in suspension with BrightFlu ZsGreen at an MOI of 0.75 FFU/cell. The virus was mixed within the cell suspension and then seeded (totalling 9×10^4 cells/well) onto 13 mm glass coverslips within wells of a 24 well plate and rocked. The cells were incubated at 37 ℃ for 20 hours and formaldehyde was diluted to 4% in prewarmed serum free DMEM. The cells were washed with PBS and fixed with this 4% formaldehyde/DMEM mix for 15 minutes. The cells were was three times with 2% FBS and stained with DAPI [1:1000] for 30 minutes before mounting coverslips onto glass slides as done previously.

2.2.12 Microscopy

2.2.12.1 Super resolution confocal

Confocal microscopy was performed using the Zeiss LSM 880 (63x oil immersion objective, 1.4 numerical aperture). Super resolution imaging of TLSs and budding filaments was performed using Airyscan fast detection. Post-acquisition auto processing was performed within Zen Black (Zeiss) software (v14.0.29.201). For TLS quantification, a single field of view encompassed two adjacent tiles stitched together. In total, 14 randomly selected fields of view with a suitable distribution of cell nuclei were selected per technical replicate. Each biological replicate consisted of two technical replicates. Imaging of filaments on coverslips was performed using similar settings, except that only the Gallium Arsenide Phosphide (GaAsP) detector was used.

Thick tissue section confocal microscopy was performed on the Zeiss LSM 880 with Airyscan fast detection as detailed above. In addition, Z-stacks encompassing 3D regions of interest was performed by manually moving the plane of focus through the sample and setting the first and last planes of focus. The optimal number of slices between these positions, as automatically determined by the Zen Black (Zeiss) software (v14.0.29.201), was then selected. Maximum intensity projections of 3D Airyscan processed Z-stacked images were created using the Zen Black software.

For mitochondrial imaging, a 63x or 20x objective was used were indicated, using the Zeiss LSM 880 with Airyscan fast detection. For quantitation of mitochondrial transfer, mock or infected monocultures or cocultures were

imaged using the 20x objective. Three images of mock or infected monocultures, and eight images of mock and infected cocultures constituted each biological replicate. Three biological replicates were performed.

2.2.13 Image analysis

2.2.13.1 Filament measurement

Filament measuring was performed using published Image J macro scripts (310). Micrographs were auto-thresholded to generate binary images, and debris with a circularity between 0.5 and 1 was removed via the Particle Remover tool. The dimensions of quantified remaining particles were extracted with the Ridge Detection tool and figures created on GraphPad prism.

2.2.13.2 Microplaque imaging Analysis

Microplaque image analysis was performed on a Nexcelom Celigo image cytometer using a 90% well mask. A gating area of 600 μm2 was selected on the Celigo analysis software to distinguish microplaques (i.e. fluorescent areas > 600 μm2) from single infected foci. This area was optimised on the Celigo by manually adjusting the gating size till single infected cells (as determined by both NP and DAPI staining) were only classified uniquely as being from fluorescent regions encompassing at least two adjacent infected cells. The percentage of total foci that existed as microplaques was determined alongside the mean microplaque area, as measured by the Celigo.

2.2.13.3 Tunnelling nanotube-like structure scoring

TNT-like structures (TLS) were quantified manually using characteristic features of TNTs that differentiate them from other protrusions. These include the presence of a narrow structure that appears to connect two or more cells and contains F-actin along its length. This excludes the false classification of nanopodia which typically lack F-actin (311). Structures also had to exceed a minimal length threshold of 5 μm to be positively classified as a TLS to help distinguish them from filopodia that rarely extend beyond this length (193). The structure must connect cells which have a visibly intact nucleus and are not showing signs of recent cell division, e.g. cellular midbodies, as have been done

in previous analysis (213, 278). Lengths of positively identified TLSs were measured using the distance tool in ZEN blue (Zeiss, v3.4.91). Quantification of micrographs was performed blind to the experimental condition where possible to avoid analyst bias.

2.2.13.4 FlowJo analysis of imaging data

To quantify the presence of multiple fluorescent signals within live adherent cells, data from the Celigo imaging cytometer was analysed using FlowJo. Cell detection was performed on the Celigo by first using the Hoescht stain to apply a mask for nuclei (see Figure 4-11 a). A dilation radius of 5 µm was then applied to capture perinuclear and cytoplasmic red or green signal. The percentage of cells negative, singly positive, or dual positive for active caspase 3/7 and ZsGreen was performed within FlowJo software (v10.10). Cell population gating was established based on mock infected nuclei-stained controls and then applied to all samples, as done above (see 2.2.3).

2.2.13.5 Imaris 3D rendering

Three-dimensional surface renders of fluorescent objects within thick tissue sections were created from Z-stack images on Imaris (Andor) using binary masks. Any further background removal required was performed by adjusting the min/max values (the gamma value remained unchanged at a value of 1) within Imaris according to samples derived from naïve mice. Equivalent adjustments were applied to all images.

2.2.13.6 MitoTracker coculture analysis

All micrographs were imaged in FIJI ImageJ (ImageJ v1.54f, (312)). Background subtraction was performed using the mock infected monocultures of the DMSO treated MDCK cells (i.e. unstained WT MDCKs). This was performed by taking an average of background fluorescent intensities across all technical replicates for each biological replicate. Cell segmentation was performed with the DAPI channel, which underwent thresholding using the “Default dark” method with scale conversion enabled, followed by morphological operations including dilation, hole filling, and watershed segmentation to produce binary masks. These masks were used to define regions of interest for subsequent

measurement across the remaining channels. Particle analysis was performed with a size threshold of 20 pixels and the results generated included cell area and fluorescence intensity (FI) for each non-DAPI channels. To determine the degree of mitochondrial exchange, the ratios of Deep Red (aka Far Red) to Red MitoTracker FI signal was determined.

Chapter 3

3 Measuring the direct cell to cell spread of influenza A viruses

3.1 Introduction

Chapter 1 of this thesis outlined the many mechanisms and advantages of virus direct cell to cell spread (see 1.3). In addition, I outlined the current evidence for the direct cell to cell spread of IAV infection (see 1.3.3), which revealed a need for clarity with regards to the ways in which IAVs perform this. In order to address this, careful considerations of experimental strategies used to study IAV direct cell to cell spread is required to interpret the mechanistic evidence they provide. It is only after this, can experiments be performed that both help provide mechanistic clarity, as well as progress our understanding of how efficiently different IAVs mediate direct cell to cell spread (i.e. aim 1 of this thesis). Therefore, in sections 3.1.1 and 3.1.2 of this chapter, I detail the strategies used to isolate and quantify IAV direct cell to cell spread and how these strategies may be influencing the proposed mechanism. Following this, I detail in sections 3.1.3 to 3.1.4, known and hypothesised factors that mediate direct to cell spread of IAV infection, with a view to explore how the efficiency of IAV direct cell to cell spread may vary between strains, the evidence for which is equally as conflicted.

3.1.1 Strategies to quantify IAV direct cell to cell spread

Previous studies have implemented different ways to examine the direct cell to cell spread of IAVs. The results of these studies ,which evidenced efficient IAV direct cell to cell spread, are detailed in Chapter 1 section 1.3.3, and is summarised in Table 3-1. In this section I will focus on how these studies compare in their approaches to isolate the effects of IAV direct cell to cell spread, through the restriction of cell free virion mediated spread. The first example of this was performed by Mori *et al.* where they mutated the NA gene of the A/WSN/1933 (H1N1) IAV strain. Specifically, the sialidase catalytic domain of NA was replaced with the *enhanced green fluorescent protein* (*eGFP*) gene (227). In this way, infected cells fluoresced green, and with viruses being unable

to cleave the sialic acids that tethered the newly formed virion to the cell surface, they were unable to spread freely from the cell. Evidence of direct cell to cell spread was provided by fluorescent signal across a cluster of adjacent cells. Furthermore, the authors investigated the direct cell to cell spread capabilities of WSN by assessing the sensitivities of the wild type and NA-deficient virus to restriction by increasing concentrations of neutralising antibodies (227). Additionally, the authors used the antiviral drugs oseltamivir and amantadine, on cells infected with the Udorn IAV strain. Oseltamivir mimics sialic acids and competitively inhibits NA, preventing the NA catalysed release of sialic acid tethered virus, and with it the spread of cell free IAV virions. Amantadine, on the other hand, inhibits cell free virion spread by binding to the M2 ion channel transmembrane domain, preventing the acidification of the virus core which is required during entry for the uncoating and release of the viral genome into the cytoplasm (227). Then by using immunofluorescence against intracellular NP, direct cell to cell spread can be measured by the expansion of infection foci between confluent cells.

The use of genetically modified IAVs and antiviral drugs has since been routinely used in subsequent studies of IAV direct cell to cell spread. For example, similar use of antiviral drugs was seen in the study by Roberts *et al.* which investigated the mechanisms of Udorn direct cell to cell spread (222). Within an assay they refer to as the microplaque assay, zanamivir (a similar competitive inhibitor of NA to oseltamivir) was used to inhibit the release of Udorn virions from MDCK cell surfaces, thereby, restricting infection spread to routes of direct cell to cell spread (222). The number of adjacent NP positive cells, referred to as microplaques, was used as a measure of direct cell to cell spread (222). Additionally, the authors performed a similar assay, using ammonium chloride in place of zanamivir (222). Ammonium chloride prevents HA fusion to endosomes by raising the intraluminal pH, as well as inhibiting the M2 ion channel (229). In this way ammonium chloride is similar in its purpose to amantadine that was used in other studies, such as that performed by Mori et al. (227).

In a study by Ganti *et al.*, the spread of HA-deficient, fluorescently labelled A/Netherlands/602/2009;[NL09, pH1N1], and A/Panama/2007/99; [P99,H3N2] viruses was analysed (230). Similar to the NA deficient viruses used by Mori *et al.* (227), these viruses are unable to complete virion mediated spread (230). The

number of single infected cells, as well as the number of multi-cell infected foci (i.e. microplaques) was scored by confocal microscopy (230), in a manner similar to that performed by Roberts *et al.*(222). Additionally, the authors used these HA-deficient viruses to infect cells that were then cocultured with cells stably expressing HA (230). Evidence of direct cell to cell spread was then assessed by plaque assay, with plaques indicating the presence of HA containing virions within the supernatant. The authors propose that the formation of these viruses can only occur if the viral genome was successfully delivered from the HA-deficient virus infected cell to a neighbouring HA expressing cell (230). Therefore, this HA transcomplementing system provides an indirect measure of IAV direct cell to cell spread.

Cocultures, in the presence of neutralising antibodies and/or neuraminidase inhibitors, also formed the basis of direct cell to cell spread detection in additional studies (223, 231). In particular Kumar *et al*. used a thorough approach, using a recombinant PR8 virus encoding a GFP tagged NS1 protein to visualise the spread of infection between A549 cells (223). In summary, the infected cells (GFP positive) were sorted by fluorescence-activated cell sorting (FACS) and then cocultured with equal amounts of uninfected A549s, stably expressing red fluorescent protein (RFP). Cell free virion spread was inhibited by the inclusion of both oseltamivir and neutralising antibodies (223). After a 4 to 6 hour incubation, the cells were sorted again, with green fluorescence in red cells indicating the transfer of viral protein and/or viral genomes through routes of direct cell to cell spread (223). To confirm that direct cell to cell spread could result in productive infection and not just the transfer of viral proteins, the authors tested the ability of infectious viruses (containing a complete viral genome) to be produced from newly infected cells, as well as performing RT-qPCR for each viral gene segment within cells of the sorted populations (223).

Table 3-1: Summary of strategies used to provide direct evidence of IAV direct cell to cell spread.

Reference	Strategy	Result
Mori *et al.* **(227)**	NA-deficient WSN virus used to infect MDCK cells.	Cell to cell transmission still occurred between confluent MDCKs with a reduced sensitivity to antibody neutralisation. Enhanced with exogenous TPCK trypsin.
	WT Udorn infected MDCK cells treated with oseltamivir and amantadine (with exogenous TPCK-treated trypsin).	Size of Udorn infected regions reduced with oseltamivir, and was reduced further with the additional treatment of amantadine.
Roberts *et al.* **(222)**	Udorn infected confluent MDCK cells treated with zanamivir or ammonium chloride.	44% of Udorn NP positive foci consisted of 3 or more adjacent cells in the presence of zanamivir. Similar results seen with ammonium chloride treatment.
Ganti *et al.* **(230)**	HA-deficient viruses used to infect WT A549/MDCK cells in monoculture or coculture with HA expressing cells.	HA-deficient viruses spread to adjacent WT cells to form multi-cell infected foci. Cocultures resulted in a significant increase in infectious virus titres.
Kumar *et al.* **(223)**	Coculture of reporter virus infected A549 cells with membrane labelled uninfected A549s in the presence of oseltamivir and neutralising antibodies.	Following a brief coculture, a significant number of initially uninfected cells became positive for viral proteins and viral RNA.

3.1.2 Mechanistic insights into IAV direct cell to cell spread

The variations in these above strategies complicates the quantitative comparison of direct cell to cell spread of IAVs between studies, but consistent between them is the apparent efficiency by which IAVs perform direct cell to cell spread. Another commonality in these studies is the strong suggestion that certain mechanisms of direct cell to cell spread predominate over others. Such mechanistic insights are detailed in the introduction (see 1.3.3), and are summarised in Table 3-2.

Table 3-2: Summary of the mechanistic insights of IAV direct cell to cell spread.

Reference	Evidence	Broad mechanism
Mori *et al.* **(227)**	The spread of the NA-deficient WSN virus was supported by HA cleavage, and was reduced by amantadine.	Cell associated virion transfer, requiring canonical virus entry, i.e. not cytoplasmic genome transfer.
Roberts *et al.* **(222)**	Treatment with zanamivir or ammonium chloride produced comparable Udorn microplaques.	Independent of virion entry. Cytoplasmic viral genome transfer strongly suggested.
Ganti *et al.* **(230)**	Multi-cell infection foci formed independent of HA. Rab11 was required for vRNP trafficking and spread to neighbouring cells. Cytoskeletal disruption reduced direct cell to cell spread but not virion production.	Cytoplasmic viral genome trafficking and transfer. Virion association with cell and canonical virus entry prevented by the lack of HA.
Kumar *et al.* **(223)**	Viral protein and vRNA detected in labelled cells shortly after coculture with infected cells. Direct cell to cell spread was reduced following similar cytoskeletal disruption as Ganti *et al.*	Cytoplasmic viral genome and protein transfer. Cell associated virion transfer not investigated.

Overall, studies of IAV direct cell to cell spread presents two broad mechanisms – the transfer of cell associated viruses and cytoplasmic viral genome transfer (see 1.3.3 and Table 3-2). However, there is a lack of consensus into which predominant mechanism is contributing to IAV direct cell to cell spread and a simultaneous involvement of both is yet to be reported (Table 3-2). It is possible that the variations in the strategies used to inhibit cell free virion spread (see 3.1.1) is contributing to this division in the field. For example, it is unknown if the accumulation of virions retained on the cell surface through the use of neuraminidase inhibitors or NA-deficient viruses could elevate the occurrence of cell associated virus transfer. This uncertainty has arisen from previous studies having not tested either the effects of the neuraminidase inhibitor and amantadine/ammonium chloride in combination, or having done so only in the presence of an exogenous protease that could by itself support cell associated virus entry (see Table 3-1). Nevertheless, the majority of evidence does suggest a pivotal role of cytoplasmic genome transfer, which has commonly been shown to require the cytoskeleton (222, 223, 230). Such factors required for IAV direct cell to cell spread will be discussed further in the next section, and assists in further characterising the relevant mechanisms of IAV direct cell to cell spread.

3.1.3 Factors involved in IAV direct cell to cell spread

In addition to mechanistic insights, studies have provided details into the host and virus factors that are required for IAV direct cell to cell spread.

3.1.3.1 Host factors

The small GTPase, Rab11a, is known to be responsible for the delivery of cytoplasmic IAV vRNPs to the plasma membrane (129). This intracellular trafficking of the vRNP-Rab11a complex is thought to require an intact microtubule network and the motor protein dynein (313-315). It is therefore perhaps unsurprising that it was found that Rab11a was required for the direct cell to cell spread of IAVs (230). The significance of Rab11a during direct cell to cell spread was further demonstrated when it was shown to be required for frequent coinfection and viral genome mixing that resulted from this route of intercellular transmission (230). Additionally, it was found that NP colocalised with Rab11a within TNTs and rarely was NP located within a TNT without Rab11a

(230). These findings strongly suggest that Rab11a is required for the incorporation and trafficking of cytoplasmic vRNPs through TNTs, and given the interaction of Rab11a with dynein, suggests that this trafficking is also driven by motor proteins.

The F-actin component of the cytoskeleton has been repeatedly shown to be required for IAV direct cell to cell spread, with its disruption by drugs (such as cytochalasin D and IPA-3) reducing the detection of viral protein and/or viral genomes in adjacent cells (222, 223, 230). These results correlated with a reduction in TNT formation, which could be responsible for this direct cell to cell spread (222, 223). The involvement of microtubules in IAV direct cell to cell spread is more complex. It was found that stabilising microtubules with taxol reduces the frequency of IAV direct cell to cell spread (correlating with a reduction in TNTs) (222). Conversely, destabilising microtubules with nocodazole increased IAV direct cell to cell spread and this correlated with an increase in TNTs (222). Similarly, it was found that nocodazole increased the viral titre at later time points within an HA transcomplementing system, again suggesting that destabilising microtubules enhances IAV direct cell to cell spread (230). These results suggest that microtubules may not be directly involved in IAV direct cell to cell spread, but instead their disruption could be leading to the induction of mechanisms and structures (i.e. TNTs) that could be facilitating it.

3.1.3.2 Virus factors

Our understanding of the virus factors that influence IAV direct cell to cell spread is limited. Nevertheless, some studies have indicated that the virus, or a component of it, could be highly influential. This includes the function of the virus surface glycoprotein HA, which was found to be required for the direct cell to cell spread of an NA deficient WSN H1N1 virus (227). However, as already mentioned, H3N2 and H1N1 viruses lacking HA were still able to undergo direct cell to cell spread (230). This creates the possibility that the influence of virus proteins, particularly HA, in facilitating direct cell to cell spread could vary between virus strains.

Evidence for a strain-dependent effect of IAV direct cell to cell spread is conflicting. A study found that avian H5N1 underwent actin-dependent direct

cell to cell spread more than a human H1N1 virus, within a fixed period of time (up to 6 hours) (231). This seemed to confirm that IAV direct cell to cell spread was not always consistent between different strains. However, comparable levels of actin-dependent direct cell to cell spread of HA-deficient human NL09 (pH1N1) and P99 (H3N2) viruses was seen after 48 hours post infection (230). Therefore, further investigation is needed to understand how IAV strain differences regulate direct cell to cell spread.

3.1.4 IAV filaments and direct cell to cell spread have common immune evading properties

An unexplored factor that could be regulating IAV direct cell to cell spread is the morphology of the virion. IAV virions are pleiomorphic, with morphologies ranging from spherical to filamentous (see 1.2.3.2) (156, 157). The filamentous form is the clinical morphology, being selected for in vivo (159-161). This suggests that the ability to form filaments might provide an advantage within the host. In support of this idea, it has recently been shown that filamentous virions can enhance infectivity and fusion even in the presence of neutralising antibodies (162). This demonstrated involvement of the filamentous virion morphology in conferring an immune evading phenotype - a characteristic trait of mechanisms of direct cell to cell spread - creates the hypothesis that the direct cell to cell spread of IAVs could be influenced by virion morphology. Indeed, the possibility that the filamentous morphology of IAVs may be enhancing direct cell to cell spread of IAV infection has already been proposed (157).

Although the relationship between virion morphology and IAV direct cell to cell spread has yet to be directly investigated, it is notable that observed strain-dependent effects in a previous study likely correlated with a difference in virion morphology. The study in question found that an avian H5N1 virus underwent direct cell to cell spread more than the human PR8 H1N1 virus (231). The latter is a lab adapted strain known to produce predominately spherical virions (316), and H5N1 viruses have been shown to require a filamentous morphology for their efficient replication and pathogenicity (317), suggesting that H5N1 viruses are more likely to be filamentous due to selective pressures (but this requires confirmation for the specific strain used, especially after

possible sequential passage *in vitro*). Conversely, a separate study that utilised more than one strain found no obvious difference in direct cell to cell spread frequency between an H3N2 and H1N1 virus. However, the authors did not assess possible differences in virion morphology (230). Overall, I speculate that studies showing a strain-dependent difference in IAV direct cell to cell spread included strains that differed in virion morphologies, whereas those that didn't was (at least in part) because of a lack of significant difference in virion morphologies. Ultimately, I hypothesise that IAV virion morphology is an important factor regulating the immune evading direct cell to cell spread of IAV infection.

3.1.5 Chapter aims

In summary, several studies have examined IAV direct cell to cell spread with each revealing different, and sometimes conflicting insights into the mechanism and factors required. What is clear is that a variety of IAVs can undergo direct cell to cell spread, highlighting the possible significance of this route of intercellular transmission. However, the focus of previous studies on mechanisms requiring components of the host cell has meant that the virological factors influencing direct cell to cell spread efficiency, including differences between strains, are not well understood.

Therefore, in this chapter I aimed to:

1. Establish and validate an assay that robustly inhibited cell free, virion-mediated spread of IAVs.

2. Compare the efficiency by which different IAV strains, of different virion morphologies, undergo direct cell to cell spread.

3. Investigate the mechanisms by which these IAV strains performed direct cell to cell spread.

3.2 Results

3.2.1 Preventing cell free, virion-mediated spread of IAVs

In order to investigate the direct cell to cell spread of IAVs, I needed to first establish an experimental system that robustly inhibited the spread of cell free virions. This system needed to be effective with different IAV strains. To do this, I adopted a similar approach as used previously by Roberts *et al.* (222). This approach, referred to as the microplaque assay, starts by infecting a confluent layer of MDCK cells with an IAV at a low MOI (≤ 0.0004 PFU/cell, Figure 3-1 a). This ensures that infected cells are well distributed, and that infection foci are unlikely to merge following the spread of infection. After virus adsorption, cells were bathed briefly in an acid wash (Table 2.1.8, Figure 3-1 b). Treatment with an acid causes an irreversible conformational change of HA, the receptor binding protein of IAVs. This therefore inactivates uninternalised IAVs, by preventing them from being able to trigger membrane fusion. To inhibit the release of progeny IAV virions, which form at the end of the IAV replication cycle, I used a media overlay containing the antiviral drug zanamivir (Figure 3-1 c). Zanamivir is a neuraminidase inhibitor and prevents the ability of this viral protein to cleave the sialic acids that tether the newly formed virions to the infected cell surface. Therefore, by including this drug in the overlay I should be able to restrict infection spread to alternative routes that are independent of cell free IAV virions, i.e. the mechanisms of direct cell to cell spread.

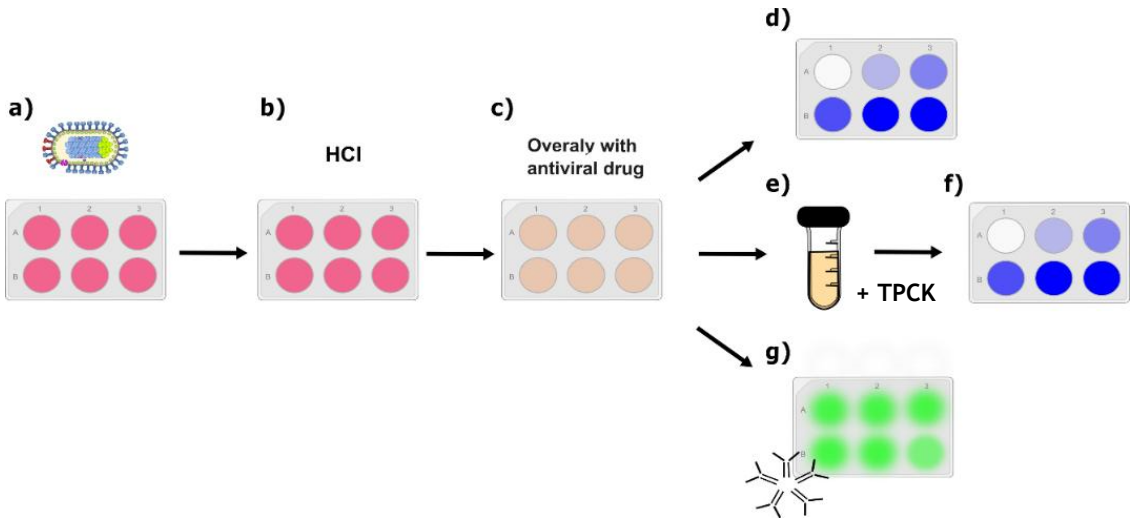

Figure 3-1: Microplaque assay workflow. Schematic showing the key steps of the microplaque assay (a-c, and g) and variations performed during assay validation (d-f). All iterations of this assay began with a low MOI infection of confluent MDCK cells seeded into 12- or 6- well plates, with an IAV (a). Virus was adsorbed and internalised by incubating the inoculated cells at 37 ℃ for 2 hours,

after which uninternalized virus was inactivated by washing cells briefly with an acidic solution (HCl, pH 3.0) (b). An overlay containing drugs that inhibit virion mediated spread was then added to washed cells (c), and incubated for 48 hours. To verify that the conditions of this assay reduced multicycle IAV replication, the overlay was removed and CPE visually inspected following Coomassie staining (d). Additional validation was performed (e & f) by collecting the media over cells, and priming any released virions by adding exogenous trypsin (e). This supernatant was then adsorbed onto fresh cells and the presence of any infectious virions detected by plaque assay (f). Once the conditions of the assay were fully validated, the microplaque assay was used to detect and quantify the direct cell to cell spread of IAVs. This was done as before (a-c), but for this analysis the overlay was removed, and cells immunostained for intracellular NP (g). Fluorescent foci were imaged and assessed using the Nexcelom Celigo imaging cytometer.

The overlay of the microplaque assay further suppresses IAV virion spread as it is devoid of TPCK-treated trypsin. This exogenously provided protease supports multicycle IAV replication by cleaving HA. This cleavage exposes the hydrophobic fusion peptide within the N-terminus of the cleaved HA2 subunit and therefore primes the virus for endosomal membrane fusion during entry (see 1.2.2.1).

To assess the inhibitory effects of the microplaque assay, I first assessed the extent by which two common lab adapted strains of IAVs (PR8 and Udorn, Table 2.1.5) caused CPE when cultured under a variety of semi solid overlay conditions differing in TPCK trypsin and zanamivir content (Figure 3-1 d, Figure 3-2). CPE is an indicator of extensive multicycle IAV replication, and when localised virion spread occurs, CPE presents as regularly shaped circles of cell free areas referred to as plaques. Plaques are then made visible by staining surviving cells with Coomassie cell staining solution and the extent of CPE can be visually assessed by the inspecting the integrity of the cell monolayer. Using this approach, I investigated the reduction of plaques (or CPE) following the exclusion of TPCK trypsin and increasing concentrations of zanamivir within the overlay (Figure 3-2).

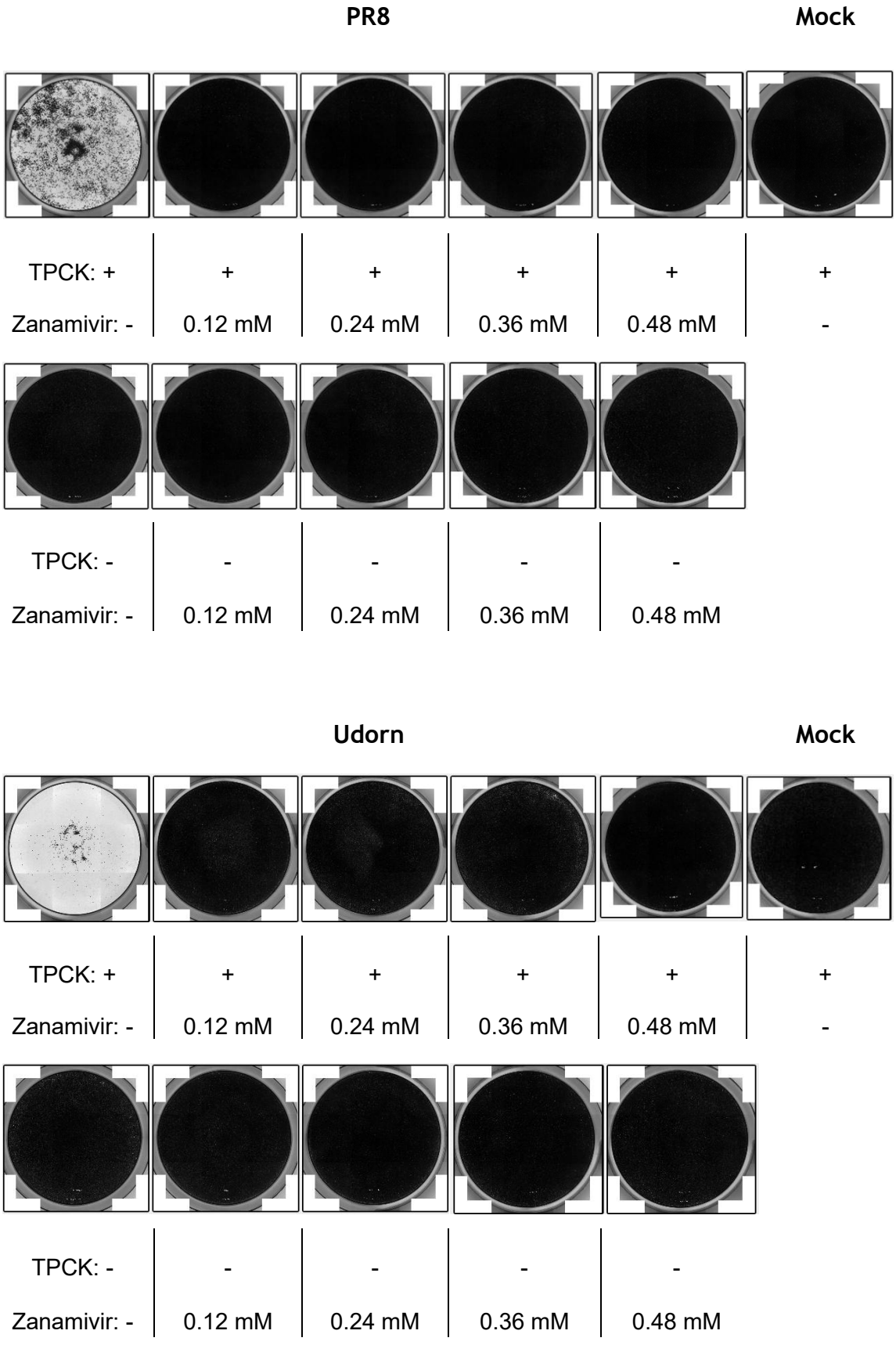

Figure 3-2: Reduction of CPE under microplaque assay conditions. Coomassie stained MDCK cells in 12 well plates, 48 hours post infection (MOI ≤ 0.0004 PFU/cell) with the IAV strains PR8 (upper panel) or Udorn (lower panel) under microplaque assay conditions. The influence of increasing concentrations of zanamivir as well as the presence (+) or absence (-) of TPCK trypsin (1 µg/mL) was assessed by visually assessing the extent of cytopathic effect (CPE). Images are representative of two biological replicates.

The extent of CPE caused when PR8 and Udorn infected cells were cultured with an overlay containing TPCK trypsin and lacking zanamivir was so great that there was near complete cell loss (Figure 3-2). This indicates that the infected regions, or plaques, expanded into each other when virion spread was supported. This was in direct contrast with the lack of any plaques observed 48 hours post infection with either strain when TPCK was excluded, revealing that these viruses are heavily reliant on the inclusion of exogenous proteases for multicycle replication (Figure 3-2). A similar lack of CPE was seen in all conditions that included zanamivir, even at the lowest concentration tested (0.12 mM). The inhibitory effect of zanamivir is further demonstrated by the lack of any CPE observed when this drug is added with TPCK trypsin (Figure 3-2), indicating that the antiviral effect of the drug is greater than the proviral role of TPCK trypsin.

The above plaque reduction assays clearly demonstrated a significant inhibitory effect. However, direct cell to cell spread is measured at the scale of individual cells and their neighbours, and the lack of CPE does not mean that cell free virion spread is not occurring at low levels between individual cells. Therefore, to verify that zanamivir is preventing the release of cell free IAV virions, I tested the growth medium 48 hours post PR8 and Udorn infection for the presence of infectious virions. To do this, I performed plaque assays with harvested media that lacked TPCK trypsin and differed in the presence or absence of 0.36 mM zanamivir (Figure 3-1 e and f). Cell debris that may carry IAVs was removed by low speed centrifugation. The supernatant was then supplemented with TPCK trypsin to ensure that all virions released into the microplaque assay overlay would be capable of infecting cells of the plaque assay. Following adsorption of the supernatant, the cells were washed to remove residual zanamivir that could prevent plaque formation, and the agarose overlay was supplemented with TPCK trypsin. In this way, any infectious IAV virions capable of breaking through zanamivir would be detected as individual plaques.

Microplaque assay overlays that excluded both TPCK trypsin and zanamivir (DMSO control), resulted in complete cell loss 72 hours post plaque assay inoculation (Figure 3-3), confirming that infectious virions are released from the cells of the microplaque assay. However, the lack of any plaques following the inoculation of cells with overlays containing 0.36 mM zanamivir confirms that this overlay prevents the release of all infectious cell free virions (Figure 3-3).

Therefore, the spread of infection between individual cells when cultured under the microplaque assay overlay (lacking TPCK trypsin and containing 0.36 mM zanamivir) cannot be explained by the transfer of cell free IAV virions. This validates the appropriateness of this approach for the study of direct cell to cell spread following infection with PR8 and Udorn IAVs.

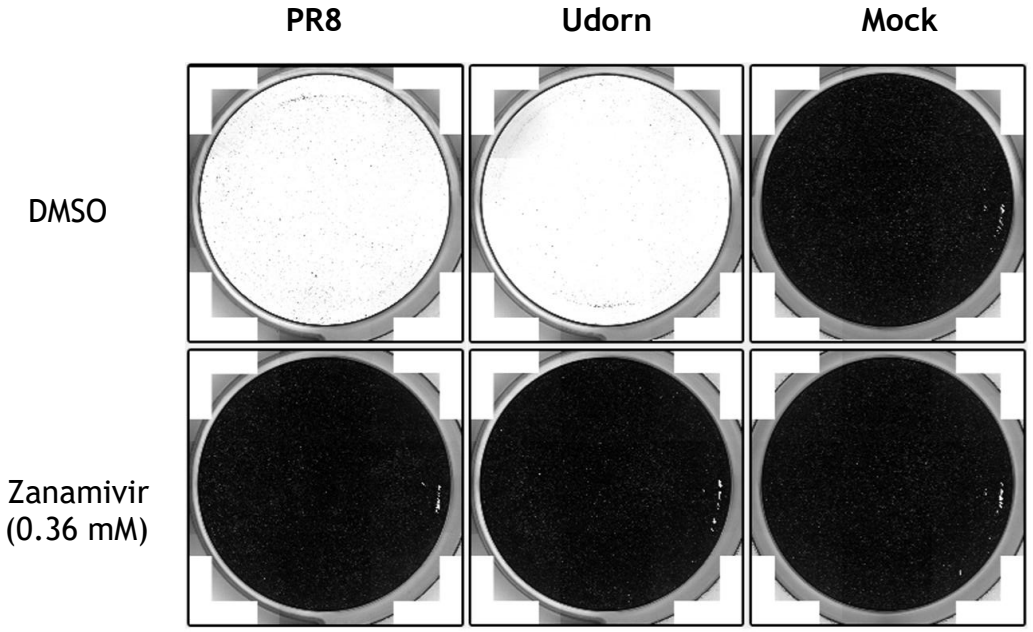

Figure 3-3: The inhibitory effect of zanamivir on virion release. Coomassie stained MDCK cells within 12 well plates, 72 hours after inoculation with TPCK trypsin treated supernatants, collected from PR8 or Udorn infected microplaque assays performed in the presence of DMSO or 0.36 mM zanamivir. After adsorption onto the plaque assay wells, the inoculum was discarded and cells were cultured under an Avicel overlay containing 1 µg/mL TPCK trypsin. Images are representative of three biological repeats.

3.2.2 Defining the role of strain and virion morphology in the direct cell to cell spread of influenza A viruses

Having established an assay that enabled us to isolate the direct cell to cell spread of IAV infection, I next wanted to test the frequency with which different strains of IAVs perform direct cell to cell spread, with a particular focus on how the morphology of the virion could be influencing this. To investigate this, I used the PR8 and Udorn strains of IAV. These strains were selected as they are both lab adapted viruses known to maintain either a predominately spherical or filamentous virion morphology respectively, and have not acquired resistance to zanamivir, the latter of which was experimentally validated (Figure 3-3). Additionally, swapping the segment 7 gene between these strains (which encodes the matrix protein, the major determinant of virion morphology), has been reported to alter the virion morphology (93, 121). A reassortant PR8 virus

with the matrix gene of Udorn (referred to as PR8 MUd) is expected to be more filamentous when compared to WT PR8. Similarly, a reassortant Udorn virus with the matrix gene of PR8 (referred to as Udorn MPR8), is expected to be more spherical than WT Udorn. This ability to alter virion morphology between two IAVs can provide a very useful tool to investigate the influence of virion morphology on the behaviour of these viruses

To confirm the virion morphologies of the PR8 and Udorn virus stocks, I used immunostaining against the virus surface glycoprotein HA. This enabled me to visualise IAV virions budding from cell surfaces 16 hours post infection (Figure 3-4 a), as well as virions from infection supernatants that were harvested 48 hours post infection and fixed onto coverslips (Figure 3-4 b). From super resolution confocal micrographs it was clear that PR8 viruses were largely unable to produce lengthy structures that could be interpreted as filamentous virions (Figure 3-4). Indeed, the majority of HA positive material from PR8 infection supernatants could not be distinguished from cell debris, which also appear as rounded spheres (Figure 3-4 b). In contrast, HA positive material from Udorn infection shows very striking and clear structures that can be positively identified as filamentous virions (Figure 3-4). The filamentous virions display similar properties to those of previous reports, including the apparent association of individual filaments together forming cord-like structures as they bud from the cell surface (158) (Figure 3-4 a), as well as their very straight appearance in the absence of freeze thawing (310) (Figure 3-4 b). Smaller, rounded HA positive material, similar to those seen with PR8, is still present in Udorn infected samples (Figure 3-4 b). However, as the resolution limit of the Zeiss CSLM 880 with Airyscan processing (approximately 140 nm) is greater than the diameter of spherical IAV virions (approximately 100 nm in diameter), it is not possible to distinguish between spherical virions and cell debris. Therefore, it is possible that Udorn infection produces large quantities of both spherical and filamentous virions.

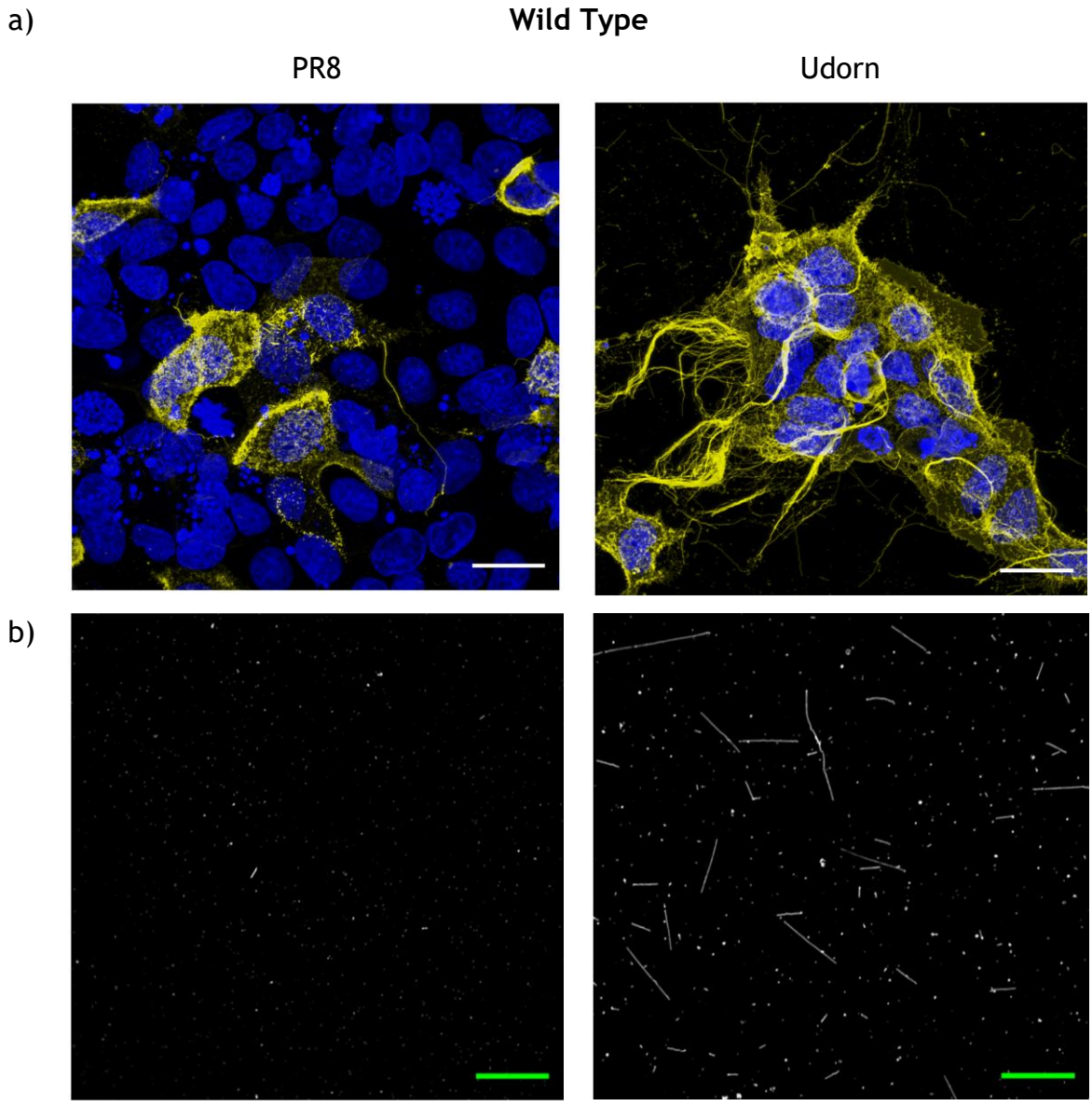

Figure 3-4: Virion morphology of wild type PR8 and Udorn IAVs. (a) Maximum intensity projections of surface hemagglutinin (HA) labelled MDCK cells, at 16 hours post infection with either the PR8 or Udorn IAV strains (MOI 0.25 PFU/cell). DAPI (blue), HA (yellow). Scale bars (white) = 20 μm. (b) Representative immunofluorescence images of PR8 and Udorn IAV virions, harvested and fixed on coverslips at 48 hours post infection. Virions were immunostained with anti-HA (white) and imaged with super resolution confocal microscopy. Scale bars (green) = 20 μm.

Next, I performed identical experiments with PR8 MUd and Udorn MPR8 reassortants to confirm that the morphologies of these viruses have been altered relative to the WT. The resulting confocal micrographs of stained infected cell surfaces (Figure 3-5 a) and harvested virions (Figure 3-5 b), revealed that more filamentous particles were formed by PR8 MUd (Figure 3-5) when compared to the WT PR8 virus (Figure 3-4). However, these filaments were not as abundant or as lengthy as those seen with WT Udorn (Figure 3-4). Similarly, more filaments were seen following infection with Udorn MPR8 than from WT PR8, but these are much less abundant and are considerably shorter than those formed from WT Udorn infection (Figure 3-4 & Figure 3-5). Therefore, these micrographs provide

confirmation that WT PR8 and Udorn viruses have considerable differences in their ability to produce filamentous virions, and that an intermediate phenotype can be generated by swapping the matrix gene segments between these viruses.

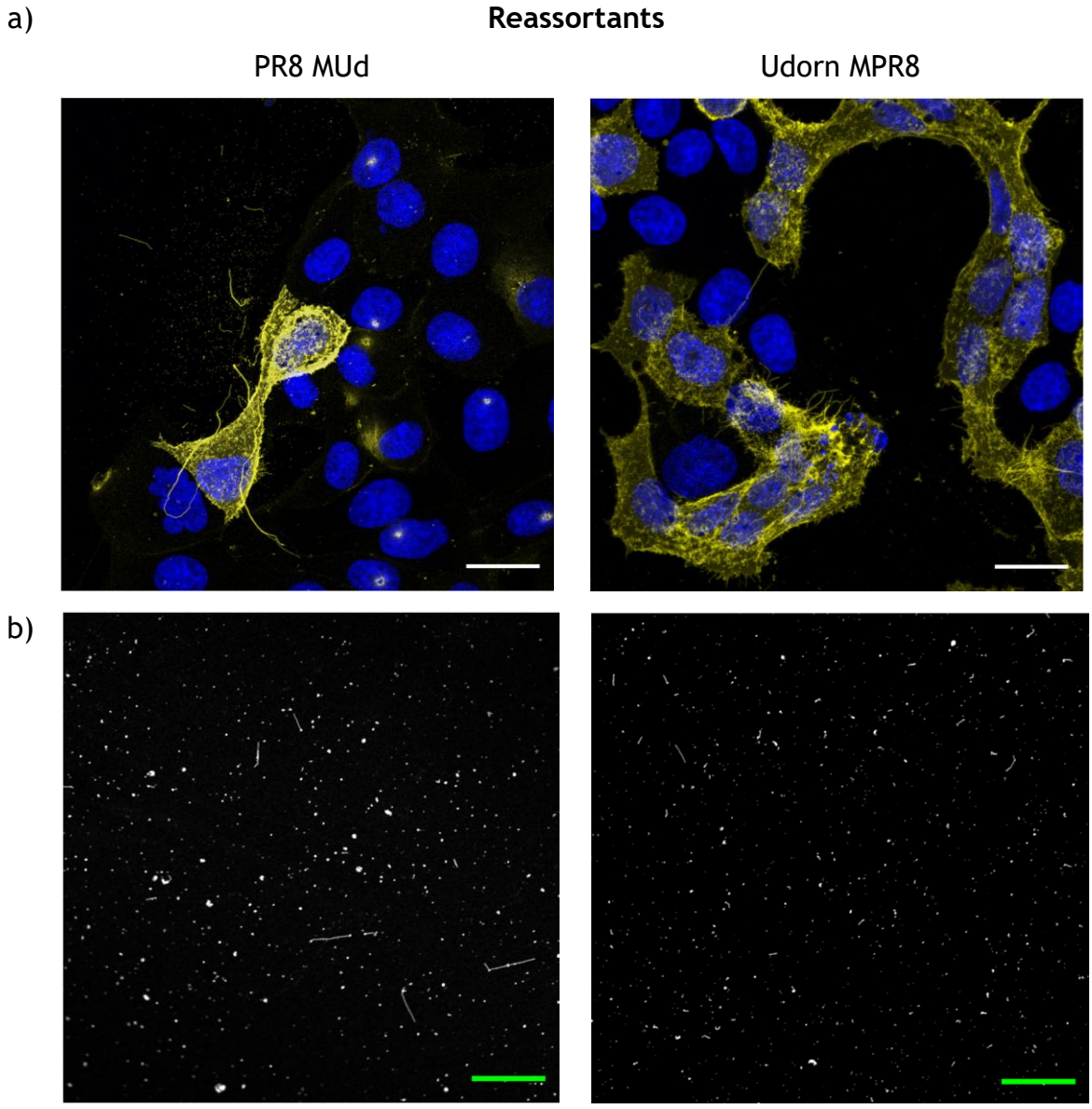

Figure 3-5: Virion morphology of segment 7 reassortant IAVs. (a) Maximum intensity projections of surface HA labelled MDCK cells, at 16 hours post infection with PR8 MUd or Udorn MPR8 reassortant IAVs (MOI 0.25 PFU/cell). DAPI (blue), HA (yellow). Scale bars (white) = 20 μm. (b) Representative immunofluorescence images of the reassortant IAV virions, harvested and fixed on coverslips at 48 hours post infection. Virions were immunostained with anti-HA (white) and imaged with super resolution confocal microscopy. Scale bars (green) = 20 μm.

Using a previously published image analysis pipeline that identifies and measures filamentous IAVs of lengths ≥ 1.5 μm ((310), see 2.2.13.1), I was then able to quantify both IAV filament lengths (Figure 3-6 a) and concentrations (Figure 3-6 b) from confocal micrographs of harvested virions (Figure 3-4 b and Figure 3-5 b). This quantitation showed more clearly the differences between the ability of WT and reassortant viruses to produce filamentous virions. Most striking is the

comparison between WT PR8 and Udorn with there being significant differences in both filament length and concentration, with Udorn producing the most and the longest filaments out of all viruses tested (Figure 3-6). The consequence of the segment 7 swap on virion morphology is clearly seen with the similarities in filament lengths between WT PR8 and Udorn MPR8. However, a significant difference in filament length was still seen between PR8 MUd and both WT viruses (Figure 3-6 a). Whilst Udorn MPR8 produces significantly smaller filaments compared to PR8 MUd (Figure 3-6 a), I do note that Udorn MPR8 still produces more filaments, albeit this difference was not significantly different (Figure 3-6 b). Nevertheless, the differences in filament lengths between the WT viruses and PR8 MUd, together with the lack of a significant difference in the concentration of filaments between the reassortant and WT viruses, emphasises that the reassortant viruses have an intermediate phenotype when it comes to filamentous virion formation.

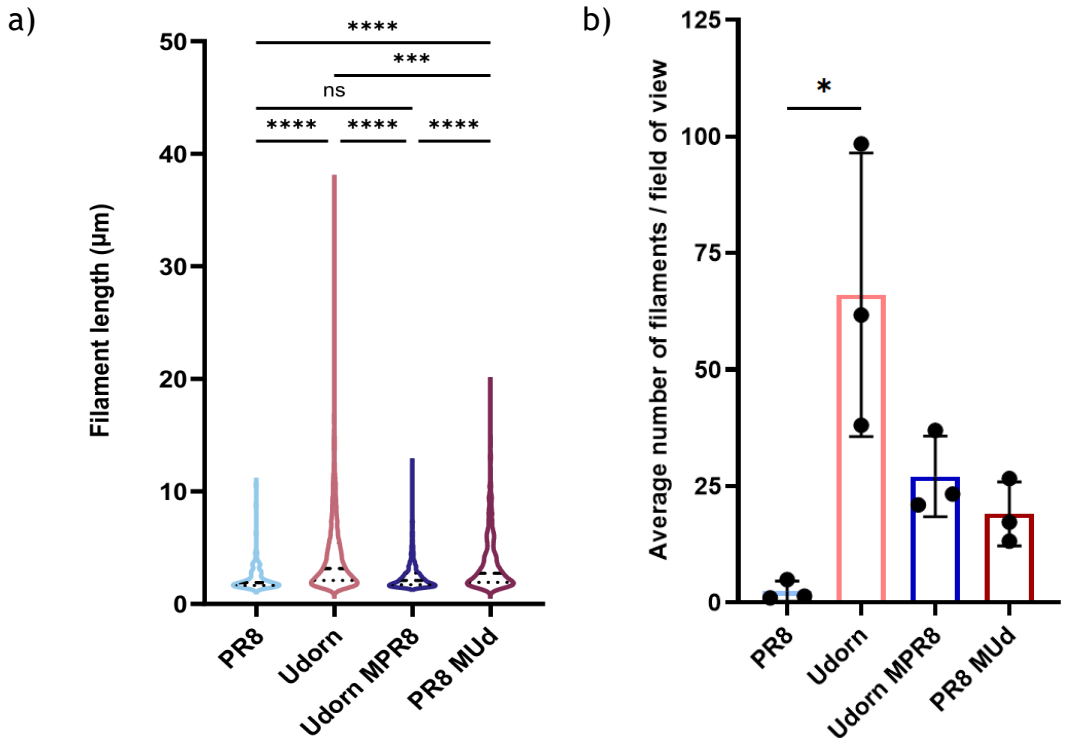

Figure 3-6: Length and concentration of IAV filaments. (a) Violin plot of the filament lengths formed by different IAV strains, with the median and the upper and lower quartile values indicated by dashed lines. Individual filament lengths across three independent experiments were plotted. (b) Average number of filamentous IAV virions per field of view (see Figure 3-5 b) between IAV strains. The mean and standard deviation (SD) is shown (n = 3). Differences in the mean filament length and concentration of filaments between strains was tested for significance by Kruskal-Wallis test (ns $p > 0.05$, *$p < 0.05$, ***$p < 0.001$, **** $p < 0.0001$).

After verifying differences in virion morphology, I sought to measure and compare the ability of each of these viruses to undergo direct cell to cell spread

within the microplaque assay (3.2.1). To achieve this, I looked at the formation of microplaques 48 hours post infection in the presence of zanamivir (Figure 3-1 g). Microplaques are classified as two or more adjacent cells positive for an infection marker. In this study, I used immunofluorescence against NP. Adjacent NP positive cells cannot be a result of cell free virion spread, as this was inhibited by the optimised microplaque assay overlay (see 3.2.1), and the low MOI infection of these confluent MDCK cells means that it is highly unlikely that adjacent cells were infected by different viruses at the start of the experiment. Therefore, microplaques are evidence of direct cell to cell spread having occurred.

Using these criteria, I then aimed to quantify two features of the resulting microplaques. Firstly, the frequency of microplaques relative to all NP positive foci, including single NP positive cells (i.e. the percentage of cells that were able to directly spread infection to their neighbours), and secondly, the area over which the microplaque extends. This analysis was performed with the Nexcelom Celigo image cytometer, which was able to both image and score NP positive fluorescent foci (Figure 3-7). Using the gating tool, with the help of the DAPI nuclear stain, I defined the area of both a single infected cell (approximately 300 μm^2 as measured by the Celigo software), as well as the minimum area of a microplaque (approximately 600 μm^2). This established a size threshold (600 μm^2) which was then used to categorise NP positive foci as either a single cell (below the threshold, outlined in red) or as microplaques (matching or exceeding the threshold, outlined in green) (Figure 3-7 b). Once microplaques had been gated, the Celigo then provides the mean area of these NP positive regions encompassing at least two cells.

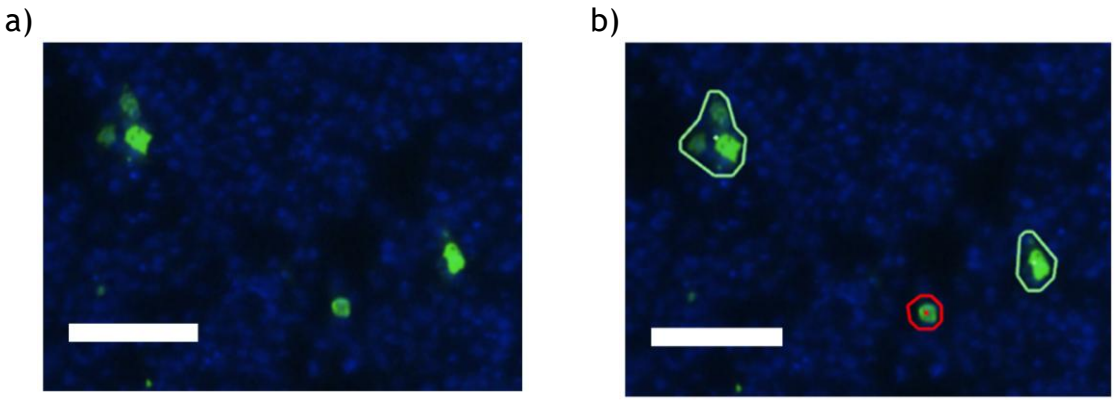

Figure 3-7: Microplaque imaging and classification. (a) Representative images of infected MDCKs at 48 h after PR8 infection (MOI 0.0004 PFU/cell) under microplaque assay conditions (i.e.

in the presence of 0.36 mM zanamivir and the absence of TPCK trypsin), imaged by a Nexcelom Celigo image cytometer. (b) Gating thresholds were applied, identifying microplaques (adjacent NP positive cells, circled in green) or isolated infected cells (circled in red). Nuclei (blue), NP (green). Scale bars = 100 μm.

As part of the comparison of direct cell to cell spread between strains, I was curious how zanamivir inhibition would influence the frequency and scale of microplaque formation following infection with either PR8 or Udorn viruses. Furthermore, I wanted to confirm that both viruses had similar sensitivities to zanamivir inhibition when looking at the much finer scale of intercellular spread as opposed to virus release. To do this, I performed a titration of zanamivir within the microplaque assay overlay, as done previously (Figure 3-2), and then analysed the microplaques that formed 48 hours post infection. This analysis revealed that the lowest concentration of zanamivir tested (0.12 mM) reduces the frequency of direct cell to cell spread of both PR8 and Udorn viruses (Figure 3-8 a). This difference was not significant and I hypothesise that this is due to the lack of TPCK trypsin within the microplaque assay overlay, which I already found is required for these viruses to perform multicycle replication (Figure 3-2). Nevertheless, this reduction in microplaque formation with zanamivir suggests that the inclusion of this antiviral drug is required to prevent the low levels of virion mediated spread that can still occur in the absence of TPCK trypsin.

Interestingly, when zanamivir concentration was increased above 0.12 mM there was no further reduction in the formation of PR8 or Udorn microplaques, and at the highest concentration tested (0.48 mM) the percentage of Udorn infected foci that were microplaques increased to levels comparable to the control (Figure 3-8 a). This suggested that PR8 and Udorn viruses had different sensitivities to zanamivir, particularly at higher concentrations. To look at this more carefully, I used the untreated (0 mM zanamivir) samples to normalise the percentage of PR8 and Udorn foci that were microplaques at each concentration of zanamivir (Figure 3-8 b). This revealed that PR8 and Udorn had similar sensitivities to zanamivir at concentrations up to 0.36 mM, with similar reductions in the frequency of direct cell to cell spread seen (Figure 3-8 b). However, at 0.48 mM zanamivir the difference between PR8 and Udorn microplaque formation was confirmed, with Udorn forming microplaques at comparable frequencies as the untreated group, whereas PR8 microplaque formation was comparable to those that formed at lower concentrations (Figure 3-8 b). Similar results were seen when I looked at the mean area of PR8 and

Udorn microplaques (Figure 3-8 c). However, the microplaque areas for both viruses remained consistent at all concentrations tested (Figure 3-8 c), indicating that 0.48 mM zanamivir only increased the ability of individual cells to directly spread Udorn infection to one or two neighbouring cells and did not sustain the continued direct cell to cell spread of infection.

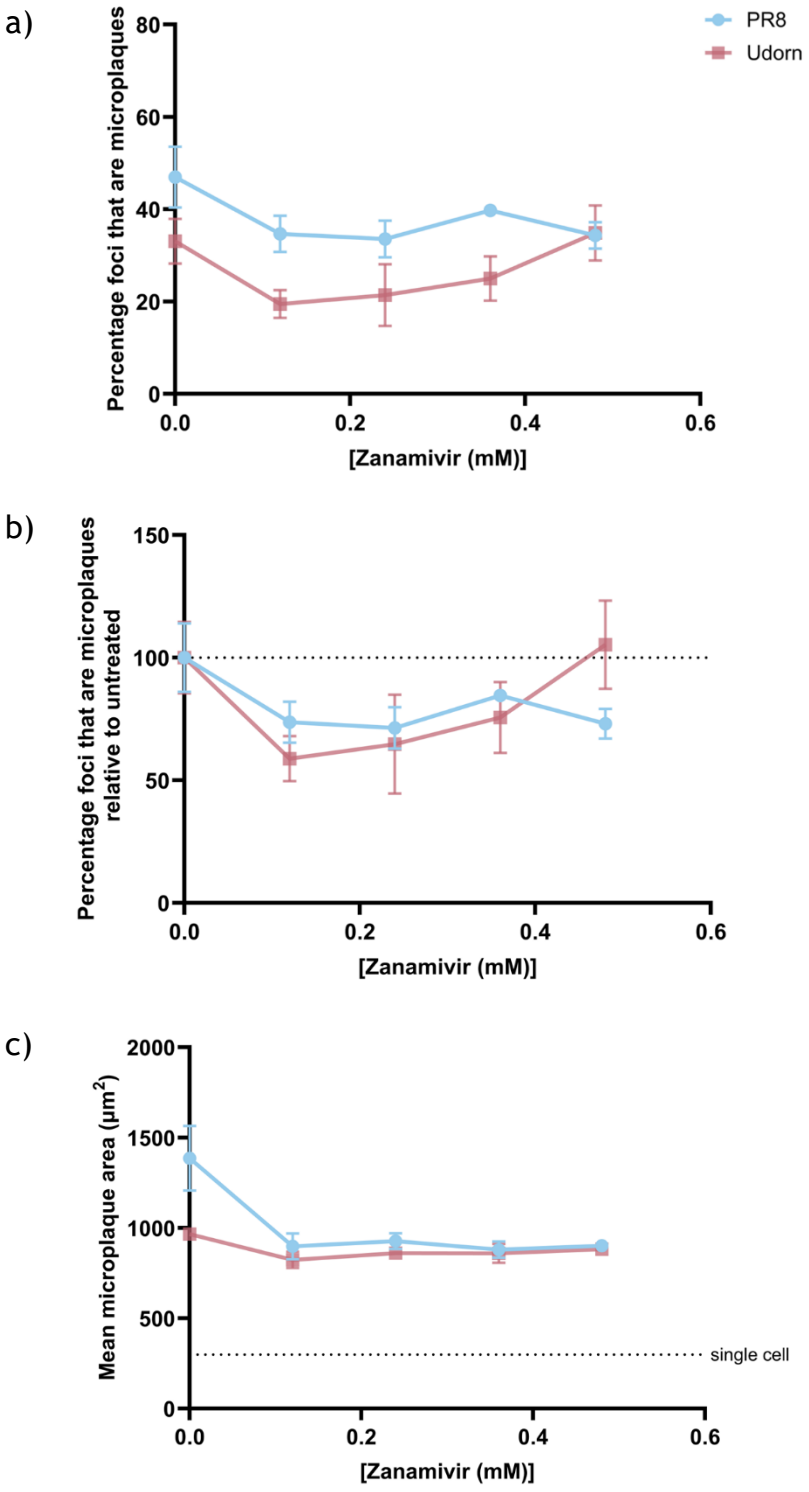

Figure 3-8: Zanamivir reduces the intercellular spread of IAVs. (a) The percentage of NP positive foci that are microplaques under increasing zanamivir concentrations. Differences between viruses at each concentration were tested for significance by Mann-Whitney test, and differences between concentrations were tested by Kruskal-Wallis test (n.s. $p > 0.05$). The means and

standard deviations of three biological replicates are shown. The same data are shown in (b) with each virus normalised to its behaviour in the absence of zanamivir. (c) Mean microplaque area under increasing zanamivir concentrations, with a dashed line showing the approximate area of a single cell. The means and standard deviations of three biological replicates are shown. The significance of differences between viruses was determined by Kruskal-Wallis test (n.s. $p > 0.05$).

With 0.36 mM zanamivir reducing the intercellular spread of IAVs by inhibiting the release of IAV virions (Figure 3-8 and Figure 3-3), I then compared the ability of PR8 and Udorn to undergo direct cell to cell spread at this concentration. Whilst both viruses were able to frequently undergo direct cell to cell spread (≥25% of NP positive foci being microplaques), I found that PR8 formed significantly more microplaques than Udorn (Figure 3-9 a). This suggests that IAVs can differ in their ability to undergo direct cell to cell spread, but this is not dependent on the ability of an IAV to produce lengthy filamentous virions (Figure 3-6). To explore whether the increased ability of PR8 to undergo direct cell to cell spread was being influenced by the spherical virion morphology of this virus, I performed the same experiment using the segment 7 reassortants. I found that the spherical Udorn MPR8 did not increase the ability of this virus to undergo direct cell to cell spread compared to filamentous WT Udorn (Figure 3-9 a). Similarly, the frequency of direct cell to cell spread of the more filamentous PR8 MUd virus was not significantly different from the spherical WT PR8 virus (Figure 3-9 a). Additionally, I found that all viruses produced microplaques of similar mean areas, which corresponded to an area of approximately 2 to 3 cells (Figure 3-9 b).

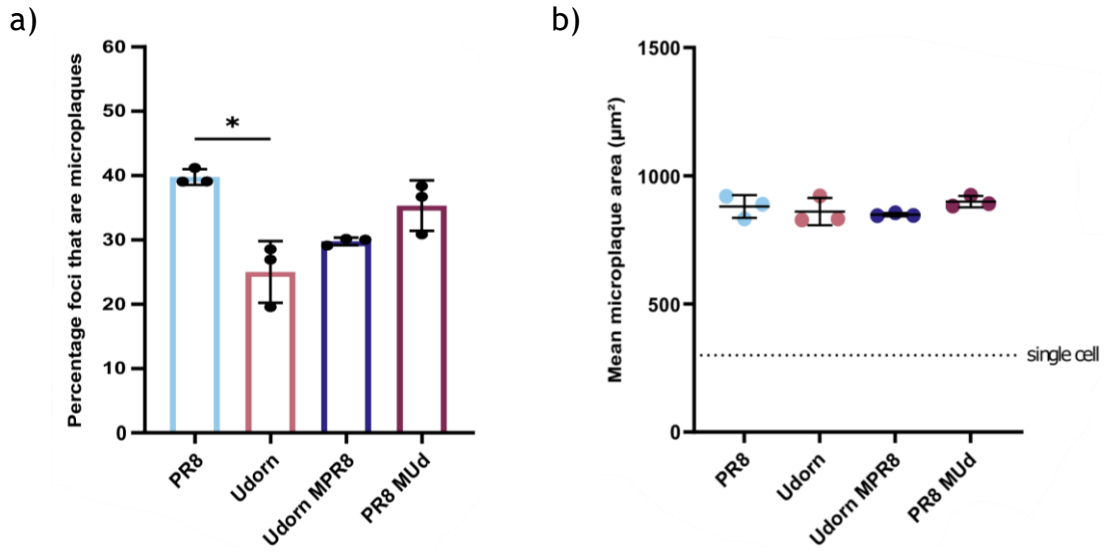

Figure 3-9: The direct cell to cell spread of IAV is independent of virion morphology. MDCK cells were infected with WT or segment 7 reassortant viruses (MOI ≤ 0.0004 PFU/cell) in the presence of 0.36 mM zanamivir for 48 h and (a) the percentage of NP positive foci that are microplaques and (b) the mean microplaque area were determined. The significance of differences

between strains was determined using a Kruskal-Wallis test (n.s. $p > 0.05$, * $p < 0.05$). For all data the mean and SD are shown (n = 3).

3.2.3 Determining the role of the endosomal pathway during influenza A virus direct cell to cell spread

I hypothesised that the difference in the frequency of microplaque formation between PR8 and Udorn viruses (Figure 3-9 a) could result from a strain-dependent preference for the mechanism of direct cell to cell spread. Currently, two broad parallel mechanisms for the direct cell to cell spread of IAVs have been proposed, which could operate simultaneously: the transfer of cell associated viruses, requiring the endosomal pathway following internalisation of virions (227), and the transfer of viral genomes directly between cells with involvement of the actin cytoskeleton (see 3.1.2) (222, 230). To distinguish between these I used amantadine, an M2 ion channel blocker which prevents virion uncoating during entry, an approach used previously to assess the contribution of cell associated virus transfer (227).

I first characterised the antiviral effect of amantadine by titrating this antiviral drug within the overlay of the microplaque assay (see 3.2.1). I confirmed previous reports that PR8 and Udorn have some resistance to amantadine (227, 318), with CPE seen at all concentrations tested when added in combination with TPCK trypsin (Figure 3-10). Cytopathic effects were also seen in both infected wells treated with 500 μM amantadine in the presence or absence of TPCK trypsin (Figure 3-10), indicating that these viruses cannot be completely inhibited by tolerated concentrations of amantadine. Nevertheless, until amantadine concentration exceeded 50 μM, a reduction in CPE occurred in a concentration dependent fashion (Figure 3-10), an effect which could be utilised in subsequent experiments.

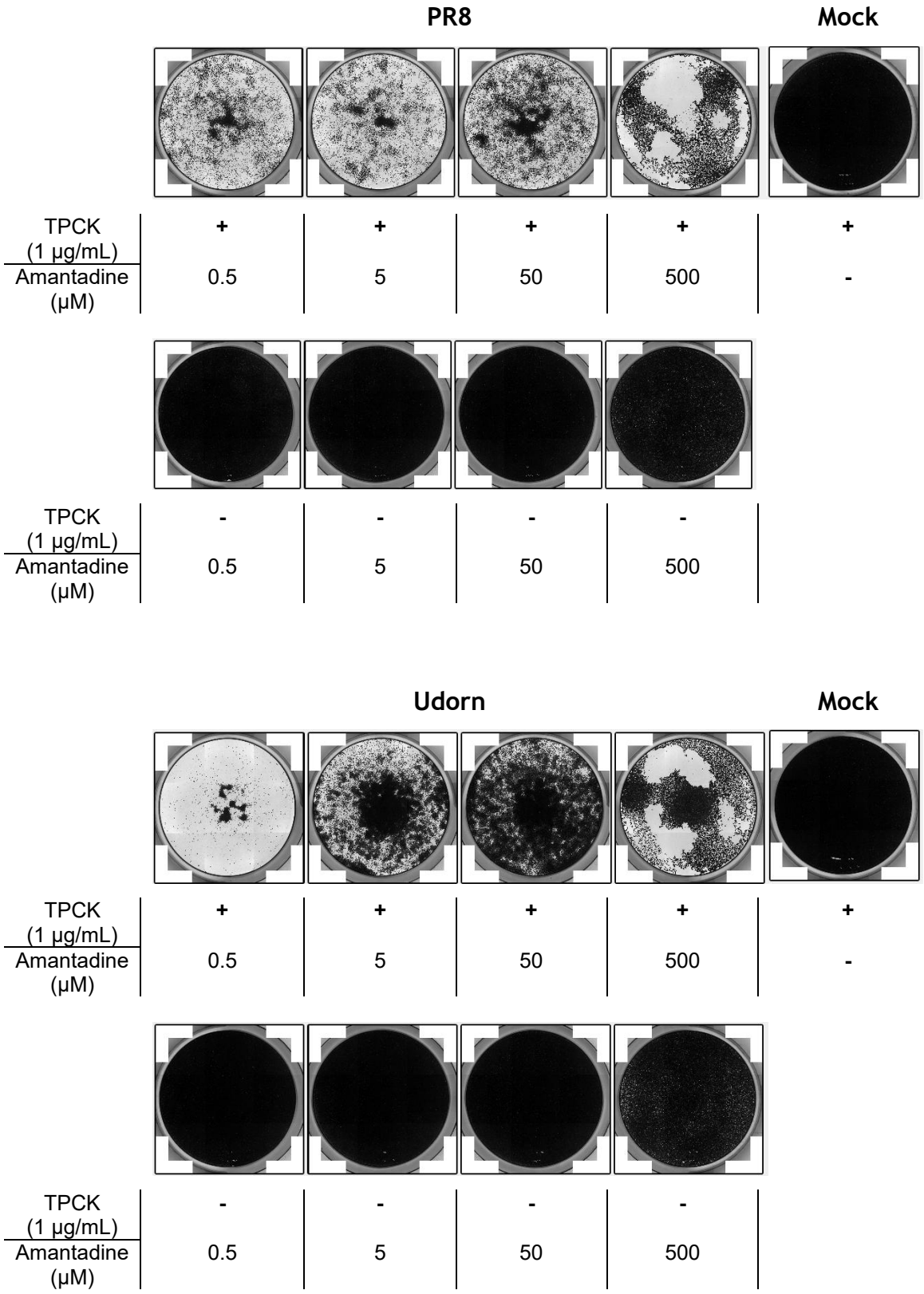

Figure 3-10: Amantadine has a concentration dependent effect on IAV induced cytopathic effect. Coomassie stained MDCKs within a 12 well plate, 48 hours post infection (MOI ≤ 0.0004 PFU/cell) with either PR8 (upper panel) or Udorn (lower panel), in the presence (+) or absence (-) of TPCK trypsin at increasing amantadine concentrations. Images are representative of two biological replicates.

Next, I repeated this titration of amantadine within the microplaque assay which also contained 0.36 mM zanamivir (a concentration which is effective with both PR8 and Udorn viruses (Figure 3-3)). In this way, virion release is prevented by

the neuraminidase inhibitor, and any spread of cell associated viruses should be increasingly reduced with the increase in amantadine concentration. Analysis of the resulting microplaques, 48 hours post infection, showed that increasing concentrations of amantadine caused no further reductions in microplaque formation relative to the zanamivir only treated samples (Figure 3-11 a). Similarly, there was no reduction in the mean microplaque area (Figure 3-11 b). The complete absence of any reduction strongly suggests that the entry and uncoating of cell associated viruses is not responsible for the efficient direct cell to cell spread of both PR8 and Udorn viruses which I observed (Figure 3-9 a). Furthermore, the lack of a difference in microplaque formation between PR8 and Udorn viruses at each amantadine concentration suggests that the differences between these viruses in their ability to undergo direct cell to cell spread (Figure 3-9 a), can not be explained by a difference in their reliance on cell associated virus transfer mechanisms. The alternative to this is mechanisms, used by both IAVs, that can transfer cytoplasmic viral genomes directly from cell to cell, such as transport through open-ended TLSs (222, 223, 230). However, other mechanisms of direct cell to cell spread can not be ruled out.

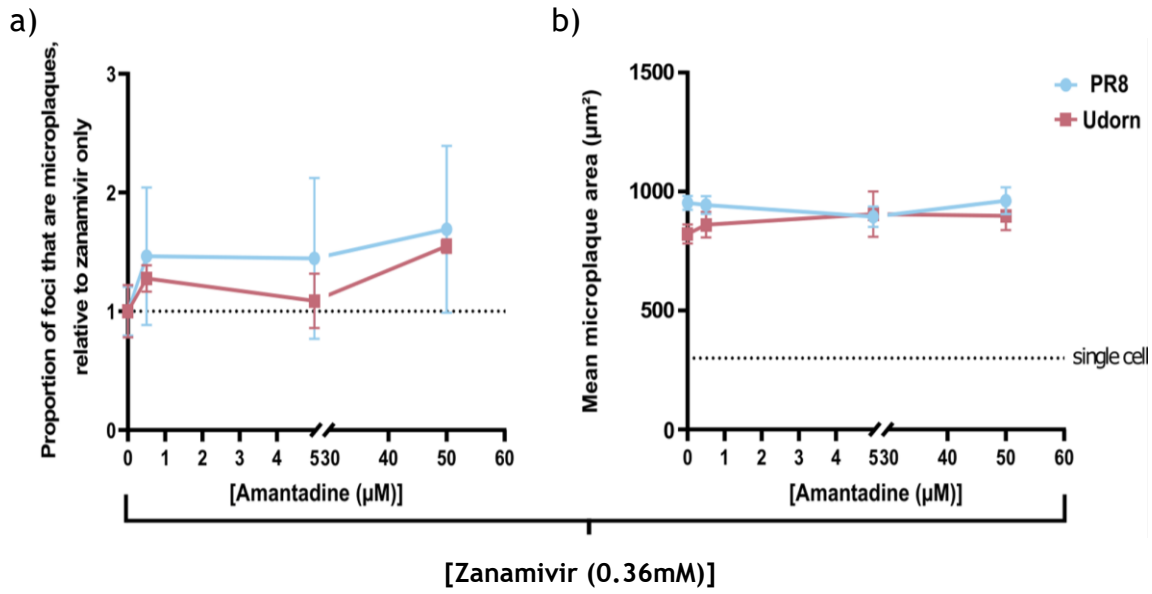

Figure 3-11: The direct cell to cell spread of IAV is independent of the endosomal pathway. MDCK cells were infected with WT PR8 or Udorn virus (MOI ≤ 0.0004 PFU/cell) in the presence of 0.36 mM zanamivir and varying concentrations of amantadine for 48 hours. (a) The proportion of NP positive foci that are microplaques, relative to zanamivir only treatment, and (b) the mean microplaque area, with the dashed line indicating the mean area of a single cell. Differences between strains at each concentration were tested for significance by a Mann-Whitney test, and differences between the same strain at different concentrations were tested by Kruskal-Wallis test (n.s. $p > 0.05$). For all data the mean and SD are shown (n = 3).

3.2.4 Assessing the consequence of cytoskeletal disruption on the direct cell to cell spread of influenza A viruses

The mechanisms of cytoplasmic transfer of IAV genomes by direct cell to cell spread is thought to typically require an interaction between the vRNP complex and components of the cytoskeleton, such as filamentous actin (F-actin) and microtubules (222, 230). Consistently with this, treatment of IAV infected cells with a variety of drugs that target these components has been shown to reduce the direct cell to cell spread of IAVs (222). Having found no evidence of cell associated virus transfer (Figure 3-11), I next wanted to confirm that the direct cell to cell spread of IAV, that I observed, was primarily occurring through cytoskeleton dependent cytoplasmic genome transfer.

To explore this, I tested the effect of cytochalasin D (Cyto. D), IPA-3 and taxol (Table 2.1.4), which are drugs with unique mechanisms of targeting either F-actin or microtubules (see Table 3-3). These drugs have been used in previous studies of IAV direct cell to cell spread (222). However, since intracellular vRNP trafficking involves the cytoskeleton, its disruption can have an antiviral effect (315), which can complicate the interpretation of these experiments. Therefore, I first wanted to establish the most effective concentration of each drug that was neither antiviral nor cytotoxic. To do this, I infected MDCKs with PR8 at an MOI of 0.6 PFU/cell, and overlayed the cells with drug titrated in serum free DMEM media. Cells were fixed 16 hours post infection and then stained with DAPI and phalloidin to visualise both the nucleus and F-actin respectively, as well as immunostained for NP. Following super resolution confocal imaging, I assessed whether the subcellular localisation of NP was disrupted, which would indicate an antiviral effect at that drug concentration. The successful disruption of the cytoskeleton was determined by inspecting the effect each drug dilution had on F-actin or cell morphology. Furthermore, I looked for signs of cytotoxicity by assessing the changes of the nucleus, e.g. chromatin condensation or loss of nuclear integrity. The MOI and time point post infection was selected as they are appropriately low to prevent considerable CPE that could confuse cell death caused by IAV infection and that caused by the drug.

Table 3-3 Drugs used to disrupt the cytoskeleton and their mechanisms of action.

Drug	Target	Mechanism	Ref.
Cyto. D	F-actin	Binds to the barbed end (growing end) of actin filaments, preventing the addition of G-actin monomers and F-actin polymerisation.	(319)
IPA-3	F-actin	Inhibits p21-activated kinase 1 (PAK1), resulting in cofilin dephosphorylation and activation.	(320)
Taxol	Microtubules	Binds to ß-tubulin within microtubules, locking them in a polymerized state and preventing disassembly.	(321)

Following DMSO treatment, I observed strong NP signal within the cytoplasm of all infected cells, as expected for this infection time point (Figure 3-12, Figure 3-13, and Figure 3-14). The cells were flat and frequently in contact with their neighbours, morphology typical of healthy MDCK cells. Furthermore, the nuclei of the cells appeared to be regularly shaped and of typical sizes, with variability in a minority of cells, typical of normal cell division or low levels of CPE (Figure 3-12, Figure 3-13 and Figure 3-14).

Cytochalasin D caused a notable disruption of F-actin which became more pronounced with an increase in drug concentration (Figure 3-12). This initially appeared as fractured F-actin, that then escalated to a near complete collapse of F-actin, with phalloidin stained material forming concentrated spheres near the nucleus of shrunken cells (Figure 3-12). This effect was also reported with Cyto.D treated BSR-T7/5 and Vero cells (279). At 20 µM cells became almost completely separated, but it appeared that the cells had more branch like extensions, indicative of cells in the process of shrinking and becoming more rounded. When assessing the subcellular localisation of NP, it was clear that concentrations up to 20 µM did not inhibit the trafficking of NP into and throughout the cytoplasm of infected cells. Higher concentrations led to a more restricted NP localisation, mostly to perinuclear regions (Figure 3-12). However, this may be a consequence of the shrinkage of the cytoplasm with the disruption of the cytoskeleton. A concentration of 20 µM was selected for future experimentation as this displayed both a significant level of F-actin disruption

and cell morphology change, whilst displaying the most convincing evidence of an undisturbed IAV replication cycle.

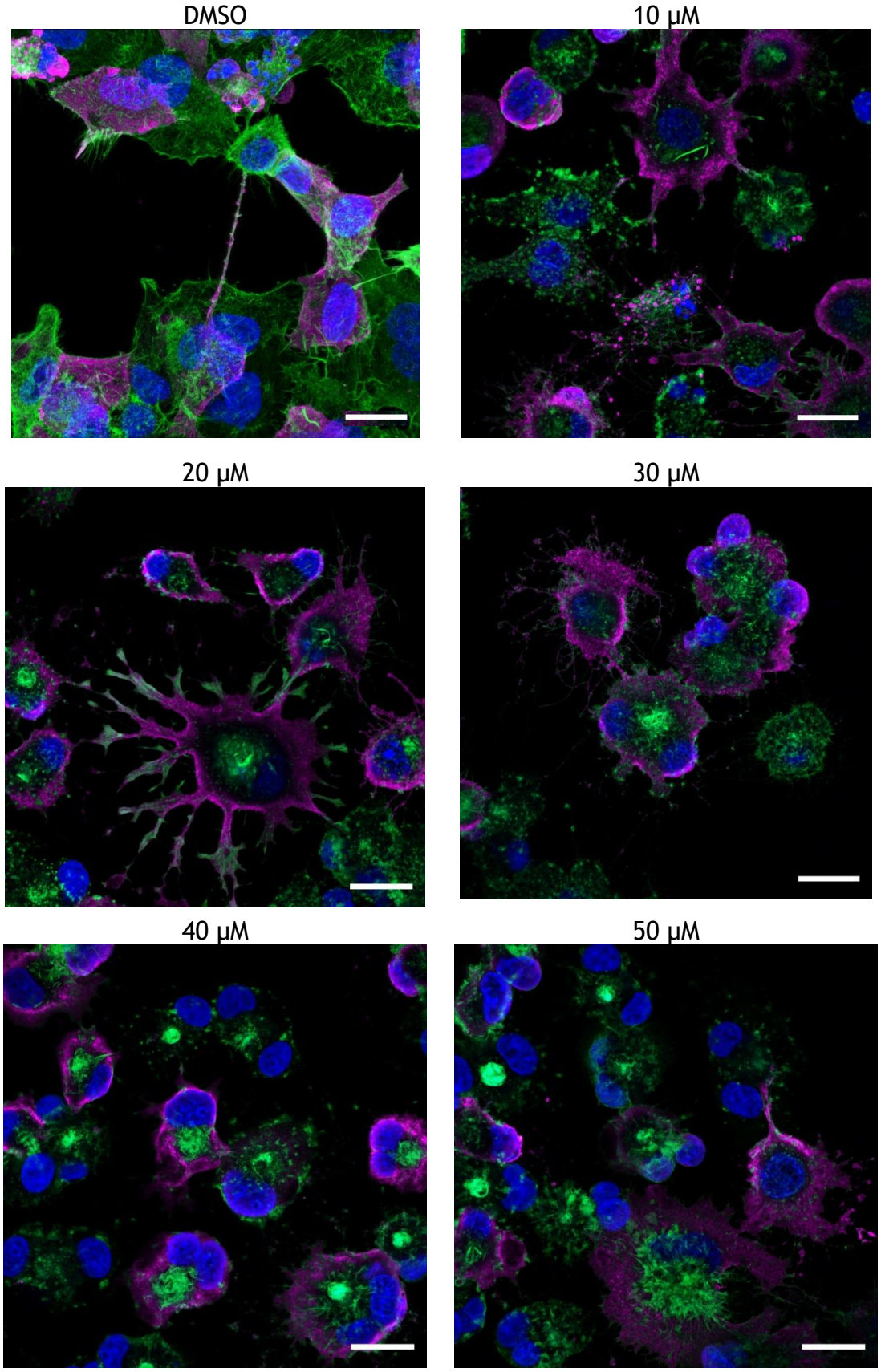

Figure 3-12: The titration of cytochalasin D. Representative confocal micrographs of MDCKs infected with PR8 at a MOI 0.6 PFU/cell, and treated with either DMSO, or increasing

concentrations of cytochalasin D 1 hour post infection. Cells were fixed and immunostained for NP 16 hours post infection. Nuclei (blue), F-actin (green), NP (magenta). Scale bar = 20 μm.

The titration of IPA-3 showed a similar concentration dependent effect on the extent of F-actin disruption (Figure 3-13). However, unlike with Cyto. D, this drug did not appear to cause a fracturing of F-actin, but instead appeared to reduce the abundance of F-actin within the cells (Figure 3-12 and Figure 3-13). This resulted in a near complete loss of all F-actin signal within cells treated with 5 μM IPA-3 (Figure 3-13). This difference in effect between drugs can be explained by their different mechanisms of action (Table 3-3), with IPA-3 increasing F-actin depolymerisation and Cyto. D decreasing F-actin polymerisation. Whilst NP localisation was broadly cytoplasmic at all concentrations tested (with the exception of 5 μM), I observed significantly more nuclear disruption at a concentration of 4 μM (Figure 3-13). This extent of nuclear disruption was greater than expected levels of CPE under these infection conditions, indicating cytotoxicity at this concentration. Therefore, an IPA-3 concentration of 3 μM was selected for future work.

Taxol targets microtubules (Table 3-3), and to evaluate the effect that this drug has on the cytoskeleton, I assessed the changes in cell morphology following the titration of this drug (Figure 3-14). This was made possible through the F-actin stain which can also be used to approximate cell boundaries as cortical F-actin lines the inner surface of the plasma membrane. Increasing concentrations of taxol caused cells to become increasingly rounded (Figure 3-14), indicating the successful disruption of the cytoskeleton. Concentrations of 120 μM, or higher, caused considerable chromatin condensation as well as cell loss. However, nuclear disruption was seen at all concentrations tested (Figure 3-14). Therefore, to select an optimal concentration of taxol, I identified the highest concentration that did not demonstrate increased cytotoxicity relative to the lowest concentration tested (60 μM), but still resulted in cytoplasmic NP signal. This criteria was fulfilled following treatment with 100 μM of taxol (Figure 3-14), and therefore this concentration was used in subsequent experiments.

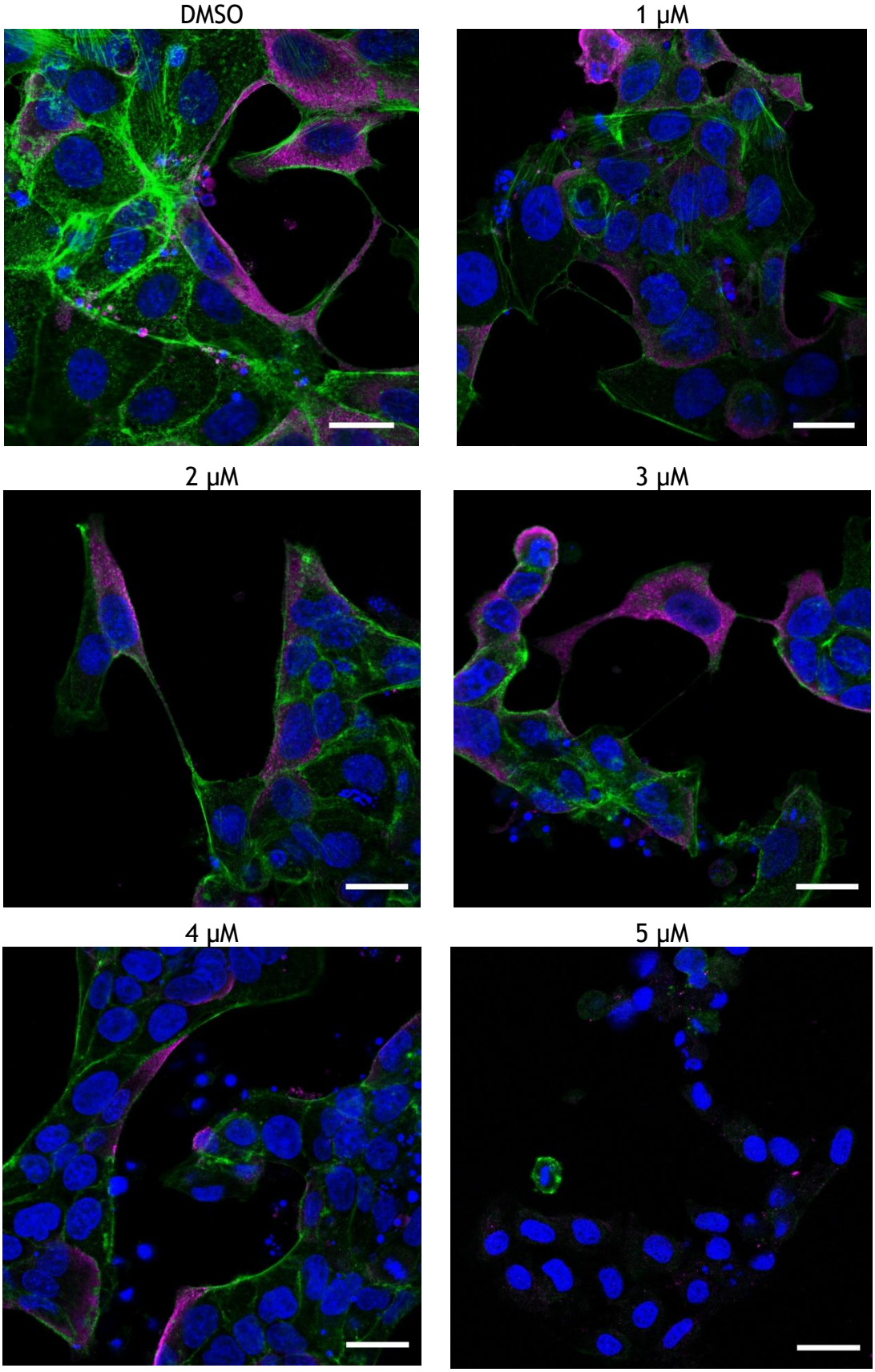

Figure 3-13: The titration of IPA-3. Representative confocal micrographs of MDCKs infected with PR8 at an MOI 0.6 PFU/cell, and treated with either DMSO, or increasing concentrations of IPA-3 1 hour post infection. Cells were fixed and immunostained for NP 16 hours post infection. Nuclei (blue), F-actin (green), NP (magenta). Scale bar = 20 µm.

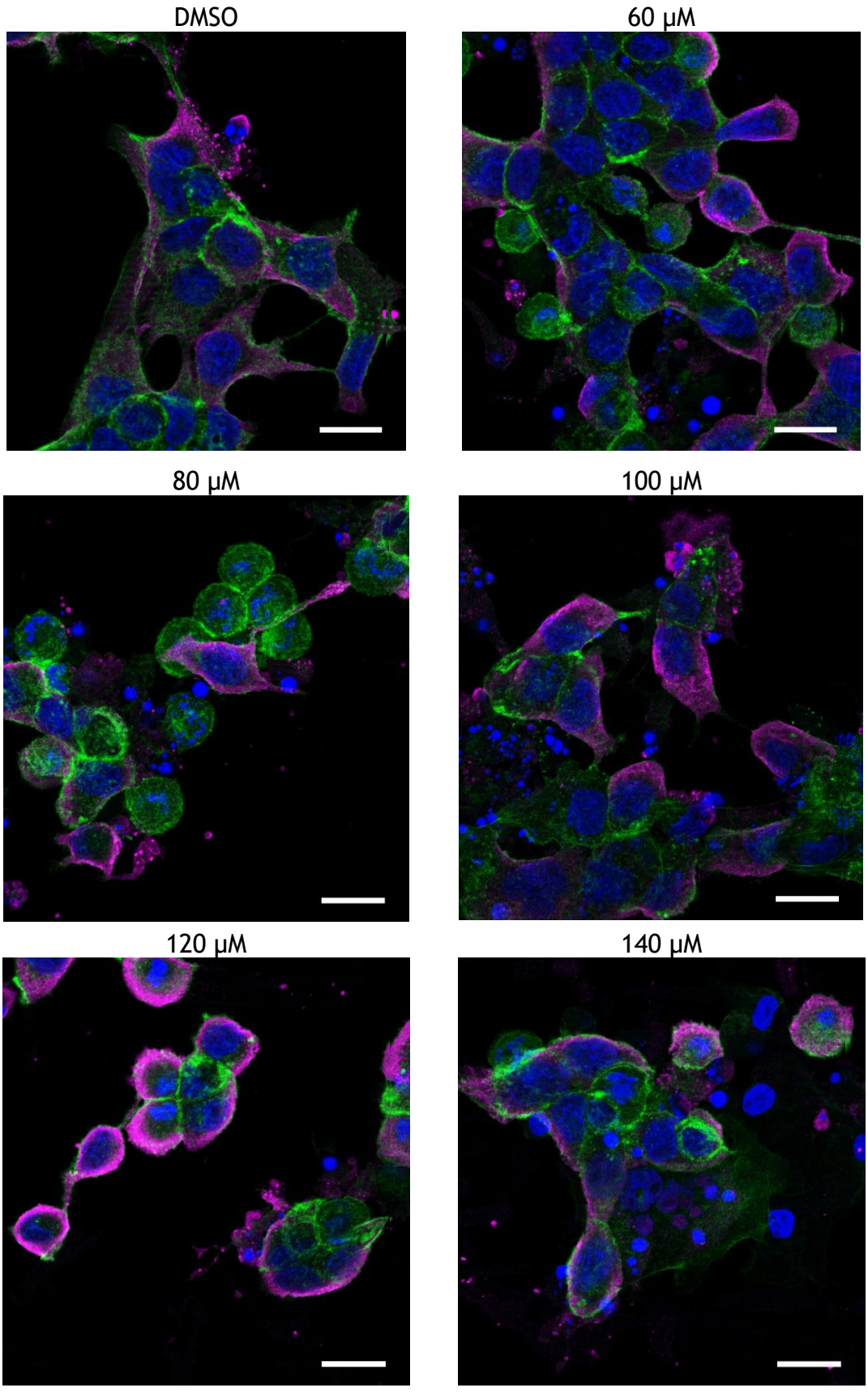

Figure 3-14: The titration of Taxol. Representative confocal micrographs of MDCKs infected with PR8 at an MOI 0.6 PFU/cell, and treated with either DMSO, or increasing concentrations of taxol 1 hour post infection. Cells were fixed and immunostained for NP 16 hours post infection. Nuclei (blue), F-actin (green), NP (magenta). Scale bar = 20 µm.

Optimal concentrations of each drug were then added to the microplaque assay overlay and the effect of each on direct cell to cell spread of IAV was assessed by measuring the resulting PR8 microplaques that formed 48 hours post infection. Similarly to previous experiments (Figure 3-8), I found that the inclusion of zanamivir only slightly reduced the frequency and scale of microplaques, with the exception of cells treated with Cyto. D or taxol (Figure 3-15). Interestingly, and contrary to the literature, these drugs increased the formation of microplaques regardless of the addition of zanamivir (Figure 3-15 a). This difference was statistically significant between the DMSO and Cyto. D treatments. Whilst IPA-3 did not increase microplaque formation, I found that this drug resulted in similar levels of direct cell to cell spread as the DMSO control group (Figure 3-15). Therefore, in our hands these drugs differed in their effects on IAV direct cell to cell spread relative to previous studies, with drugs targeting both F-actin and microtubules appearing to promote the direct cell to cell spread of IAVs. This was most pronounced with Cyto. D, and this effect was immediately clear when imaging PR8 infected cells in the presence of Cyto. D and in the absence of zanamivir (Figure 3-16). Given the unexpectedness of these results, I hypothesised that these drugs, Cyto. D in particular, either weakened the effectiveness of zanamivir in inhibiting cell free virion spread, or supported the direct cell to cell spread of IAV infection within the microplaque assay.

a)

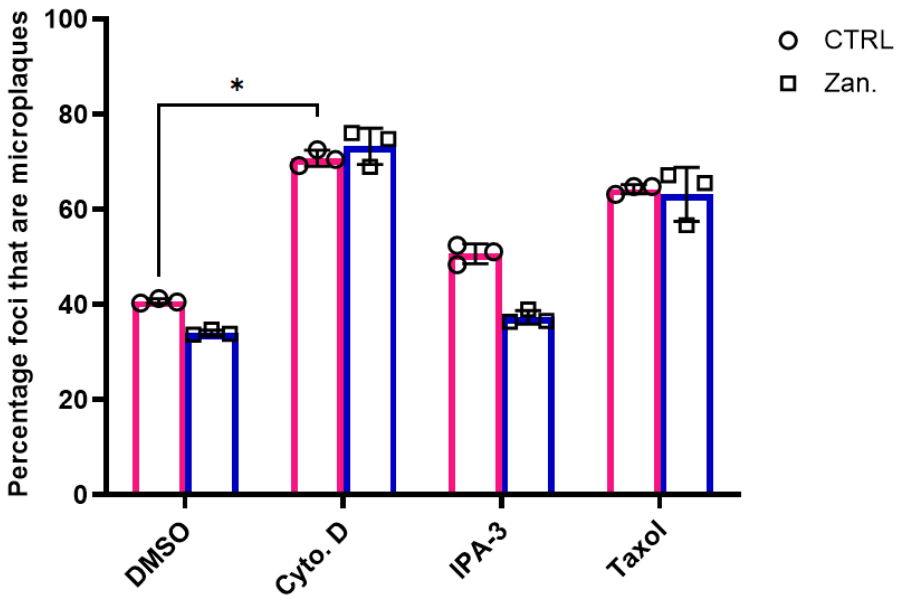

b)

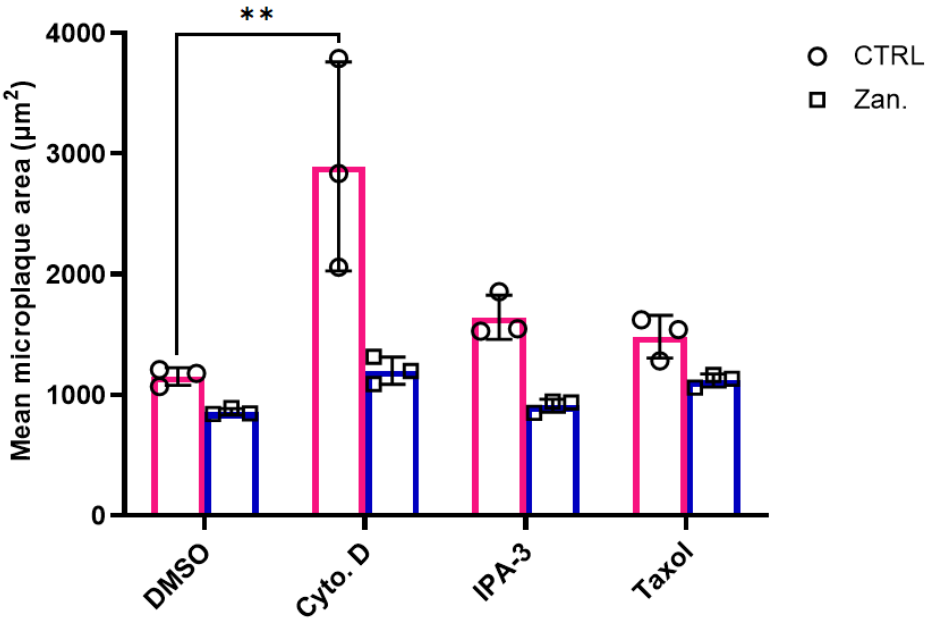

Figure 3-15: Direct cell to cell spread of IAV is not inhibited by drugs disrupting the cytoskeleton. (a) The percentage of NP positive foci that are microplaques in the absence of TPCK trypsin and (b) the mean area of microplaques with and without 0.36 mM zanamivir treatment, in the presence of a panel of drugs targeting the cytoskeleton. Confluent MDCKs were infected with PR8 at a MOI of 0.0004 PFU/cell, and 2 hours post infection an overlay containing either DMSO, cytochalasin D (20 µM), IPA-3 (3 µM), or taxol (100 µM) was added. Cells were fixed 48 hours post infection, immunostained for NP and imaged on the Nexcelom Celigo image cytometer Differences between mock and zanamivir treatments was tested for significance using a multiple Mann-Whitney test (n.s. $p > 0.05$). Differences between drug treatments relative to the DMSO control, either as part of the control or zanamivir treated group, were tested for significance using a Kruskal-Wallis test (n.s. $p > 0.05$, *$p < 0.05$, **$p < 0.01$). For all data the mean and SD are shown (n = 3).

a) DMSO b) Cytochalasin D (20 μM)

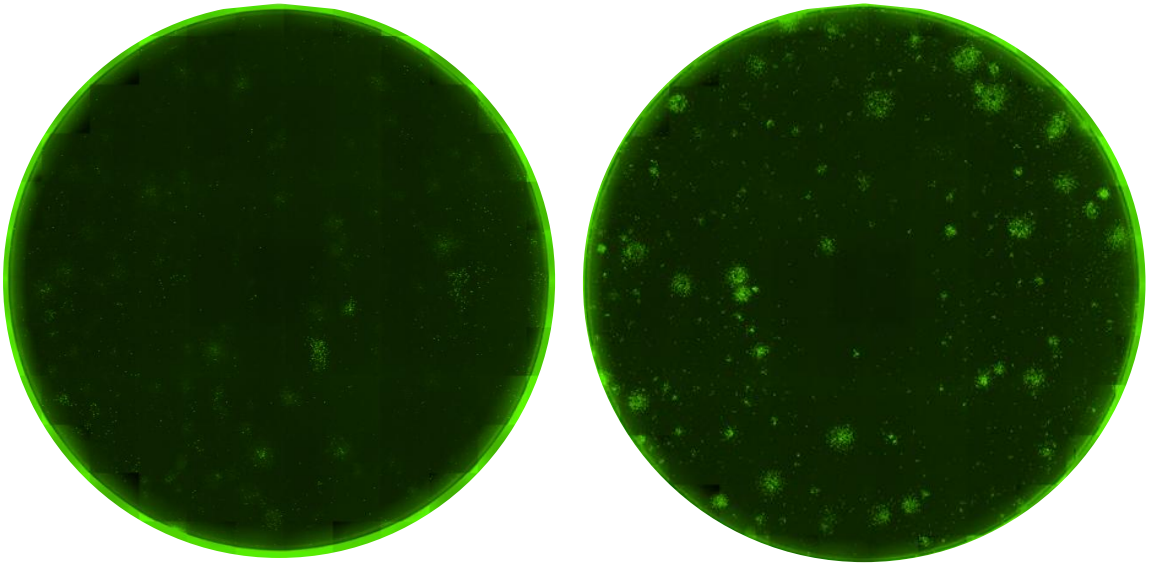

Figure 3-16: The effect of cytochalasin D on IAV infected foci. Representative images of scanned 12 well plates containing confluent MDCK cells infected with PR8 (MOI 0.0004 PFU/cell) and treated with either DMSO or 20 μM cytochalasin D, in the absence of zanamivir. Cells were fixed 48 hours post infection and immunostained for intracellular NP (green). Plates were scanned on the Nexcelom Celigo image cytometer and are representative of three biological repeats.

To investigate whether these drugs enabled virus breakthrough of zanamivir I performed a virus release assay, as done previously (Figure 3-3), with the inclusion of each drug in the overlay either individually or in combination with 0.36 mM zanamivir. As before, I found complete cell loss from infected wells treated with DMSO in the absence of zanamivir and no plaques when zanamivir was included (Figure 3-17), confirming successful inhibition of virion release. Following Cyto. D and IPA-3 treatment, CPE was only seen when zanamivir was excluded (Figure 3-17). Taxol treatment appeared to cause a thinning of the monolayer, either through the cell rounding or the cytopathic effect that I previously saw (Figure 3-14). Nevertheless, I only observed one possible plaque across three biological replicates in the well inoculated with the media containing taxol and zanamivir (Figure 3-17). Overall, these results indicate that these drugs (particularly Cyto. D and IPA-3) did not increase the amount of cell free virion spread when zanamivir was present. Therefore, the significant increase in microplaque formation in the presence of Cyto. D is more likely to be a consequence of this drug supporting IAV direct cell to cell spread within the microplaque assay.

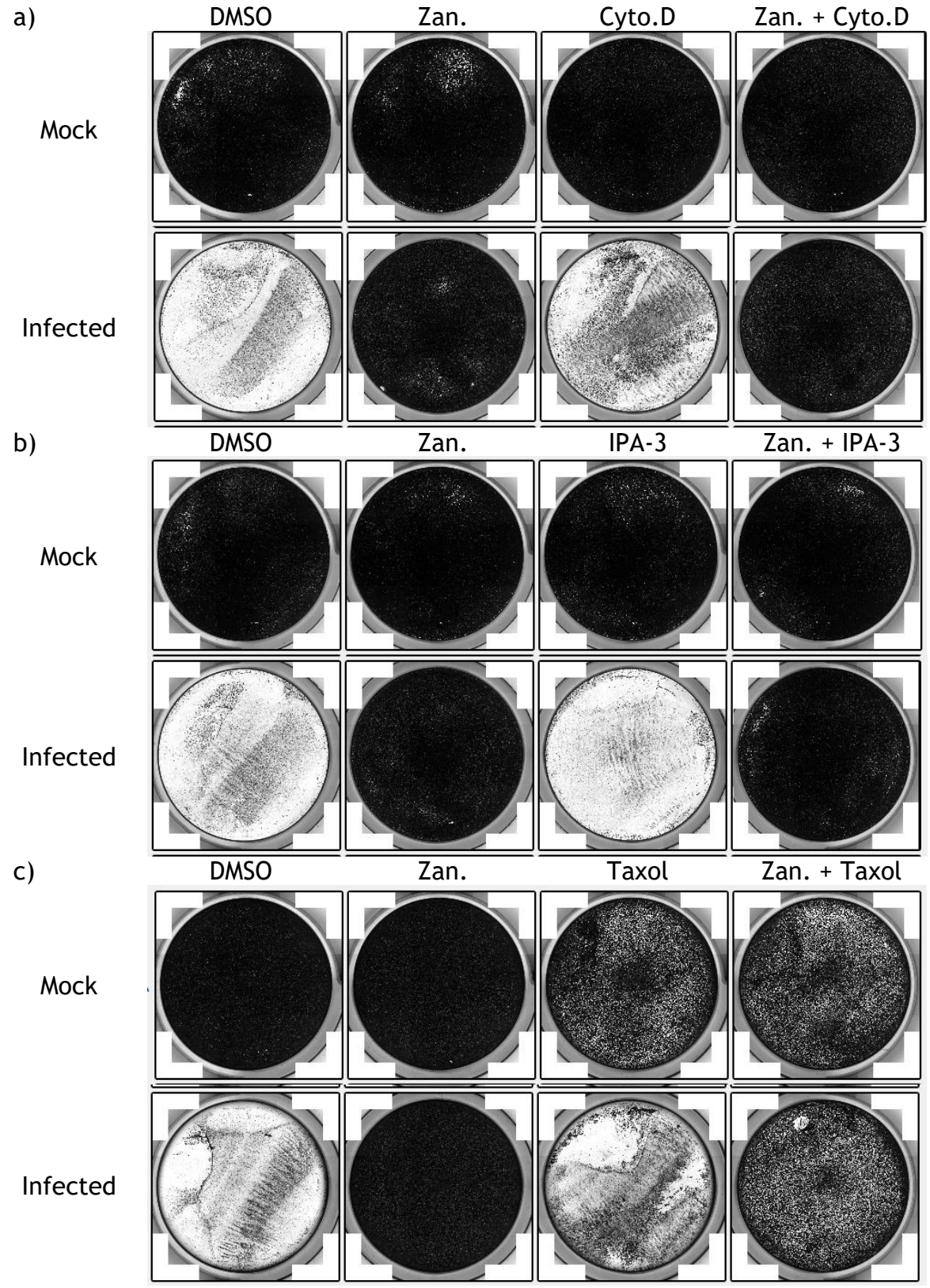

Figure 3-17: The effect of cytoskeleton disrupting drugs on zanamivir inhibited virion release. Coomassie stained MDCK cells within 12 well plates, 72 hours after inoculation (which was performed for 1 hour at 37℃, with occasional rocking) with TPCK trypsin treated supernatants collected from PR8 infected microplaque assays performed in the presence of DMSO or 0.36 mM zanamivir in isolation or in combination with a cytoskeleton disrupting drug. These drugs included (a) cytochalasin D (20 μM), (b) IPA-3 (3 μM) and (c) taxol (100 μM). After adsorption onto the plaque assay wells, the inoculum was discarded, cells washed and cultured under an Avicel overlay containing 1 μg/mL TPCK trypsin. Images are representative of three biological repeats.

To investigate the Cyto. D mediated increase in IAV direct cell to cell spread more closely, I performed a microplaque assay with PR8 using overlays differing in zanamivir and Cyto. D content. I then fixed samples at different time points post infection, and compared the resulting microplaques that formed between treatments over time (Figure 3-18). For all overlays, the biggest increase in microplaque formation occurred between 6 and 16 hours post infection, and the levels then remained consistent (Figure 3-18 a). It is unlikely that individual infected MDCK cells survived 48 hours of infection with these viruses. Therefore, instead of direct cell to cell spread appearing to stop at 16 hours post infection, I hypothesise that this levelling effect is due to IAV direct cell to cell spread occurring at a steady rate. In other words, IAV infected cells directly spread IAV infection to neighbouring cells at rates comparable to their loss. This would also help to explain the largely consistent mean area of microplaques over time (Figure 3-18 b). The frequency of microplaque formation was consistent at each time point between DMSO or zanamivir only treatments, as expected from previous findings (Figure 3-15 a). However, Cyto. D had a positive effect on the formation of microplaques from as early as 16 hours post infection, when IAV direct cell to cell spread appears to first occur (Figure 3-18 a). This supports the hypothesis that in this assay Cyto. D increases the ability of IAV infected cells to spread infection directly to their neighbours.

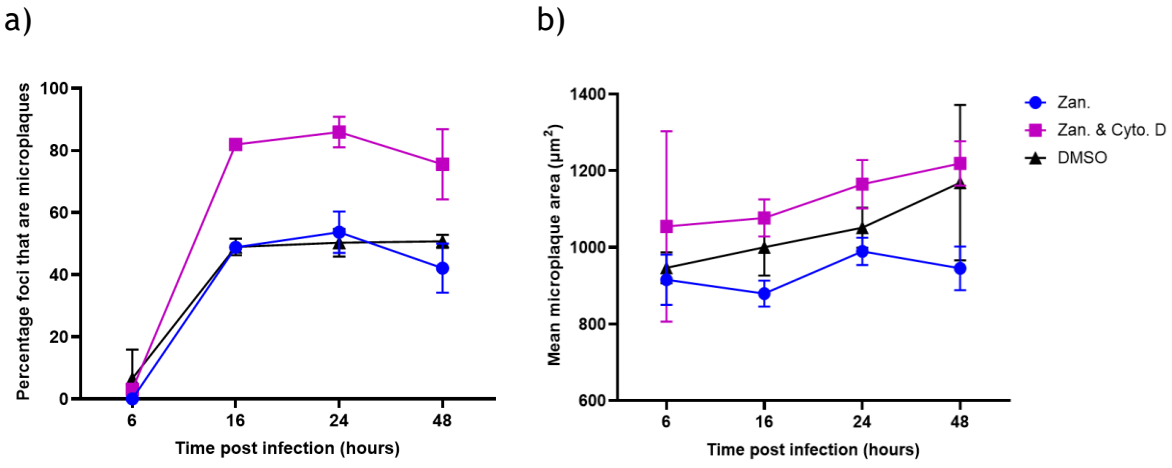

Figure 3-18: Microplaque formation following cytochalasin D treatment over a time course of infection. Confluent MDCKs were infected with PR8 as done previously in the microplaque assay. Two hours post infection, the cells were washed and treated with an overlay containing either DMSO (mock treated), 0.36 mM zanamivir, or both cytochalasin D (20 µM) and 0.36 mM zanamivir. At the specified time points, the overlay was removed and cells fixed, and immunostained for intracellular NP. Microplaques were imaged and analysed as done previously (see Figure 3-7), and (a) the percentage of NP positive foci that were microplaques as well as (b) the mean area of these microplaques was determined. Differences in microplaque formation between overlays was tested for significance at each time point by Kruskal-Wallis test (n.s. $p > 0.05$). The mean and SD are shown (n = 2).

Within the microplaque assay, the cells are confluent and multiple mechanisms of direct cell to cell spread are theoretically able to function simultaneously. Therefore, I hypothesised that this increase with Cyto. D could be due to opposing effects of this drug on different mechanisms of direct cell to cell spread, with some being positively regulated whilst others are inhibited. In order for this scenario to be true, and still result in such a significant increase, the mechanisms of direct cell to cell spread that are positively regulated by Cyto. D must drastically exceed the function of mechanisms that are inhibited by it. Such a net positive effect would be surprising. I was then curious if the conditions of my microplaque assay (that differed to those used in published literature (222)) could already be inhibiting mechanisms of direct cell to cell spread, particularly those that would otherwise be inhibited by Cyto. D. If so, this could explain both the disparity between studies, as well as possibly how mechanisms possibly enhanced by Cyto.D could so greatly exceed that of the DMSO controls. In other words, if mechanisms sensitive to the inhibitory effect of this drug are already inhibited by the assay conditions, only the effects of mechanisms positively regulated by Cyto.D would then be captured upon addition of the drug - resulting in the significant increase in microplaque formation that I observed.

To explore this hypothesis I identified the ways in which the microplaque assay I established differed from those of previous studies. The assays were very similar, however, my microplaque assay primarily differed by the use of a semi-solid overlay which I achieved with Avicel. It was therefore possible that this semi-solid overlay was inhibitory to some mechanisms of direct cell to cell spread. To test this, I performed a microplaque assay with both PR8 and Udorn using overlays with different combinations of Avicel and zanamivir. Comparing between samples differing only by Avicel content, there was no significant difference in the frequency or scale of PR8 and Udorn microplaques (Figure 3-19). Furthermore, Avicel content had no consequence on the effect of zanamivir, with reduction in microplaques being minimal regardless of the presence of Avicel (Figure 3-19). Therefore, these results do not support the hypothesis that functioning mechanisms of IAV direct cell to cell spread are inhibited by the inclusion of Avicel. Overall, these results suggest that the

Cyto.D-associated increase in apparent direct cell-to-cell spread is unlikely to be an artefact of the Avicel-based overlay conditions used in the microplaque assay.

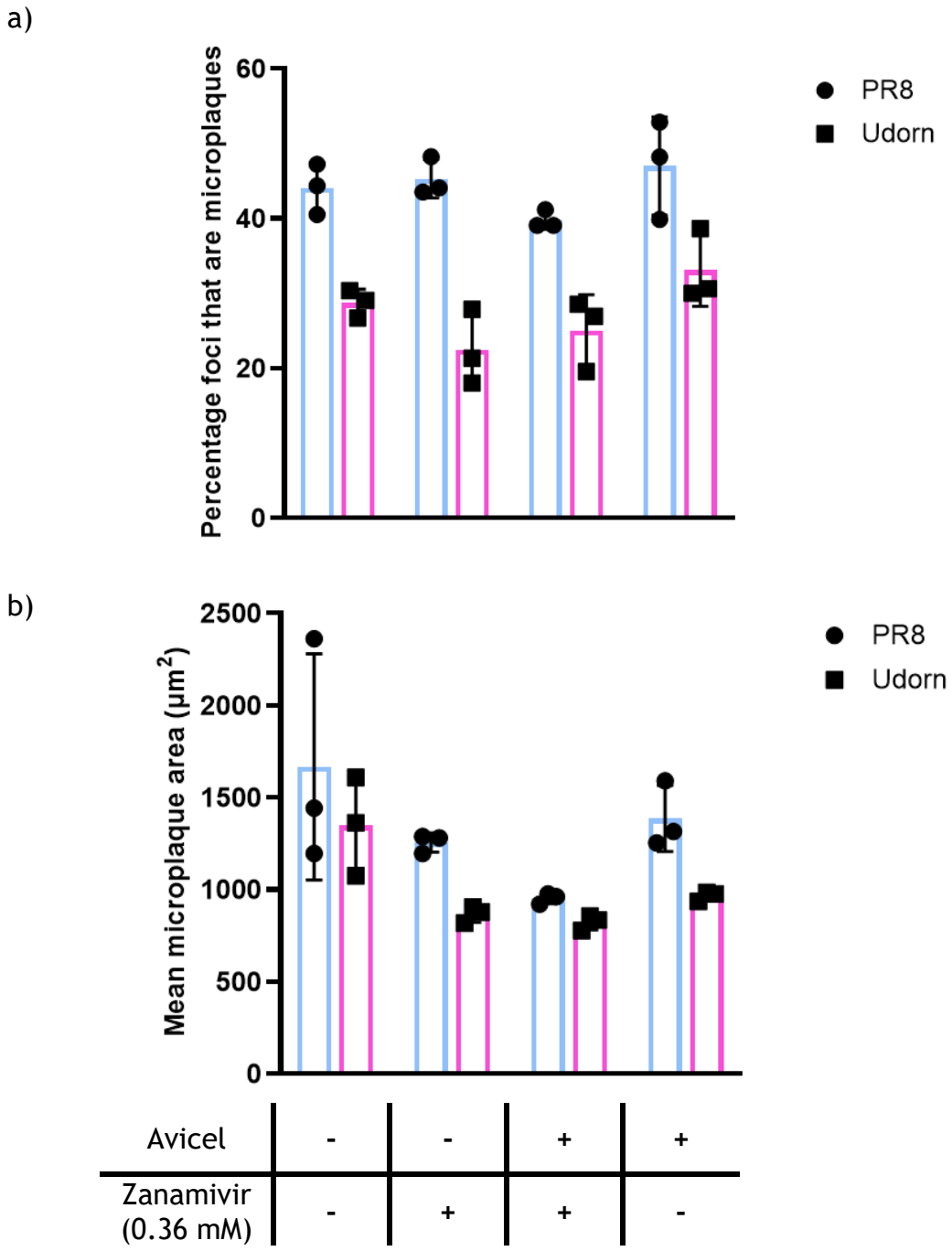

Figure 3-19: The effect of Avicel on microplaque formation. Confluent MDCKs were infected with either PR8 or Udorn as done previously in the microplaque assay. Two hours post infection, the cells were washed and treated with an overlay containing a combination of either DMSO (-) or 0.36 mM zanamivir (+) and 1.2% Avicel or serum free DMEM. Forty-eight hours post infection, the overlay was removed, cells fixed, and immunostained for intracellular NP. Microplaques were imaged and analysed as done previously (see Figure 3-7), and (a) the percentage of NP positive foci that were microplaques as well as (b) the mean area of these microplaques was determined. Differences in microplaque formation between overlay conditions was tested for significance by Kruskal-Wallis test (n.s. $p > 0.05$). The mean and SD are shown (n = 3).

3.3 Discussion

In this chapter I measured and compared the ability of IAVs with different virion morphologies to undergo direct cell to cell spread. Firstly, I established and validated an assay that inhibited virion release and enabled the visualisation and measurement of IAV direct cell to cell spread. I then used this system to investigate the efficiency by which IAVs undergo direct cell to cell spread, investigating the role of virion morphology and the broad mechanisms of IAV direct cell to cell transfer.

I showed that the ability to form abundant filamentous virions of lengths greater than 12 μm did not provide any advantage for the cell to cell spread of IAV infection within a microplaque assay (Figure 3-9). Indeed, the spherical PR8 strain was more effective at directly infecting neighbouring cells than the filamentous Udorn strain ($p = 0.0134$, Kruskal-Wallis test). This difference was not seen between the segment 7 reassortant viruses which displayed an intermediate virion morphology relative to the wild-type virus (Figure 3-9). This strongly suggested that the difference in direct cell to cell spread between the WT viruses was not primarily conferred by the morphology of the budding virion. However, the intermediate phenotypes of the segment 7 reassortants, particularly when it comes to the concentration of filaments (Figure 3-6 b), may indicate that these viruses may not provide the sensitivity required to investigate the consequence of virion morphology changes. That being said, the method used to determine the concentration of filaments makes several assumptions. By measuring concentration as the amount of filaments per field of view following a dilution of harvested supernatants, this assumes that the replication kinetics and amount of virus produced is consistent between strains and that the filaments of different lengths spin on to the glass coverslips with equal efficiencies. These assumptions mean that any deviation from them would alter the outcome of the analysis and ultimately the concluded concentration of filaments produced from these strains. To address these limitations, future methods of determining filament concentrations should seek to normalise the abundance of filaments with either the amount of spherical virions produced (not possible with the resolution limits of the light microscope used) or the infectious titre of virus supernatants as determined by a parallel plaque assay. Nevertheless, the data collectively indicates that the ability of IAVs to undergo

direct cell to cell spread is not determined by the ability of an IAV to produce abundant, lengthy filamentous virions.

I found that all IAVs tested were capable of efficient direct cell to cell spread, with between 25 and 40% of infected cells spreading infection directly to their neighbours (Figure 3-9). A high efficiency of IAV direct cell to cell spread has been previously shown in the study by Roberts *et al*. that used the microplaque assay to measure the direct cel to cell spread of Udorn (222). Whilst the authors grouped infected foci consisting of either 1 or 2 neighbouring cells together, when they looked at microplaques consisting of 3 or more cells they found that this constituted approximately 44% of NP positive foci. This frequency of Udorn microplaque formation is nearly double what I observed with the same strain and is closer to that observed following PR8 infection. The source of this discrepancy can not be explained by differences in microplaque assay overlay as the inclusion of Avicel within the assay I established had no effect on Udorn or PR8 microplaque formation (Figure 3-19). Furthermore, the time point post infection that the cells are fixed (48 hours) and then immunostained for NP, is also consistent between studies. Of note, Roberts *et al*. infected MDCK cells at an MOI of 0.1 (222), which was 250-fold higher than the MOI I optimised to provide a large number of infected foci with an appropriate distribution from each other. Therefore, it is possible that the higher amounts of Udorn microplaques reported by Roberts *et al*. could be a result of a higher probability that neighbouring cells were infected at the beginning of the experiment, as opposed to direct cell to cell spread.

Furthermore, previous reports showing a greater amount of microplaque formation were scored by manual inspection of confocal micrographs (222, 230). In contrast, I performed microplaque analysis with an imaging cytometer (Figure 3-7). This enabled me to apply a set of optimised parameters for the consistent analysis of entire wells across treatments and replicates (see 2.2.13.2). However, this approach does not provide the same resolution or sensitivity as confocal microscopy. Therefore the analysis parameters I established on the imaging cytometer, such as fluorescence intensity thresholds, may be more conservative and could lead to a reduction in the detection of infected cells, particularly if the NP signal intensity is close to background levels.

It is also of note that Roberts *et al.* used a much higher concentration of zanamivir (10 mM) than what I deemed to be most effective in my assays (0.36 mM) (222). I found that the highest concentration of zanamivir that I tested (0.48 mM) actually resulted in an increase in Udorn microplaque formation, to levels comparable to the DMSO control (Figure 3-8). It is therefore interesting to hypothesise that the higher frequency of Udorn microplaques observed by Roberts *et al.* could have resulted from this higher concentration of zanamivir. Future work should investigate the potential positive influence that higher concentrations of zanamivir (between 0.48 and 10 mM) has on IAV direct cell to cell spread, perhaps in the manner hypothesised in section 3.1.2.

Until this is addressed, investigating past evidence of efficient IAV direct cell to cell spread in the absence of antiviral drugs can provide valuable insights into whether antiviral pressure is amplifying this route of intercellular transmission. The work by Ganti *et al.,* using HA-deficient viruses, elegantly quantified direct cell to cell spread without requiring antiviral drugs or neutralising antibodies (230). The authors found that infection with these viruses, 48 hours post infection, also resulted in a high frequency of direct cell to cell spread (230). However, by using the total number of infected cells to score microplaques, the analysis by Ganti *et al.* does not show how many individual microplaques are formed. From this data, I calculated that approximately 75% and 70% of NL09 and P99 infected cells, respectively, were part of microplaques (230). From this I can then calculate an estimated percentage of foci that were microplaques if I assume that the majority of microplaques consisted of 2 to 3 cells (similar to what I observed with PR8 and Udorn viruses). This results in a percentage of foci that are microplaques between 23 and 38% which is similar to the range of percentages seen with the viruses I tested with zanamivir (25 to 40%). Therefore, this strong similarity between studies that differed in the use of antiviral drug to measure IAV direct cell to cell spread provides some suggestion that 0.36 mM zanamivir did not artificially amplify my findings. However, with my observation that the frequency of IAV direct cell to cell spread varies by strain (Figure 3-9), the consequence of antiviral drug inclusion should be tested with the strains used by Ganti *et al.* before any definitive conclusions can be drawn. Interestingly, the frequency in NL09 and P99 direct cell to cell spread

does not display a strain difference, suggesting that the significant difference I observed between PR8 and Udorn may be unique to these viruses.

I showed that the majority of IAV direct cell to cell spread occurs between 6 and 16 hours post infection, with a sharp increase in the percentage of NP positive foci that are microplaques seen between these time points (Figure 3-18). With the detection of microplaques being dependent on the expression of NP within newly infected cells, requiring approximately 6 to 8 hours for expression to reach detectable levels, we can assume that the delivery of viral genomes to neighbouring cells occurred approximately 8 to 10 hours post infection. At this time point in infection, newly replicated vRNPs will be accumulating within the cytoplasm, interacting with the cytoskeleton, and host factors, facilitating their intracellular trafficking towards the plasma membrane. Also by this time, IAV replication, particularly NS1 expression, is likely to have caused cell cycle arrest (322, 323), which strongly suggests that this sharp increase in microplaque formation can not be explained by an infected cell that has recently divided (albeit the cells were not synchronised). What is not expected to have occurred by this time in infection is viral genome assembly, packaging and virion-mediated transmission. These processes are typically thought to occur after approximately 12 hours post infection. Therefore, the timings of when direct cell to cell spread begins does not coincide with when virus particle formation peaks. This supports the idea that infection spread can occur at earlier time points through mechanisms of direct cell to cell spread when compared to virion-mediated spread.

Furthermore, this infection time course supports my other findings involving the use of amantadine (Figure 3-11), that strongly suggested that IAV direct cell to cell spread within the microplaque assay is occurring through mechanisms that deliver cytoplasmic viral genomes, as opposed to the transfer of cell associated viruses. This is consistent with studies proposing that the transfer of cytoplasmic genomes is the primary mechanism of IAV direct cell to cell spread (222, 230). These studies include both the use of antiviral drugs (222), and HA-deficient viruses (230). However, Mori *et al.* reported that cell associated IAV transfer was the major driver of IAV direct cell to cell spread (227). I hypothesise that this discrepancy between studies could be due to the effects of TPCK trypsin and the scale of infection spread these authors looked at. The exclusion of TPCK trypsin

within the microplaque assay performed by Robers *et al*. and by myself (Figure 3-2), is likely to be suppressing cell associated virus transmission, as protease cleavage of HA is still required for this to occur. Similarly, HA-deficient viruses are not likely to be associated with the cell due to the lack of any receptor binding capabilities of the budding virions, and therefore have a reduced ability of cell associated virus transfer. Given that I saw no decrease in IAV direct cell to cell spread with increasing concentrations of amantadine (Figure 3-11), it is unlikely that the retention of virions to the cell surface (through the effects of zanamivir), is by itself enhancing the transfer of cell associated virus, and indeed the HA dependency as reported by Mori *et al*. is likely to be caused not only by the retention of the virus to the cell surface, but also the cleavage of HA by TPCK trypsin (227). Importantly, the study by Mori *et al*. measured the area of infected foci and uniquely did not score direct cell to cell spread at the scale of 2 to 3 cells. Therefore, it is possible that the formation of larger microplaques can occur through cell associated virus transfer, but only when TPCK trypsin is supplied. Future work is required to assess the contributions of cell associated virus transfer during IAV direct cell to cell spread and how TPCK trypsin may not only be facilitating this, but possibly enhancing it.

Additionally, I showed that cytoskeleton disrupting drugs did not reduce direct cell to cell spread of IAVs (Figure 3-15), and Cyto. D actually increased the frequency of microplaque formation (Figure 3-16). This data is contrary to previous reports, however, I showed that the differences between the microplaque assay I established and that published by Roberts *et al*. (222) did not reveal the source of this discrepancy (Figure 3-19). I hypothesised that since multiple mechanisms of IAV direct genome transfer could be functioning between the confluent cells of the microplaque assay, the enhanced direct cell to cell spread of IAVs following Cyto. D treatment could be due to this drugs ability to increase the efficiency of some of these mechanisms. For example, actin is known to modulate the permeability of tight junctions through interactions with tight junction proteins such as ZO-1 and occludin (324, 325). It is perhaps unsurprising that Cyto. D disruption of actin has been shown to increase the permeability of tight junctions between MDCK cells (324). The relevance of viral genome transfer through tight junctions has been demonstrated for some viruses such as HCV (see 1.3.1.2). Future work is

required to assess whether IAVs can use tight junctions to perform direct cell to cell spread, and how Cyto. D may in turn influence this.

Overall, the findings of this chapter revealed that the direct cell to cell spread of IAV infection is an efficient route of intercellular transmission. Whist the frequency of direct cell to cell spread varies between IAVs, the implication that viral genomes are being directly transferred is consistent. This suggests a critical role of select mechanisms of direct cell to cell spread known to perform this function, such as the trafficking of cytoplasmic cargo through TNTs. However, I demonstrated that drugs presumed to inhibit this transfer did not have an antiviral effect, suggesting that alternative or multiple mechanisms of IAV viral genome transfer are functioning in the microplaque assay. In the next chapter of this thesis, I explore this further by examining in greater detail the contribution of TNT-like structures (TLS) to the direct cell to cell spread of IAV infection across a range of contexts.

Chapter 4

4 Investigating how IAVs induce tunnelling nanotube-like structures and exploring their potential for spreading infection within the host

4.1 Introduction

4.1.1 TNTs and TNT-like structures

As introduced in chapter 1 of this thesis, TNTs are cellular structures that can be induced by a number of viruses to facilitate their direct cell to cell spread. Research of IAV direct cell to cell spread (as explored in chapter 3) strongly suggests a role of TNTs in facilitating the direct transfer cytoplasmic IAV genomes between cells. Therefore, this warrants a closer examination of how IAVs could be exploiting these cellular structures.

However, TNTs are well defined, unique cellular structures that can be confused with other cellular protrusions (see 1.3.1.4). Due to the challenges demonstrating all of the definitive properties of TNTs (see 1.3.1.4) when classifying these fragile and transient cell connecting structures (202), it is often impractical to apply each of these criteria when analysing large quantities of imaging data. Therefore, intercellular connections that meet most but not all of these criteria are typically referred to as TNT-like structures (TLSs) (206-209). Whilst most of the defining properties of TNTs are unique and easily distinguishable (meaning the likelihood of false positives are relatively low), this classification helps to provide much needed clarity as to the nature of the structures examined, and acknowledges the common methodological limitations currently affecting this field, whilst not preventing meaningful work into the role of TLSs in both health and disease.

4.1.2 TNT-like structures and IAV infection

In the case of IAV infection, it is clear that these viruses efficiently induce the formation of TLSs between A549 and MDCK cells following high MOI infections (222, 223, 230, 231). Crucially it is not understood how these viruses are inducing the formation of these structures, and more is understood about the

host factors required for viral genome trafficking through TLSs, such as Rab11a. These factors were found not to regulate TLS formation (230), and separates the mechanism of induction from cytoplasmic cargo incorporation and trafficking.

As discussed in chapter 3, the disruption of actin polymerisation with a variety of drugs (cytochalasin D and IPA-3) reduces IAV direct cell to cell spread (see 3.1.2). These drugs also reduce TLS formation, and this correlation provides strong evidence that TLSs induced by IAVs are functioning to traffic infection directly between cells (222). Furthermore, immunostaining of a variety of IAV proteins has revealed the incorporation of HA, M, M2, PA and NP within these cell connecting structures (222). The latter two proteins are components of the vRNP complex and their presence within TLSs indicates the incorporation of vRNP complexes. This was further supported with the colocalization score of NP with Rab11a within TLSs being consistent with the known complex interaction mediated by the PB2 protein (a member of the heterotrimeric polymerase that associates with the vRNPs) (230). These reports, together with the mechanism studies of IAV direct cell to cell spread discussed in chapter 3, suggests that TLS mediated IAV direct cell to cell spread is performed by TLS mediated cytoplasmic genome transfer, as opposed to the virion “surfing” on the extracellular surface of the TLS towards the recipient cell, the latter of which is seen with HIV-1 and SARS-CoV-2 (281, 326). Therefore, unless proven otherwise, it is reasonable to assume that the TNTs induced by IAVs are open-ended and provide cytoplasmic continuity between cells.

Studies that quantified TLS induction by IAVs used only a single strain, with some going on to measure direct cell to cell spread of multiple strains (222, 230). Therefore, it remains to be seen if differences between IAV strains could be influencing the extent of TLS induction in a way that correlates with direct cell to cell spread frequency, which could provide important mechanistic evidence behind these processes. This hypothesis of a strain-dependent effect is made more attractive when it was reported that an H5N1 virus was able to undergo cell to cell spread more readily than a PR8 virus, with a suggestion that this correlated with trogocytosis and then TNT formation (231). However, in this instance the induction of TLSs was only scored following infection with the H5N1 virus, and a connection between these strains and triggered processes is unclear.

As already explained in chapter 3, the studies that assessed IAV direct cell to cell spread frequency did not directly compare between strains and did not examine the influence of virion morphology (222, 223, 230). Therefore, in addition to investigating a strain-dependent effect, I was also curious as to how virion morphology could be underlying this. It is striking to note the many parallels that exist between filamentous IAV virions and TLSs. Both are similar in their dimension, composition and cellular processes involved in their formation (summarised in Table 4.1). To date, an investigation on virion morphology and TLS induction has not been performed and both filamentous (Udorn IAV and Ebola) and non-filamentous viruses (e.g. Zika and SARS-CoV-2) have been shown to induce them (Table 1-3). A link between TLS and filamentous virion formation is yet to be demonstrated, with the closest example perhaps being the structures formed by the PRD1 bacteriophage (327). This phage was seen to transform its protein-rich virus membrane into protruding nanotube structures which can deliver its DNA genome into gram negative bacteria *in vivo* (327). However, these phage structures are distinct from TLSs, with the former having an average length of approximately 50 nm (327). It remains to be seen whether variations in virion morphology influences TLS formation and given the similarities between them, I hypothesised that the extent of TLS induction would be strain-dependent and that this would reflect a greater ability of filamentous virions to induce TLSs when compared to spherical virions.

Table 4.1: The similarities between budding filamentous IAV virions and TNTs.

	IAV filaments	TNT	Ref.
Dimension	Diameter – approximately 100 nm. Length – variable, but can exceed 30 µm.	Diameter – range of 50 to 1500 nm. Length - ranges from 6 to 100 µm.	(157, 235)
	Can interweave causing cord like bundles	Can interweave causing cord-like bundles.	(158, 245)
Composition	Membranous projections containing F-actin.	Membranous projections containing primarily F-actin and thicker TNTs contain microtubules.	(202, 222, 223, 328)
Formation	Cytoskeletal involvement – vRNPs associate with actin and Rab11 is recruited to traffic vRNPs to budding sites. Actin polymerisation contributes to virion morphology (jasplakinolide ablated IAV filament formation).	Cytoskeletal involvement – actin structural core and Rab11a is required for vRNP incorporation.	(132, 144, 145, 202, 230,

	Membrane curvature – viral HA, NA and M2 protein induces membrane curvature at lipid rafts. M1 scaffolding drives filament elongation.	Membrane curvature - Local membrane nanodomain segregation (PIP2 enriched) and curvature sensing by proteins (e.g. IRSp53) generate protrusions, reinforced by actin polymerisation.	235, 329-332)
Role in infection spread	Incorporates and packages viral genomes within the virion for delivery to new cells.	Incorporates and traffics viral genomes to the cytoplasm of connected cells.	(157, 162, 222, 223)
	Hypothesised to be immune evading.	Facilitates IAV direct cell to cell spread in the presence of neutralising antibodies and antiviral drugs.	

4.1.3 TNT-like structures in the lung

To date, TLSs following IAV infection have only been observed *in vitro*, and in order for TLSs to be considered relevant for IAV infection *in vivo* they first need to be observed to be forming from IAV infected cells within the lung epithelium.

The visualisation of TLSs *in vivo* and *ex vivo* have been mostly limited to tissues with relatively lower cell densities and/or higher rigidities (333-336), with only some non-infection-based stresses or pathologies studied (e.g. lipopolysaccharide treatment (333), or solid tumours (257, 336, 337)). Therefore, tissues have been imaged with low complexity staining and tissue manipulation (257, 265, 337), and it is yet to be demonstrated that TLSs connect healthy and diseased cells within tissues. This consideration is critical to assessing whether TLSs can deliver an infection to an uninfected neighbour.

TLSs have been observed within solid lung tumours (265). However, TLSs within the lung epithelium (the typical site of IAV infection in mammals), is yet to be demonstrated. Therefore, the detection of TLSs involving IAV infected cells within the lung would provide not only the first evidence of TLSs connecting epithelial cells *in vivo*, but also the first evidence of TLSs at the site of an infection; supporting a possible physiological relevance of these structures in facilitating direct cell to cell spread.

4.1.4 Chapter aims

Multiple studies have reported the induction of TLSs following single high MOI IAV infections (222, 223, 230), but the reason for this was unknown. I therefore compared TLS induction across different IAV strains and evaluated their role in promoting viral spread *in vitro*. Additionally, the physiological relevance of TLSs following IAV infection *in vivo* was unexplored and I therefore searched for there presence in IAV infected lungs.

Therefore, in this chapter I aim to:

1. Investigate how IAVs induce the formation of TLSs.

2. Assess the contribution of virion morphology to TLS formation.

3. Determine the contribution of TLSs in IAV direct cell to cell spread.

4. Explore the physiological relevance of TLSs during IAV infection by determining if they are present in infected lung tissues.

4.2 Results

4.2.1 Do IAVs induce tunnelling nanotube-like structures through extracellular signalling molecules?

To begin to investigate how IAV infection induces the formation of TLSs *in vitro,* I needed to define the criteria of TLSs for scoring micrographs and then ensure that IAV infection conditions allowed the cells to form structures, that when fixed and imaged, meet these criteria. The developed experimental system must also be easy to manipulate and be amenable to high throughput super resolution confocal imaging. Furthermore, I needed to establish infection conditions that were characterised by robust viral replication, without causing too much CPE or cell loss even at high MOI infection.

To do this, I used MDCK cells due to their high permissiveness to IAV infection, their ability to produce innate immune signals, and their previous use for the study of TLS induction (222, 338). I emulated the conditions of previous reports that showed robust viral replication and TLS induction following approximately 16 to 18 hours of infection at an MOI >1 (222). Specifically, I infected subconfluent cells with an IAV at an MOI of 1.5 PFU/cell (ensuring that every cell had the opportunity to be infected), and applied an optimised fixation method (see 2.2.7, (285)), to IAV infected cells at 16 hours post infection. I then imaged cells via super resolution confocal microscopy having stained them for nuclei, F-actin and IAV NP.

In this work, I classified F-actin containing structures appearing to connect cells over a minimum distance of 5 µm as TNT-like, and excluded those that have likely resulted from recent cell division or death (e.g. structures with cellular midbodies, or involving cells with fragmented nuclei). This criteria reduces the likelihood that non-TNT structures are positively scored. For example, filopodia have an average length much shorter than the 5 µm threshold (see 1.3.1.3), and nanopodia typically lack F-actin (311). However, in the absence of verified 3D

suspension and functional trafficking through TNT-like structures they can not be classified as definitive TNTs.

Micrographs of IAV infected, subconfluent MDCK cells revealed TLSs with a variety of thicknesses, and presumed stabilities, suggesting that my approach was not disrupting even the most thin and fragile TLSs (Figure 4-1 a). Consistent with previous cell culture based studies, I found that by this infection time point, infected cells typically produce straight TLSs that contain punctae of viral nucleoprotein (NP), which has been used previously to indicate the incorporation and transport of the viral ribonucleoprotein (vRNP) complex (Figure 4-1 a) (222, 223, 230). Overall, this demonstrates the suitability of our *in vitro* approach for studying how IAV infection induces TLS formation.

Having confirmed the ability to detect TLSs, I next examined whether IAVs could induce their formation via innate immune signalling—a mechanism previously documented outside the context of infection. (see 1.4.2.1). To explore this, I collected the medium from MDCK cells 16 hours post infection (by which point abundant viral replication has occurred and TLSs can be readily observed, Figure 4-1 a) with Udorn virus (a lab adapted human IAV strain that has previously been shown to induce TLSs (222)). The virions within this harvested media were inactivated with U.V. irradiation before overlaying the media onto fresh cells (Figure 4-1 b). This therefore enables the investigation of extracellular factors that are secreted following IAV infection without the presence of actively replicating virus. Sixteen hours post treatment with U.V., I then used immunofluorescence to confirm virus inactivation (Figure 4-1 bi).

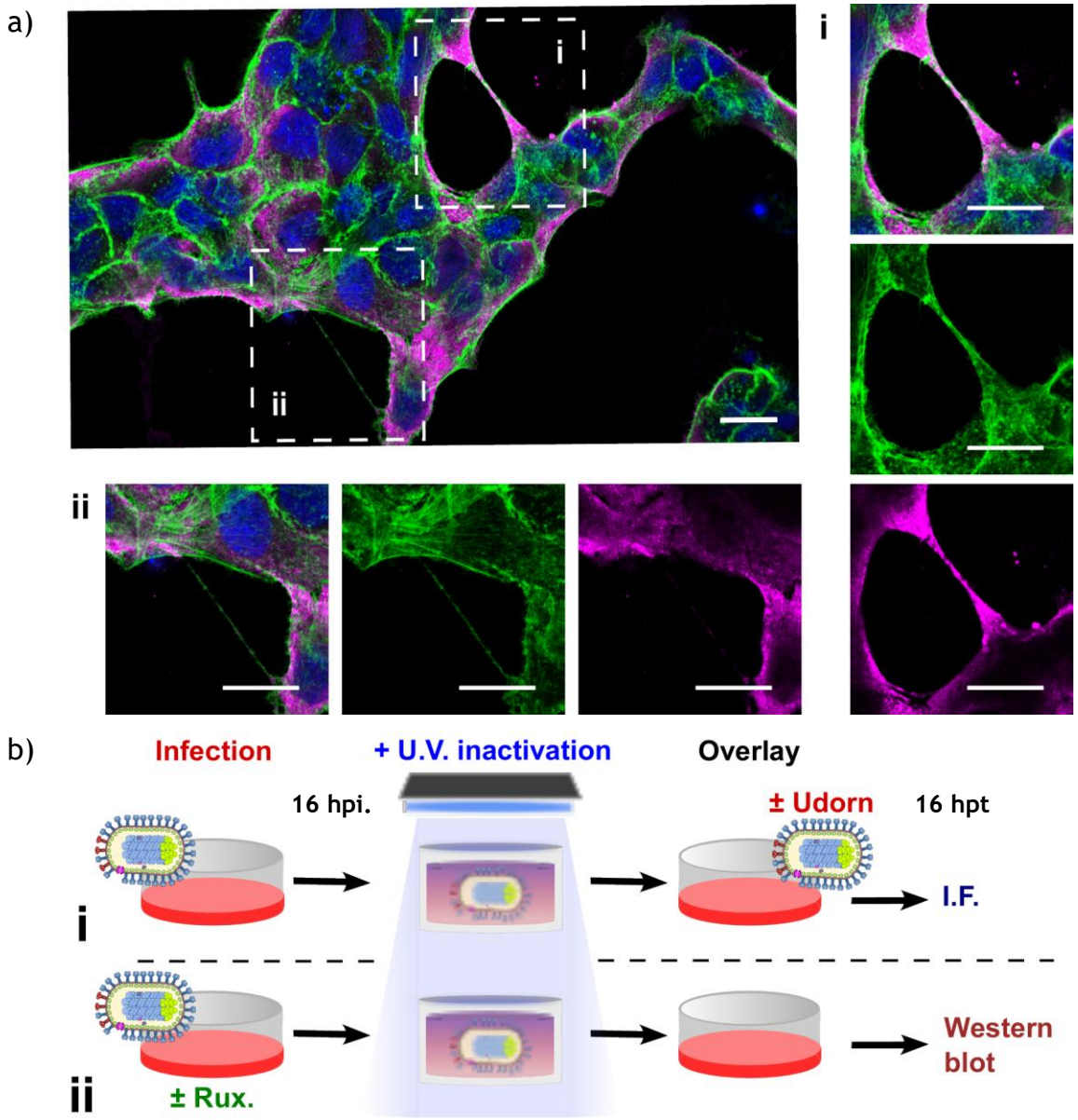

Figure 4-1: Validating TLS formation and capturing the effects of secreted factors through U.V. inactivation of conditioned media. (a) Tiled image (63x magnification) of MDCK cells infected with an IAV (MOI 1.5 PFU/cell) for 16 hours. Image is representative of those used for TLS quantification, capturing TLSs of varying thickness. Magnified insets are also shown and labelled (I or ii) accordingly. Nuclei (blue), F-actin (green), nucleoprotein (magenta). All scale bars = 20 μm. (b) Schematic of experimental design, showing the U.V. treatment of conditioned media collected from either mock or Udorn infected cells at 16 hours post infection (hpi), overlaid onto fresh cells for either downstream (i) immunofluorescent (I.F.) staining and confocal imaging or (ii) cell lysate harvesting and western blotting, both performed 16 hours post treatment (hpt) with treated conditioned media. Where indicated ruxolitinib (Rux.) was added at a concentration of 2 μM.

When mock U.V. treated conditioned media harvested from an infection was overlaid onto fresh MDCK cells, NP signal was detected in approximately 25% of cells 16 hours later (16 hours post treatment (hpt)) (Figure 4-2). Whilst robust viral protein expression was seen within these infected cells, the majority of cells remained uninfected. I hypothesise that this is due to the inefficiency of Udorn virus entry when exogenous TPCK trypsin is omitted (Figure 3-2). Nevertheless, this demonstrates that in the absence of U.V. treatment,

infectious Udorn virus is transferred to the fresh cells. As a positive control for the prevention of virus transfer, I used zanamivir, which I show inhibited virion release (see Figure 3-3). With the inclusion of this drug I saw no NP expression in MDCK cells 16 hpt with mock U.V. treated infection conditioned media, indicating the successful prevention of Udorn virus release and transfer with this drug (Figure 4-2). Not knowing how zanamivir could alter cell behaviour and signalling, I preferred to implement U.V. light as this treatment could inactivate virus with brief exposure to the supernatant and not the cells. To confirm this, I then looked for the presence of NP signal within cells overlaid with U.V. treated conditioned media harvested from an infection. Once again no NP signal was detected within these cells, confirming successful inactivation of the virions within the harvested conditioned media (Figure 4-2). The success of U.V. treatment in achieving this inactivation is evidenced by the observation that there was no added benefit when zanamivir was added ahead of U.V. treatment (Figure 4-2).

	Conditioned media source	
Treatment	Mock infection	Infection
Mock	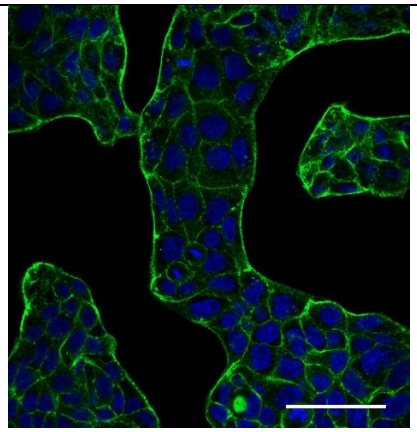	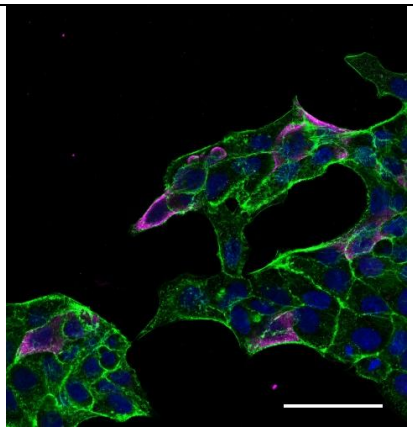
Zan. (0.36 mM)	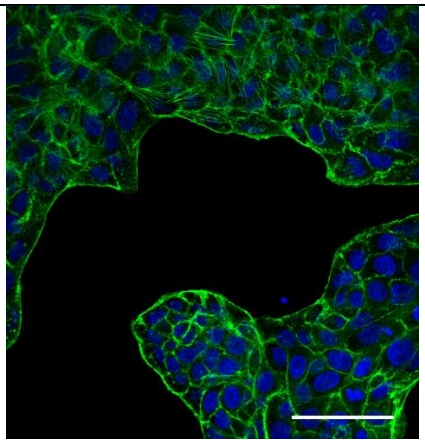	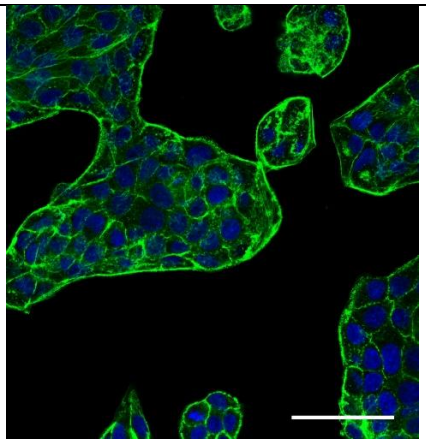
U.V.	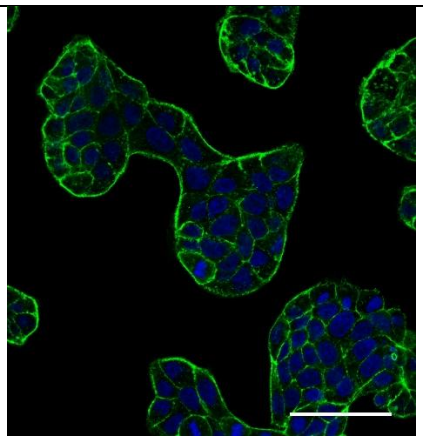	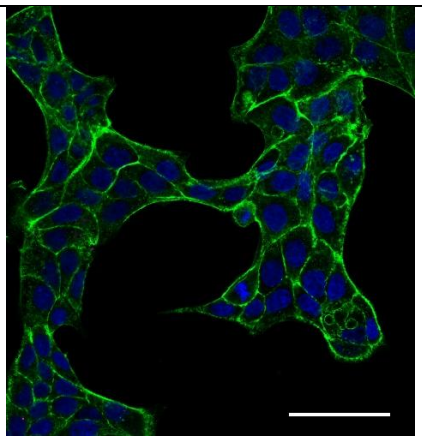
U.V. & Zan. (0.36 mM)	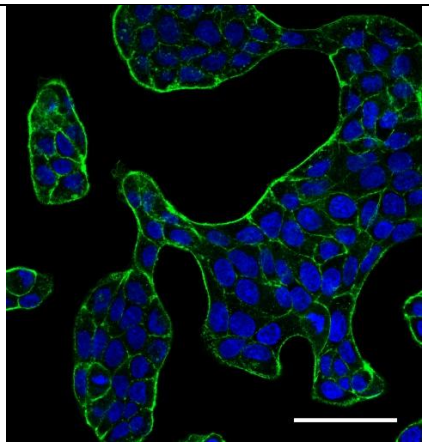	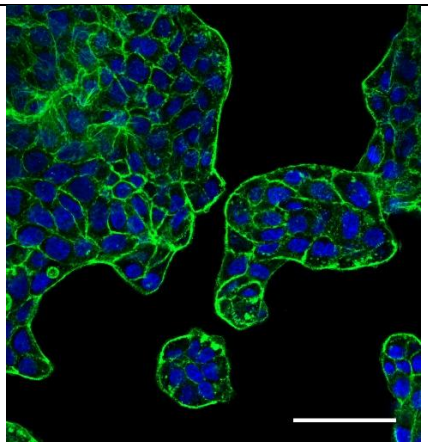

Figure 4-2: U.V. inactivation successfully prevents the transfer of infectious IAVs. MDCK cells were either infected with Udorn at an MOI of 1.5 PFU/cell or mock infected. Where indicated zanamivir (0.36 mM) was added to the media 2 hours post infection. Following a 16 hour infection, the conditioned media was harvested and either treated with U.V. light or mock treated. The treated conditioned media was then overlaid onto fresh MDCK cells and incubated for 16 hours, after which the cells were fixed and immunostained for NP. Representative confocal micrographs are shown. Nuclei (blue), F-actin (green), NP (magenta). Scale bar = 50 μm.

To test whether innate immune signals (such as interferon (IFN)) within the conditioned media are successfully transferred to fresh cells post U.V. treatment, I harvested cell lysates both at 16 hours post infection (prior to U.V. treatment, i.e. 0 hpt) as well as at 16 hours post treatment (either U.V. treated or mock treated). From these cell lysates I performed immunoblotting to detect phosphorylated STAT1 (pSTAT1), a signalling molecule phosphorylated during type 1 IFN signalling (Figure 4-1 bii). As additional controls, 2 μM ruxolitinib (a broad-spectrum Janus kinase (JAK) inhibitor which prevents the phosphorylation of STAT1) or 1000 U/mL IFN-ß (which activates the JAK-STAT signalling pathway leading to the phosphorylation of STAT1) was included in the overlay 1 hour post infection.

The resulting western blots showed that pSTAT1 is present within mock infected MDCK cells, which was absent in the presence of 2 μM ruxolitinib confirming that the former was due to active innate immune signalling cascades (Figure 4-3 a). Curiously, IFN-ß did not seem to clearly increase pSTAT1 abundance relative to the DMSO control (Figure 4-3 a). This was seen for both mock and infected cells. However, comparisons between infection conditions and treatments are difficult to make by eye and required quantitation of band intensities once normalised to the loading control within the same lane.

Once this was done, I wanted to compare the effect of U.V. on the transfer of innate immune signals as detected by pSTAT1 in the 16 hpt cell lysates. Importantly, I noticed that despite the infections (in the presence of DMSO, rux. or IFN-ß) being performed in duplicates (to provide at least one sample for downstream mock and U.V. treatments), at 16 hpi there was a notable difference in pSTAT1 band intensities between them (Figure 4-3 a). This could introduce differences when comparing pSTAT1 abundances between cell lysates of the second western blot performed at 16 hours post treatment, and skew the interpretations on the effect of U.V. treatment. Therefore, I normalised the relative pSTAT1 abundances seen at 16 hpt to the levels seen in cells at 16 hpi,

the latter of which provided the conditioned media that was treated with or without U.V. (i.e. the pSTAT1 levels of the second western blot was normalised to the matching sample of the first). This analysis generated positive scores for all infection conditions, revealing that all cell lysates at 16 hpt (regardless of U.V. treatment) had elevated abundances of pSTAT1 relative to those at 16 hpi (Figure 4-3 b). It is curious that this was the case, especially given that U.V. treated samples do not have actively replicating virus. This suggests that actively replicating virus, following a high MOI infection, could be suppressing the phosphorylation of STAT1. This suppression could plausibly occur through the well known innate immune antagonistic properties of IAV NS1 (95). However, how do we still see elevated pSTAT1 abundances when IAVs are not inactivated with U.V.? I hypothesise that this is due to the aforementioned inefficiency by which Udorn viruses enter cells without TPCK trypsin, post mock U.V. treatment, resulting in the majority of cells being uninfected (Figure 4-2). Therefore, the majority of cells treated with this conditioned medium will not be expressing NS1 and will phosphorylate STAT1 upon receiving innate immune signals from both the conditioned media, as well as from the minority of neighbouring cells that were newly infected. This could possibly explain why there was a slight (though non-significant) increase in the relative pSTAT1 abundances from mock treated samples when compared to U.V. treated samples (Figure 4-3 b). In other words, I hypothesise that the lower abundance of pSTAT1 post U.V. treatment is due to the lack of actively replicating IAVs in these cells, but the positive score nevertheless indicates the successful transfer of innate immune signals which have not been suppressed by the expression of viral proteins. Once again, IFN-ß did not result in an elevated abundance of pSTAT1 over that which was achieved by infection alone, suggesting the poor induction of the phosphorylation of STAT1 with this drug.

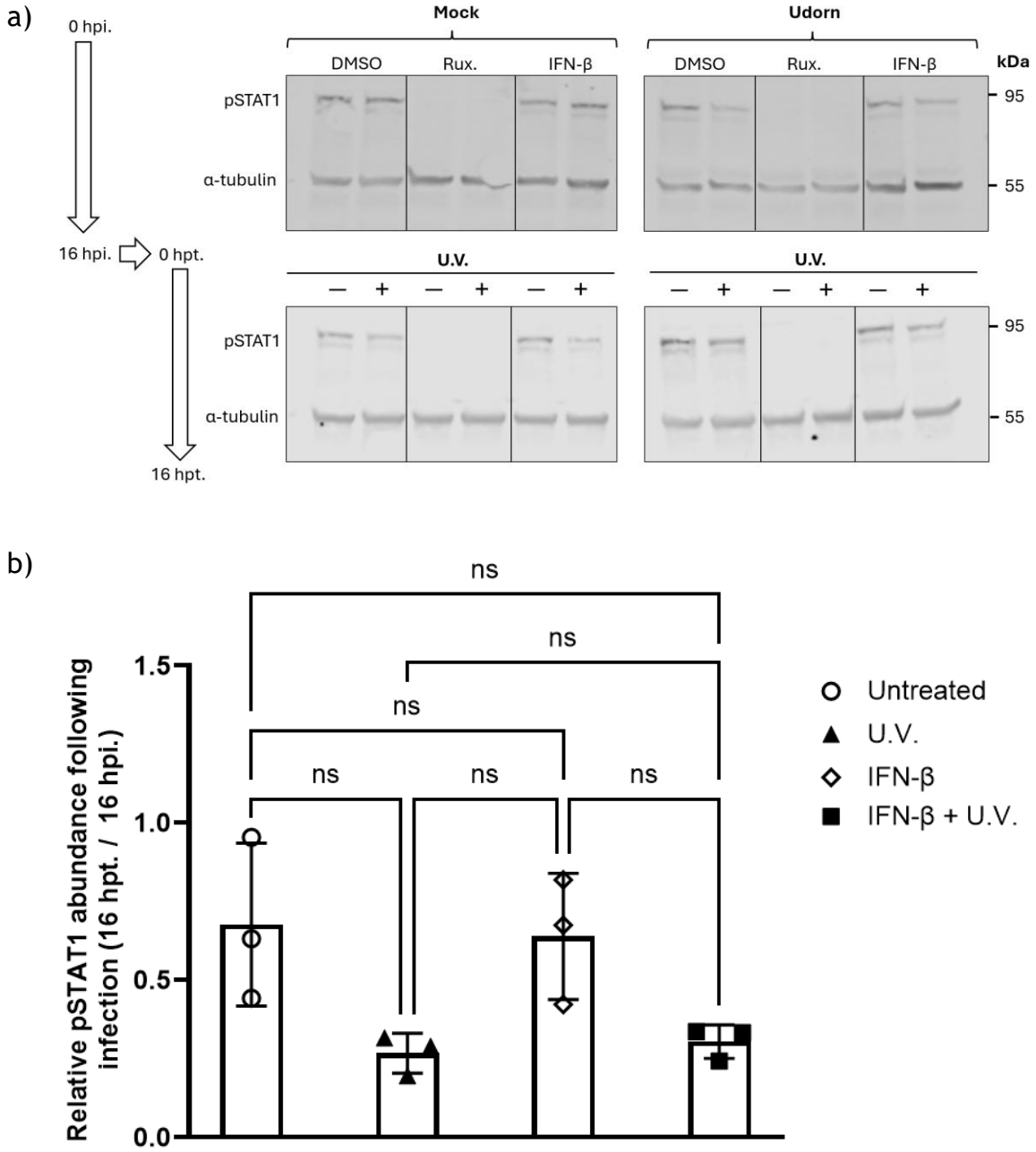

Figure 4-3: Western blots of pSTAT1 shows the transfer of innate immune signals. (a) Western blots generated from MDCK cell lysates harvested 16 hours post infection (hpi) with Udorn (MOI 1.5 PFU/cell) or mock infection and probed with anti-pSTAT1 and α-tubulin. Where indicated infection was performed in the presence of either DMSO, 2 μM Rux. or 1000 U/mL IFN-β (upper panel). The conditioned media from this infection was then taken and either mock or U.V. treated before overlaying on to fresh MDCK cells. At 16 hours post treatment (hpt) cell lysates were harvested and probed as before (lower panel). Images are representative of 3 biological repeats. (b) Relative abundances of pSTAT1 at 16 hpt with infection conditioned media treated with or without U.V., normalised to the abundance at 16 hpi. The significance of differences between treated conditioned media was determined using a Kruskal-Wallis test (ns $p > 0.05$). The mean and SD are shown (n = 3).

To quantify the influence of infection during the transfer of innate immune signals post U.V. treatment I normalised the relative abundance of pSTAT1 from infection to those of the mock infection at the same time point and treatment (with the exception of Rux.). This analysis revealed that in the absence of U.V. inactivation there was a highly variable effect on pSTAT1 abundances (Figure

4-4), possibly owing to the varied efficiency by which IAVs enter cells without trypsin across biological replicates and cells of increasing passage. This theory is supported by the much more reproducible elevation seen post U.V. inactivation (Figure 4-4). Indeed, I observed that pSTAT1 abundance doubled in cells overlaid with U.V. treated conditioned media taken from infected cells when compared to media taken from mock infected cells (Figure 4-4). Overall, these results demonstrate that U.V. treatment did not prevent the conditioned medium from carrying functional innate immune signalling molecules, but did prevent the transfer of infectious virus.

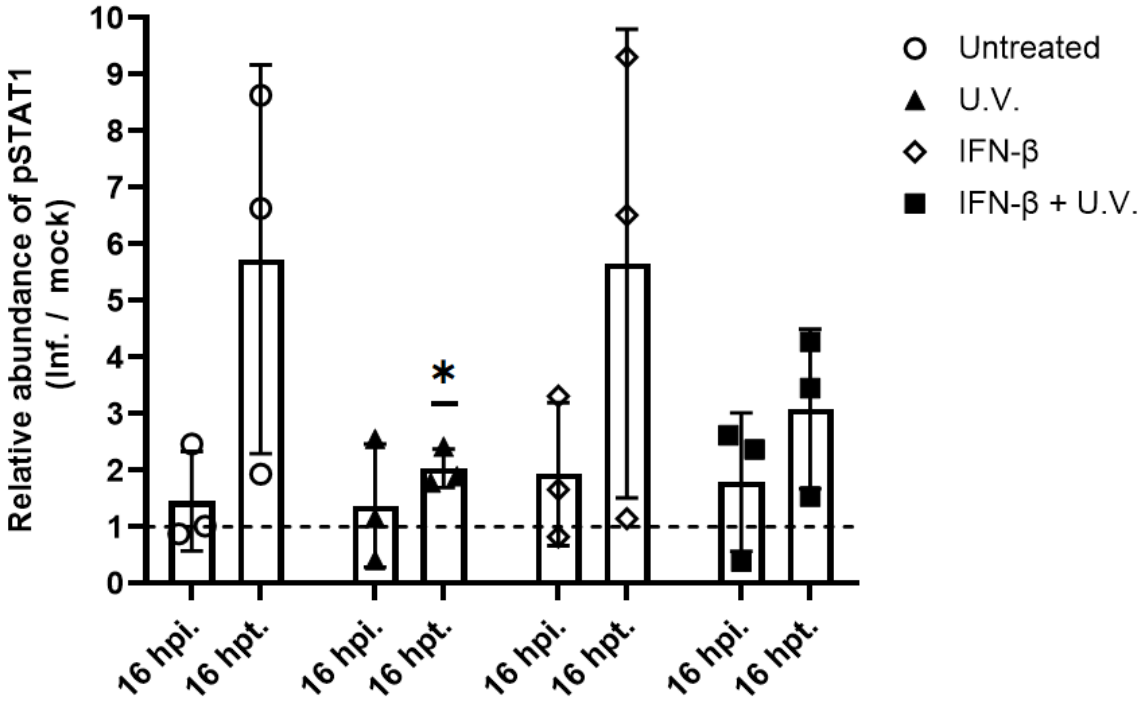

Figure 4-4: The elevation of pSTAT1 abundance following infection and conditioned media treatments. Ratio of the relative abundances of pSTAT1 at either 16 hpi or 16 hpt with infection, normalised to mock infection. No change relative to mock levels is indicated by a dashed line; the significance of the difference from this was tested by a one-sample t-test (n.s. $p > 0.05$, *$p < 0.05$).

Having confirmed successful inactivation of virions and the transfer of functional innate immune signals, I then assessed the influence that U.V. treated conditioned media had on TLS induction. Cells that were overlaid with U.V.-treated conditioned media taken from an infection lacked any induction of TLSs, with levels comparable to that with cells treated with media from mock infections (Figure 4-5 i & ii). TLS induction only occurred when additional, replication-competent virus was added to cells overlaid with U.V. inactivated conditioned media (Figure 4-5 iii). This suggests that TLS induction by IAVs does

not occur through the production of innate immune signals from infected cells, but requires the presence of infectious virus.

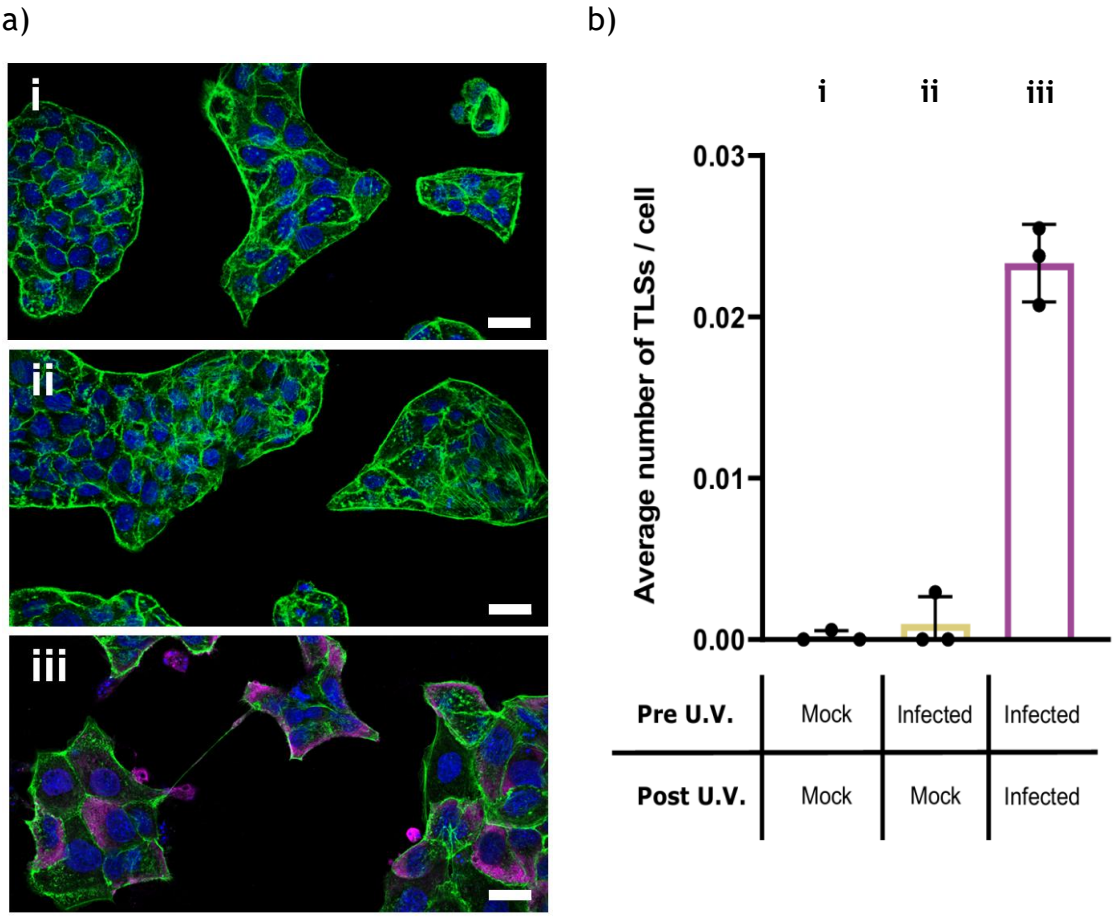

Figure 4-5: Conditioned media does not induce TLSs, but rather induction requires an actively replicating virus. (a) Representative confocal images of MDCK cells treated with the following overlays: (i) U.V. treated supernatant from mock infected cells, (ii) U.V. treated supernatant from infected cells and (iii) U.V. treated supernatant from infected cells, and additional Udorn virus. Nuclei, (blue), F-actin (green), NP (magenta). Scale bar = 20 μm. (b) Average number of TLSs per MDCK cell at 16 hours following treatment with the overlay media (I – iii) described.

To further examine the hypothesis that TLS induction was not caused by innate immune signalling, I treated MDCK cells with 2 μM ruxolitinib, which I showed prevented the phosphorylation of STAT1 (Figure 4-3). Despite the inhibition of interferon signalling, IAV infection still clearly induced the formation of TLSs above mock infected levels (Figure 4-6 a). Furthermore, the TLSs that formed in the presence of ruxolitinib frequently contained NP (approximately 80% positive of NP signal) (Figure 4-6 b). Interestingly, most cells that were in connection by a TLS were joined by just a single TLS – rarely were the same cells connected by more than one TLS, suggesting a lack of redundancy of these connections (Figure 4-6 c). Overall, our findings of the lack of TLS induction by conditioned media and the lack of inhibition by ruxolitinib, strongly suggest that TLS induction during IAV infection is independent of secreted extracellular factors, including

the production of cytokines that signal through the JAK/STAT1 pathway. Instead, our data point to a requirement for the intracellular replication of an IAV.

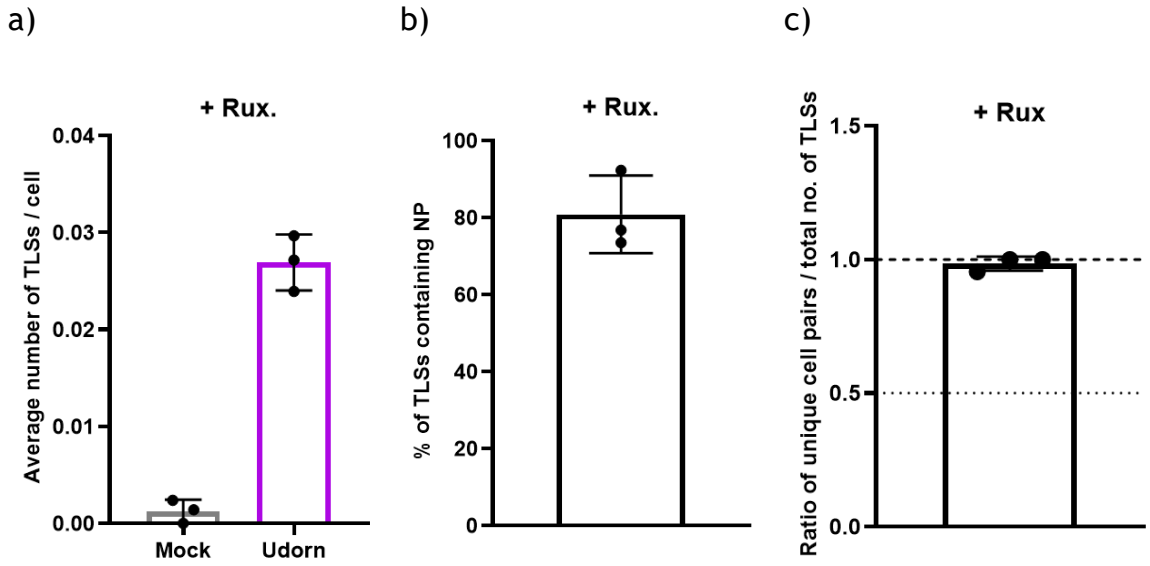

Figure 4-6: Ruxolitinib does not prevent the induction of TLSs, with the majority of TLSs containing NP and singly connecting a pair of cells. (a) Average number of TLSs per cell in the presence of 2 μM Rux. following mock or Udorn infection. (b) The percentage of TLSs containing NP, and (c) the ratio of unique cell pairs / total number of TLSs in the presence of 2 μM Rux, with the dashed line indicating a single TLS connecting a pair of cells and the dotted line indicating two TLSs connecting a pair of cells. For all data the mean and SD are shown (n = 3).

4.2.2 Examining the impact of virion morphology in tunnelling nanotube-like structure induction.

As the induction of TLSs was dependent on viral replication, I reasoned that it might be caused by some feature of the viral replication cycle, and I looked to see if differences in the levels of TLS induction caused by different strains of IAV could help to understand this. In particular, I noted a striking similarity between the filamentous virions formed by some IAVs (see 1.2.3.2) and the physical features of TLSs, with both being comparable in their dimensions, composition, and in the cellular processes involved during their formation (Table 4.1). For these reasons, I hypothesised that the ability to form filamentous virions might correlate with the ability of IAVs to induce TLSs.

To test this, I used PR8 and Udorn viruses, which I showed in chapter 3 retain a predominantly spherical or filamentous virion morphology respectively (Figure 3-4). Any differences in TLS induction between these viruses suggestive of a virion morphology influence, can be followed up with the segment 7 reassortants; Udorn MPR8 or PR8 MUd, which show more intermediate virion morphologies (Figure 3-5).

I first infected subconfluent MDCKs with either WT PR8 or Udorn at an MOI of 1.5 PFU/cell. At 16 hours post infection the cells were fixed, stained, and TLSs quantified from super resolution confocal micrographs (an example is shown in Figure 4-1 a). I found that both viruses significantly induced the formation of TLSs when compared to mock infected cells (Figure 4-7 a), and that many of these TLSs contained NP (means ≥ 80%, Figure 4-7 b), suggesting that they could incorporate and transport viral genomes. However, I found no statistically significant difference in the degree of TLS induction between the two WT viruses (Figure 4-7 a). Indeed, the greatest number of TLSs per cell (though this was not significantly different) was induced by the spherical virus, PR8. This suggests that TLS induction is a common feature of IAV infection, and that the ability of a virus to produce filaments with a length greater than approximately 12 μm does not enhance TLS formation. To confirm this and to examine whether a spherical morphology instead conferred an enhanced ability to form TLSs, I tested the predominately spherical Udorn virus that had the matrix gene segment of PR8. I found that the levels of TLS induction were comparable to levels seen with filamentous WT Udorn (Figure 4-7 a), suggesting that the greater induction of TLSs following PR8 infection is not likely to be due to the spherical morphology of this virus. Curiously, a significantly lower percentage of Udorn MPR8 induced TLSs contained NP when compared to WT Udorn (Figure 4-7 b). This suggests that the ability of induced TLSs to incorporate viral genomes and traffic infection may be influenced by the compatibility of gene segments and their ability to interact with each other.

Once again, I note that most TLS mediated cell pairs were being connected by a single TLS (ratio of unique cell pairs / total number of TLS approximately 1, Figure 4-7 c). This was seen previously when Udorn infected cells were treated with ruxolitinib (Figure 4-6 c), and remains true when cells are infected with either filamentous or spherical viruses in the absence of cell signalling disrupting drugs (Figure 4-7 c). Overall, this suggests that the lack of redundancy in TLS connections is not influenced by innate immune signalling or the budding processes of filamentous virions.

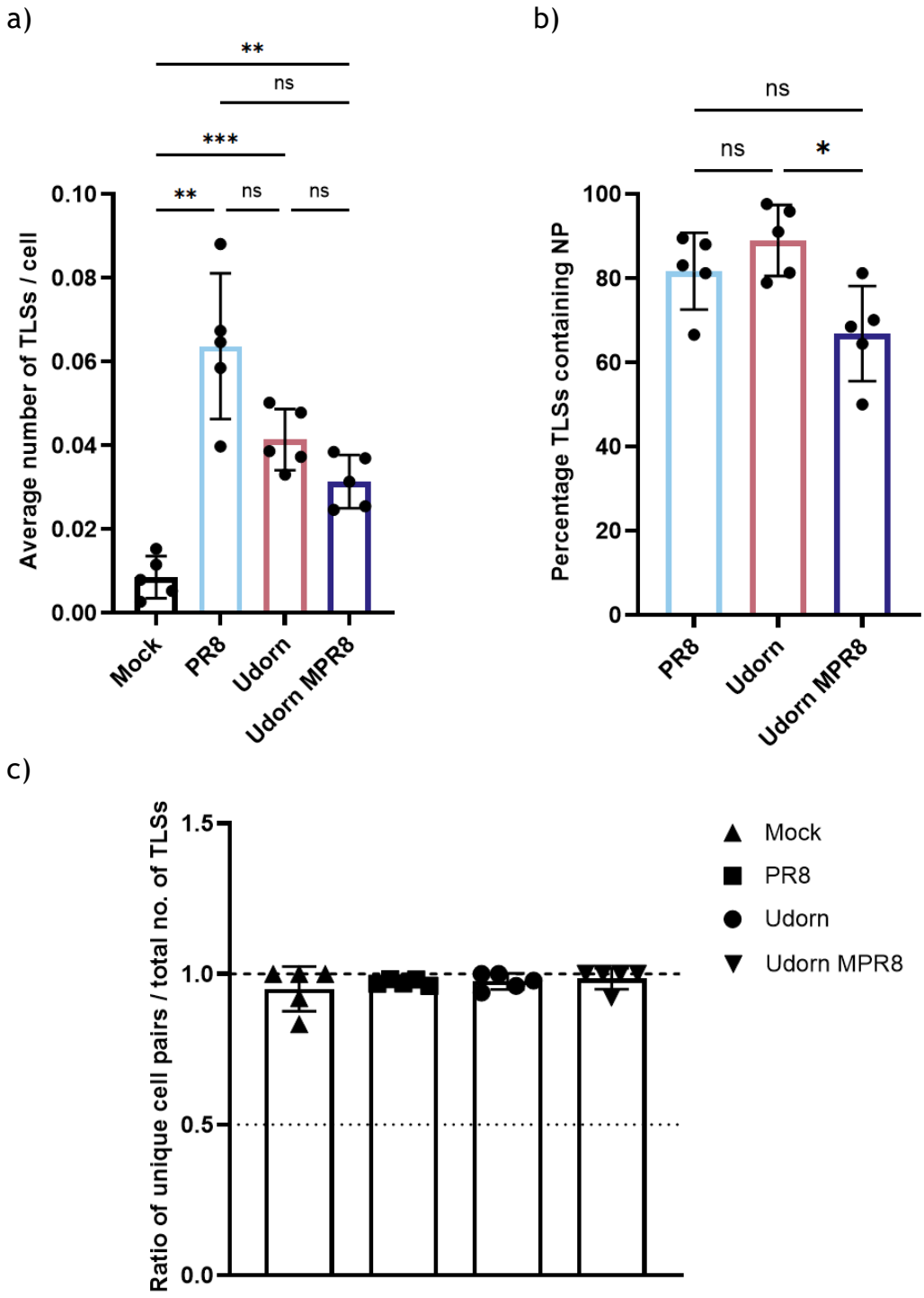

Figure 4-7: TLSs are induced by IAVs of different virion morphologies. (a) The average number of TLSs per MDCK cell 16 hpi with either spherical (PR8 and Udorn MPR8) or filamentous (Udorn) viruses at an MOI of 1.5 PFU/cell. (b) The percentage of TLSs that contained NP following infection with each virus as well as (c) the ratio of unique cell pairs / total number of TLSs, with the dashed line indicating a single TLS connecting a pair of cells and the dotted line indicating two TLSs connecting a pair of cells. Differences between strains in TLS induction and in the incorporation of NP were tested for significance by one-way ANOVA (ns $p > 0.05$, *$p < 0.05$, **$p < 0.01$, ***$p < 0.001$). The mean and SD from 5 independent experiments is shown.

It is not known how the density of cells could influence the formation of TLSs by IAVs, and its likely that an optimal density exists with both extremes (sparse cells and confluent cells) imposing challenges for long range, fragile TLSs. Furthermore, different viruses can cause cell loss at different rates that could then influence this cell density. Such a scenario could help to explain the

differences in TLS induction between IAVs that I observed (Figure 4-7 a). Plotting the number of TLSs against the number of cells within the same field of view revealed a poor correlation between the two variables, as shown by the very low R2 values (Figure 4-8 a & b). This was true for both viruses. Furthermore, there was no significant difference between the total number of cells imaged following either PR8 or Udorn infection (Figure 4-8 c). This analysis does not suggest that either virus influenced cell densities in a way that could benefit the formation of TLSs, and therefore points to a different explanation of why PR8 was able to induce more TLSs (Figure 4-7 a). TLSs were equally present in fields of view containing cell numbers ranging from approximately 15 to 80 (Figure 4-8 a & b). However, whilst a wide range of cell numbers were imaged, this analysis does not robustly examine the influence of cell density on TLS formation as randomly selected regions of the coverslip with too few cells or confluent cells were not imaged.

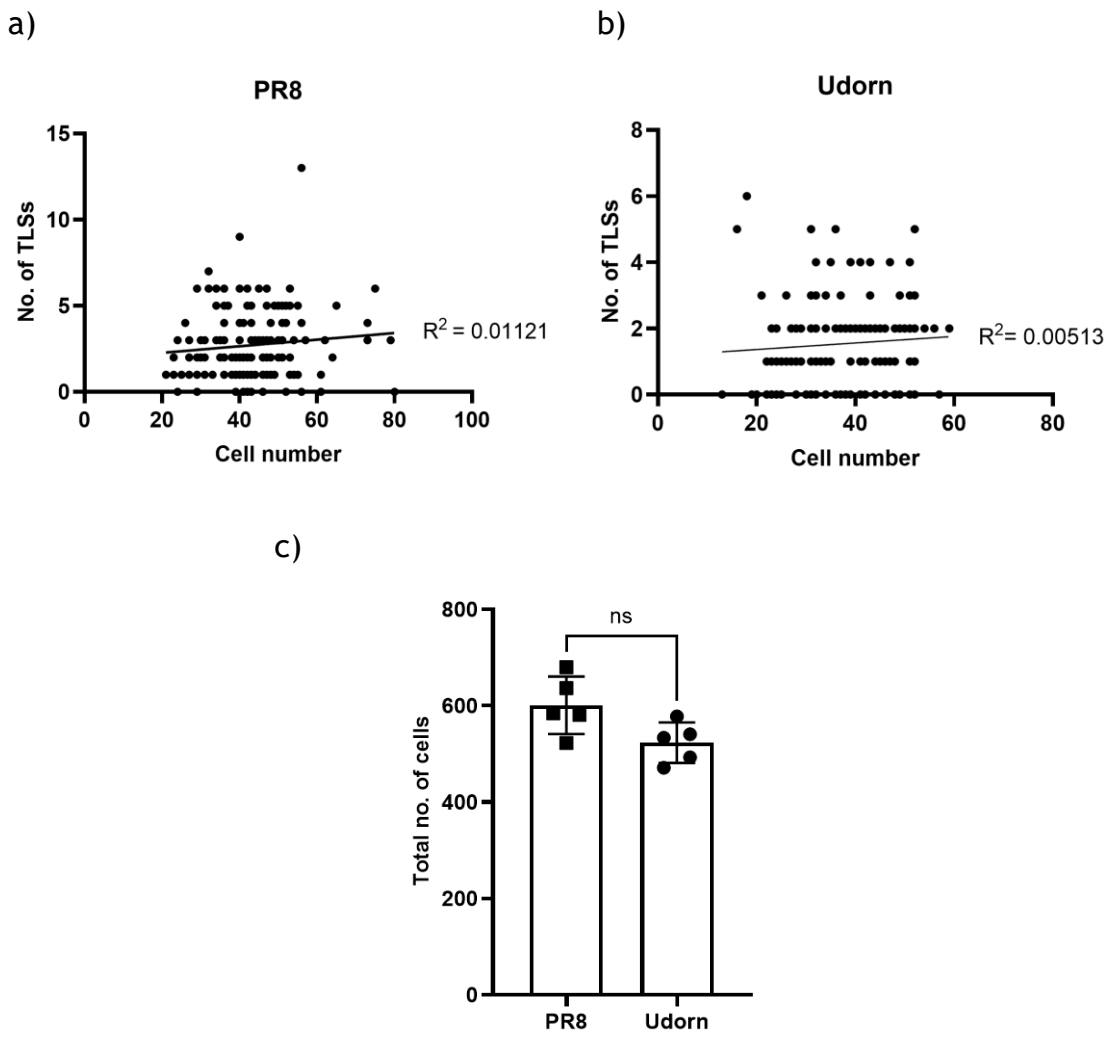

Figure 4-8: The density of cells does not correlate with TLS presence. Scatter plots showing the relationship between the number of cells in each field of view, and the presence of TNTs 16 hpi

with either (a) PR8 or (b) Udorn. A non-linear regression model was used to fit the trend, generating the shown R^2 value. (c) The total number of cells that were imaged 16 hpi with either PR8 or Udorn at an MOI of 1.5 PFU/cell. Differences between cell numbers was tested for significance by Mann-Whitney test (ns $p > 0.05$). The mean and SD are shown (n = 5)

4.2.3 Revealing the intracellular host responses to IAV infection that drives tunnelling nanotube-like structure induction.

Thus far the data revealed that TLS induction is a common feature of IAV infection and that the triggering of this does not involve extracellular signals, is U.V. sensitive and requires replicating virus within cells. This suggested that the induction of TLSs by IAVs follows an intracellular host response to infection. One of the most striking responses of the cell to IAV infection is the onset of apoptosis, and previous reports have found that apoptosis can trigger the formation of TLSs between stressed and healthy cells (264, 339). U.V. inactivated IAVs fail to induce apoptosis (340), and as is often the case in IAV infections, I observed significant evidence of apoptosis (nuclear fragmentation, membrane blebbing and apoptotic bodies) under infection conditions where TLSs were induced (e.g. Figure 4-5 a iii). Therefore, I hypothesised that the triggering of apoptosis by IAVs is required for the induction of TLSs.

To test this, I first wanted to determine whether the triggering of TLS formation correlated with the onset of IAV induced apoptosis. To do this, I performed a time course of infection with BrightFlu, a modified PR8 virus encoding the ZsGreen fluorophore (149), in MDCK cells overlaid with media containing a live cell active caspase 3/7 detection reagent. Infected cells were imaged every 4 hours up to 16 hours post infection (Figure 4-9) and I found that, although infection (cells positive for ZsGreen) was comparably high at both 12 and 16 hours, apoptosis (detected by caspase 3/7 activation) was only observed at the latter infection timepoint (Figure 4-9 b). These two time points (12 and 16 hours) enabled us to test the hypothesis that the onset of apoptosis coincides with TLS induction by IAVs.

a)

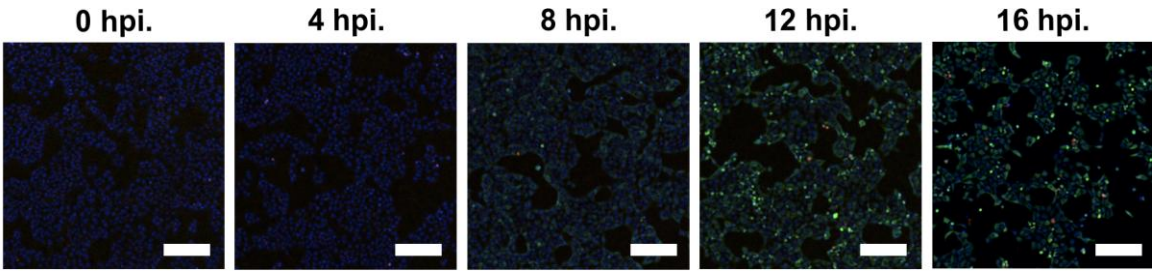

b)

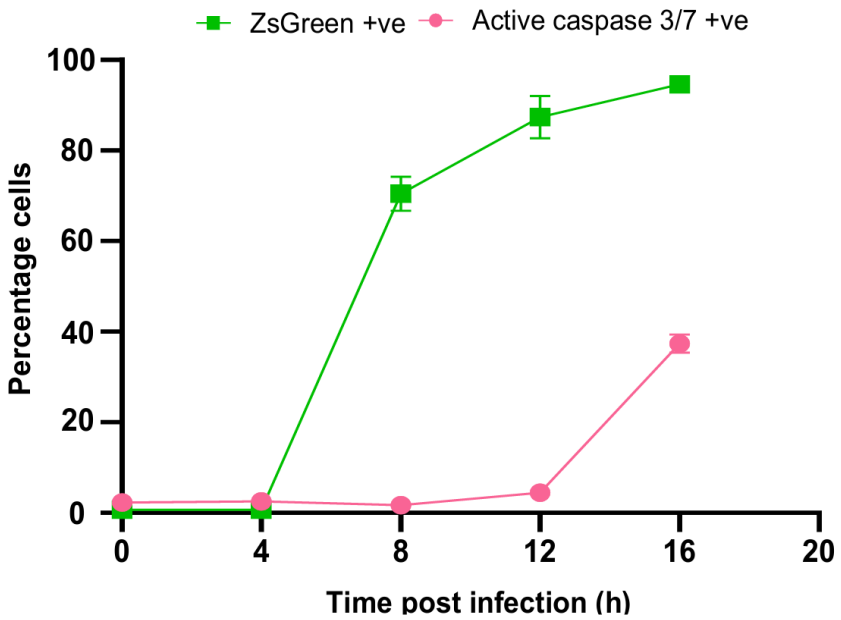

Figure 4-9: The activation of caspase 3/7 occurs several hours after BrightFlu ZsGreen expression. (a) Representative images of BrightFlu ZsGreen infection time course. MDCK cells were infected at an MOI of 1.5 PFU/cell, then overlaid with media containing 0.36 mM zanamivir and 60 µM active caspase 3/7 detection reagent and wells scanned live every 4 hours on the Nexcelom Celigo image cytometer. Nuclei (blue), BrightFlu ZsGreen (green), active Caspase 3/7 (red). Scale bar = 200 µm. (b) The percentage of cells ZsGreen positive, i.e. infected (represented by the green line), and the percentage of cells positive for active caspase 3/7, i.e. apoptotic (represented by the pink line), at each time point. The mean and SD are shown (n = 3).

At 16 hours post infection with BrightFlu, when infection levels and caspase activation were both high (Figure 4-9), TLSs were induced (Figure 4-10 a), In contrast, I found that at 12 hours post infection, when infection levels were high but caspase activation was low (Figure 4-9), there was no induction of TLSs with comparable levels to mock infection (Figure 4-10 a). This correlation supports the hypothesis that the induction of TLSs by IAVs results from the onset of virus-induced apoptosis.

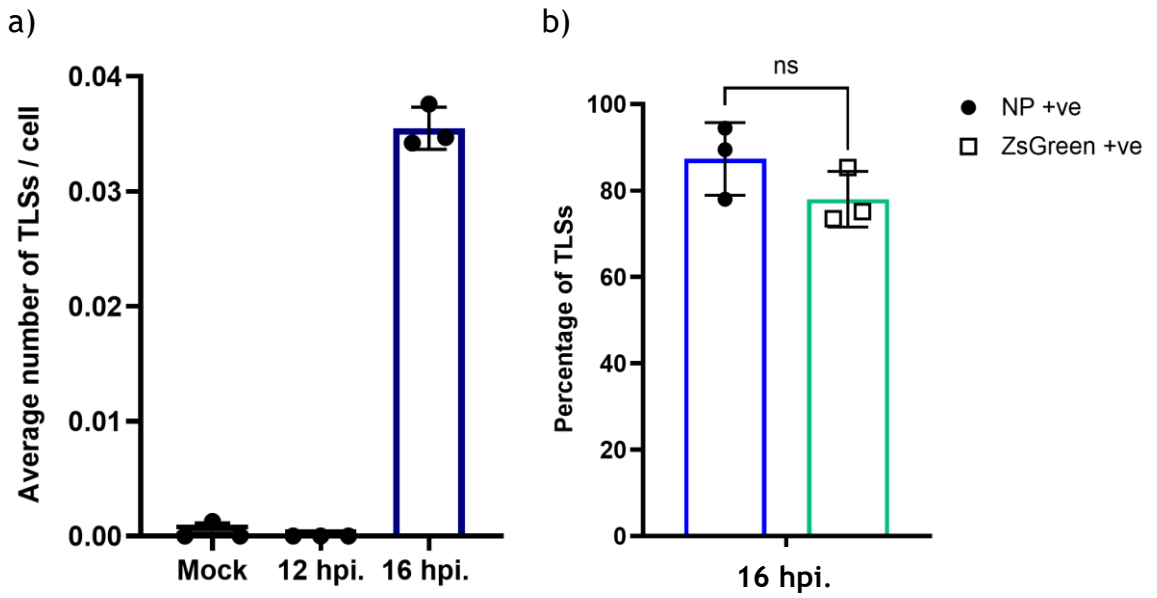

Figure 4-10: The induction of TLSs does not occur at earlier infection time points and incorporate both NP and ZsGreen. (a) Average number of TLSs per MDCK cell 12 and 16 hours post infection with BrightFlu at an MOI of 1.5 PFU/cell. (b) The percentage of TLSs that formed 16 hpi that contained NP and/or ZsGreen. Differences between NP and ZsGreen incorporation within TLSs was tested for significance by Mann-Whitney test (ns $p > 0.05$). For al data the mean and SD are shown (n = 3).

Of note, the percentage of TLSs (that were induced by 16 hpi) that contained NP or ZsGreen were very similar (Figure 4-10 b). Whilst it was known that GFP-tagged NS1 can be incorporated within TLSs (222), these results demonstrate that ZsGreen (co-translationally cleaved from the NS1 segment) is incorporated into TLSs similar to NP (Figure 4-10 b). Therefore, BrightFlu ZsGreen can be used instead of NP to assess the incorporation of cytoplasmic material within TLSs following IAV infection. Additionally, the detection of ZsGreen within a TLS and recipient cell would strongly suggests the co-transfer of NP (or vRNPs) without the need for additional staining.

To confirm a functional role of apoptosis in TLS induction, I sought to inhibit this IAV induced cell death response. The pan-caspase inhibitor Z-VAD-fmk was selected as it has been used previously to inhibit apoptosis of IAV infected cells (341). I first applied Z-VAD-fmk at increasing concentrations to MDCK cells which had been infected with BrightFlu at an MOI of 1.5 PFU/cell. At 16 hours post infection, apoptotic and infected cells were imaged and classified into gated populations with the help of a nuclei mask that identified individual cells (Figure 4-11 a). I found that at this time point, infection resulted in approximately 95% of cells being positive for ZsGreen signal, with 35% also positive for active caspase 3/7 (Figure 4-11 b). Treatment with increasing concentrations of Z-VAD-

fmk (up to 100 µM) reduced the percentage of infected cells that were positive for active caspase 3/7 to 16% (Figure 4-11 b). Importantly, the percentage of cells infected remained consistent with the mock treated samples across all Z-VAD-fmk concentrations tested (~96% of cells ZsGreen positive) suggesting that there was no antiviral effect within this concentration range (Figure 4-11 b).

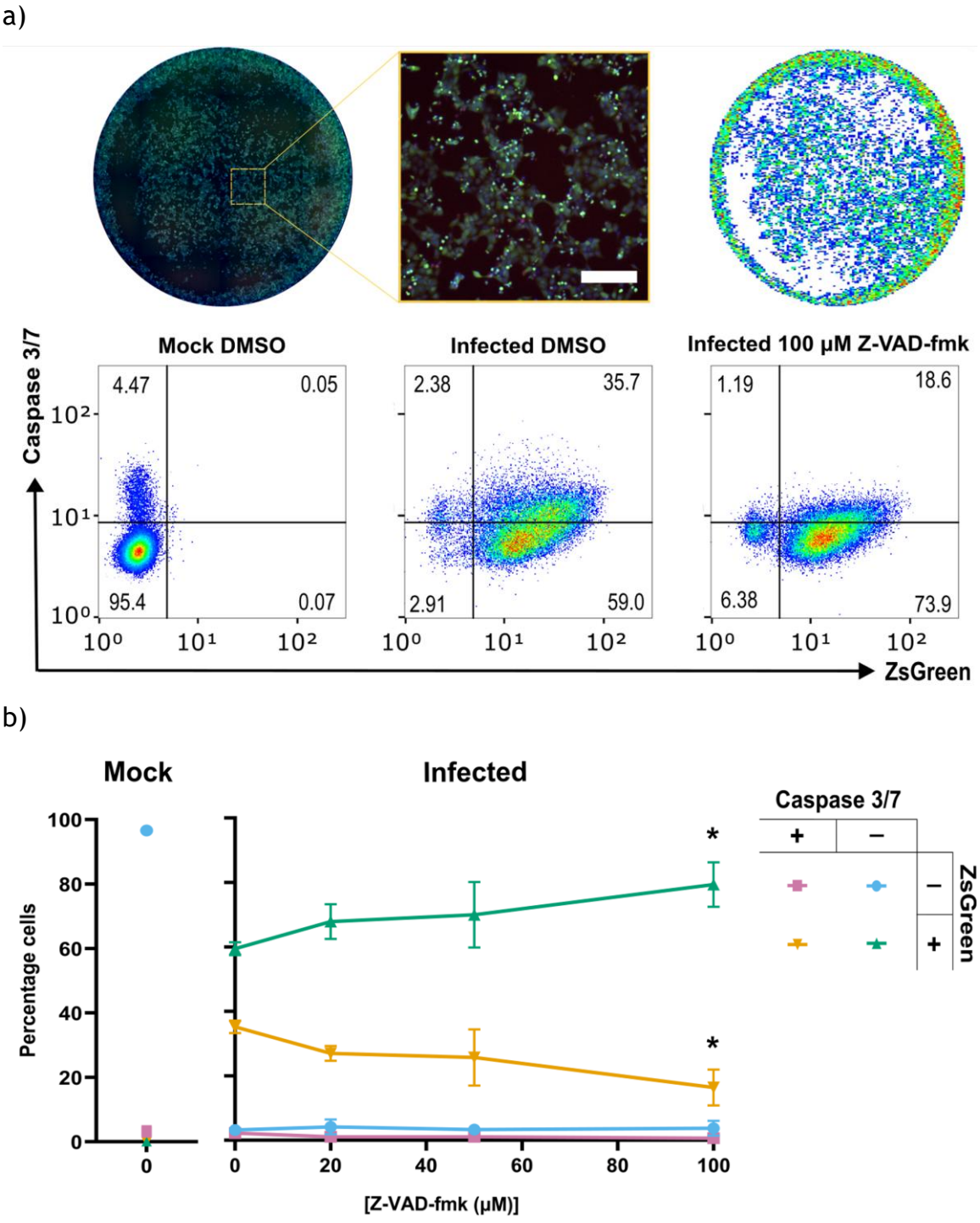

Figure 4-11: Z-VAD-fmk reduces the percentage of BrightFlu infected cells that are positive for active caspase 3/7 in a concentration dependent manner. (a) Representative images of an infected DMSO treated well 16 hours post BrightFlu infection (MOI 1.5 PFU/cell), alongside a magnified inset (nuclei stain (blue), BrightFlu ZsGreen (green), active caspase 3/7 (red). Scale bar = 200 µm) and the nuclei masks applied during the analysis pipeline following imaging (upper

panel). Representative FlowJo analyses plots (lower panel) of mock or BrightFlu infected MDCK cells, treated 1 hour post infection with either DMSO (mock) or 100 μM Z-VAD-fmk. Cell populations were classified according to the expression of ZsGreen as a marker of infection, and the presence of active caspase 3/7 as a marker of apoptosis. Gating's were established according to a mock DMSO control in the absence of active caspase 3/7 detection reagent. (b) The percentage of MDCK cells positive or negative for active caspase 3/7 and ZsGreen, at 16 hpi with BrightFlu at an MOI of 1.5 PFU/cell, in the presence of 0.36 mM zanamivir and DMSO (mock) or increasing concentrations of Z-VAD-fmk (added 1 hour post infection). The percentage cells negative for both red and green signal is shown by the blue line, uniquely red or green by the pink and green lines respectively, and the yellow line represents the percentage cells positive for both red and green signal. The reductions in the percentage of cells singly positive for ZsGreen, or doubly positive for caspase 3/7 and ZsGreen, when compared to the infected DMSO control, were tested for significance using a Kruskal-Wallis test (n.s. $p > 0.05$, $*p < 0.05$).

To confirm that Z-VAD-fmk inhibited apoptosis without having an antiviral effect, I then added 100 μM of this drug to MDCK cells infected with BrightFlu (MOI 1.5 PFU/cell) and assessed the effect this had on cells with super resolution confocal microscopy (Figure 4-12 a & b). With the DMSO treated cells, I observed expected cytological signs of apoptosis, including nuclear fragmentation and membrane blebbing (Figure 4-12 a). Also, robust expression of both NP and ZsGreen was evident, with the former mostly located near the plasma membrane, which is to be expected for this time point in infection (Figure 4-12 a). Similar expression and subcellular localisation of NP and ZsGreen was seen following treatment with 100 μM Z-VAD-fmk, suggesting that there was no disruption to the viral replication cycle (Figure 4-12 b). This is also supported by the lack of any difference in the percentage of cells positive for NP or ZsGreen signal following either DMSO or Z-VAD-fmk treatment (Figure 4-12 c). A notable difference following 100 μM Z-VAD-fmk treatment was the lack of any cytological indicators of apoptosis, confirming the success of this drug for this targeted effect (Figure 4-12 b).

a) DMSO

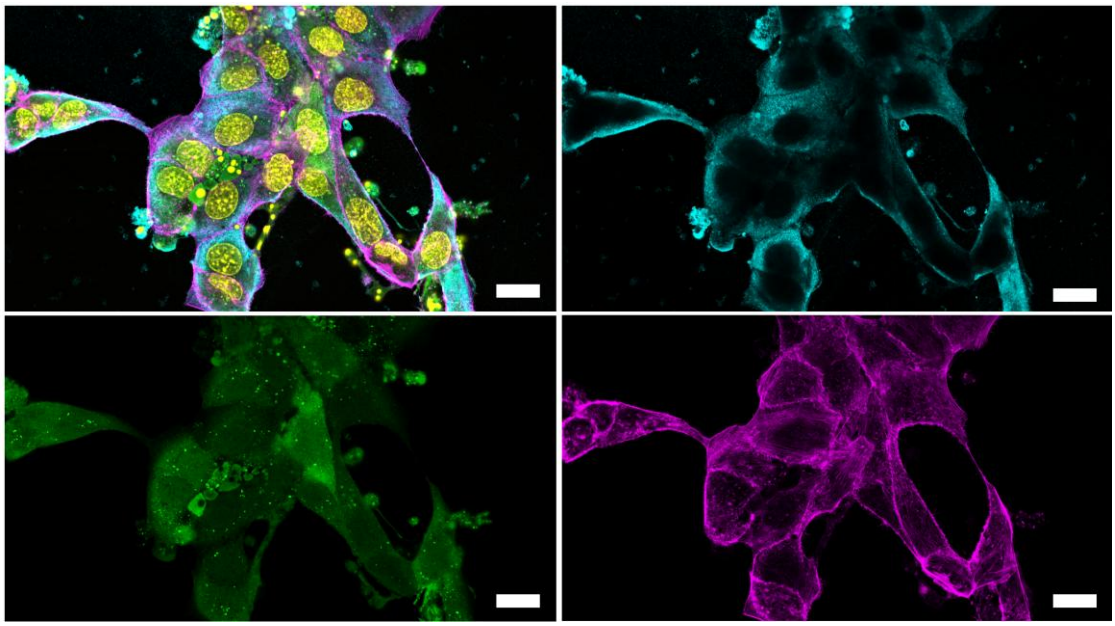

b) Z-VAD-fmk (100 μM)

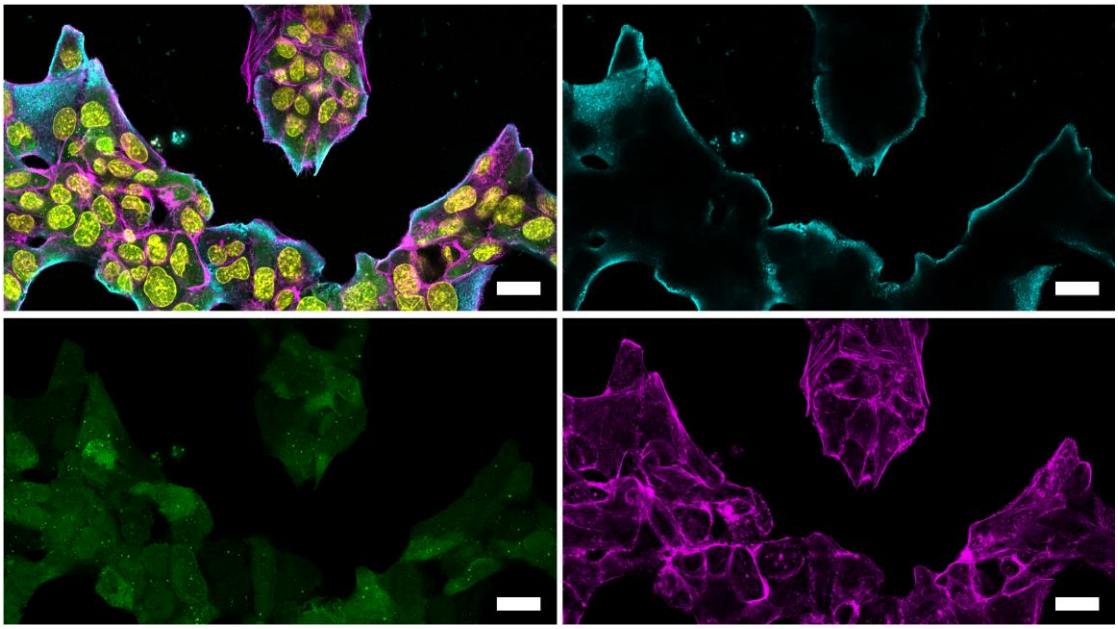

c)

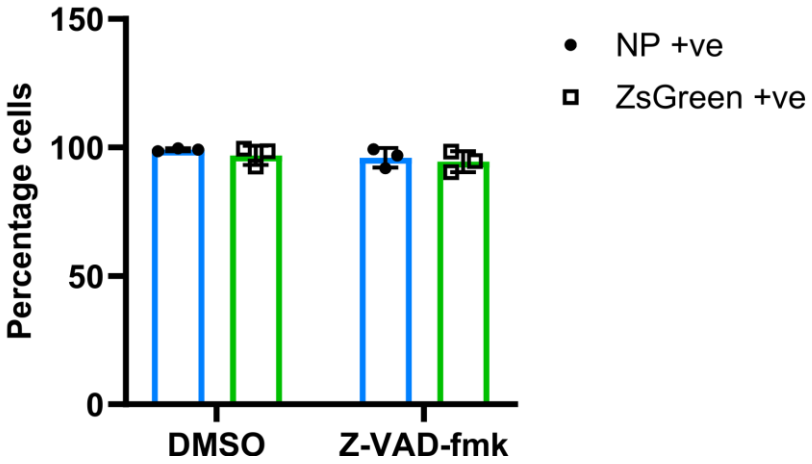

Figure 4-12: Z-VAD-fmk does not have an antiviral effect. Representative confocal images of MDCK cells infected with BrightFlu at an MOI of 1.5 PFU/cell and incubated 1 hpi with either (a) DMSO or (b) 100 μM Z-VAD-fmk and fixed at 16 hpi. Nuclei (yellow), NP (blue), BrightFlu ZsGreen (green), F-actin (magenta). Scale bar = 20 μm. (c) The percentage of cells positive for NP and ZsGreen following treatment with either DMSO or 100 μm Z-VAD-fmk. The mean and SD are shown (n = 3)

Using these conditions, I then quantified the effect that Z-VAD-fmk had on TLS induction at 16 hours post infection. The induction of TLSs was observed following DMSO treatment of BrightFlu infected subconfluent MDCK cells, as expected (Figure 4-13). However, in the presence of 100 μM Z-VAD-fmk, IAVs were unable to induce the formation of TLSs (Figure 4-13). This inhibition of TLS formation in the presence of a caspase inhibitor, at a time point post infection where both apoptosis and TLS induction is otherwise seen, strengthened our conclusions that the induction of TLSs by IAVs requires the triggering of apoptosis.

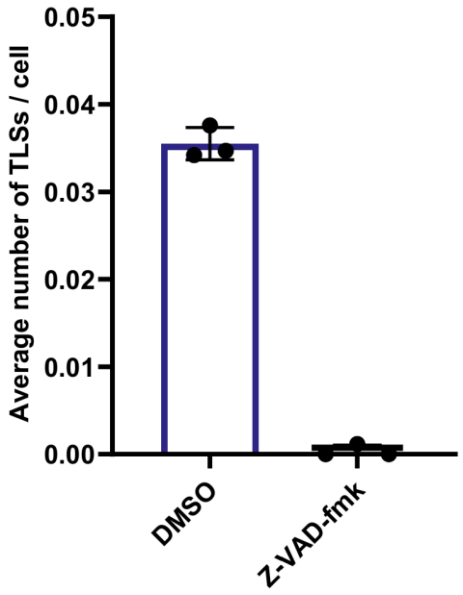

Figure 4-13: Inhibition of apoptosis with Z-VAD-fmk prevents the induction of TLSs by IAVs. Average number of TLSs per MDCK cell at 16 hours post infection with BrightFlu at an MOI of 1.5 PFU/cell in the presence of DMSO or 100 μM Z-VAD-fmk (added after virus absorption, i.e.1 hour post infection). The mean and SD are shown (n = 3).

To investigate whether apoptosis alone was responsible for the induction of TLSs by IAVs, I tested the effect of cisplatin. Cisplatin is a chemotherapeutic drug known to induce apoptosis within cancer cells (including MDCK cells) through the activation of caspases (342). Following a time course with cisplatin at increasing concentrations (up to 1000 μM), I found that the duration of cisplatin treatment was more effective than dose in inducing apoptosis. Incubating cells with 30 μM of this drug for 16 hours significantly increased the percentage cells positive for

active caspase 3/7. In contrast, none of the concentrations of cisplatin tested induced the activation of caspase 3/7 at the earlier time points (Figure 4-14 a). This suggested that 16 hour treatment with 30 µM of this drug was most efficient in inducing apoptosis. I then added 30 µM cisplatin to subconfluent MDCKs for 16 hours and confirmed the effect this drug had on MDCK cells with super resolution confocal microscopy. I found that this treatment caused MDCK cells to display the cytological indicators of apoptosis that I expected, without changing the distribution of cells, indicating that as desired, this treatment did not cause a significant loss of cells (Figure 4-14 b & c).

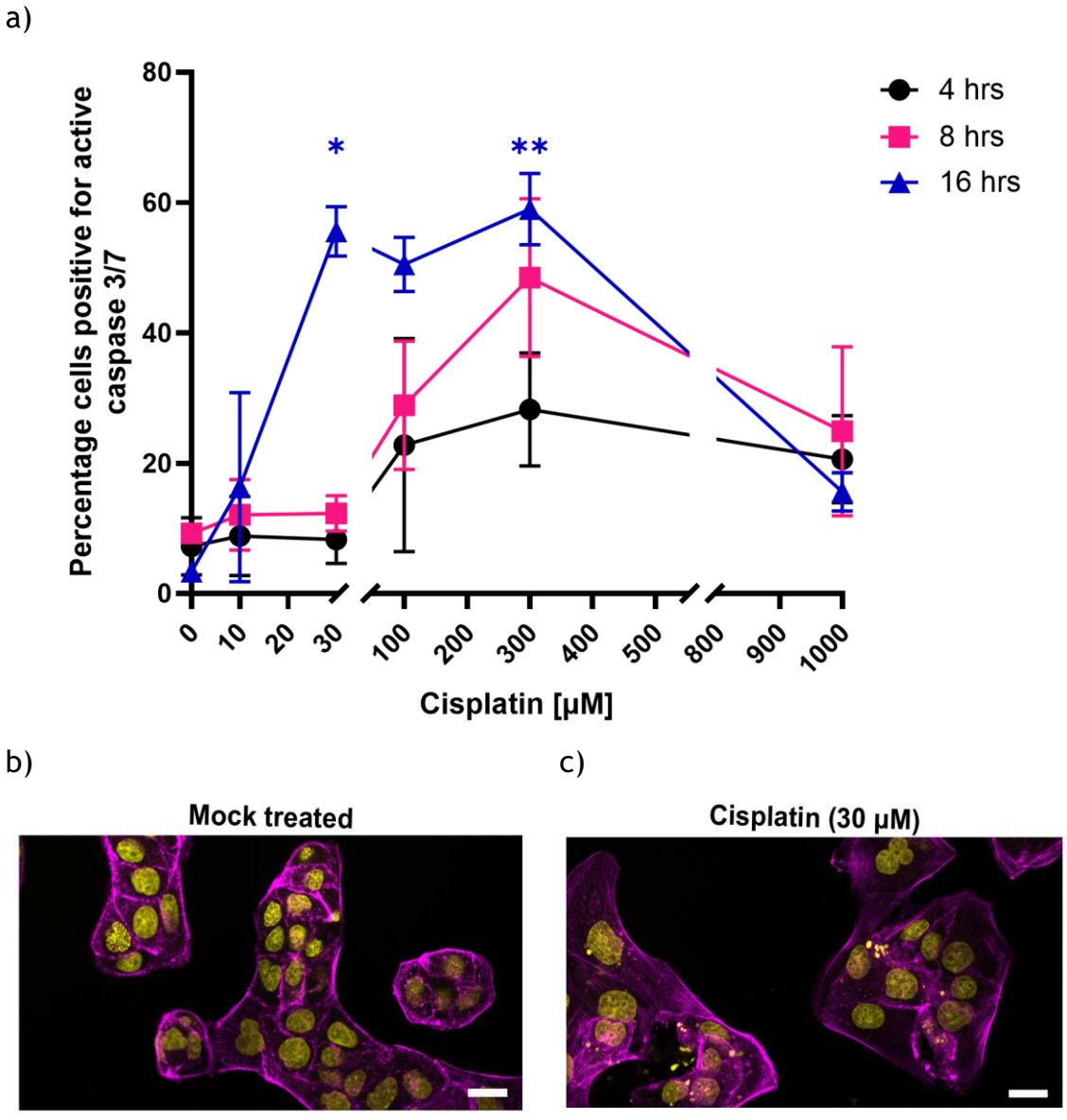

Figure 4-14: Apoptosis of MDCK cells can be triggered by prolonged exposure to cisplatin. (a) The percentage of cells positive for active caspase 3/7 at 4, 8 and 16 hours post treatment with increasing concentrations of cisplatin. Differences relative to the mock treated control (0 µM) were tested for significance using a Kruskal-Wallis test (n.s. $p > 0.05$, * $p < 0.05$). The mean and SD are shown (n = 3). (b&c) Representative images of 2x tiled super resolution confocal micrographs of

MDCKs treated with either (b) PBS (mock) or (c) 30 μM cisplatin for 16 hours. Nuclei (yellow), F-actin (magenta). Scale bar = 20 μm. Images are representative of 3 biological replicates.

I then utilised these conditions to study TLS induction from uninfected, cisplatin treated, subconfluent MDCK cells. I found that 30 μM cisplatin treatment did not significantly induce the formation of TLSs above mock treated levels at 16 hours post treatment (Figure 4-15 a). Therefore, I hypothesised that although apoptosis is required for IAVs to induce TLS formation, apoptosis alone is not sufficient. This is consistent with our data showing that TLS formation requires both replication competent virus, and the activation of apoptosis during infection (Figure 4-5 b & Figure 4-13).

Based on this hypothesis, I wondered if cisplatin treatment could increase TLS formation at an earlier infection time point. To explore this, I treated MDCK cells with 30 μM cisplatin for 4 hours, then infected the same cells with an IAV before adding the cisplatin-containing overlay for a further 12 h. Individually, cisplatin treatment (for 16 hours) and earlier IAV infection (12 hours) did not lead to an induction of TLSs (Figure 4-10 a & Figure 4-15 a). However, when both conditions are applied in combination, TLSs are induced (Figure 4-15 a). This therefore confirms that TLS induction by IAVs requires both intracellular virus replication and the triggering of apoptosis.

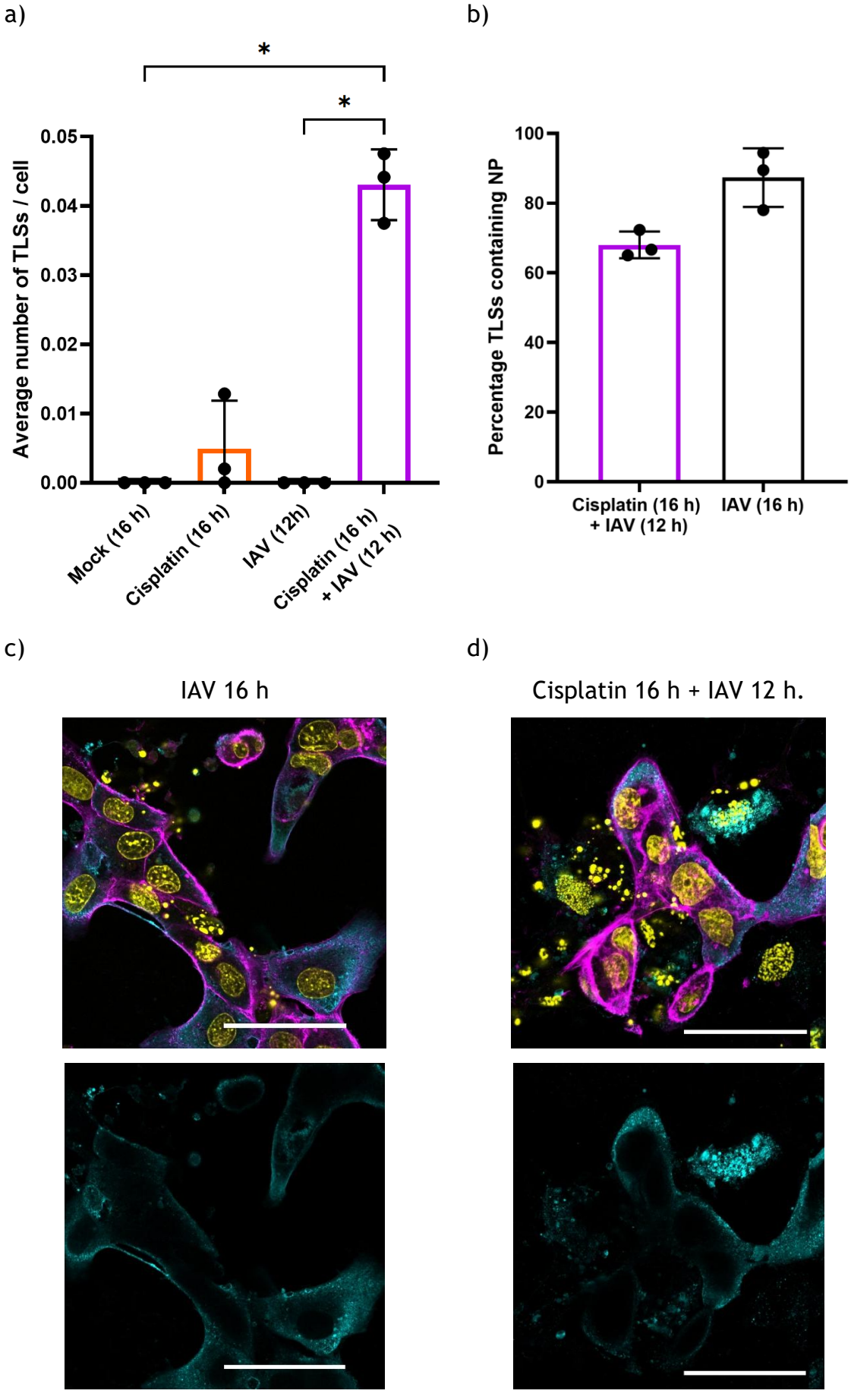

Figure 4-15: TLSs are induced when IAV infection is coupled with the triggering of apoptosis. (a) Average number of TLSs per MDCK cell 16 hours post treatment with 30 μM cisplatin, or mock treated, in the presence or absence of an IAV infection (MOI 1.5 PFU/cell)

performed for 12 hours. Data relating to the single 12 hour infection is replotted from figure 4-10 a. Differences in the average number of TLSs / cell between conditions was tested for significance by Kruskal-Wallis test (n.s. $p > 0.05$, $*p < 0.05$). (b) The percentage of TLSs that contained NP following induction with cisplatin for 16 hours, and infected for 12 hours or infection for 16 hours in the absence of cisplatin. Differences in the percentages of TLSs containing NP was tested fro significance using a Mann-Whitney test (n.s. $p > 0.05$-. For all data the mean and SD are shown (n = 3). (c &d) Representative confocal micrographs of subconfluent MDCKs either (c) 16 hours post infection with an IAV (MOI 1.5 PFU/cell) or (d) 16 hours post treatment with cisplatin and 12 hours post infection. Nuclei (yellow), NP (blue), F-actin (magenta). Scale bars = 50 μm.

I was interested to note that the TLSs which are induced earlier in infection with cisplatin had a lower likelihood of containing NP (Figure 4-15 b). I observed that at 12 hpi, in the presence of cisplatin, approximately 67% of TLSs contained NP, whereas at 16 hours post infection, I observed approximately 80 % of TLSs positive for NP (Figure 4-15 b). Whilst this difference was not statistically significant, it is interesting to hypothesise as to the cause of this disparity. Because there are comparable levels of infection between 12 and 16 hours (Figure 4-9), and no obvious difference in NP expression between 12 hpi with cisplatin and 16 hpi without cisplatin (Figure 4-15 c & d), I do not predict that this difference is due to NP availability (although a comprehensive analysis of NP expression would be required). Instead, I hypothesise that an interaction with a host factor, required for NP incorporation within TLSs, either occurs after 12 hpi and is separate from the mechanism of TLS induction, or that this interaction is somehow lessened by the effects of cisplatin. More experimental work will be needed to test these predictions, and it was not possible to investigate this further within the scope of this thesis.

4.2.4 Assessing the role of IAV infection induced tunnelling nanotube-like structures in facilitating direct cell to cell spread.

With TLSs being shown to facilitate the direct cell to cell spread of IAV infection (222, 223, 230), and apoptosis being required for IAV mediated TLS induction (Figure 4-13), I next wanted to assess the possible role of apoptosis in facilitating the direct cell to cell spread of IAVs.

To explore TLS driven IAV direct cell to cell spread, drugs that target either F-actin (cytochalasin D, and IPA-3) or microtubules (taxol) can be used (see Table 3-3) (222). These drugs, for which were first tested in chapter 3, can inhibit the formation of TLSs and the subsequent decrease in IAV direct cell to cell spread can be measured and reported as being driven by TLSs. Therefore, I first wanted

to verify that TLSs could be inhibited by drug treatment. I noted from the titration of these drugs in chapter 3 (Figure 3-12 to 3-14), that the manner of F-actin disruption or evidence of cytotoxicity with cytochalasin D or taxol treatment, respectively would not be appropriate for accurate measurements of TLS formation. Specifically, cytochalasin D caused F-actin to collapse and the cells to shrink in a manner that caused branched F-actin positive regions that could be falsely mistaken as TLSs (Figure 3-12), and the cytotoxic effects of taxol caused cell rounding and detachment which could reduce TLS formation indirectly. In contrast, IPA-3 treatment disrupted the cytoskeleton in a way that enabled a reliable scoring of TLS formation (Figure 3-13). In particular, F-actin did not appear as fragments, as seen with cytochalasin D, and the cells did not show signs of cytotoxicity or rounding, as seen with taxol (Figure 3-14). I then added 3 μM IPA-3 to subconfluent cells 1 hpi with PR8 (MOI 1.5 PFU/cell) and quantified the TLSs that formed by 16 hpi (Figure 4-16). I found that IPA-3 treatment caused a significant reduction in the average number of TLSs/cell (Figure 4-16 a), as well as the percentage of TLSs that contained NP (Figure 4-16 b). This suggests that IPA-3 treatment successfully reduces TLS formation, and when TLSs are formed, they have a reduced ability to incorporate NP, which suggests that this drug is a good control for the study of TLSs in facilitating IAV direct cell to cell spread.

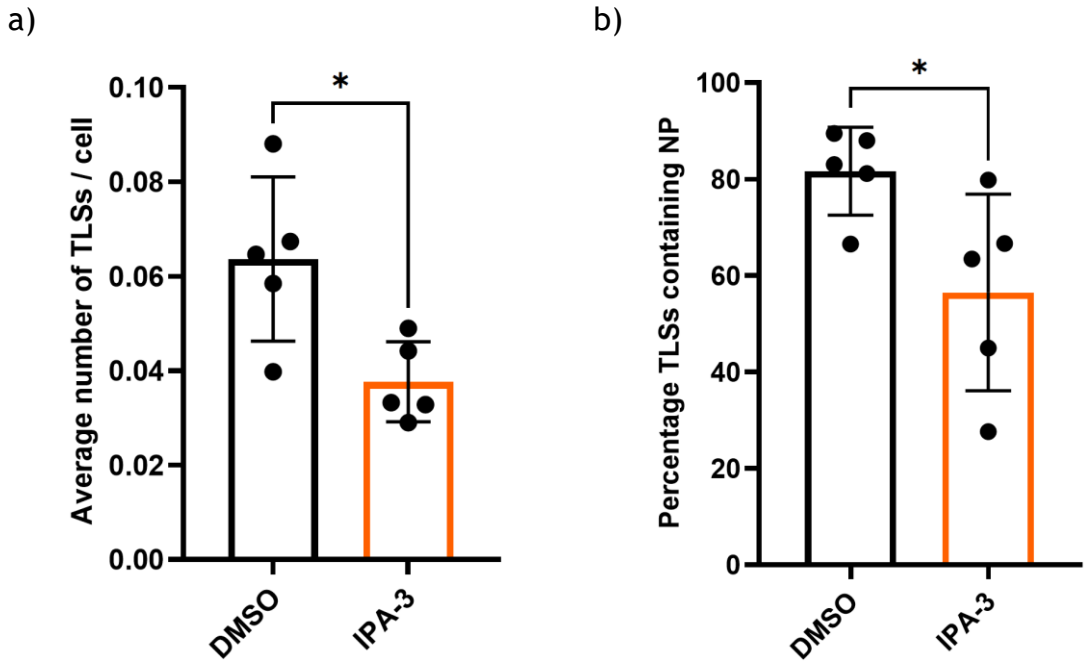

Figure 4-16: IPA-3 reduces the formation of TLSs and the incorporation of NP following IAV infection. (a) Average number of TLSs per MDCK cell 16 hours post infection with PR8 at an MOI of 1.5 PFU/cell, either in the presence of DMSO or IPA-3 (3 μM) added 1 hour post infection, and

(b) the percentage of TLSs containing NP. Differences were tested for significance by Mann-Whitney test (n.s. $p > 0.05$, $*p < 0.05$). The mean and SD are shown (n = 5).

However, in chapter 3 I showed that these TLS inhibiting drugs, including IPA-3, did not reduce the direct cell to cell spread of IAV between confluent cells (see Figure 3-15). I proposed that this was due to the alternative effects these drugs have on the different mechanism of IAV direct cell to cell spread, of which multiple could theoretically function between confluent cells simultaneously. Therefore, before investigating the effects of these drugs in reducing specifically TLS mediated IAV direct cell to cell spread, I wanted to establish an assay to measure direct cell to cell spread between subconfluent cells. In this way, the only mechanisms of direct cell to cell spread will be those that can function over a distance, such as that performed by TLSs. To study the effect of TLS inhibiting drugs on the direct cell to cell spread of IAV infection between subconfluent cells, I prevented virion mediated spread by excluding TPCK trypsin and including 0.36 mM zanamivir (as used previously in the microplaque assay detailed in section 3.2.1), and determined the percentage of cells infected with BrightFlu ZsGreen above infection input levels by flow cytometry, and across drug treatments (Figure 4-17). A reduction in IAV direct cell to cell spread would be indicated by a reduction in the total percentage cells positive for ZsGreen.

After verifying that zanamivir had no effect on TLS formation (Figure 4-18), I found that amongst the drugs targeting F-actin, cytochalasin D had no effect on the percentage of cells infected, whereas IPA-3 caused a moderate but consistent reduction (Figure 4-17). The microtubule targeting drug taxol resulted in an even greater reduction in the percentage of cells infected when compared with IPA-3 (Figure 4-17). This reveals that these drugs differ in their inhibitory effect on direct cell to cell spread when administered at concentrations that are neither directly antiviral or mostly cytotoxic. TLS targeting drugs disrupting both F-actin (IPA-3) and microtubules (Taxol) can inhibit direct cell to cell spread of IAV infection (Figure 4-17) (222). However, the greatest reduction in the percentage of cells infected was seen with the anti-apoptotic drug Z-VAD-fmk, with infection largely being unable to directly spread to any neighbouring cell as indicated by only a slight increase above infection input levels (Figure 4-17). This result correlated with our observation that Z-VAD-fmk resulted in an even greater reduction in TLS formation than IPA-3 (Figure 4-13 & Figure 4-16 a). These results, when combined with our findings on the role of apoptosis in

triggering TLS formation during IAV infection, provide strong evidence that IAVs use this cell death response to facilitate the direct cell to cell spread of infection between non-adjacent cells via long-range cell connections.

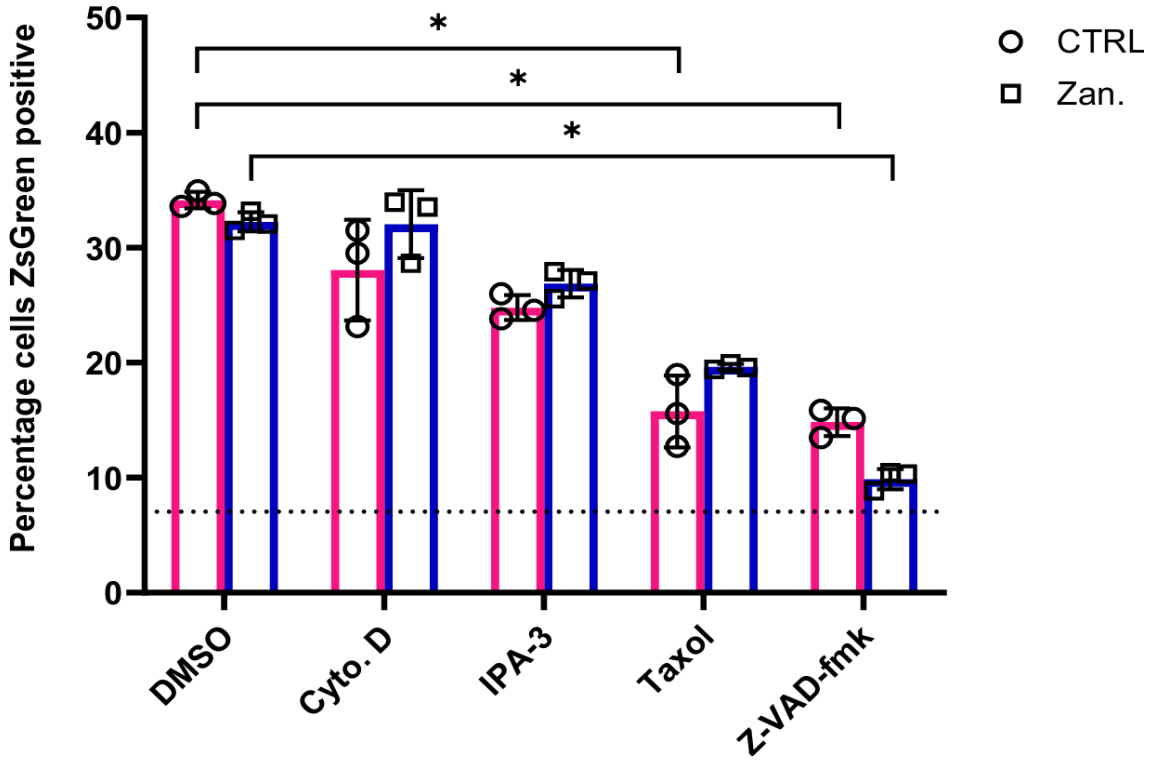

Figure 4-17: Z-VAD-fmk reduces the direct cell to cell spread of IAVs between subconfluent cells greater than alternative TLS inhibiting drugs. The percentage of cells positive for ZsGreen, as analysed by flow cytometry, 24 hours post PR8-ZsGreen (BrightFlu) infection (MOI 0.1 FFU/cell) of subconfluent MDCK cells in the presence or absence of 0.36 mM zanamivir and a panel of TLS inhibiting drugs. The dashed line indicates the percentage cells ZsGreen positive 8 hours post infection, i.e. infection levels prior to any infection spread. Differences between mock and zanamivir treatments was tested for significance using a multiple Mann-Whitney test (n.s. $p > 0.05$). Differences between TLS inhibiting drug treatments relative to the DMSO control, either as part of the control or zanamivir treated group, was tested for significance using a Kruskal-Wallis test (n.s. $p > 0.05$, *$p < 0.05$, **$p < 0.01$). For all data the mean and SD is shown (n = 3).

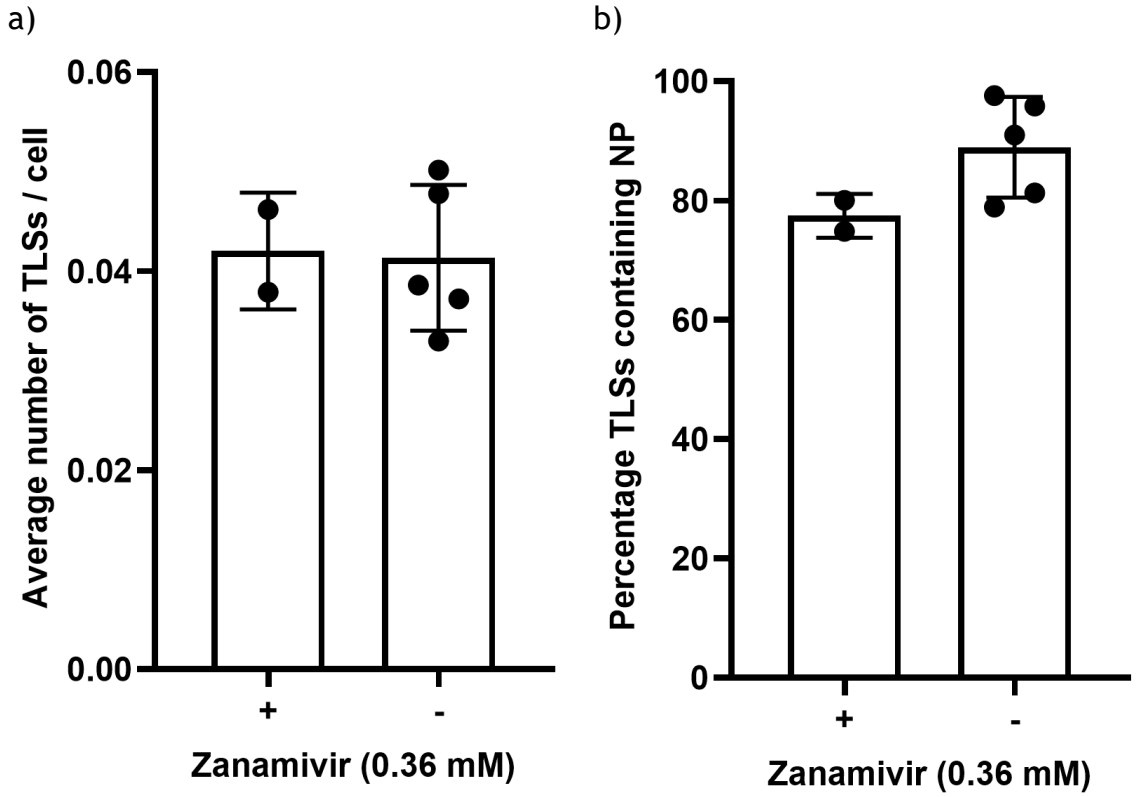

Figure 4-18: Zanamivir has no effect on TLS induction by IAVs.(a) Average number of TLSs per MDCK cell, and (b) the percentage of TLSs containing NP 16 hours post IAV infection (MOI 1.5 PFU/cell) in the presence or absence of 0.36 mM zanamivir added 1 hpi

With a significant reduction in IAV direct cell to cell spread between subconfluent cells with Z-VAD-fmk treatment, I was curious to know if this drug would also reduce the direct cell to cell spread between confluent cells in ways the other drugs failed to do (see Figure 3-15). To assess this, I performed the microplaque assay with PR8 (as detailed in section 3.2.2), with the inclusion of 100 μM Z-VAD-fmk within the cell overlay.

The finding that Z-VAD-fmk reduced IAV direct cell to cell spread between subconfluent cells used BrightFlu, which is a modified PR8 virus, the latter of which was used in the microplaque assay. Therefore, to rule out any difference in microplaque formation between these viruses, and to see if the expression of the reporter gene (ZsGreen) can be used in place of NP immunostaining for microplaque identification, I compared microplaque formation between NP immunostained BrightFlu or PR8 infected cells. The analysis of PR8 or BrightFlu microplaques revealed that Z-VAD-fmk did not reduce the percentage of foci that were microplaques relative to either the DMSO or zanamivir only treated cells (Figure 4-19). This shows that direct cell to cell spread of IAVs between confluent cells is still not reduced with drugs that potently inhibits TLSs, and

suggests that TLS may not be functioning in trafficking IAV infection between confluent cells. Interestingly, BrightFlu formed approximately 20% more ZsGreen microplaques when compared to NP positive microplaques of PR8 (Figure 4-19). This could suggest that ZsGreen is delivered to neighbouring cells more frequently than NP, or that ZsGreen expression enables the detection of infected cells more readily than immunostained NP. Given that the detection and intensity of NP signal is dependent on the performance of several reagents and efficiency of a multi-step immunostaining protocol, I believe that the expression of the fluorophore as the means of reliable microplaque detection is the more probable explanation for this difference.

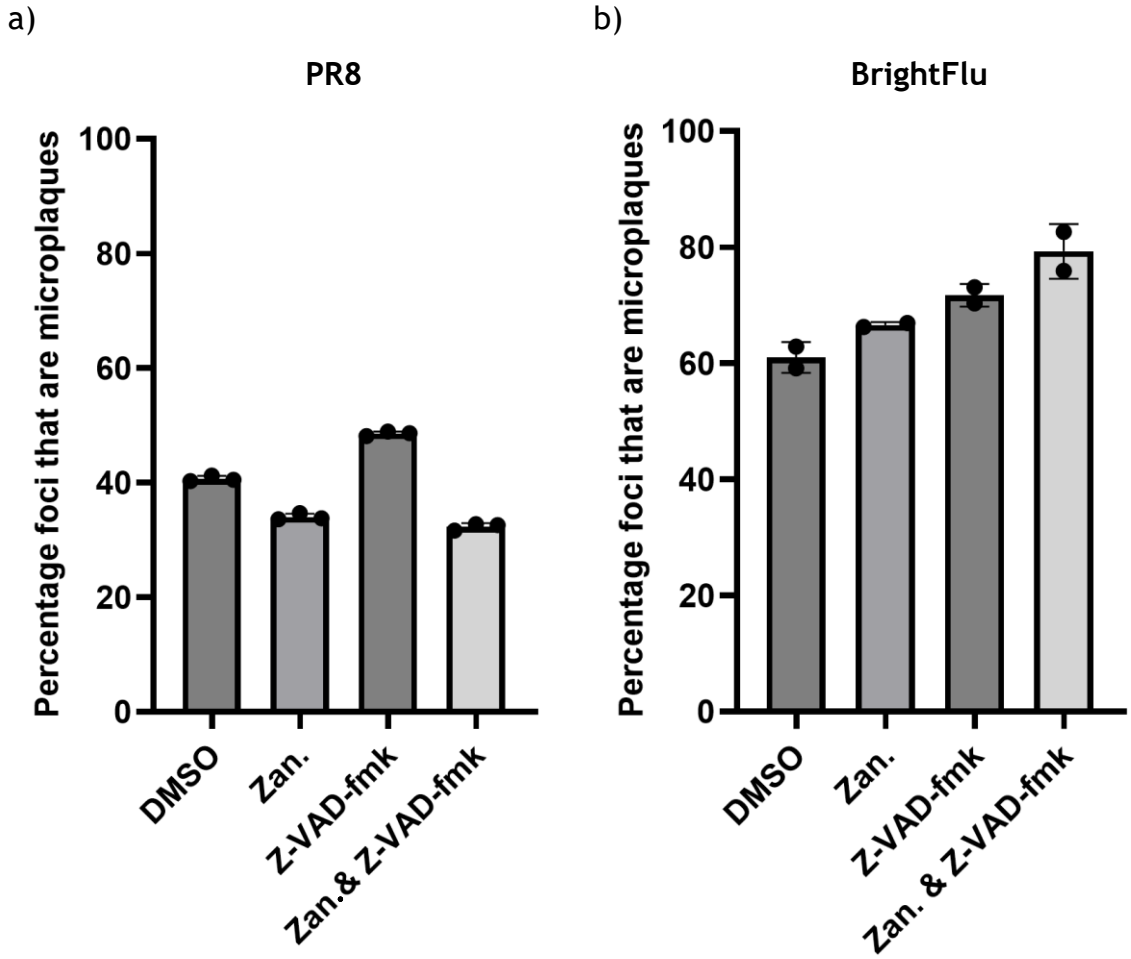

Figure 4-19: Comparing PR8 and BrightFlu microplaque formation. The percentage of NP or ZsGreen positive foci that are microplaques following (a) PR8 or (b) BrightFlu infection, respectively. Confluent MDCKs were infected with PR8 at a low MOI, and 2 hours post infection an overlay containing either DMSO, zanamivir (0.36 mM) and/or Z-VAD-fmk was added. Cells were fixed 48 hours post infection, stained with DAPI and immunostained for NP (for PR8 infected samples) and imaged on the Nexcelom Celigo image cytometer. Differences between drug treatments was tested for significance using a Kruskal-Wallis test (n.s. $p > 0.05$). For all data the mean and SD is shown (PR8 n = 3, BrightFlu n = 2).

With this difference in microplaque formation when using BrightFlu ZsGreen as the marker of infection, I next wanted to test the effect of other TLS inhibiting

drugs with this virus. The percentage of foci that were microplaques with zanamivir and cytochalasin D treated BrightFlu infected cells was similar to those seen previously with PR8 (approximately 70%) (Figure 3-15 a & Figure 4-20 a). Whilst this was significantly higher than the DMSO PR8 control, this difference was not significant for BrightFlu due to the elevated microplaque formation with the DMSO control (Figure 4-20 a). The mean microplaque areas with BrightFlu was largely consistent with PR8 (Figure 3-15 b), with the exception that cytochalasin D did not result in a significant increase in microplaque area when zanamivir was excluded (Figure 4-20 b). These results confirm that the marker of infection used can alter the frequency with which microplaques are detected, but regardless of what protein was detected, no evidence of a reduction in microplaque formation with TLS inhibiting drugs is seen.

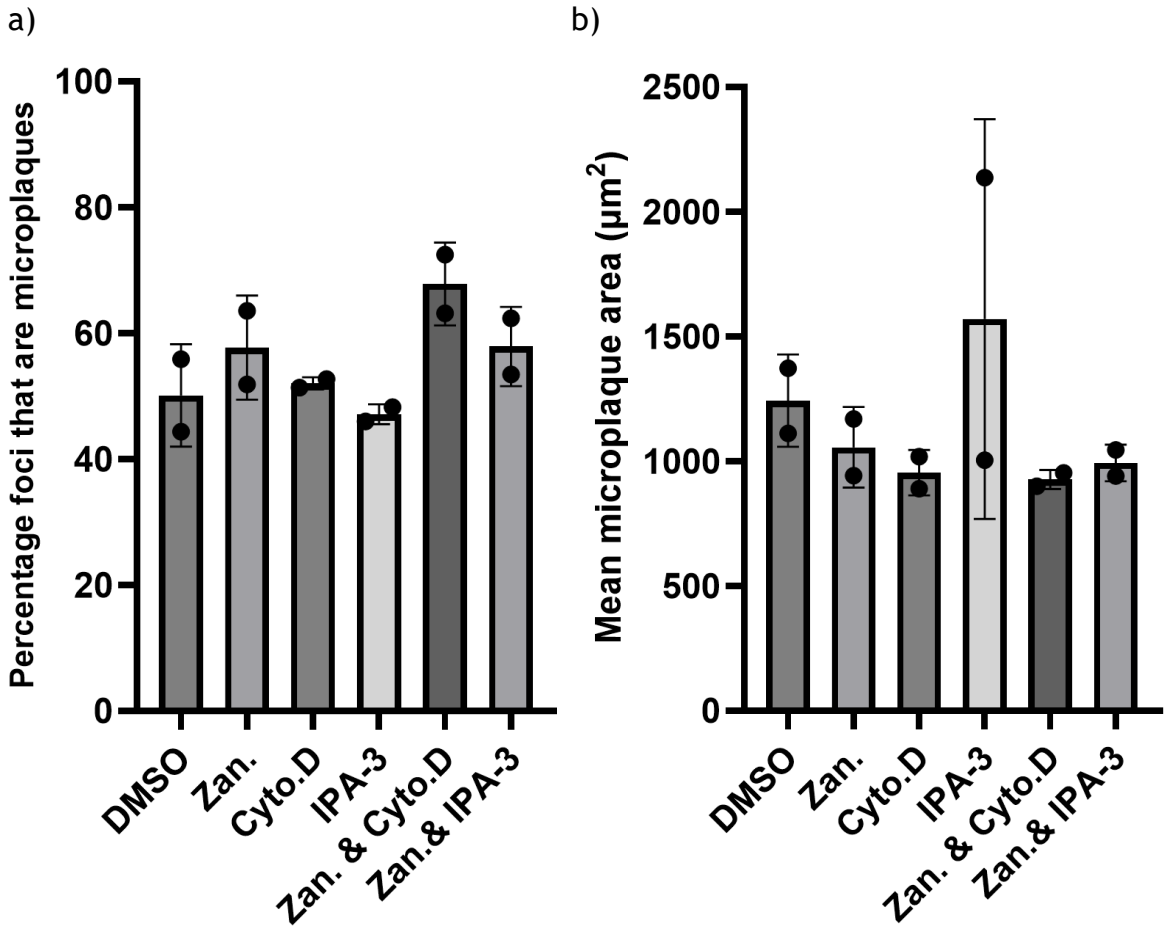

Figure 4-20: BrightFlu microplaques are unaffected by other TLS inhibiting drugs. (a) The percentage of ZsGreen positive foci that are microplaques in the absence of TPCK trypsin and (b) the mean area of microplaques, in the presence of a panel of drugs targeting the cytoskeleton with and without zanamivir (0.36 mM). Confluent MDCKs were infected with PR8 at a low MOI, and 2 hours post infection an overlay containing either DMSO, zanamivir (0.36 mM), cytochalasin D (20 µM), IPA-3 (3 µM), or taxol (100 µM) was added. Cells were fixed 48 hours post infection, and imaged on the Nexcelom Celigo image cytometer Differences between drug treatments, was tested

for significance using a Kruskal-Wallis test (n.s. $p > 0.05$, *$p < 0.05$, **$p < 0.01$). For all data the mean and SD is shown (n = 2).

4.2.5 Exploring the physiological relevance of tunnelling nanotube-like structures during IAV infection.

Our results, showing that TLS inhibiting drugs only reduced IAV direct cell to cell spread when the cells were subconfluent, call into question whether TLSs can function to spread infection between confluent cells. This is an important consideration for when thinking about the unexplored physiological relevance of TLSs during IAV infection.

The natural site of IAV infection is the epithelial cells of the respiratory tract. These cells form a dense tissue, coated in secreted mucus, that is constantly expanding and contracting with every breath. Additional movement is also seen at the cellular level with cilia beating. Collectively these conditions present a challenging environment for these already fragile and transient structures, and in order for them to form in this cell-dense, motile and complex environment they would need to be able to withstand mechanical deformations, as well as be able to penetrate solid tissue or survive mucociliary flow.

It was unknown if TLSs could form within non-tumorous lung tissue let alone whether they could form from IAV infected epithelial cells *in vivo*. Most imaging of TLSs *in vivo* has been achieved using methods with minimal staining and tissue manipulation (257, 265, 337), and the study of TLS formation between epithelial cells following respiratory virus infection is challenged by the need to distinguish between infected and healthy cells. Therefore, to assess the ability of TLSs to form at the site of a respiratory infection, I needed a method which uniquely labelled infected cell membranes with minimal tissue manipulation to maintain TLS integrity prior to imaging. I did this using the mT/mG reporter mouse system, in combination with a PR8 IAV which has been genetically modified to encode the Cre recombinase (PR8 Cre) (343). The mT/mG mice encode a membrane-targeted tdTomato (mT) fluorophore flanked by *loxP* sites, such that when Cre recombinase is expressed, the *tdTomato* gene is replaced by a downstream membrane-targeted *GFP* gene (mG, Figure 4-21 a) (343). The result is that infection with a Cre-expressing virus permanently changes the membrane fluorescence of a cell from red to green. To investigate this, Dr Ed Roberts

(Cancer Research UK Scotland Institute) intranasally infected mT/mG mice with 1000 PFU of PR8-Cre and, six days post infection, Jack McCowan (Cancer Research UK Scotland Institute) harvested the lungs, which I prepared for confocal microscopy (see section 2.2.6). Infected cells were identified by mG positive membrane fluorescence, with infected regions also lacking mT signal (Figure 4-21 b). I observed IAV infected epithelial cells in the lower respiratory tract which had the appearance of pseudostratified columnar epithelial cells, known to support IAV infection (344, 345).Therefore, this system, as expected, enabled the identification of IAV infected epithelial cells, and I anticipated that this would provide suitable contrast between infected and uninfected cell membranes required to detect TLSs within a dense tissue.

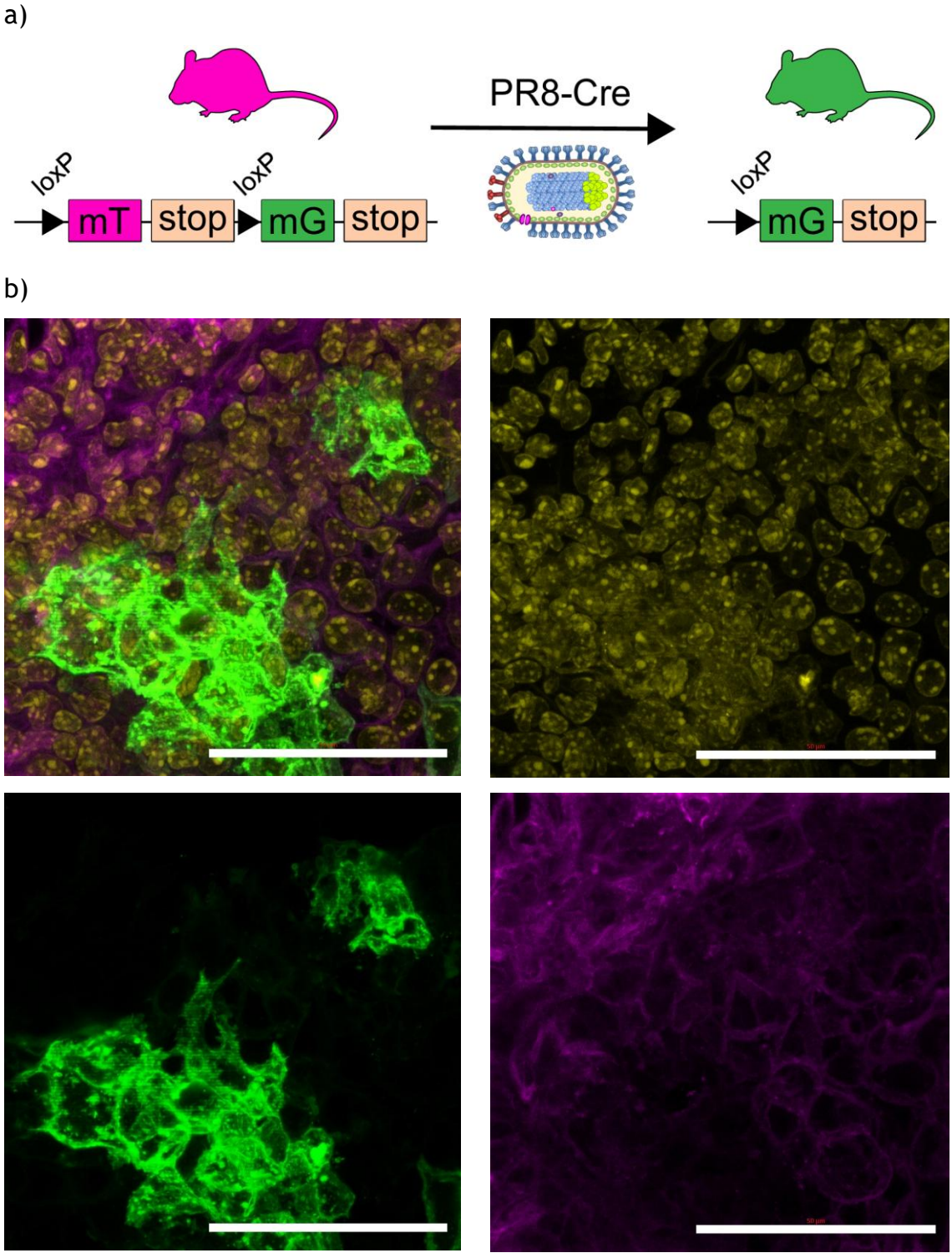

Figure 4-21: Intranasal infection of mT/mG mice with PR8-Cre enables the visualisation of infected cell membranes within the lungs. (a) Schematic of mT/mG reporter mouse system in combination with an IAV encoding for Cre (PR8-Cre), with arrows indicating loxP sites that flank the tdTomato fluorophore. Following intranasal infection and Cre recombinase expression, the membrane targeted tdTomto (mT) is replaced with a membrane targeted GFP (mG) fluorophore. Six days after intranasal infection with PR8-Cre, lungs were harvested from mT/mG mice and thick sections were prepared for confocal microscopy. (b) Split channel, maximum intensity projections of 100 µm thick lung tissue sections showing showing PR8-Cre infected cell distinguished by the expression of membrane GFP. Nuclei (yellow), mG (green), mT (magenta). Scale bars = 20 µm.

If cellular projections were to be found within the infected lung, I anticipated that they would be of various lengths and orientations within the tissue.

Therefore, to increase the likelihood that TLSs connecting cells would be captured, super resolution confocal imaging of thick tissue sections incorporating Z-stacks (to facilitate 3D rendering of structures and maximum intensity projections) was routinely performed. However, further consideration into optimal thickness of tissue sections was first required. Thicker tissue sections increase the chance of fully capturing longer TLSs that lie obliquely to the section plane. However, thicker tissue sections (greater than 100 µm) needed to be cut on a vibratome, which is performed at room temperature with the help of a vibrating blade. These conditions easily compromise the integrity of the tissue, and are likely to be disruptive to delicate structures, such as TLSs, within the section. Alternatively, if the thickness of the tissue section was reduced, this would increase the chances that the TLSs themselves would be cut during sectioning, but since it is performed with frozen tissue embedded in OCT, the rigidity this provides may reduce deformations of the sample during sectioning, that would otherwise likely compromise TLS integrity. Therefore, I selected 100 µm thick tissue sections for the visualisation of TLSs *in vivo*.

To validate this selection, I sectioned infected mT/mG lung tissue at different thickness with either the vibratome (200 µm thick sections) or CryoStat (100, 50 or 25 µm thick sections) and visualised the sections with super resolution confocal microscopy, generating maximum intensity projections. I found that the PR8-Cre infection of mice did not frequently result in the formation of large mG positive lesions (Figure 4-22), possibly due to the loss of the Cre reporter. Nevertheless, the limited area of mG fluorescence would prove ideal for looking at thin membrane projections extending out from individual infected cells. However, this also meant that at the thinnest tissue section of 25 µm, only spurious mG fluorescence was detected (Figure 4-22). This indicates that only a few cells are actually encompassed in their entirety at this thickness, and rarely would these be infected. This result is perhaps unsurprising given that most pseudostratified columnar epithelial cells, typical of the major airways of the lung, have a length (basal to apical) of between 20 and 30 µm (346). With increasing tissue section thickness, cut with the cryostat (50 and 100 µm), more mG positive membrane was visualised, demonstrating that the thicker the section, the more infected cells are imaged. However, the 200 µm thick section cut with the vibratome did not result in the imaging of any membrane

fluorescence. I hypothesise that this was due to the rapid deterioration of membrane fluorescence signal during cutting without freezing and with exposure to ambient lighting. Based on these results, I concluded that sectioning mT/mG mouse lung lobes at 100 µm thickness with the CryoStat was optimal for the imaging of infected cell membranes.

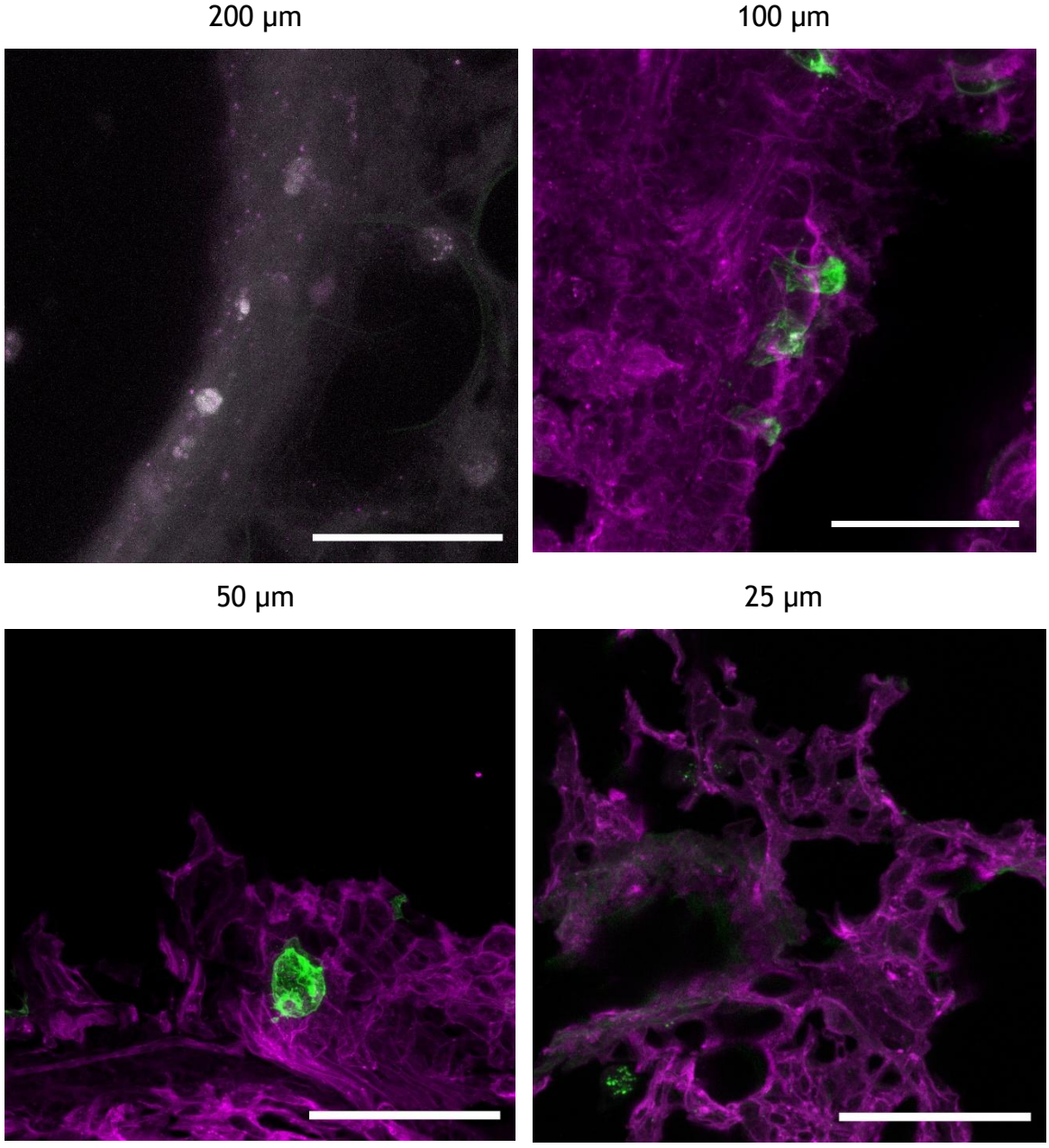

Figure 4-22: Determining the optimal tissue section thickness. Maximum intensity projections of PR8-Cre infected inflated mT/mG mouse lungs, with tissue sections cut at 200, 100, 50 or 25 µm thicknesses. All tissue section thicknesses, with the exception of 200 µm which was cut with the vibratome, was performed by Colin Nixon of the Cancer Research Uk, Scotalnd Institute histology lab using the cryotome. All samples were mounted in Ce3D for at least 30 minutes before imaging. mG (green), mT (magenta). Scale bars = 50 µm.

Another consideration was how handling and processing of the lungs, post harvesting, affected the tissue and any possible fragile structures within.

Typically, lungs are inflated by introducing agarose into the airway to support softer areas of the lung, such as the parenchyma, that would otherwise collapse, and to enable more consistent sectioning. However, it was unknown how the artificial expansion of the lung by pipetting a viscous liquid within them might disrupt fragile TLSs on the apical surface of the cells of the major airways. Therefore, I wished to avoid the inflation of the lungs, and rely on the immediate freezing of the dissected lobes to maintain the shape of the lung structures during sectioning. To investigate the consequence of this, I examined how the infected major airways and parenchyma differed between inflated verses non-inflated lobes (Figure 4-23). Additionally, I performed staining with DAPI and Phalloidin prior to imaging to assess their benefit and risk when examining the structures within the tissue (Figure 4-23).

I found that major (large-lumen) airways and spaces within the parenchyma could be just as easily observed from micrographs of uninflated lung lobes as those from the inflated lobes (Figure 4-23). There was no obvious difference in the appearance of tissue sections, suggesting that inflation may not influence the integrity of the structures of the tissue. However, the effort to preserve fragile TLSs warranted this omission, even if it was in an abundance of caution. Furthermore, the additional DAPI and phalloidin staining had varied success. It proved difficult for DAPI staining to penetrate deep within the tissue and some micrographs lacked any nuclei staining (Figure 4-23). Phalloidin staining was more reproducible, however, due to the abundance of F-actin in these tissues, it often did not provide useful information about the structures of individual cells (Figure 4-23). In addition, the process of handling these tissue sections during staining often compromised the integrity of the sample, with the section frequently folding or breaking during washing steps. Therefore, the risks to TLS preservation during additional staining steps was deemed to outweigh the limited benefits these steps provided, and they were omitted in future experiments.

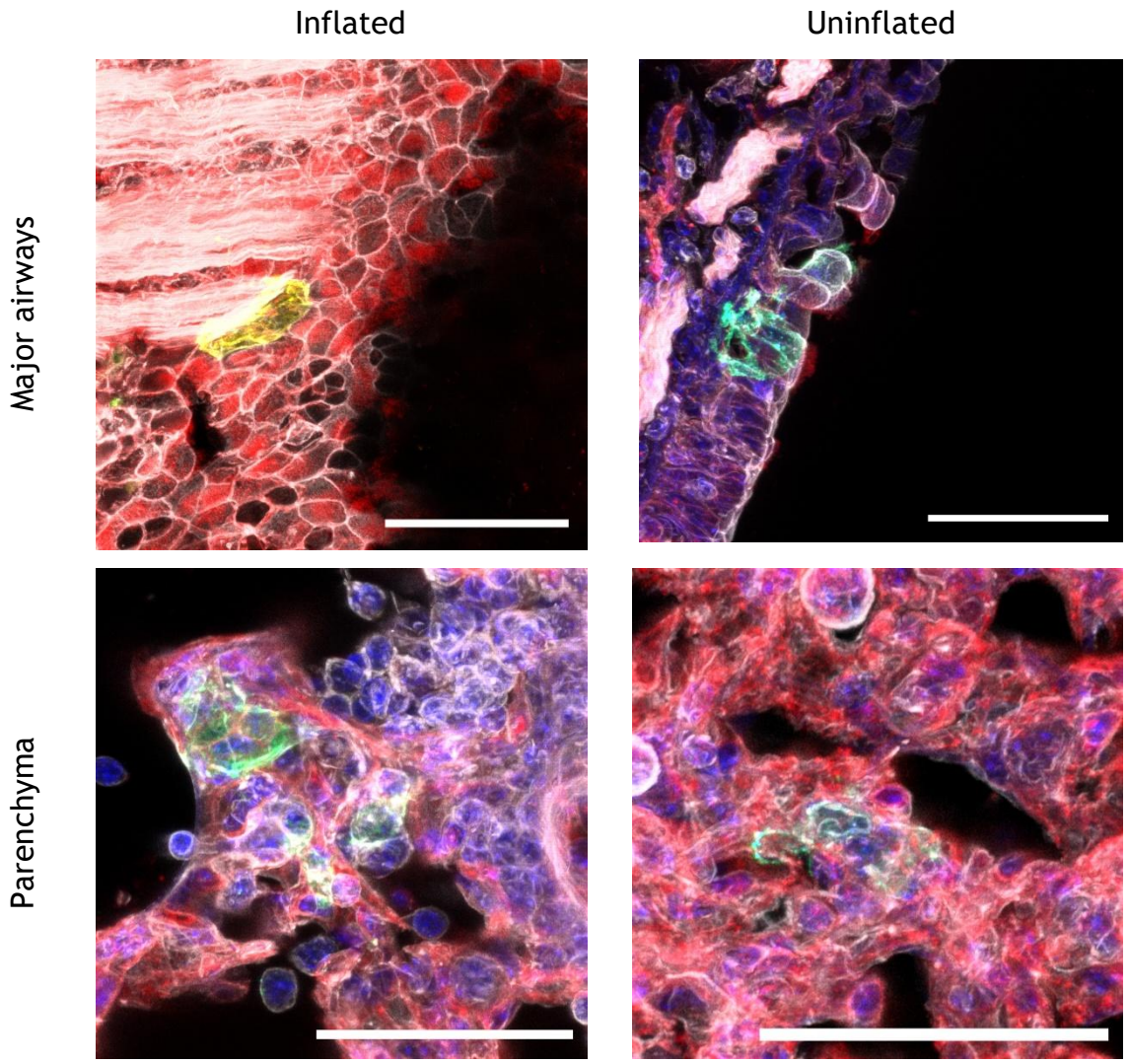

Figure 4-23: The major airways and parenchyma of infected mT/mG mouse lung lobes with and without agarose inflation. Maximum intensity projections of PR8-Cre infected mT/mG mouse lung lobes that were either inflated with 1.2% agarose or left uninflated post lung harvesting. Tissue sections were cut at 100 µm thicknesses with the CryoStat and mounted in Ce3D tissue clearing solution for at least 30 minutes prior to imaging. mG (green), mT (red), nuclei (blue), F-actin (white). Scale bars = 50 µm.

Within infected, 100 µm thick, uninflated mT/mG lung lobe tissue sections I could observe the protrusion of thin TLSs (Figure 4-24 & Figure 4-25). Interestingly, these appeared to have formed in the spaces between cells of the epithelium rather than through the lumen of the airway, resulting in curved structures that followed the contours of neighbouring cells (Figure 4-24). In addition, TLSs seemingly connecting infected cells were seen (Figure 4-25), suggesting that TLSs might be capable of transferring IAV infection within a tissue, or of facilitating the interaction of separately infected cells. The structures I observed in the airway epithelium have similar characteristics to those previously seen in mammalian tissues such as the cornea of mice, in which TLSs are often curved and have a bulbous structure at their terminus (Figure 4-24 b) (333).

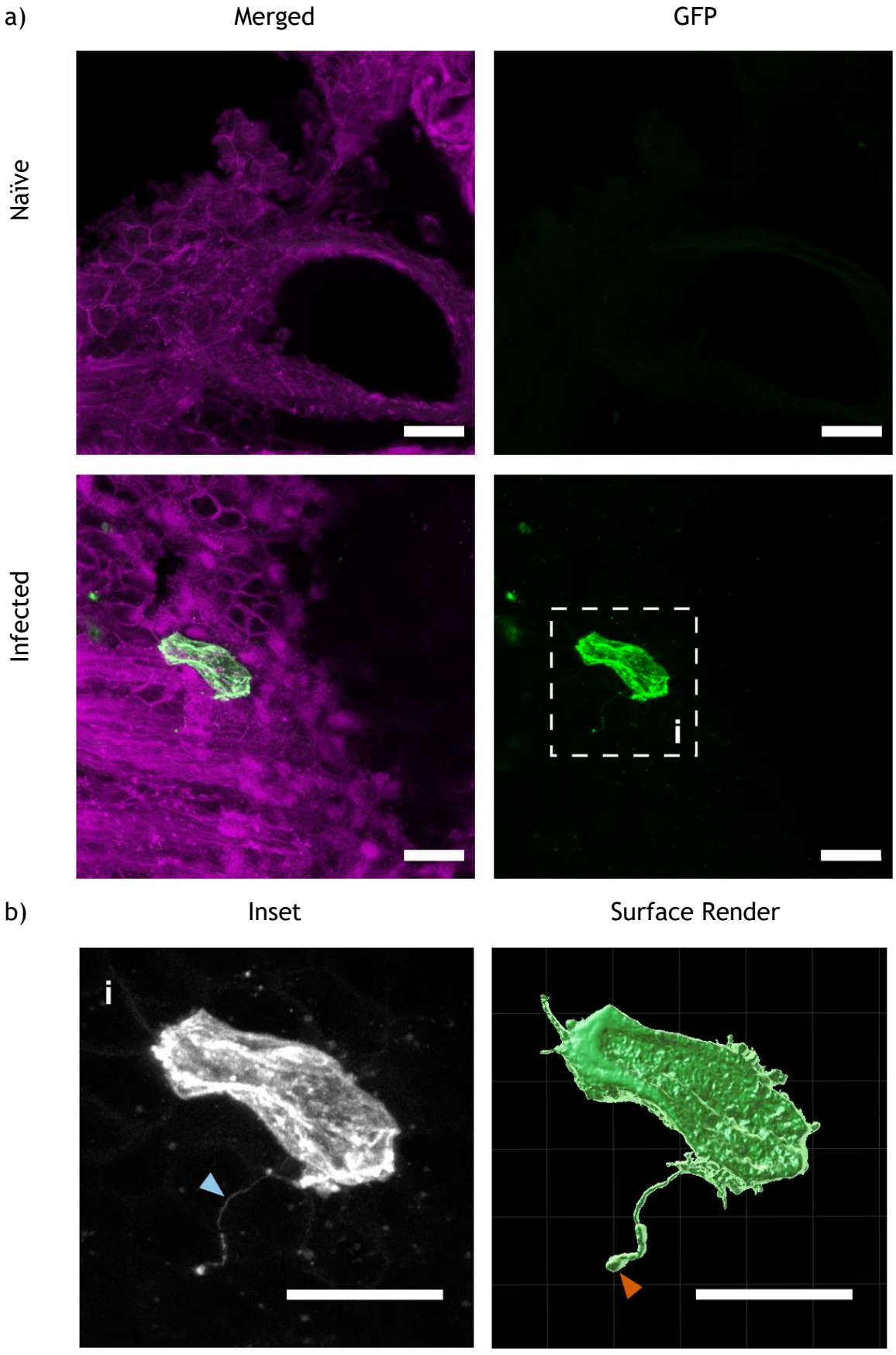

Figure 4-24: TNT-like protrusions extending from IAV infected cells are observed *in vivo*. (a) Maximum intensity projections of 100 µm thick uninflated naïve or infected mT/mG lung lobes, the latter showing a TNT-like protrusion projecting from an isolated PR8-Cre infected cell (distinguished by the expression of GFP). (b) Magnified insets outlined in white boxes are shown alongside surface renders. Membrane labels are tdTomato (magenta) and GFP (green/white). Blue

arrowheads indicate the presence of TLSs, and orange arrowheads indicate the bulbous termini of TLSs.

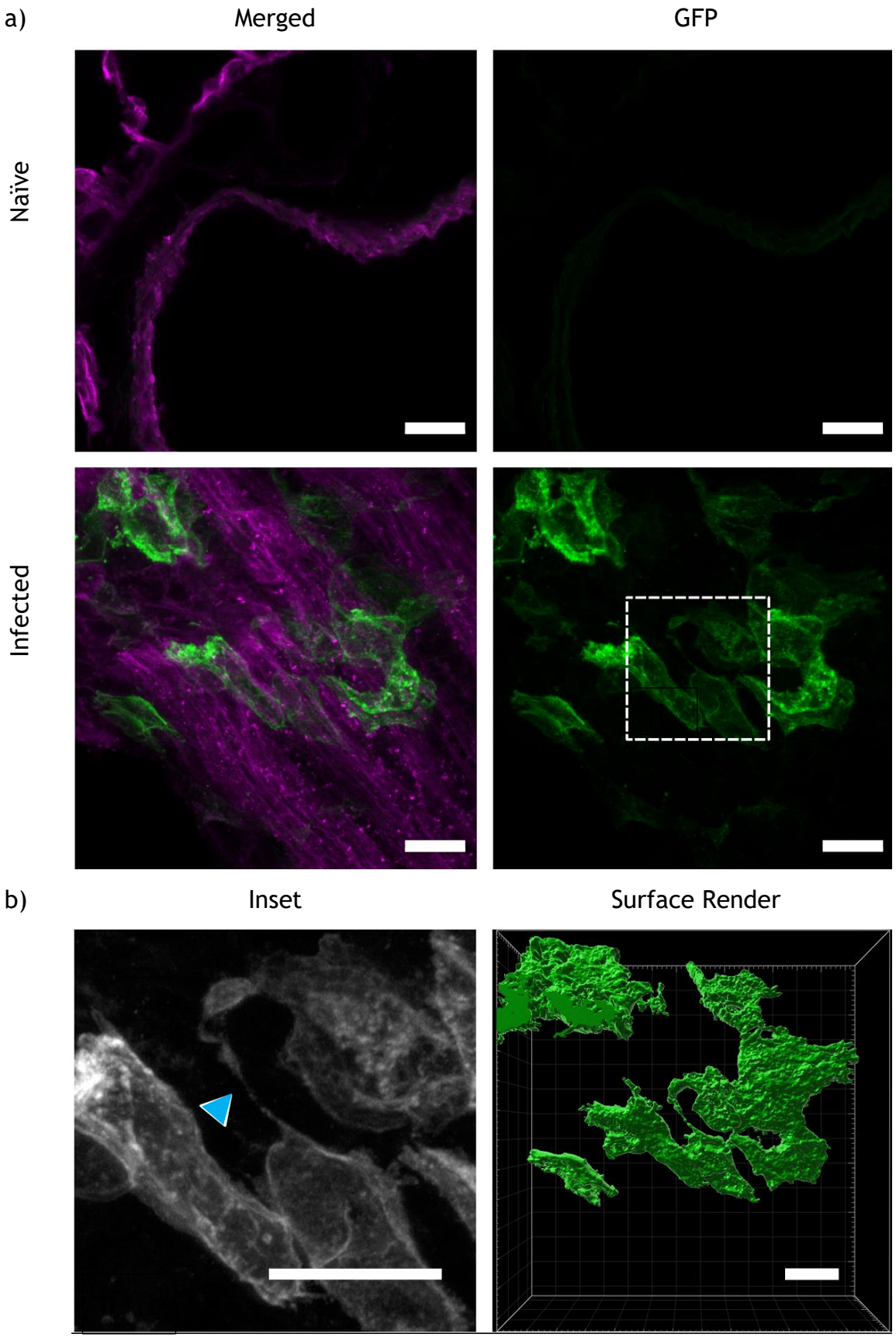

Figure 4-25: TNT-like structures involving IAV infected cells are observed *in vivo*. (a) Maximum intensity projections of 100 µm thick uninflated naïve or infected mT/mG lung lobes, the latter showing a TNT-like structure appearing to connect PR8-Cre infected cells (distinguished by the expression of GFP). (b) Magnified insets outlined in white boxes are shown alongside surface

renders. Membrane labels are tdTomato (magenta) and GFP (green/white). Blue arrowhead indicate the presence of TLSs.

4.3 Discussion

The formation of TLSs has been shown to mediate the direct cell to cell spread of IAV infections *in vitro* (230). However, it was unknown if this effect could occur in the crowded, mobile environment of the respiratory tract, and in particular the dynamic pseudostratified respiratory epithelium. Additionally, it remained to be found as to how IAV infection induced the formation of TLSs. Therefore, in this chapter I investigated how different IAVs (spherical verses filamentous) induced TLSs, and how this influenced the ability of IAVs to undergo direct cell to cell spread. Additionally, I used *in vivo* models to explore the presence of TLSs in infected lung tissue in order to better understand the potential physiological relevance of TLSs during IAV infection.

Using high MOI infections *in vitro* I found that the induction of TLSs is driven by the presence of replicating virus (Figure 4-5). This effect was not mediated through paracrine signalling between cells (Figure 4-5), or through IAV's ability to form filamentous virions that resemble TLSs (Figure 4-7). Instead, IAVs induce TLS formation through intracellular virus replication, triggering apoptosis (Figure 4-5 & Figure 4-13). Apoptosis was already known to contribute to the pathology of IAV infection (347), and my study shows that it can also be used by the virus to facilitate its direct cell to cell spread (Figure 4-17).

Apoptosis can be distinguished from other cell-death programmes such as necroptosis and pyroptosis by its reliance on caspases, and by the limited involvement of extracellular pathogen- or damage associated molecular patterns as stimuli (reviewed in (348, 349)). Recent studies have demonstrated that caspase 8 is also involved in the activation of pyroptosis, in a process independent of extracellular PAMPS or TNF (reviewed in (349)). However, there are redundant pathways for pyroptosis activation, with nuclear programmed-death ligand 1 (nPD-L1) also capable of progressing the cascade (350). Furthermore, treatment of IAV infected dendritic cells and mouse embryonic fibroblasts with a pan-caspase inhibitor did not prevent necroptosis (351, 352). Therefore, the pan-caspase inhibitor Z-VAD-fmk can be considered primarily as

an inhibitor of apoptosis in my experiments, in line with its use in other studies (255, 339, 341).

How apoptosis induces TLS formation is complex, as multiple stages of apoptosis can be important for TLS induction. For example, one study found that mitochondrial cytochrome c release within U.V. treated PC12 cells induced the formation of microtubule-containing TLSs (339). Another study found that the presentation of phosphatidylserine (PS) on the outer leaflet of the plasma membrane was required (264). Coating PS with annexin V prevented TLS induction from stressed cells but had no effect on the frequency of other cellular projections (264). This suggests that the presentation of PS on the extracellular surface could increase the rate at which cell projections (or TLS precursors) can interact with recipient cell membranes, thereby completing and inducing the formation of TLSs.

Apoptosis is a cell death programme which is already known to positively influence IAV virus titres in vitro and can be seen in vivo following IAV infection (340, 353, 354). IAVs have been shown to modulate apoptosis in ways that can benefit virus propagation (340, 355). The increased formation of TLSs following the onset of apoptosis (Figure 4-10), could also benefit the virus by facilitating the direct cell to cell spread of IAV genomes, and so spreading IAV to a healthy new host cell that can continue viral replication.

However, the lack of TLS induction by cisplatin treatment, in the absence of an IAV infection (Figure 4-15), suggests that the triggering of apoptosis alone is not sufficient for TLS induction. This is supported by previous research which showed a continued induction of TNTs between H_2O_2 treated rat primary astrocytes and neurons even when apoptosis was inhibited by Z-VAD-fmk (255). Cisplatin induces apoptosis in a broadly similar way to IAV infection, as both can trigger the intrinsic and extrinsic apoptotic pathways (reviewed in (356, 357)). Unique to the mechanism of apoptosis by IAV infection is the function of viral proteins (reviewed in (356)), most notably PB1-F2, which induces the permeabilisation of mitochondrial membranes leading to cytochrome c release and the activation of the intrinsic pathway (84, 358). My results showed that when apoptosis is triggered pharmacologically, TLSs can be induced from infected cells at earlier time points post infection (Figure 4-14 & Figure 4-15). These results collectively

reveal that the mechanism of TLS induction by IAVs is due to a combination of virus replication and the onset of apoptosis, and therefore, potentiates an involvement of IAV proteins that either directly or indirectly influence this cell death response.

For some other viruses, viral proteins are known to be directly involved in the induction of TLSs (reviewed in (283)). For example, the Nef and Env protein of HIV-1, as well as the US3 proteins of the alphaherpesviruses, pseudorabies virus (PRV), Herpes-Simplex virus 2 (HSV-2), and bovine herpesvirus 5 (BoHV-5), have been shown to trigger TLS formation (194, 241, 272, 286, 359). Intriguingly these proteins are also known to regulate apoptosis (241, 286, 360-362), and in the case of HIV-1 Nef and US3 of alphaherpesviruses, these proteins have the ability to negatively regulate apoptosis (255, 286, 360, 363). This suggests that other viruses may also depend on the apoptotic pathway to trigger TLS formation. However, the instances of TLS inducing viral proteins that simultaneously negatively regulate apoptosis could indicate that TLS induction may not always occur through the activation of this pathway, but instead could suggest a requirement of a more nuanced regulation of the pathway. Alternatively, TLSs can facilitate the transfer of cytoplasmic cargo that can suppress apoptosis within the recipient cells (264, 271, 339). Therefore, the ability of viral proteins to suppress apoptosis may be linked, or is downstream to its ability to induce TLSs, a concept which I explore further in chapter 5.

Here, I show that drugs that inhibit TLS formation reduce the ability of IAVs to spread directly between subconfluent cells (Figure 4-17). This strongly supports a functional role of apoptosis in facilitating the transfer of IAV infection to neighbouring, distant cells via TLSs. Whilst previous reports showed that several of these drugs reduced direct cell to cell spread of IAV infection between confluent cells (222, 230), in our hands these drugs did not reduce the frequency and scale of microplaque formation (Figure 3-15 & Figure 4-20). This dependency on the cells being subconfluent for a reduction to be seen supports the hypothesis that the alternative mechanisms of IAV direct cell to cell spread, that can function between confluent cells, could be differently regulated by these drugs.

In chapter 3 I showed that the efficiency of IAV direct cell to cell transfer of cytoplasmic viral genomes varied between IAV strain, with PR8 significantly forming more microplaques than Udorn (Figure 3-9). This was not influenced by the differences in virion morphologies, suggesting that other factors were responsible. In this chapter, I noted that PR8 induced slightly more TLSs than Udorn, and this was also not being determined by virion morphology (Figure 4-7). Therefore, the differences in IAV direct cell to cell spread frequencies correlated with the subtle differences that these viruses induced TLSs. This suggests that the differences in the ability of PR8 and Udorn viruses to undergo direct cell to cell spread could be determined by this difference in TLS induction, however, other mechanisms of direct viral genome transfer can not be ruled out. It is possible that these viruses interact differently with host factors that traffic viral genomes. For example, in the case of TLS mediated IAV direct cell to cell spread, Rab11a is required for the incorporation and trafficking of NP (used as a proxy for vRNPs) (230). Although this is an interesting finding, the lack of a difference in the amount of NP positive TLSs between IAV strains (Figure 4-7 b) suggests that this particular factor may not account for the differences observed here (230).

I found that the TLSs induced by both PR8 and Udorn infection frequently incorporated NP (>80%), whereas a reduction in NP positive TLSs was seen following Udorn MPR8 infection (approximately 65%) (Figure 4-7 b). This suggests that NP is readily taken up as cargo within TLSs, emphasising the potential role of TLSs in mediating IAV direct cell to cell spread. However, the reduction seen with Udorn MPR8 suggests that NP and possibly vRNP incorporation is influenced by intersegment interactions or RNA-protein interactions, that can then in turn be influenced by viral gene segment origin. No bias against individual IAV genome segments, during TLS mediated IAV trafficking has been reported, however, these studies used viruses of a single strain background (223, 230). Indeed research using cotransfection of cells with gene segments of different IAV strain origin (including PR8 and Udorn) has shown that gene segments of the same virus tend to cosegregrate due to strain specific, prominent RNA-RNA interactions (364). In other words, gene segments of the same strain can show notable preferences for interacting with each other. Therefore, I hypothesise that weaker intersegment RNA-RNA interaction sites exist between the matrix

gene segment of Udorn and the gene segments of the PR8 background, and this results in the incorporation of fewer vRNP complexes within TLSs. However, it is unlikely that vRNP discrimination of one segment would likely result in the significant reduction of NP signal within TLSs that I observed. Nevertheless, how intersegment RNA-RNA interactions could influence co-trafficking of vRNPs through TLSs could be an interesting area of future research.

Interestingly, when I compare TLS induction and the incorporation of NP within them with the frequency that these viruses formed microplaques (as a measure of direct cell to cell spread) in chapter 3, it appears that TLS formation is more influential than the frequency of NP detection. For instance, greater PR8 microplaque formation correlated with a greater induction of TLSs when compared to Udorn, but both viruses induced TLSs with comparable levels of NP incorporation (Figure 4-7). However, there was no difference in Udorn MPR8 microplaque formation relative to the WT Udorn (Figure 3-9) which correlated with comparable TLS induction between them, despite TLSs induced by Udorn MPR8 being less likely to contain NP (Figure 4-7). Whilst I propose that TLSs may not be able to form or be functional between the confluent cells of the microplaque assay, if we assume they do, this result would suggest that TLS formation is more important than the ability to detect abundant NP within them. This could suggest that TLSs could still deliver IAV viral genomes; seeding infection within the recipient cell, even if NP is poorly incorporated within them, and ultimately NP signal within TLSs could be a poor indicator of whether the structures could traffic infection.

I observed that TLS formation poorly correlated with cell numbers (Figure 4-8), suggesting that if there was an optimal cell distance for TLS formation, it is not a single precise value but instead a broad range of distances. However, since cells were seeded with only gentle rocking to distribute the cells, it was common that a variety of distances existed between them. Therefore, cell density is not the best indicator of whether optimal cell distances exist. A more comprehensive analysis of the data would be required for a more accurate assessment, including measuring all cell distances represented in each field of view and whether TLSs were able to cross these distances. Furthermore, this manner of cell culture enables both the protrusion extension and cell dislodgement mechanism of TLS formation, and it is possible that each of these

mechanisms have a corresponding optimal TLS distance. A technically impressive study by Henderson *et al*. used micropatterning to incrementally increase the distances between individual CAD cells, limiting TLS formation to the protrusion extension mechanism (193). They found that most TLSs formed when cells were separated at a distance of 15 to 30 μm, with a similar percentage of TLS connected micropatterns separated at 15, 20 or 30 μm (193). This supports my findings that suggested a range of cell distances can equally support TLS formation. However, at 40 μm they report a significant reduction in TLS connected micropatterns (193), thereby confirming that longer cell distances can prove challenging for the formation of TLSs that form from protrusion extension. Similar experiments could be performed with infected MDCK cells to determine the intercellular distances that IAV induced TLSs can operate.

Here, I provided the first evidence that TLSs do form at the sites of IAV infections, using an *in vivo* reporter mouse system to demonstrate that TLSs can form from IAV infected cells in the airway epithelium (Figure 4-21, Figure 4-24 & Figure 4-25). This shows that TLSs have the potential to contribute to the within-host spread of IAV infections, and also expands the range of tissues known to be conducive to TLS formation (333). I note that the structures observed were shorter than those seen in some other mammalian tissues, such as solid lung tumours (265). This would be compatible with the previously posed hypothesis that TLS length is limited in tissues with higher cell densities (longer TLSs are reported in the centre of the cornea when compared with the periphery of this tissue, the latter of which has a higher density of cells) (333).

To the best of our knowledge, this is the first demonstration of TLSs within infected, but otherwise normally structured lung tissue, and the first demonstration of these structures being able to form within a layer of epithelium. Quantitation of TLS formation *in vivo* was not possible, due to high levels of variability in both the tissue structure and the distribution of IAV infection across tissue sections, as well as the likelihood of damage to these fragile structures if samples underwent additional staining. Nevertheless, the presence of a number of TLSs within a tissue that undergoes repetitive expansion and deflation suggests a surprising degree of robustness for TLSs in the lung compared to the properties of these structures *in vitro* (202).

Overall, in this chapter I reveal that IAVs induce the formation of TLSs through triggering the onset of apoptosis. I reveal this this cell death response was also required for IAVs to directly spread to distant neighbouring cells, strongly suggesting a functional consequence of TLSs induced by IAV triggered apoptosis. Furthermore, with the observation that TLSs are robustly induced by diverse IAV strains and are present in infected lung tissues, this chapter presents a compelling case for their involvement in the intra-host dissemination of IAVs. This relevance of TLS formation during IAV infection spread underscores the need for a deeper exploration of their broader impact on infection outcome—an inquiry that will be pursued in the following chapter.

Chapter 5

5 Exploring the consequences of infected - uninfected cell interactions beyond virus transmission.

5.1 Introduction

5.1.1 TNT-like structures can be directed towards chemokine producing cells in a process referred to as TLS pathfinding

The consequences of TLSs are largely determined by the cells they connect. Curiously, during the extension of a TLS precursor structure (as part of the protrusion extension mechanism of TLS formation), secreted factors produced by neighbouring cells can establish a concentration gradient of chemokines which guide these structures from the TLS donor toward the TLS recipient cell (235). This process of directional TLS formation is referred to as TLS pathfinding (see 1.4.1.1). The proposed mechanism of TLS pathfinding requires the production of extracellular signalling cues by a subset of cells, distinguishing them as TLS recipients (235). Therefore TLS pathfinding is thought to be context dependent. TLS pathfinding has been demonstrated to occur within homotypic astrocyte cultures as well as cocultures with HEK293 cells. In this instance is was found that TLS pathfinding occurred along a concentration gradient of the small extracellular protein S100A4 (234).

In the context of virus infection, evidence of TLS pathfinding varies and appears to be virus-specific. For example, approximately 50% of TLSs connecting HTLV-1 positive and negative cells in a co-culture originated from the infected cell, confirming the absence of HTLV-1 mediated TLS pathfinding (278). In other cases, directional TLS formation has been observed, for example during vaccinia virus infection – though in this case it was driven by vaccinia virus proteins on cell surfaces which, upon interacting with secondary incoming virions, trigger the growth of TLSs towards uninfected cells (201).

It was unknown if TLS pathfinding is established by IAV infection. Previous research by Kumar *et al.* showed that IAV infected and uninfected A549 cells can be involved in TLS connections, with both infected and uninfected cells observed

originating the TLS (223). However, without a quantitative assessment of TLS origin and receipt, TLS pathfinding during IAV infection remains a possibility. Theoretically, IAV infection could provide the context by which TLS pathfinding occurs, as IAV infected cells produce a wide variety of extracellular signalling molecules, such as interferon (IFN; reviewed in (365, 366)), that ultimately triggers a response in neighbouring cells. I therefore hypothesised that a potential TLS chemoattractant could be amongst the paracrine innate immune signals produced by IAV infected cells. If this was the case, I would expect to observe TLSs preferentially forming from uninfected to infected cells. Such an investigation is important to determine if TLSs preferentially establish cell connections between uninfected and infected cells (increasing the spread of infection). Alternatively, if TLS pathfinding is absent and TLS connections between infected cells are just as likely, this could increase the possibility of superinfection or coinfection (see 1.2.3.3).

5.1.2 TNT-like structures involving healthy cells can rescue stressed cells from apoptosis

A comprehensive understanding of how TLSs influences both the spread of IAV infection and the wider behaviour of the cells in connection, requires an investigation beyond that which focuses only on the trafficking of vRNPs from infected to uninfected cells. The ability of uninfected cells to be in connection with infected cells suggests that the former can deliver cytoplasmic cargo that could impact the latter and the replicating virus. An investigation into whether the transfer of uninfected cellular material might influence viral replication within the infected cell was prompted by the knowledge that TLSs can connect IAV infected and uninfected cells (223), trafficking of cytoplasmic cargo through TLSs during IAV infection is bidirectional (230), and that TLSs connecting healthy and diseased (including virally infected) cells can rescue the latter from apoptosis (264, 271, 339).

Evidence for the role of TLSs in rescuing cells from apoptosis is growing, and TLS connections could represent a major regulator of cell fate decisions, potentially contributing to health and disease. For example, Wang *et al.* cocultured U.V. treated PC12 cells with healthy PC12 cells and found that U.V. stressed cells could be rescued from apoptosis (339). The authors found that when TLS

formation was inhibited with cytochalasin B, the healthy PC12 cells were no longer able to rescue the U.V. treated cells, supporting a function of TLSs in conferring this phenotype. Interestingly, the authors found that the stressed cells formed TLSs and that these structures contained microtubules in addition to F-actin. It was then found that this rescuing effect was dependent on the U.V. treated cells having lost cytochrome c without yet entering the execution phase of apoptosis, characterised by the activation of caspase-3 (339).

Liu *et al.* showed that human umbilical vein endothelial cells (HUVEC) treated with oxygen glucose deprivation (OGD) and reoxygenation (RO) could be rescued from apoptosis when cocultured with mesenchymal stem cell (MSCs) (264). Treatment of the cocultures with either latrunculin-A or annexin V reduced TLS formation and correlated with a decrease in the ability of MSCs to rescue HUVECs from apoptosis (264). This again implicates TLSs in regulating apoptosis within stressed cells, with paracrine secreted factors (still produced even when TLSs are inhibited) seemingly not relevant for this phenotype. Contrary to the aforementioned work by Wang *et al.*, this rescuing effect of HUVECs was seemingly able to occur, or even dependent upon the later stages of apoptosis (post caspase activation) (264, 339). Coating of phosphatidylserine with annexin V was found to inhibit both TLS formation and the subsequent suppression of HUVEC apoptosis (264). Annexin V coats phosphatidylserine when it is presented on the outer leaflet of the plasma membrane, which is a hallmark of late stages of apoptosis. Therefore, this implicates a role of the late stages of apoptosis in MSC TLS mediated suppression of apoptosis within HUVECs.

In the context of virus infection, similar findings were reported following PRRSV induced apoptosis of porcine umbilical cord stem cells (271). When infected cells were cocultured with mock-infected cells, the proportion of infected cells that were apoptotic was reduced compared to infected cells kept in monoculture. This effect was somewhat reversed when the infected/mock coculture was treated with the TLS inhibiting drug cytochalasin D (271). This therefore provides evidence that apoptosis induced from viral infection, can be rescued through TLS mediated cell interactions with neighbouring uninfected cells. Furthermore, the regulation of apoptosis by PRRSV infection is thought to be important for supporting virus replication, initially suppressing this cell death response to facilitate accumulation of more viral copies (367, 368). PRRSV infection has been

found to induce TLSs, and these studies reveal that these TLSs can both facilitate viral spread and suppress apoptosis (271, 290). This dual role suggests that induced TLSs may robustly regulate virus replication within multiple cells (prolonging virus replication within the initially infected cell and seeding infection within a neighbour), in a way that could also apply to other viruses capable of inducing TLSs.

IAV is an example of another virus that has been shown to modulate apoptosis in ways that can benefit virus propagation (340, 355). The induction of functional TLSs by IAVs (222, 223, 230), suggests that TLSs could also be used for this regulation of apoptosis within IAV infected cells. Additionally, my earlier findings in chapter 4 revealed a requirement for IAV mediated activation of apoptosis, suggesting that TLSs may form to directly suppress this cell death response and could represent a routine function of TLSs beyond trafficking infection.

5.1.3 TNT-like structures suppress apoptosis by delivering mitochondria from healthy to stressed cells

Mitochondria are master regulators of apoptosis, harnessing pro-apoptotic factors (e.g. Bcl-2), and maintaining reactive oxygen species (ROS) homeostasis (369). Therefore, it is perhaps unsurprising that studies that report a role of TLSs in suppressing apoptosis within stressed or diseased cells, correlated this phenotype with the trafficking of mitochondria from the healthy cells (264, 271, 339). It is generally believed that the trafficking of entire organelles (such as mitochondria) through TLSs, requires them to also contain microtubules alongside F-actin. Indeed thicker, microtubule containing TLSs were observed by Wang *et al.* and the authors found that these TLSs incorporated and trafficked mitochondria from healthy PC12 cells to U.V. stressed cells (339). When mitochondria trafficking through TLSs was inhibited, or mitochondria rendered defective by sustained culturing in ethidium bromide (mutating and depleting mitochondrial DNA), apoptosis was no longer suppressed (339).

Similar approaches were used by Liu *et al.*, also demonstrating that TLS dependent mitochondria trafficking from MSCs to stressed HUVECs restored oxygen consumption rates and decreased the extracellular acidification rate,

indicating the delivery of functional mitochondria (264). Interestingly, the authors found that mitochondria trafficking was bidirectional between healthy MSCs and HUVECs in coculture, with similar percentages of cells with mitochondria of both cell types (264). However, when MSCs where cocultured with stressed HUVECs there was a significant increase in both TLS formation and the percentage of HUVECs with mitochondria of MSCs (264). The finding that the percentage of MSCs with mitochondria of stressed HUVECs did not also increase suggests that mitochondrial trafficking switches from bidirectional to unidirectional when HUVECs become stressed and apoptotic (264).

During PRRSV infection, live cell microscopy showed mitochondria transiting from healthy cells to infected macrophages through TLSs (271). Additionally, it was shown that this trafficking of functional mitochondria could also rescue infected cells from necrosis as well as apoptosis (271). Interestingly, mitochondrial membranes were found to incorporate a range of PRRSV proteins (nsp1α, nsp1β, nsp4, and N) and Guo *et al*. propose that mitochondrial trafficking through TLSs could be a way in which these viral proteins are transported to neighbouring cells in large quantities (271). However, in order for the healthy cells to both donate apoptosis suppressing mitochondria and receive viral protein containing mitochondria, mitochondrial trafficking would have to be bidirectional. Such a requirement is challenged by Liu *et al*. who reported predominately unidirectional trafficking from healthy to stressed cells (264). The influence of cell type and cell stress verses infection has an unknown effect of TLS trafficking directionality and evidence for bidirectional trafficking of cytoplasmic cargo through TLSs has been reported following IAV infection (230). Therefore, the possibility of bidirectional mitochondrial exchange specifically during virus infection remains a possibility that should be explored.

Overall, mounting evidence suggests that TLSs (including those that are formed from a virus infection) can suppress apoptosis within diseased or infected cells specifically through the transfer of mitochondria from healthy cells. This trafficking of mitochondria could be performed in parallel, or synonymously, with the intercellular spread of infection. It is currently unknown if IAV induced TLSs traffic mitochondria, and whether mitochondrial exchange between uninfected and infected cells in coculture occurs, is elevated or is unidirectional.

5.1.4 Chapter aims

Although TLS trafficking during IAV infection has primarily been studied in the context of viral spread, the tendency for uninfected cells to initiate and receive TLSs—and the downstream consequences of these interactions beyond viral genome transfer—remains largely unexplored.

Therefore, in this chapter I aim to:

1. Assess how a cell's infection status affects its propensity to initiate or receive TLSs, i.e. TLS pathfinding during IAV infection.

2. Assess whether uninfected cells can suppress apoptosis within IAV infected cells through the formation of TLSs.

3. Quantify and compare the rates of mitochondrial exchange between IAV infected and uninfected cells.

5.2 Results

5.2.1 Determining how IAV infection influences the cellular origin and receipt of tunnelling-nanotube like structures.

Investigating TLS directionality, and how IAV infection could drive this, required an *in vitro* system that differentiated between the membranes of neighbouring cells. With this aim, I first tested the lipophilic dyes 1,1'-dioctadecyl-3,3,3',3'-tetramethylindodicarbocyanine perchlorate (DiD) and 3,3'-dioctadecyloxacarbocyanine perchlorate (DiO). The Vybrant DiD and DiO dyes was selected as they are well tolerated by cells (i.e. low cytotoxicity) and are well retained within cells with infrequent transfer between differently labelled monocyte and lymphocytes in coculture up to 120 hours (370). Therefore, I hypothesised that when DiD and DiO labelled MDCK cells were cocultured together and infected at a low MOI, the cell membranes would be uniquely DiD or DiO positive and the cellular origin of TLSs connecting DiD and DiO cells could be determined by the membrane fluorescence of the intercellular connecting structure. This then could allow me to assess if IAV infected cells disproportionately originated or received the TLS.

I first attempted to optimise Vybrant lipophilic dye staining for MDCK cells by testing a range of incubation times (ranging from 5 to 20 minutes) with the dyes at a concentration of either 0.5x or 1x (Figure 5-1). Unexpectedly, I found that at all conditions tested the lipophilic dye signal was mostly punctate and present within cells, as opposed to being present at the cell membrane, the boundaries of which were clearly marked with the F-actin stain phalloidin (Figure 5-1). This suggests that in MDCK cells these dyes accumulate on intracellular membranes, as opposed to on the plasma membrane. Furthermore, I frequently found cells positive for both DiD and DiO signal, which was most pronounced at the higher concentration (1x) and at the shorter incubation times (5 to 10 minutes) during the initial cell staining step (Figure 5-1). Therefore, with the lack of a continuous plasma membrane stain and the frequent intercellular exchange of labelled material, it made the identification of cellular TLS origin and receipt unreliable or even impossible.

Inspired by previous research looking at TLS directionality (259, 278), I selected a premade lentivirus from TakaraBio, which when used to transduce cells leads to the stable expression of the *Aequorea coerulescens* Green Fluorescent Protein (AcGFP) fluorophore. The AcGFP is fused to the N-terminal 20 amino acids of the protein neuromodulin, the latter of which contains a palmitoylation site targeting it to the inner leaflet of the plasma membrane (304). Using this lentivirus, I transduced both MDCK and A549 cells and selected for the expressing cells with puromycin. Both cell lines were passaged in parallel with mock transduced cells until the latter died from the puromycin treatment.

I then wanted to see whether this method of membrane labelling enabled me to distinguish between AcGFP positive and negative cells during IAV infection, and whether this could be done over multiple cell passages. To assess this I cocultured WT and AcGFP labelled MDCK or A549 cells and infected at a low MOI, either as soon as the mock transduced cells died (passage X) or after two more cell passages (passage X+2) (Figure 5-2). At passage X, I found that both MDCK and A549 AcGFP expressing cells could be distinguished through robust expression of the AcGFP fluorophore, with no WT cells containing any AcGFP signal above background (Figure 5-2). Additionally, and in contrast with the lipophilic dyes, the AcGFP label seemed to match the cell boundaries as demonstrated by the F-actin stain, as well as containing some punctate

intracellular signal (Figure 5-2). Whilst I observed similar results at passage X+2 with A549s, the expression of AcGFP within MDCK cells appeared to dramatically drop, with the contrast between transduced and WT cells minimal or absent (Figure 5-2). Therefore, A549 AcGFP cells represented the much more stable cell type and would enable me to investigate TLS directionality. Importantly, A549 cells are a common *in vitro* model for the study of lung epithelial cell IAV infection, and can mount an innate immune response (371). Furthermore, A549s have been seen to be involved in TLS connections, with both infected and uninfected cells being able to produce TLSs (223), making this cell type appropriate for the quantitative study of TLS directionality and pathfinding during IAV infection.

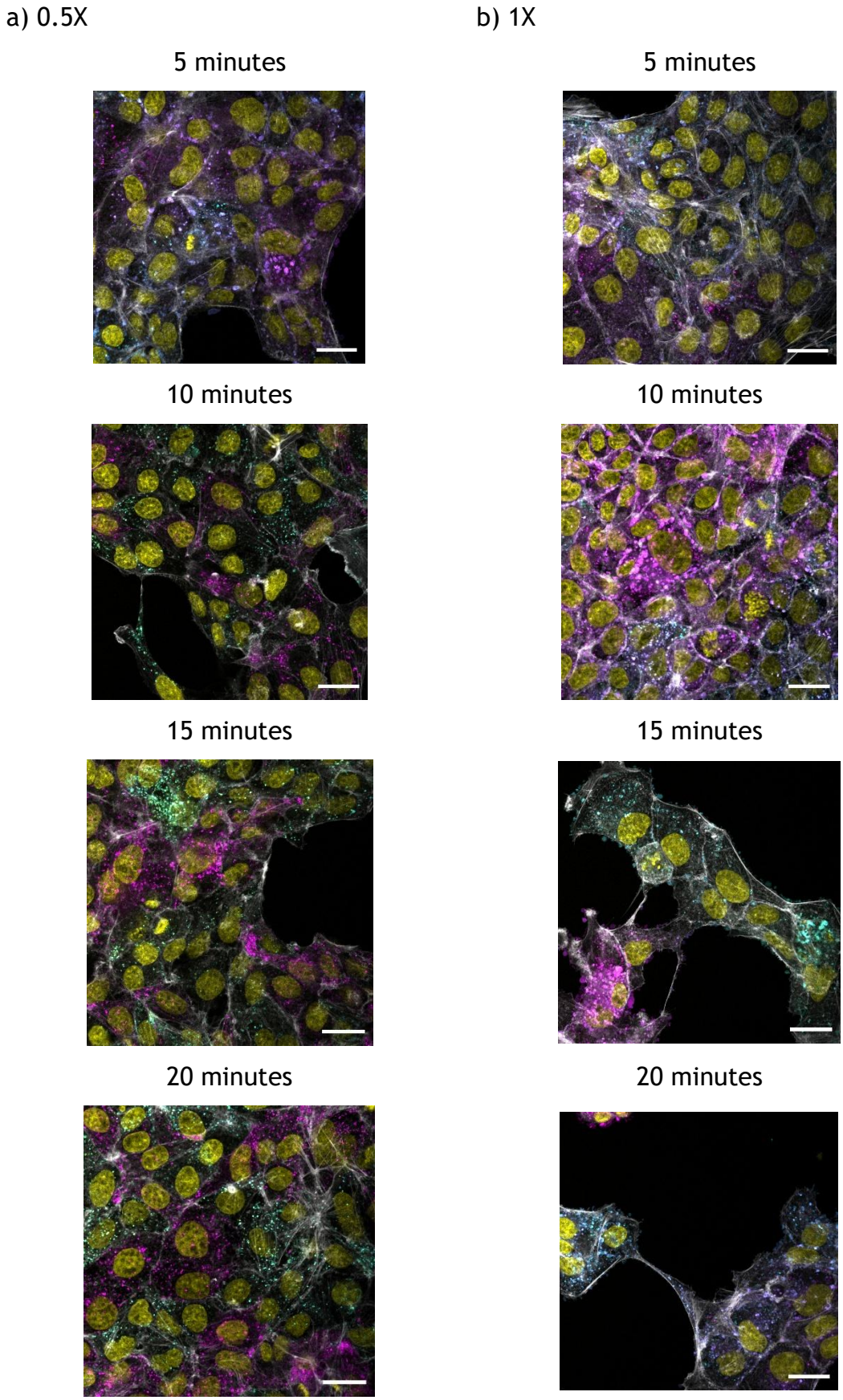

Figure 5-1: Effect of lipophilic dye concentration and duration of staining on membrane labelling. MDCKs stained with DiO or DiO at either 0.5x (a) or 1x (b) at 5-minute increasing time intervals. Cells were cocultured and infected with PR8 at an MOI of 0.6 PFU/cell 16 hours after seeding onto coverslips. Cells were fixed approximately 6 hours post infection and imaged using super resolution confocal microscopy. Vybrant DiO (blue), DiI (magenta), nuclei (yellow), F-actin (white). Scale bars = 20 μm.

a) MDCKs

Passage X

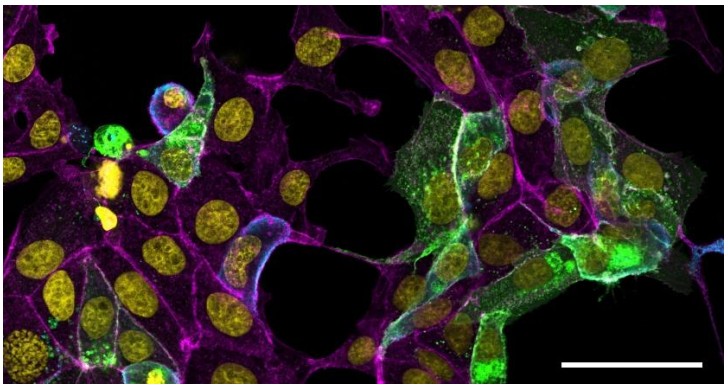

Passage X+2

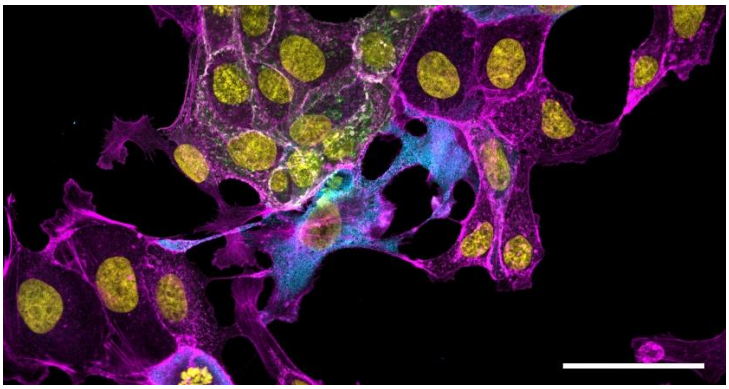

b) A549s

Passage X

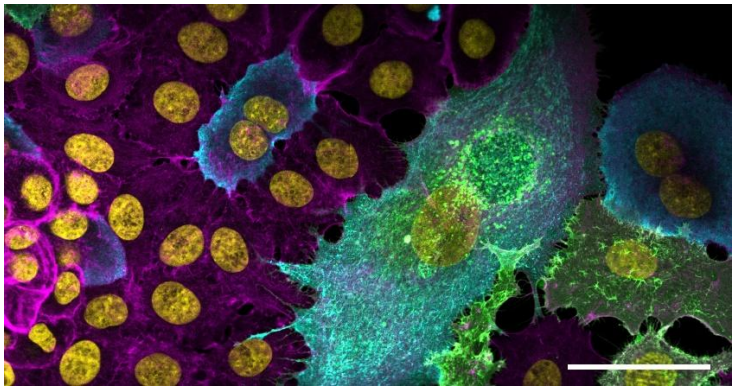

Passage X+2

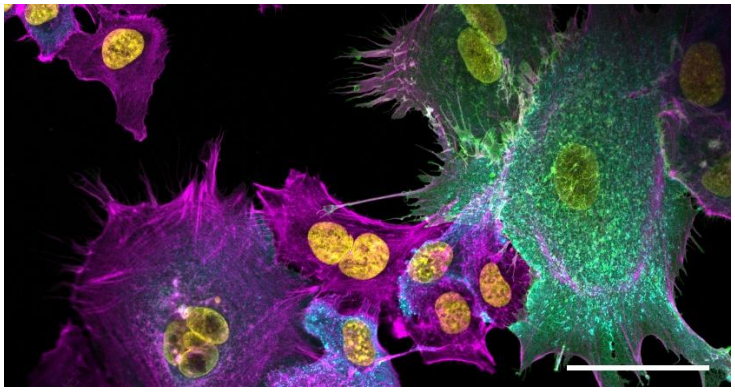

Figure 5-2: The retention of the AcGFP membrane label following MDCK and A549 passaging. Super resolution confocal micrographs of lentivirus transduced MDCK (a) and A549 (b) cells expressing a membrane targeted AcGFP fluorophore. Cells were first imaged after a series of passages in complete media supplemented with Puromycin. Once selection of transduced cells was complete, cells were seeded onto coverslips and infected with PR8 at an MOI of 0.5 PFU/cell for 16 hours (Passage X). The cells were then passaged twice, and infected as before (Passage X+2).

Subconfluent A549 cells expressing AcGFP were cocultured with wild-type cells at a 1:1 ratio and imaged following infection at an MOI calibrated to infect no more than 50% of the population. I observed that heterotypic cell pairs (involving WT and AcGFP positive cells) could be connected with a TLS (Figure 5-3). The membrane fluorescence of these structures was typically homogenous, that is to say that the TLSs were either completely GFP positive or negative throughout its entire length (Figure 5-3). Furthermore, approximately 50% of TLSs observed were AcGFP positive, meaning that modification of cell membranes with AcGFP labelling did not increase the cell's ability to form TLSs (Figure 5-4). With the exception of the occasional small, localised region of AcGFP labelled membrane in the recipient WT cells at the point of TLS contact, the heterotypic cell pairs were clearly distinguished from each other through the difference in membrane label and TLS origin could be confidently reported (Figure 5-3). Importantly, I observed that GFP-positive cells constituted roughly half of the coculture, and among the infected population, a similar proportion exhibited GFP expression (Figure 5-4). This demonstrates that modified A549s retained the membrane label well enough to be distinguished from WT cells across replicates and displayed the same susceptibility to IAV infection as WT cells. These observations validated the use of this *in vitro* system for the quantification of TLS cellular origin and receipt.

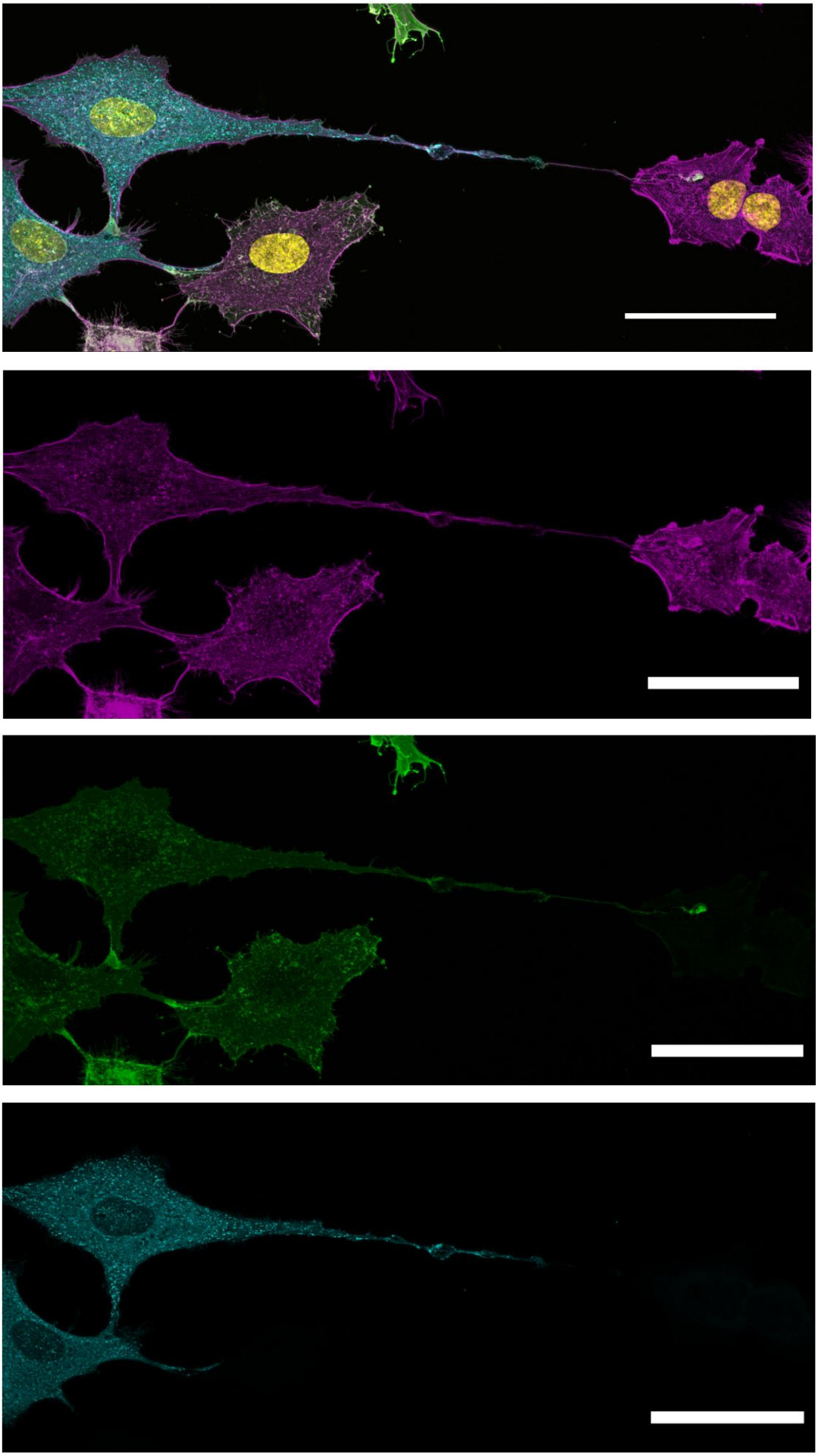

Figure 5-3: A549 AcGFP cells enables the origin of TLSs to be determined. A TLS structure forming from a PR8 infected (16 hours post infection), AcGFP membrane labelled A549 cell, connecting to an uninfected, WT A549 cell. Nuclei (yellow), F-actin (magenta), AcGFP (green), NP (blue). Scale bar = 50 μm.

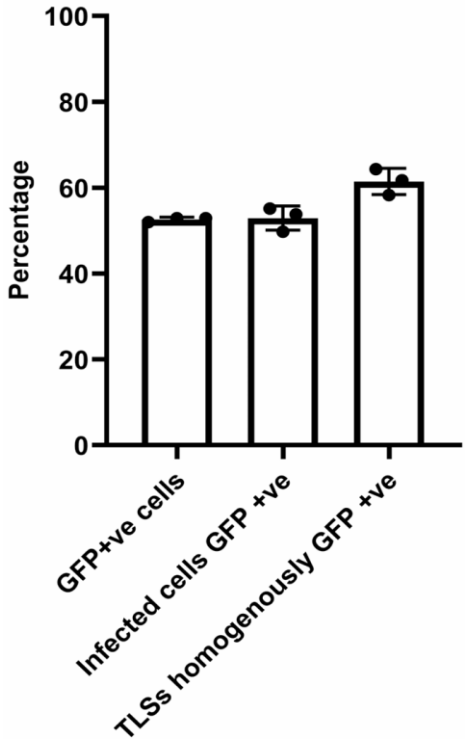

Figure 5-4: A549 AcGFP cells demonstrate similar properties to WT A549 in infected coculture. A549 AcGFP1 cells cocultured with WT A549 cells at a ratio of 1:1 and infected with PR8 at an MOI of 2.5 PFU/cell. At 16 hours post infection the cells were fixed and immunostained for NP. Following manual assessment of micrographs, the percentage of cells in coculture that were GFP positive (i.e. A549 AcGFP), GFP positive and infected and the percentage of TLS consisting of GFP labelled membrane throughout its length was determined. The means and standard deviations of three biological replicates are shown.

In this *in vitro* system, the low MOI infection condition is expected to exert an influence on all cells through the production of extracellular signalling molecules. My hypothesis that IAV infected cells produce innate immune signals that could function as TLS chemoattractants, would mean that TLSs should be observed to be preferentially forming from uninfected cells and be received by infected cells. This required the quantitation of how infection status influenced both TLS origin and receipt. I first examined TLS origin by calculating the proportion of uninfected and infected cells producing a TLS. I found no significant difference between TLSs originating from either infected or uninfected cells (Figure 5-5 a). Therefore, under the low MOI infection conditions of this assay, where not all cells were infected, the infection status of individual A549 cells did not determine their ability to initiate a TLS.

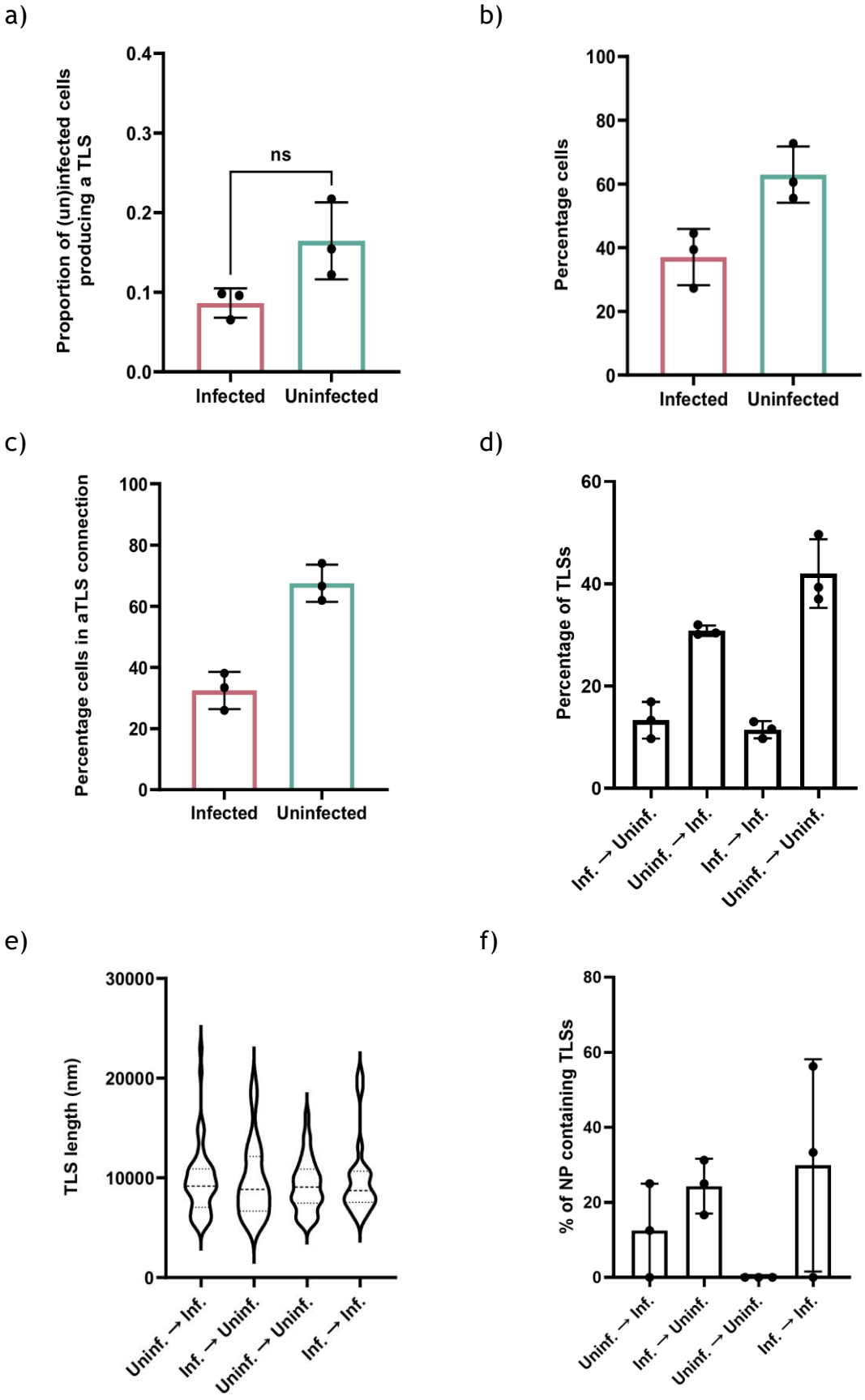

Figure 5-5: Infected and uninfected A549 cells both initiate and are contacted by TLSs at similar frequencies in co-cultures. (a) The proportion of uninfected and infected cells producing a TLS in a low MOI infection. The difference between the proportions of uninfected and infected cells that produced a TLS was tested for significance by Mann-Whitney test (n.s. $p > 0.05$). (b) The percentage of co-cultured cells that were infected or uninfected and (c) the percentage of cells of infected or uninfected cells involved in a TLS connection. (d) Percentage of TLSs originating from and being received by an infected or uninfected cell. Data were collected from connected pairs of

WT and AcGFP membrane labelled A549 cells (i.e. heterotypic cell pairs). (e) The length of TLSs connecting cells with either an asymmetric or symmetric infection status, shown as violin plots with the median and the upper and lower quartile values indicated by dashed lines. Differences in mean TLS length was tested for significance by Kruskal-Wallis test (ns $p > 0.05$). (f) The percentage of TLSs connecting cells with either an asymmetric or symmetric infection status, that contained NP. For all data, the mean and SD is shown (n = 3).

These observations of TLS origin suggested that the likelihood of uninfected and infected cells being involved in a TLS connection would be proportional to their abundance. According to NP staining, 37% of cells in the co-culture were infected and 63% uninfected (Figure 5-5 b). This was reflected in the proportion of cells involved in a TLS that were infected (Figure 5-5 c), which suggests that TLSs were not preferentially originating from or contacting infected or uninfected cells. I then focused on TLS connections between heterotypic cell pairs (connected WT and AcGFP labelled cells) as this allowed us to correlate TLS directionality to the infection status of donor and recipient cells (Figure 5-5 d). Just under 50% of heterotypic cell pairs displayed an asymmetric infection (i.e. infected and uninfected cells connected by a TLS), and of these TLS connections approximately 70% were being initiated by the uninfected cell and received by the infected cell (Figure 5-5 d). This was once again consistent with the proportion of uninfected cells in the assay (Figure 5-5 b).

This data therefore suggested that TLS directionality between infected and uninfected cells arises purely from the relative abundance of each. To further develop this argument, I modelled the directional interactions between uninfected and infected cells assuming no influence of IAV infection on TLS receipt and even distribution of infection. With uninfected cells comprising 63% of the population and infected cells 37%, the fractions are defined as:

$$f_U = 0.63$$

$$f_I = 0.37$$

The probability of an asymmetric pairing between one uninfected and one infected cell is given by:

$$P_{heterotypic} = 2 f_U f_I = 2 \times 0.63 \times 0.37 = 0.4662$$

With both infected and uninfected cells equally capable of initiating a TLS (Figure 5-5 a), the probability that the interaction is initiated by an uninfected cell and received by the infected cells is:

$$P_{U\rightarrow I} = P_{heterotypic} \times f_U = 0.4662 \times 0.63 = 0.2937 = 29.4\%$$

Conversely, the probability that an infected cell initiates the interaction is:

$$P_{I\rightarrow U} = P_{heterotypic} \times f_I = 0.4662 \times 0.37 = 0.1725 = 17.3\%$$

These probabilistic estimates closely matched our experimental observations, with approximately 30% of TLSs initiated by uninfected cells and received by infected cells, and 13.5% arising from the opposite direction (Figure 5-5 d). This strongly suggests that infected and uninfected cell interactions via TLSs is determined by their abundance and distribution as opposed to showing any preference in TLS origin or receipt according to infection status of individual cells.

Together, these data indicate that under these low MOI infection conditions *in vitro*, TLS pathfinding is not observed between individual cells displaying an asymmetric infection. Therefore, the extracellular signals produced by an IAV infected cell are seemingly not functioning as TLS chemoattractants. Additionally, I observed no difference in the average length of TLSs between the different types of cell pairings (Figure 5-5 e) and there was no obvious consequence of TLS directionality (with the obvious exception of Uninfected→ Uninfected) on the likelihood that NP was incorporated within the TLS (Figure 5-5 f). This suggests that the range over which cells can be connected by TLSs and the likelihood that they can traffic infection is not determined by the infection status of either the TLS donor or recipient cell.

5.2.2 Assessing how uninfected cell proximity and tunnelling-nanotube like structure formation regulates apoptosis within IAV infected cells.

The demonstration that uninfected cells can be in connection with infected cells supports the role of TLSs in spreading infection. However, evidence also suggests

that TLS trafficking, including that during IAV infection, can be bidirectional (230). This raises the important question as to how the trafficking of cargo from the uninfected cell could be influencing the infected cell and the replicating virus within. Research of stressed or infected cells have pointed towards a role of healthy cells in suppressing apoptosis within the former through trafficking of cargo through TNTs (see 5.1.2). I was therefore curious whether uninfected cells could suppress apoptosis within IAV infected cells through TLS connections. This is especially pertinent given also my discovery of a role for apoptosis in triggering the induction of TLSs following IAV infection (see 4.2.3).

With the aim of determining whether uninfected cells could suppress apoptosis of IAV infected cells through cell to cell interactions (including long-range TLSs), I infected subconfluent MDCK cells at increasing MOIs up to an MOI of 1 fluorescent forming unit per cell (FFU/cell). A maximum MOI of 1 FFU/cell was selected, and zanamivir included, to reduce the likelihood that a single cell could receive more than one copy of the viral genome during the course of the infection, which could accelerate the induction of apoptosis. I then assessed how the increase in MOI, and the corresponding decrease in the proportion of uninfected cells, influenced the percentage of infected cells that were apoptotic (measured as cells that were active caspase 3/7 positive). As the MOI was increased, so did the percentage of individual infected cells that were apoptotic, up to an MOI of 0.75 FFU/cell, after which the levels plateaued but the increase became statistically significant. This inverse correlation between the proportion of uninfected cells, and the percentage of individual infected cells positive for active caspase 3/7 suggests that the induction, or progression of the apoptotic pathway can be suppressed or reversed by the availability of abundant neighbouring uninfected cells. The likelihood of individual infected cells being apoptotic peaked from an MOI of 0.75 FFU/cell, at which point ≥50% of cells were infected. This suggests that the ability of uninfected cells to provide any suppression of apoptosis requires them to be in the majority.

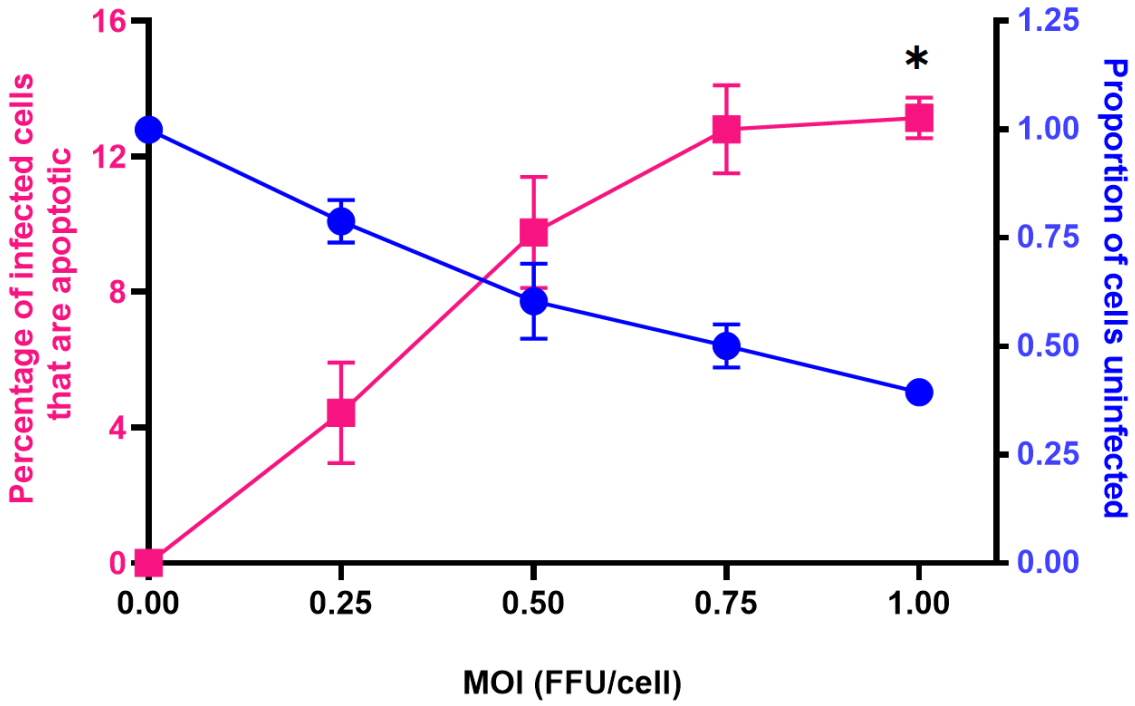

Figure 5-6: Increasing MOI increases the percentage of infected cells that are positive for active caspase 3/7. Subconfluent MDCK cells, within 24 well plates, were infected with BrightFlu ZsGreen at increasing MOIs, up to an MOI of 1 FFU/cell. Cells were infected for 16 hours and in the presence of 0.36 mM zanamivir, after which 1x Caspase 3/7 detection reagent was added to the overlay and incubated for 2 hours prior to imaging. Hoescht 33342 was added at a concentration of 5 µg/mL 20 minutes before imaging. Cells were imaged live on the Nexcelom Celigo imaging cytometer and data analysed with FlowJo as before. The proportion of cells negative for ZsGreen (i.e. uninfected), and the percentage of cells positive for both ZsGreen and active Caspase 3/7 (i.e. infected and apoptotic) was calculated and the results, including the mean and standard deviation across three biological replicates is shown. Differences between the percentage of cells infected and apoptotic at each MOI was tested for significance by One-Way ANOVA Friedman test (n.s. $p > 0.05$, * $p < 0.05$).

Curious about the potential involvement of TLSs connecting uninfected and infected cells in suppressing apoptosis within this assay, I then repeated this titration in the presence of TLS inhibiting drugs taxol and IPA-3 (Figure 5-7). I found that both IPA-3 and taxol resulted in a slightly higher proportion of cells uninfected, however this difference was not statistically significant from the DMSO control at each MOI tested, confirming that these drugs are not noticeably antiviral (Figure 5-7 a). However, I found that both drugs reduced the percentage of individual infected cells that were apoptotic at MOIs of 0.25 to 0.5 FFU/cell, and in the case of taxol this was also seen at an MOI of 0.75 FFU/cell, with the reduction being significant at MOIs of 0.5 and 0.75 FFU/cell (Figure 5-7 b).

It was possible that these drugs could be supressing apoptosis separately from their inhibition of TLSs and to assess this I compared the percentage of mock infected cells positive for active caspase 3/7 across drug treatments. In the

absence of infection, TLSs are infrequently observed (Figure 4-7) and therefore, any reduction in caspase 3/7 activation from these drugs is likely separate from the inhibition of TLSs. In the absence of drugs, an average of 3% of cells were positive for active caspase 3/7, whereas IPA-3 reduced this to an average of 0.6%, and taxol caused a slight increase with an average of 4.4% of cells active caspase 3/7 positive (Figure 5-7 c). In light of this, it is possible that the reduction seen with IPA-3 could be an anti-apoptotic effect of this drug. However, this can not explain the significant reduction seen with taxol. It is unclear how these drugs are suppressing apoptosis, and as to why this suppression is only seen at MOIs less than 1 FFU/cell (Figure 5-7 b). With apoptosis being required for the induction of TLS formation following IAV infection, it is possible that the suppression of apoptosis by these drugs, whether directly (seemingly done by IPA-3, Figure 5-7) or indirectly (by taxol, Figure 5-7), could contribute to the mechanism behind how these drugs inhibit the formation of TLSs. However, the lack of a difference at an MOI of 1 FFU/cell between these drug suggests that this is unlikely. Overall, this data does not provide evidence for the involvement of TLSs in the suppression of apoptosis within infected cells, however, further experimentation is required, particularly into how these drugs effect apoptosis in the absence of infection.

a)

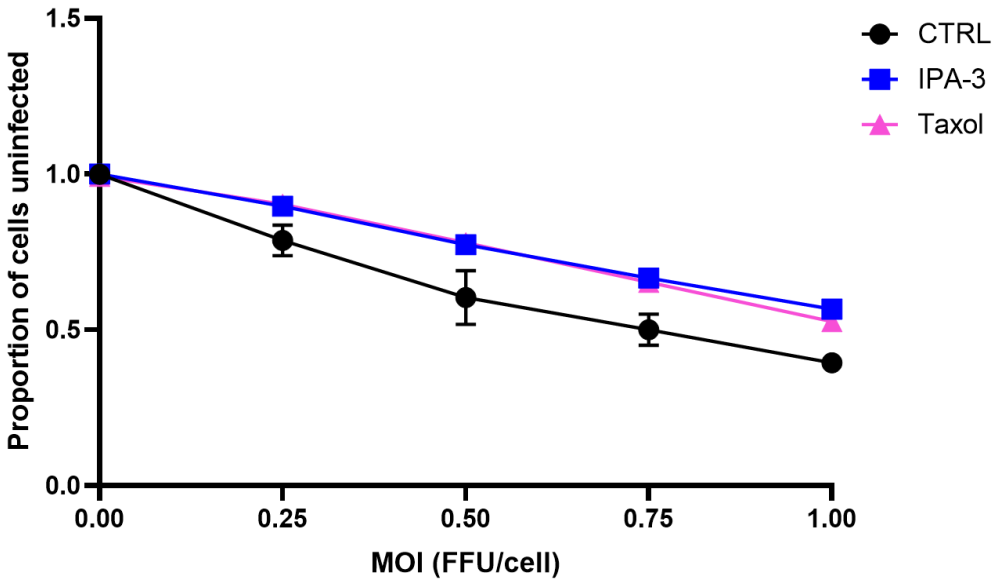
CTRL
IPA-3
Taxol
Proportion of cells uninfected
1.5
1.0
0.5
0.0
0.00
0.25
0.50
0.75
1.00
MOI (FFU/cell)

b)

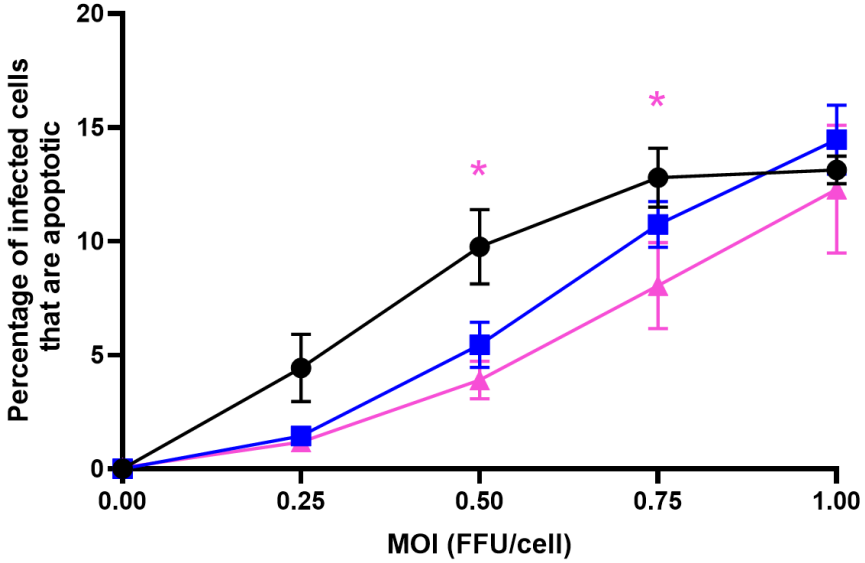
Percentage of infected cells that are apoptotic
20
15
10
5
0
*
*
0.00
0.25
0.50
0.75
1.00
MOI (FFU/cell)

c)

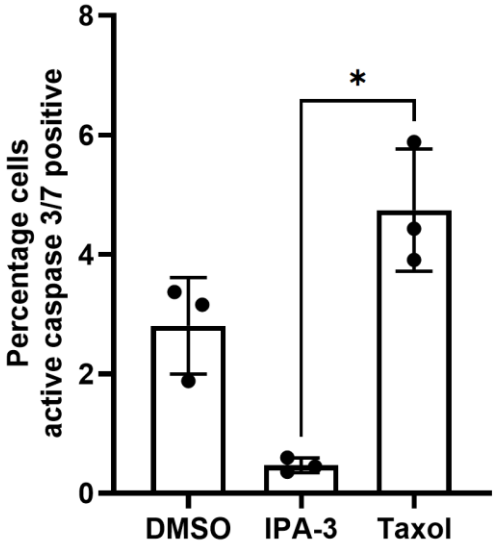
Percentage cells active caspase 3/7 positive
8
6
4
2
0
*
DMSO
IPA-3
Taxol

Figure 5-7: TLS inhibiting drugs reduce the percentage of infected cells that are apoptotic. Subconfluent MDCK cells, within 24 well plates, were infected with BrightFlu ZsGreen at increasing MOIs, up to an MOI of 1 FFU/cell. Cells were infected for 16 hours and in the presence of 0.36 mM zanamivir and either DMSO, 3 μM IPA-3, or 100 μM taxol. 1x Caspase 3/7 detection reagent was then added to the overlay and incubated for 2 hours prior to imaging. Hoescht 33342 was added at a concentration of 5 μg/mL 20 minutes before imaging. Cells were imaged live on the Nexcelom Celigo imaging cytometer and data analysed with FlowJo as before. (a) The proportion of cells negative for ZsGreen (i.e. uninfected), and (b) the percentage of cells positive for both ZsGreen and active Caspase 3/7 (i.e. infected and apoptotic) was calculated and the results, including the mean and standard deviation across three biological replicates is shown. Differences between the percentage of cells infected and apoptotic at each MOI between drug treatments was tested for significance by One-Way ANOVA Kruskal-Wallis test (n.s. $p > 0.05$, * $p < 0.05$). (c) The percentage of mock infected cells that were positive for active caspase 3/7 either in the presence of DMSO, IPA-3 or taxol. Differences were tested for significance by One-Way ANOVA Kruskal-Wallis test (n.s. $p > 0.05$, * $p < 0.05$).

This data, and the uncertainty of the effects of TLS inhibiting drugs, required a simplification of the question. Therefore, I asked whether the suppression of apoptosis seen at lower MOIs (Figure 5-6) required the ability of the uninfected cells to directly interact with the infected cells. The most notable suppression of apoptosis within infected cells of a monolayer was seen at an MOI of 0.25 FFU/cell (Figure 5-8 a). Taking the proportion of infected cells seen at this MOI, I then seeded the bottom of two wells. Within one of these wells I placed a transwell insert seeded with the proportion of cells that were uninfected at an MOI of 0.25 FFU/cell. The transwell insert contained a pore size of 3 μm which allowed small proteins like cytokines to freely diffuse through, whilst preventing uninfected – infected cell contacts, including those achieved by TLSs. I then looked to see whether the presence of these physically separated uninfected cells were still able to suppress apoptosis within the infected cells below. I found comparable levels of infected and apoptotic cells regardless of the presence or absence of the uninfected cell containing transwell insert (Figure 5-8 b). This data therefore confirm that it was the uninfected cells that suppressed apoptosis within infected cells of a monolayer and that this suppression requires the ability of the uninfected cells to directly interact with the uninfected cells.

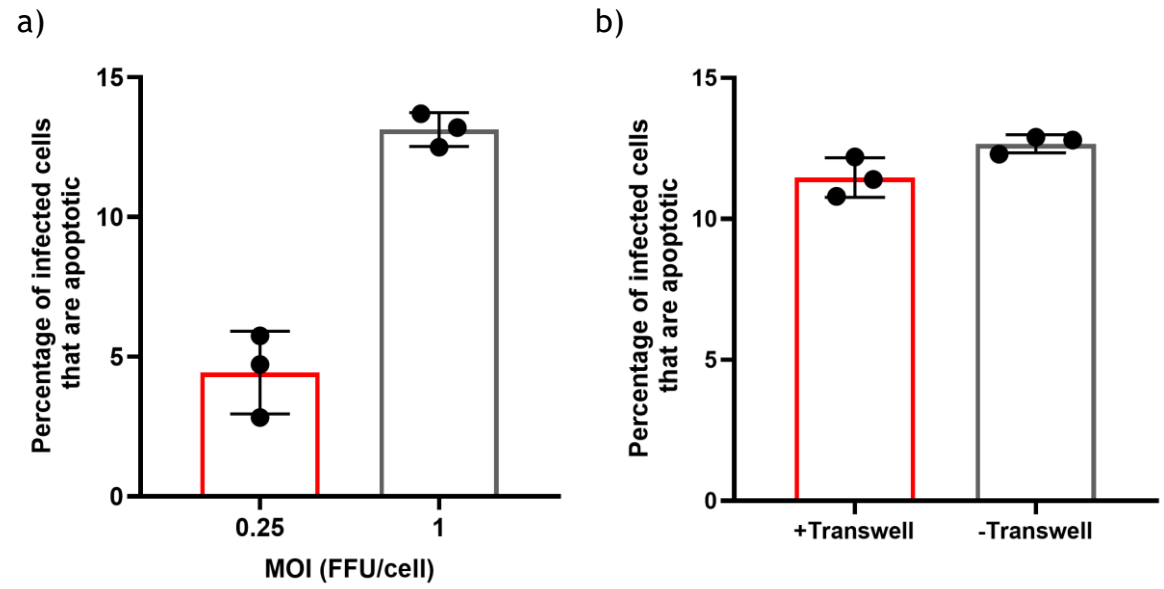

Figure 5-8: Uninfected cells can supress apoptosis within infected cells when they are able to form direct cell to cell contacts. (a)The percentage of infected cells that were positive for active caspase 3/7 (i.e. infected and apoptotic), at either an MOI of 0.25 or 1 FFU/cell. Data are replotted from figure 5-6. (b) The proportion of cells that were uninfected at an MOI of 0.25 was seeded into a transwell insert (12mm polycarbonate membrane inserts with 3µm pores) and placed over the proportion of cells infected with BrightFlu ZsGreen. In parallel, a well containing only the infected cells, in the absence of any uninfected cell containing transwell insert was included. For both culturing conditions the cells were infected for 16 hours and in the presence of 0.36 mM zanamivir. All infections were performed for 16 hours and in the presence of 0.36 mM zanamivir. After which 1x Caspase 3/7 detection reagent was added to the overlay and incubated for 2 hours prior to imaging. Hoescht 33342 was added at a concentration of 5 µg/mL 20 minutes before imaging. Cells were imaged live on the Nexcelom Celigo imaging cytometer and data analysed with FlowJo as before. For all conditions, the mean and standard deviation are shown (n = 3).

5.2.3 Exploring the intercellular transfer of mitochondria during IAV infection.

Whilst I could not conclude that TLSs were responsible for uninfected cell mediated suppression of apoptosis within IAV infected cells, the requirement of direct cell to cell contacts maintains the possibility of a role of membrane interactions and TLSs. Research has revealed that the rescue of stressed/infected cells could be facilitated by TNTs through the delivery of mitochondria from healthy cells (267, 271). I therefore hypothesised that the suppression of IAV induced apoptosis by uninfected cells was being mediated by the intercellular transfer of mitochondria through TLSs or other membrane fusion events. To test the feasibility of TLS mediated mitochondria trafficking between MDCK cells I first assessed whether mitochondria was incorporated within TLSs connecting IAV infected cells (Figure 5-9). Using super resolution confocal microscopy of IAV infected, subconfluent MDCK cells labelled with MitoTracker stain, I observed labelled mitochondria alongside NP within TLSs (Figure 5-9). Mitochondria was visible along the length of TLSs indicating that

mitochondria could be incorporated and trafficked towards neighbouring MDCK cells (Figure 5-9). The detection of NP alongside mitochondria within TLSs suggests that mitochondrial exchange and infection spread can occur simultaneously, supporting the idea that the consequences of TLSs extends beyond its demonstrated role in IAV direct cell to cell spread.

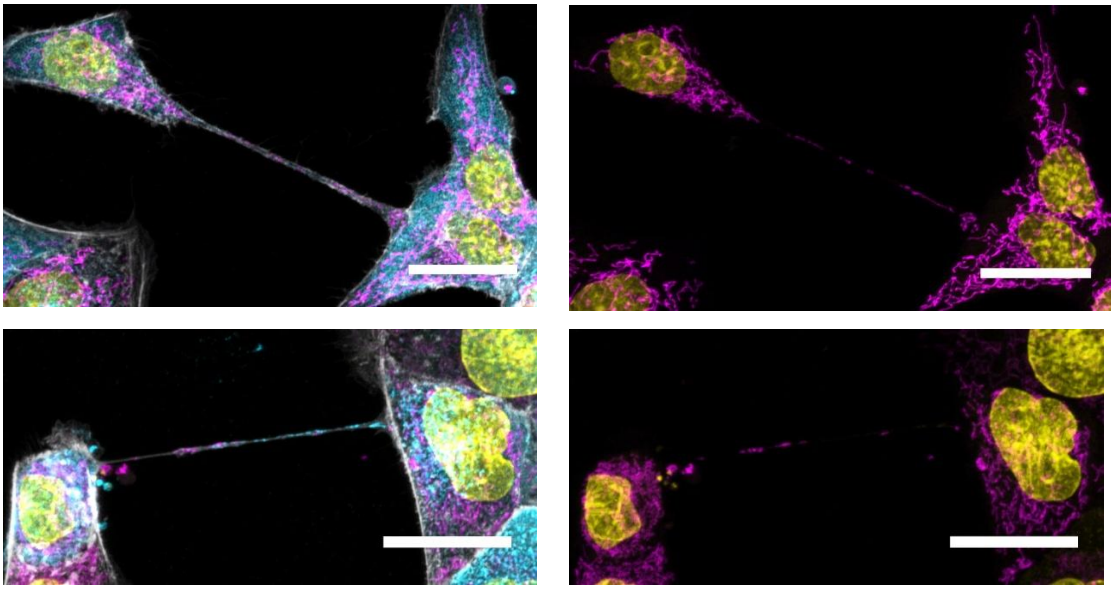

Figure 5-9: Mitochondria can be detected within TNT-like structures connecting IAV infected MDCK cells. Subconfluent MDCK cells, seeded onto coverslips, were stained with MitoTracker Red CMXRos diluted 1:1000 in SFM by incubating at 37°C for 1 hour. Stained cells were then infected with PR8 at an MOI of 1.5 PFU/cell. Cells were fixed, permeabilised with 0.2% Triton X-100 and stained with anti-NP, phalloidin and DAPI. Super resolution, maximum intensity projections of TNT-like structures connecting MDCK cells was then performed and revealed mitochondria within TLSs. NP (blue), nuclei (yellow), F-actin (white)and Mitochondria (magenta). Scale bar = 20 μm.

Even though I found no directionality of TLS formation involving infected and uninfected cells (Figure 5-5), IAV infection is known to regulate TNT formation (see chapter 4), and I therefore hypothesised that IAV infection could increase the rate of which mitochondria transfer occurs between cells.

Investigating this hypothesis required a means to measure the exchange of mitochondria between cells, and to do this I performed a coculture of MDCK cells labelled with either MitoTracker Deep Red or MitoTracker Red. After coculturing, the cells were infected with an IAV for 20 hours by which time the suppression of apoptosis was observed (Figure 5-6) and evidence of mitochondrial exchange would be expected if it was responsible for conferring this phenotype. However, with the MitoTracker probes being used to stain live cells briefly at the start of the experiment, I expected the signal to fade over

time. I therefore tested how well the signal was retained when the cells were cocultured and allowed to adhere overnight prior to infection (infection of adherent cells being the typical inoculation method). This approach meant that imaging was performed at least 36 hours post staining (16 hours to adhere and 20 hours infected). This method of infection of adherent cocultured cells resulted in a dramatic loss of the MitoTracker Red signal (Figure 5-10 a), making it unsuitable for the quantification of mitochondria exchange. Next, I tested the effects of infecting the coculture whilst the cells were still in suspension (imaging after 21 hours post staining). This method allowed for the detection of both MitoTracker Deep Red and MitoTracker Red (Figure 5-10 b), and therefore was used for future experiments.

a) Adherent

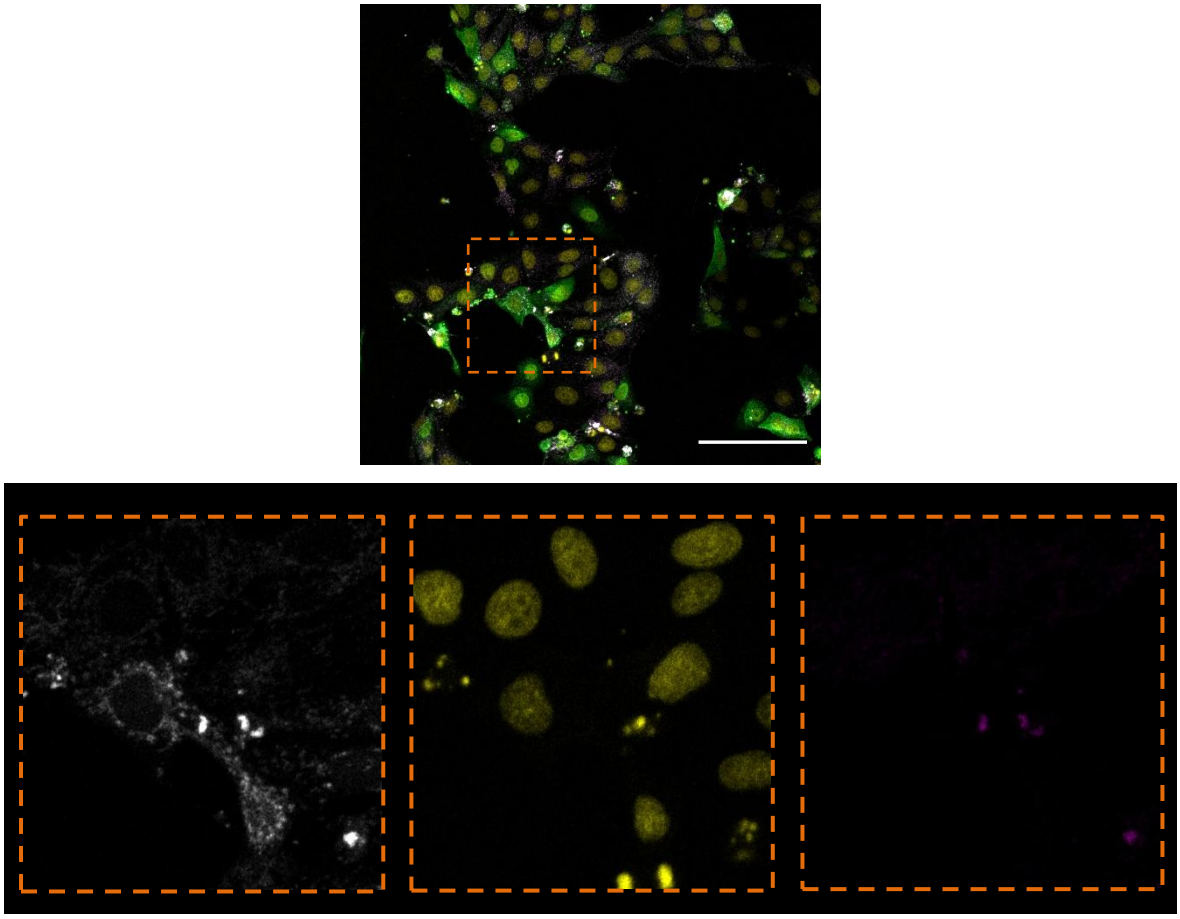

b) Suspension

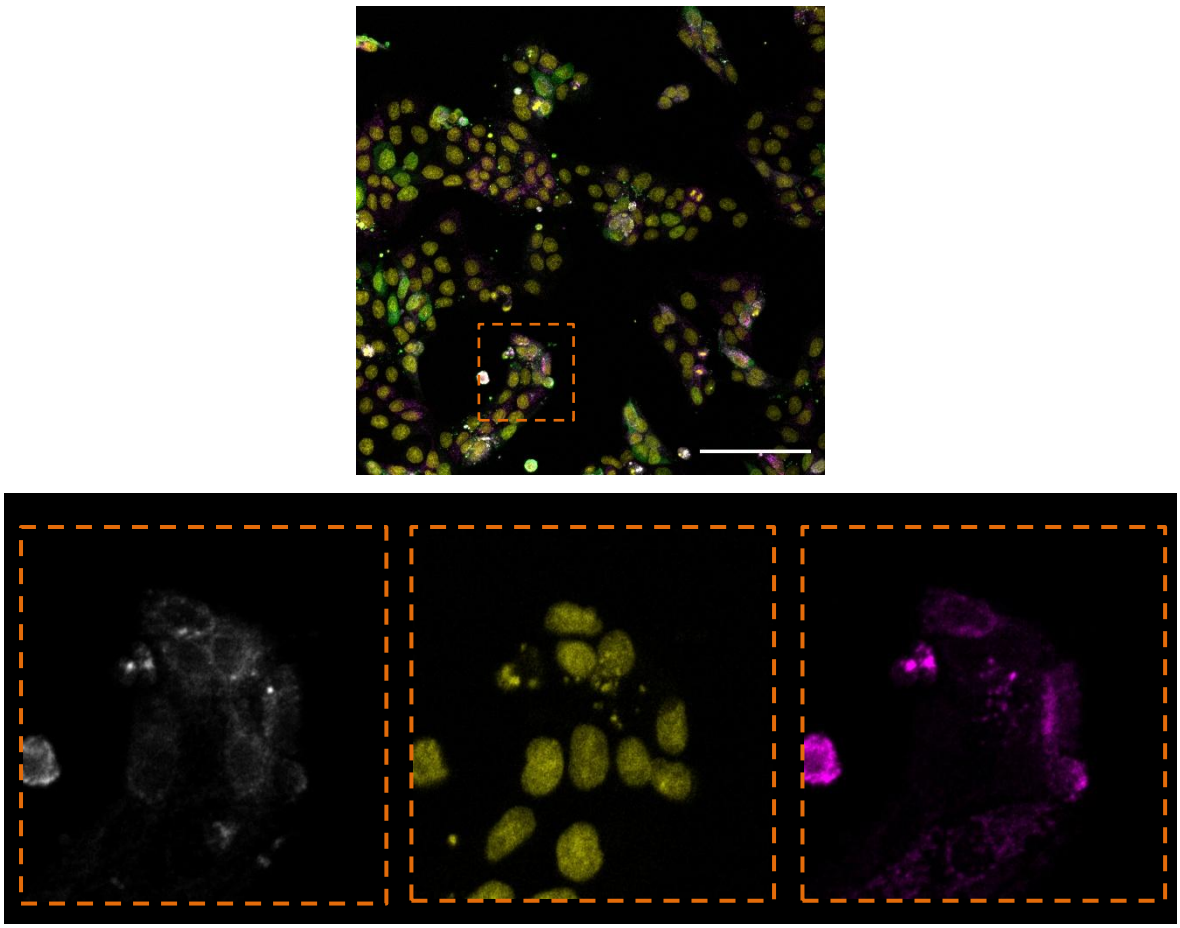

Figure 5-10: Mitochondrial label is retained when staining and infection are performed with cells in suspension. MDCK cells at a density of $1x10^6$/mL were stained with either MitoTracker Red CMXRos or MitoTracker deep red according to manufacturers protocol. Stained cells were washed twice by pelleting the cells and resuspending in complete media. Cells were then mixed at a 1:1 ratio and seeded onto coverslips. The cells were infected with BrightFlu ZsGreen at an MOI of 0.75 FFU/cell either (a) following overnight incubation and the cells were adherent (b) or immediately whilst the cells were in suspension. Cells were fixed with 4% formaldehyde 20 hours post infection. Cells were stained with DAPI and super resolution confocal microscopy was performed with the 20x objective. Accompanying inset (bottom panels) regions are indicated within the full field of view by the orange square. MitoTracker deep red (white), Mitotracker red (magenta), nuclei (yellow), BrightFlu ZsGreen (green). Scale bar = 100 μm.

Following the optimisation of MitoTracker labelling and infection, I compared how the MitoTracker staining was impacted by infection and co-culturing (Figure 5-11). With the monoculture of MitoTracker Deep Red stained cells, it appeared that infection did not affect the mitochondrial signal, albeit some cells in both mock and infected samples appeared to be negative for mitochondrial label (Figure 5-11). In contrast, MitoTracker Red monocultures showed that most mock infected cells were positively labelled. In contrast, I observed an apparent reduction in the amount of MitoTracker Red signal following infection when compared to mock (Figure 5-11). To verify these qualitative observations, I quantified the fluorescent intensities (FI) of both MitoTrackers in monoculture between mock and infection. In support of my observations, IAV infected MitoTracker Deed Red stained cells consistently had comparable average FIs as the mock infected monoculture, whereas the MitoTracker Red stained cells did show a reduction in average FI following IAV infection, although this was not statistically significant (Figure 5-12). Nevertheless, the average FI of the MitoTracker Red signal was greater than the Deep Red signal in both mock and infected samples (Figure 5-12).

Interestingly, when the differently labelled MitoTracker cells were cocultured I observed many cells containing both mitochondrial labels (Figure 5-11). This was true for both mock and infected cocultures. Once again infection seemed to reduce the MitoTracker Red signal, although the signal remained well above background and did not prevent the observation of cells positive for both mitochondrial labels. This result suggested that mitochondrial exchange occurs frequently regardless of infection, but to assess whether more transfer was occurring following IAV infection would require quantitation.

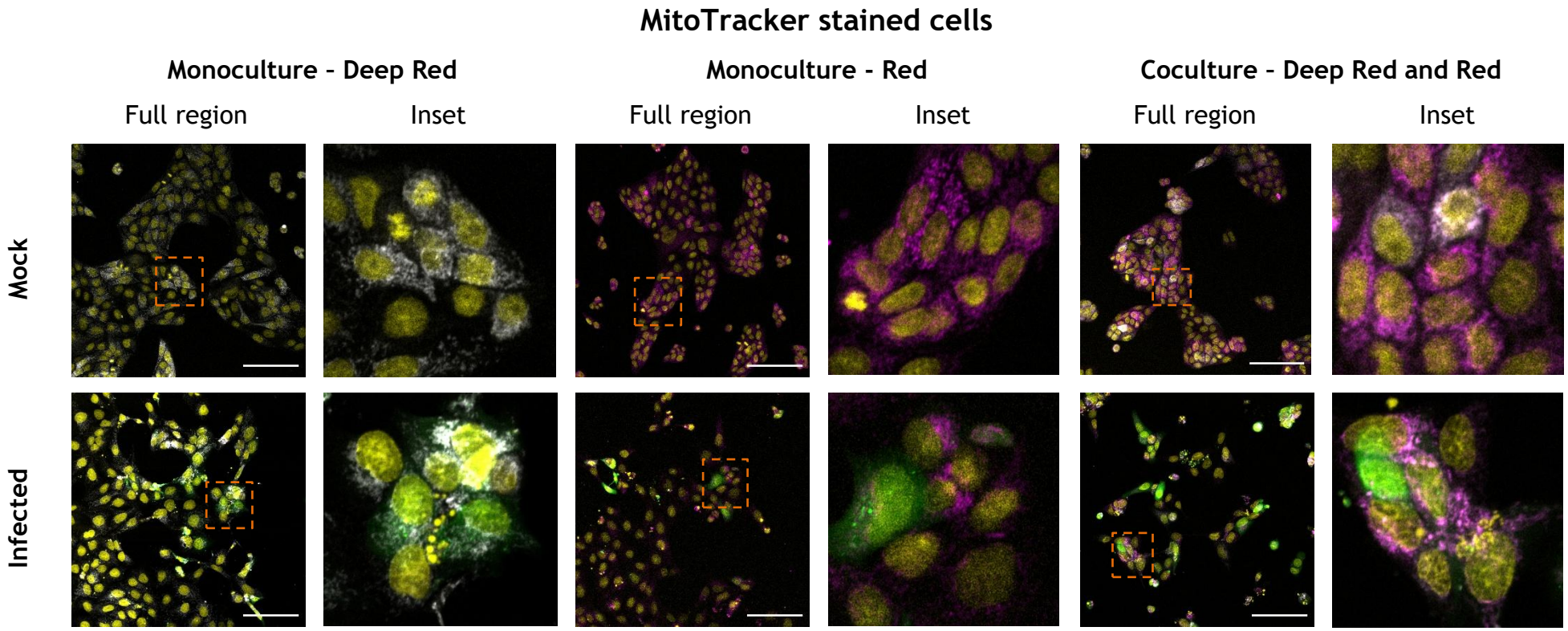

Figure 5-11: Representative super resolution confocal micrographs of mock and infected MitoTracker stained MDCK mono- and co-cultures. MDCK cells were stained with MitoTracker Deep Red or MitoTracker Red CMXRos, and seeded onto glass coverslips either as a monoculture or as a coculture (1:1 mix). Whilst the cells were in suspension they were then either mock infected or infected with BrightFlu ZsGreen at an MOI of 0.75 FFU/cell. Cells were fixed with 4% formaldehyde 20 hours post seeding and stained with DAPI. Super resolution confocal microscopy was then performed using a 20x objective lens. Accompanying magnified inset regions are indicated within the full field of view by the orange square. MitoTracker Deep Red (white), MitoTracker Red (magenta), nuclei (yellow), BrightFlu ZsGreen (green). Scale bar = 100 μm.

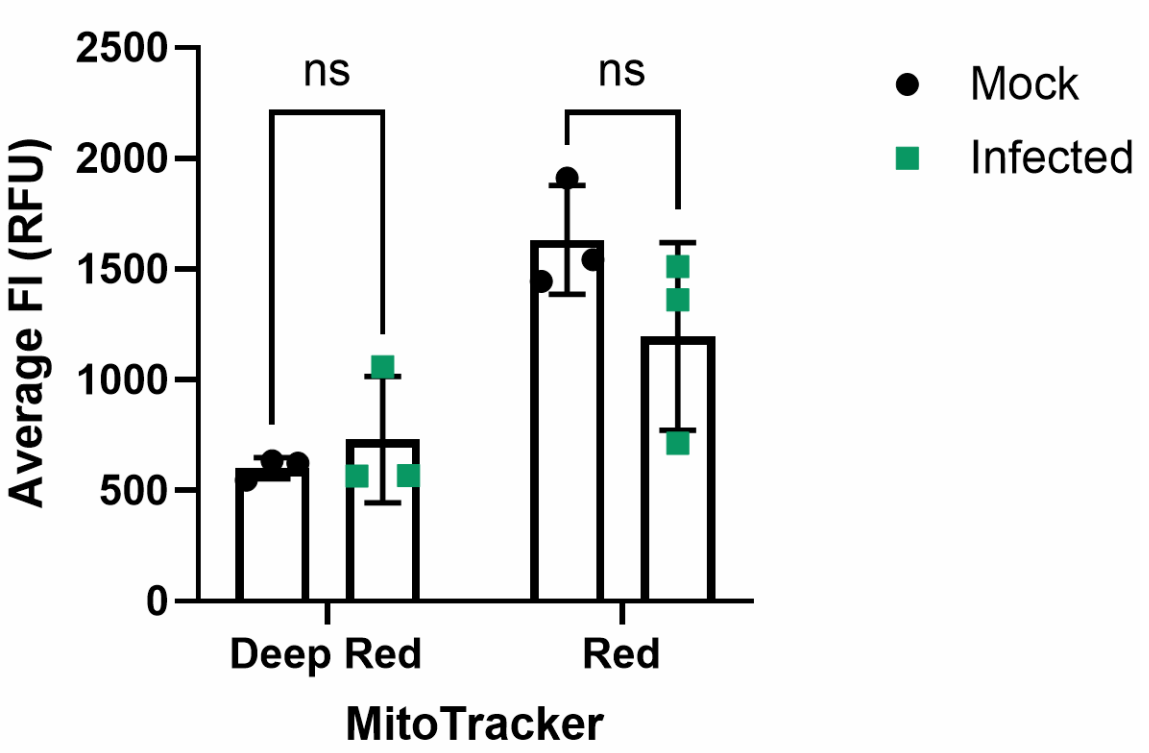

Figure 5-12: Average MitoTracker fluorescent intensity per cell in mock or infected monocultures. The mean fluorescent intensity of MitoTracker stain within each cell was determined using FIJI image J and then averaged across all cells per biological replicate. The mean and standard deviation is shown. (n =3). Differences between the average fluorescent intensity was tested for significance by Multiple Mann-Whitney test (ns $p > 0.05$).

Indeed quantitation revealed that the majority of cells, whether mock or infected, had signal of both mitochondrial labels with most cells having a proportion of MitoTracker FI less than 1 (indicating exclusively Far Red signal) and greater than 0 (indicating exclusively Red signal) (Figure 5-13 a). Noticeably, the MitoTracker FI ratio was skewed towards majority Red (around 0.1, Figure 5-13 a). This is likely due to the higher average FI of the MitoTracker Red label (Figure 5-12). When comparing between mock and infected, it appeared that the latter had more cells with a MitoTracker FI ratio closer to 0.5 (indicating a more even MitoTracker Deep Red and Red FI, Figure 5-13 a). This appeared even more pronounced when plotting only the cells robustly infected with a ZsGreen average FI of greater than 100 RFU (Figure 5-13 a). To confirm this, I then binned the cells from mock and infected (either total cells in an infected sample, or only those cells with an average ZsGreen FI > 100 RFU) samples into discrete categories of MitoTracker FI ratios (0-0.39 = FR<R, 0.4-0.59 = FR=R, 0.6-1 = FR>R) and plotted the percentage of cells that fell into each category (Figure 5-13 b).

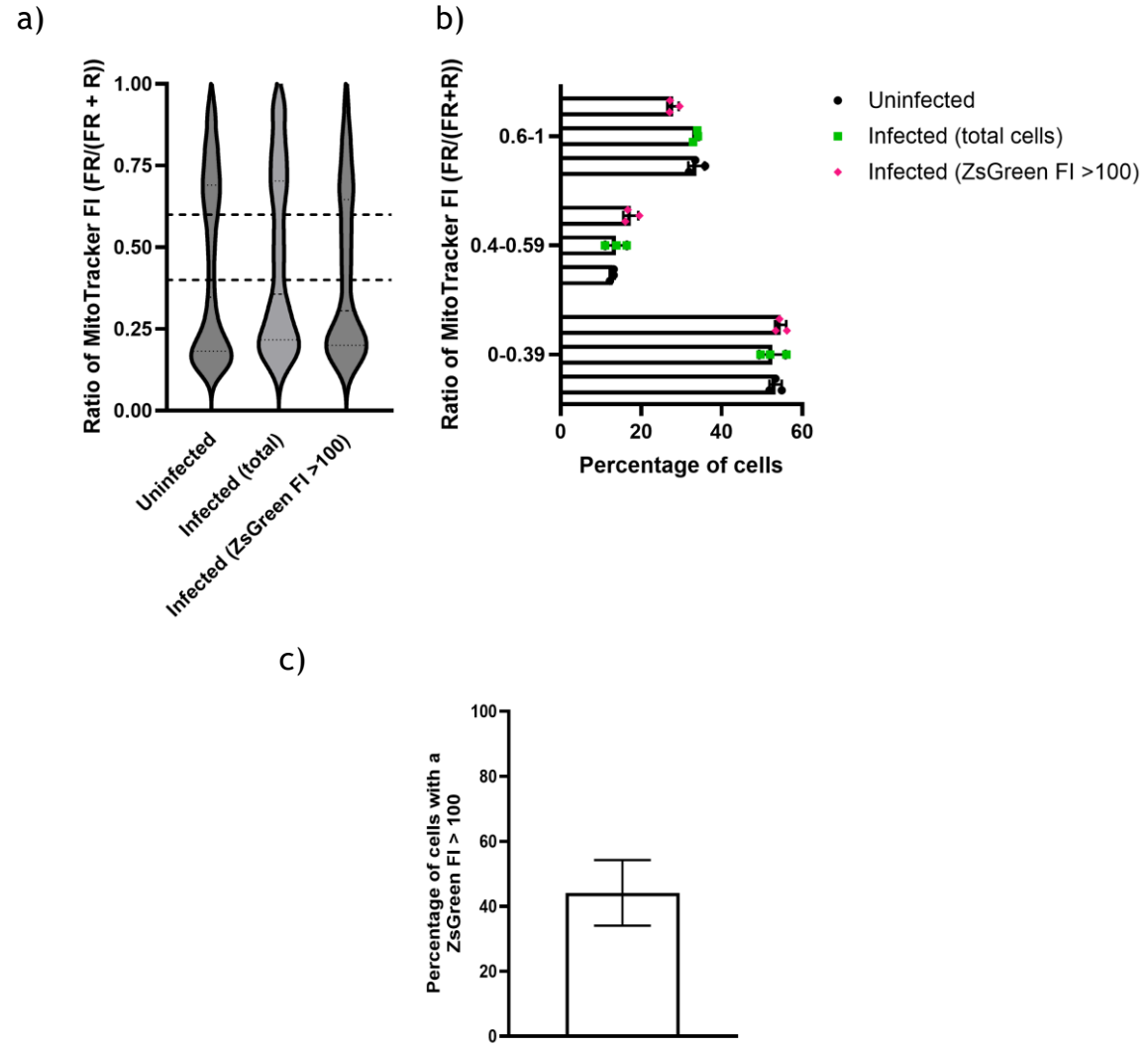

Figure 5-13: Assessing how IAV infection influences the exchange of mitochondria between cells. The proportion of MitoTracker fluorescence intensity per cell that is Far Red (FR/(FR+R)) within mock infected or infected samples. Robustly infected cells within the infected samples (individual cells with a ZsGreen FI > that 100 RFU) were then isolated and analysed separately. (a) The distribution of MitoTracker FI proportions per cell is shown in the violin plot with dashed lines indicating the median and the upper and lower quartile values. Dashed lines intersecting the y axis at either 0.39 and 6 represent the categories of which MitoTracker FI ratios were binned. (b)The proportion of MitoTracker fluorescence intensity per cell (FR/(FR+R)) from mock and infected samples/cells were binned into defined categories (0-0.39 = FR<R, 0.4-0.59 = FR=R, 0.6-1 = FR>R) and the percentage of cells belonging to each category is plotted. The mean and standard deviation is shown (n = 3). The difference in the percentages of cells between infection condition was tested for significance within each category of MitoTracker FI ratio by Kruskal-Wallis test (n.s. p > 0.05). (c) The percentage of cells within the infected sample with an average ZsGreen FI greater than 100 RFU. The mean and standard deviation is shown (n = 3)

I found that cells that were robustly infected (ZsGreen average FI > 100 RFU) consistently had a higher percentage of cells (by approximately 4.5%) that fell into the MitoTracker FI ratio category of 0.4-0.59, when compared to the mock infected sample (Figure 5-13 b). This effect did not seem to apply to all the cells of the infected sample (of which approximately 60% had an average ZsGreen FI less than 100 RFU) (Figure 5-13 b & c). This suggests that individual infected cells had a greater likelihood of receiving mitochondria from a neighbouring cell,

as opposed to uninfected cells. However, the extent by which the percentage of cells is skewed towards Red (due to the higher average FI of this MitoTracker label) suggests that the true homogenous MitoTracker FI ratio is not 0.4-0.59, but instead should also be skewed towards a lower value. Whilst it is difficult to account for differences in average FI between different MitoTrackers, the comparisons between infected and uninfected samples within a category of 0.4-0.59 is likely still revealing of mitochondrial exchange, albeit it is likely prioritising Deep Red labelled cells that received Red labelled mitochondria (this is reflected in the decrease in the percentage of cells in the 0.6-1 category between mock and infected samples) (Figure 5-13 c).

With the slight reduction in MitoTracker Red signal following infection (Figure 5-12), it is possible this effect is contributing to the infected cells having a slightly more balance in MitoTracker FI relative to the mock sample. However, within the 0-0.39 ratio category it still appears that infected samples have a comparable dominance of Red signal relative to the mock infected sample (Figure 5-13 b). Therefore, it is possible that the difference in average FI between mock and infected MitoTracker Red FI (Figure 5-12) was not significant enough to explain the increase in the percentage of cells within the 0.4-0.59 category when cells are infected (Figure 5-13 b).

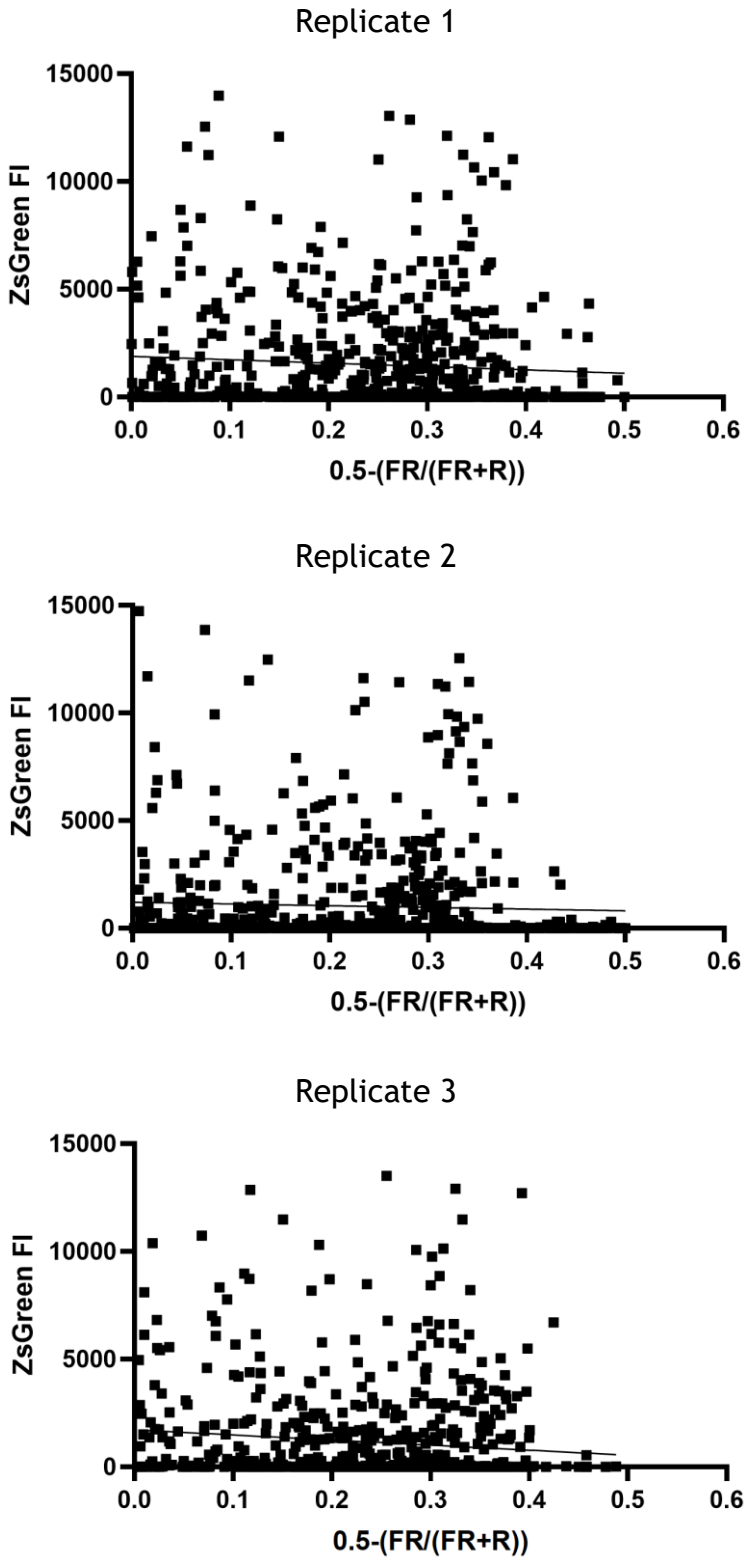

Figure 5-14: ZsGreen fluorescent intensity poorly correlates with the homogeneity in MitoTracker Far Red and Red fluorescent intensities. The difference (as absolute values) in MitoTracker fluorescent intensity ratios from a value of 0.5 (Far Red FI = Red FI) plotted against the average ZsGreen fluorescent intensities within individual cells (represent by individual data points). Scatter plots are shown for each biological replicate (n = 3). Linear regression analysis was conducted using the 'Simple linear regression' module in GraphPad Prism (version 10.3.0). Default parameters were used to fit a line of best fit for each biological replicate.

The indication that more infected cells with an average ZsGreen FI greater than 100 RFU had a MitoTracker ratio closer to 0.5, suggested that the cells with a

robust infection exchanged mitochondria more readily than uninfected cells. I was therefore curious if ZsGreen FI per cell correlated with a more homogenous FI between the MitoTracker labels. In order to assess this, I plotted the per-cell absolute difference in MitoTracker FI ratio from a uniform label distribution, represented by a value of 0.5, against the average ZsGreen FI. Across all biological replicates there was a poor correlation between the expression of IAV - ZsGreen and the extent of MitoTracker FI homogeneity within individual cells (Figure 5-14). This analysis revealed that, while IAV infection may enhance mitochondrial exchange, this effect would at most be confined to a subset of cells and appears to be triggered only once infection crosses a certain threshold, rather than scaling progressively with increasing infection levels.

5.3 Discussion

In this chapter, I quantified both TLS cellular origin and receipt, assessing whether IAV infection status predicted either. Furthermore, I investigated the consequences of uninfected and infected cell interactions by examining how apoptosis within IAV infected cells is regulated by direct cell to cell contacts with uninfected cell neighbours, with a particular focus on the role of TLSs within. Finally, in this chapter I explored whether mitochondrial exchange (which is known to rescue stressed or infected cells from apoptosis) between uninfected and IAV infected cells can be observed and whether this becomes elevated upon infection.

Using lentivirus transduced cell lines that stably expressed a membrane targeted fluorophore (Figure 5-3), I found no evidence that low MOI, IAV infection establishes the conditions for TLS pathfinding. Indeed, cell connections involving infected cells were being driven by their abundance and distribution (Figure 5-5). Furthermore, both infected and uninfected cells are able to initiate TLSs, complimenting other reports which concluded similar findings with other viruses (194, 278). Therefore, the interactions between cells, and the consequences of TLS mediated IAV infection spread (seeding new infections verses superinfection or coinfection) likely depends on how the distribution of infection changes over time.

Frequently observing uninfected cells in a TLS connection with infected cells emphasised the need to explore if uninfected cellular material delivery influences infected cells. Here I show that the availability of neighbouring uninfected cells, together with their ability to directly interact with infected cells, can suppress and/or rescue these cells from apoptosis (Figure 5-8). Whilst this phenotype was not reversed when TLS inhibiting drugs (taxol and IPA-3) were added (Figure 5-7), this anti-apoptotic effect was no longer observed when uninfected cells were physically separated from the infected cells by a transwell (Figure 5-8). This suggests that direct cell interactions are required for uninfected cells to suppress apoptosis within IAV infected cells, and secreted factors play no obvious role.

I then showed that mitochondrial exchange between MDCK cells occurs frequently, with robustly infected cells containing more mitochondria from neighbouring cells (Figure 5-13). Determining whether these observations are significant requires further optimisation in the use of MitoTracker labels (with ideally more equal fluorescence intensities), as well as additional replicates and/or more sophisticated analysis. An option for future analysis would be to segment the mitochondria within the images, and in doing so providing object counts for each mitochondria stained with either Deep Red or Red, these object counts can then be used to calculate a ratio independent of fluorescent intensities. Nevertheless, these data are consistent with the hypothesis that greater mitochondrial exchange, previously observed when healthy and diseased cells are in coculture (264, 271), could also be true for IAV infection. Therefore, our data lend some credence to the possibility that uninfected cells suppress IAV infected cell apoptosis through trafficking mitochondria following direct interaction with infected cells.

TLSs represent only one mechanism of mitochondrial exchange (372). For example, extracellular vesicles can lead to the transfer of mitochondria to neighbouring cells and has been observed *in vivo* (373, 374). The lack of apoptosis suppression when uninfected cells were separated via a transwell with a pore size of 3 μm (Figure 5-8), suggests extracellular vesicles are not responsible. Large extracellular vesicles that can encapsulate mitochondria are approximately 100 to 1000 nm in diameter (203). However, Flachi *et al.* found mitochondria containing extracellular vesicles produced from astrocytes ranging

from 1 to 8 μm in diameter (375). Therefore, it is possible that the transwell is discriminating against larger extracellular vesicles harbouring mitochondria, and only a proportion of these extracellular vesicles are able to cross to the infected cells. Interestingly, it was found that conditioned medium derived from aged osteocytes promoted mitochondrial exchange among treated osteocytes (376). Therefore, in order to rule out possible extracellular vesicle discrimination by the transwell, future experiments could be performed in which the conditioned media from the uninfected cells is collected and overlaid onto the infected cells. The difference this makes on both the amount of infected cells that are apoptotic and the rate of mitochondrial exchange could then be assessed.

An additional mechanism of mitochondrial exchange is the partial or complete fusion of cells, resulting in a shared or single cytoplasm (377). Partial fusion is a requirement for the formation of open-ended TLSs, whereas complete cell fusion is unique to the likes of syncytia formation. An interesting study by Wada *et al.* found that the distance over which two cells partially fused (in this case via a microtunnel within a microfluidics device) inversely correlated with the amount of mitochondrial exchange (378). Whilst distinct from TLSs, the distances (4.1, 5.6 or 10.0 μm), transiency and continuity of cytoplasm achieved by these microtunnels are similar, and therefore provide interesting considerations into how much mitochondrial exchange is achieved by open ended TLSs of diverse lengths. Whilst complete cell fusion fulfils the requirement of direct cell to cell contact, I did not observe significant syncytia formation in these assays and the use of cell subconfluency (prioritising long-range TLS interactions) would further reduce the occurrence of complete cell fusion. Therefore, I hypothesise that direct cell to cell contacts, that do not result in complete cell fusion, are responsible for the suppression of apoptosis and mitochondrial exchange observed.

The analysis of mitochondrial exchange does not provide insights into the direction of mitochondrial exchange as infection was performed after cells were mixed and in suspension. Whilst no directionality in TLS formation was observed, the directionality of TLS trafficking is a possibility that should be explored. Future experiments could use BrightFlu to infect one half of the MitoTracker labelled cell coculture (e.g. the MitoTracker Far Red stained cells) in suspension, and following virus internalisation the cells could be mixed and seeded with the

cells stained with a different MitoTracker (e.g. MitoTracker Red stained cells). Importantly an IAV entry inhibitor, such as amantadine, should be included to prevent the spread of infection. In this way the directionality of mitochondrial transfer can be assessed, albeit the issues with the difference in average FI between MitoTracker labels remains a hurdle when interpreting this type of data.

Overall, in this chapter I showed that TLSs can involve uninfected and infected cells, and that uninfected cells can suppress infected cell apoptosis through direct cell contacts. Furthermore, TLSs can incorporate mitochondria and mitochondrial exchange frequently occurs between cells, particularly those that are robustly infected. However, in order to conclude that TLS delivery of mitochondria from healthy to IAV infected cells is responsible for suppressing apoptosis, live cell microscopy of mitochondria trafficking would be required. Following this confirmation, cells could be cultured in ethidium bromide to render the mitochondria within these cells dysfunctional (264, 339). These cells could then be infected with increasing MOIs, as done previously with wild type cells (Figure 5-6), and the suppression of infected cell apoptosis should no longer be observed if mitochondrial transfer was responsible. TLS inhibiting drugs could also be included in the MitoTracker coculture experiments to determine the contribution of TLSs in exchanging mitochondria between IAV infected and uninfected cells. Additionally, cargo other than mitochondria can be trafficked via TLSs from healthy to diseased cells, compensating for a loss in function. For example, healthy cells can use TLSs to deliver functional lysosomes to diseased cells lacking them (296, 303). Therefore, a wider investigation into all the cargo that is exchanged between uninfected and IAV infected cells, and their consequences to each, should be investigated.

Chapter 6

6 Discussion

6.1 Summary of key findings

Several gaps in our understanding of IAV intercellular spread shaped the aims of this thesis, summarised in Table 1-4. In this section, I will review how the work presented in chapters 3 – 5 addressed these aims.

> **Aim 1:** Characterise the mechanisms and efficiency of IAV direct cell to cell spread.

In chapter 3, I established the microplaque assay to study IAV direct cell to cell spread and validated that the release of cell free virions was successfully inhibited by zanamivir. Then using two lab adapted strains, of different subtypes and virion morphologies, I compared how IAV direct cell to cell spread (microplaque formation) differed between them, with the influence of virion morphology being investigated more closely using segment 7 reassortants. I found that the frequency, but not the scale, of IAV direct cell to cell spread differed between the wild type viruses but not between the WT virus and its segment 7 reassortant. This revealed that IAV direct cell to cell spread is influenced by a property of the infecting virus, and that this property is not the morphology of the virion. I then used amantadine in combination with zanamivir to inhibit IAV endocytosis during cell associated IAV direct cell to cell spread. I found that this antiviral drug combination did not reduce microplaque formation. This suggested that these viruses used a mechanisms for direct cell to cell spread that is independent of the endosomal pathway. Finally, focusing on the mechanism of cytoplasmic genome transfer I targeted the F-actin and microtubule components of the cytoskeleton. I found that these drugs did not reduce microplaque formation, and in fact some actually increased microplaque formation. These results reveal that the primary mechanism of IAV direct cell to cell spread is independent of virion entry but involves cytoplasmic genome transfer that can be influenced by cytoskeleton disruption.

> **Aim 2:** Establish how IAV infection induces the formation of TLSs.

In chapter 4, I focused on TLSs as a mechanism of IAV direct cell to cell spread due to its known function in cytoplasmic IAV genome trafficking. I investigated how IAVs induced the formation of TLSs by first exploring the effect of extracellular signalling molecules, active virus replication and virion morphology. I found that U.V. inactivated conditioned media and ruxolitinib treatment did not influence TLSs formation, revealing that cytokines and innate immune signalling pathways are not responsible. From this work I found that TLS induction did require active virus replication within cells. I then compared how TLS induction differed between cells infected with either spherical and filamentous IAVs and found that the morphology of the replicating virus did not determine the extent of TLS induction. This suggests that TLS induction is distinct from filamentous particle formation despite a number of similar properties between these membranous protrusions. By then investigating the role of intracellular responses to IAV replication, I found that TLS induction correlated with, and was dependent upon, the activation of caspases during the apoptotic pathway. Using cisplatin to trigger apoptosis, I then showed that TLSs were not induced by the sole activation of the cell death pathway but also required active IAV replication. This work reveals that IAVs induce TLSs through the triggering of apoptosis that occurs from the replication of the virus.

> **Aim 3:** Assess the contribution of TLSs during IAV direct cell to cell spread *in vitro* and investigate their relevance *in vivo*.

In chapter 4 I also assessed how apoptosis influenced IAV direct cell to cell spread. I found that inhibition of apoptosis with a caspase inhibitor reduced IAV direct cell to cell spread when the cells were subconfluent. This result correlated with the effect this caspase inhibitor had on preventing IAV induced TLS formation. Taken together with the influence of cell confluency, this work strongly suggested that apoptosis is required for both the induction of TLSs, and the direct cell to cell spread of infection to distant cells facilitated by them. I then investigated the physiological relevance of TLSs by searching for their presence *in vivo*. Using a reporter mouse and IAV model system I observed TLSs produced from, and connecting, IAV infected cells within the lung epithelium. This reveals that TLSs are able to form at natural sites of IAV infection, suggesting that they may play a role in the within host spread of IAV infection, although definitive proof of this remains a critical gap in the field.

Aim 4: Investigate TLS pathfinding during IAV infection and explore how uninfected cell-derived cargo influences cellular outcomes.

In chapter 5, I explored whether TLS pathfinding was established following a low MOI infection. By coculturing genetically modified, membrane labelled cells with wild type cells, I was able to quantify the cellular origin and receipt of TLSs according to their infection status. I found that uninfected and infected cells formed TLSs to a comparable degree, and that the likelihood of either cell receiving a TLS was proportional to their abundance. This revealed that TLS pathfinding, if at all established, is not driven by infection. I then examined how direct cell to cell contacts between uninfected and infected cells influenced the cellular fate of the latter. I found that uninfected cells could suppress apoptosis within the infected cells when directly cocultured together. However, the inhibition of TLSs with different drugs did not prevent this uninfected cell mediated suppression of apoptosis. Nevertheless, when the uninfected cells were physically separated from the infected cells by a transwell, no apoptosis suppression was found, confirming that the original observation of cells in direct coculture was a consequence of direct cell to cell contact. With its role in regulating apoptosis, I then investigated the transfer of mitochondria between uninfected and IAV infected cells. Using mitochondrial labels and 3D super resolution confocal microscopy of IAV infected cells, I observed TLSs that contained mitochondria, confirming that TLSs can incorporate and likely transfer mitochondria to neighbouring cells. Next, I quantified mitochondrial exchange by coculturing cells labelled with different mitochondrial labels. I found that when these cocultures were infected at a low MOI, the infected cells consistently had a slightly elevated presence of both mitochondrial labels. This suggests that IAV infection increases the exchange and uptake of mitochondria. Together this suggests that this elevated, and perhaps directional, mitochondrial exchange from uninfected to infected cells in direct contact with each other could explain the earlier finding of uninfected cell suppression of infected cell apoptosis.

6.2 Evaluating the role of direct cell to cell spread during IAV infection

In chapter 3, I confirmed that direct cell to cell spread is a function that can be performed by many IAV infected cells (up to 40%), and is independent of

canonical virus entry, a finding similar to previous research with IAVs (222). This apparent efficiency is also consistent with other respiratory viruses. For example, by 24 hours post coculture, 40% of HMPV infected BEAS-2B cells directly spread infection to their neighbours (221). In the case of RSV, approximately 15% of infected HEp-2 cells directly spread infection by 24 hours post infection (379). Interestingly, this observed direct cell to cell spread of RSV infection was not observed in a well-differentiated primary human airway epithelial cell (WD PHAEC) model, despite both studies using neutralising antibodies targeting the F protein (380). This suggests that efficient virus direct cell to cell spread that occurs in 2D *in vitro* cell culture models may be restricted within more complex 3D *ex vivo* cultures that could indicate a reduced efficiency *in vivo*.

In chapter 4, I showed that TLSs can function to spread IAV infection directly between distant cells. Furthermore, I observed the first evidence of TLSs forming from IAV infected epithelial cells within the lung. Taken together, I hypothesise that TLSs can contribute to the within host spread of IAV infection, despite the complexity and motility of the respiratory tissue. To confirm this, the adoption of *ex vivo* models, such as WD PHAECs, would be required. Despite the lack of RSV direct cell to cell spread in WD PHAECs, the qualitative observation of measles virus direct cell to cell spread within WD PHAECs demonstrates that mechanisms of direct cell to cell spread can be experimentally studied within more complex models (381). Assessment of microplaques in 3D WD PHAECs or mT/mG mice (see chapter 4), using HA-deficient IAVs, could aid in the assessment of IAV direct cell to cell spread capabilities within tissues.

The involvement of non-TLS mediated mechanisms of IAV direct cell to cell spread was suggested in chapters 3 and 4, when TLS inhibition within confluent cells was shown to not reduce microplaque formation. I hypothesise that the confluency of cells enables other mechanisms of direct cell to cell spread of IAV infection (for example syncytia formation, see section 1.3.1), and may limit the relevance of long-range spread by TLSs. Currently, only a few mechanisms of direct cell to cell spread have been shown to be used by IAVs, with most thought to be able to occur between distant cells (such as transfer of genomes through TLSs) (222, 227, 230). A targeted investigation in the use of virological synapses

and cell junctions (see 1.3.1) is required to determine whether IAVs can use these mechanisms that typically occur over shorter distances.

As IAV infection progresses, tissues can become disrupted (356), and regions of cell loss could theoretically restrict and favour different mechanisms of direct cell to cell spread. For example, intact epithelium would have many cells in close association with each other and could favour mechanisms such as syncytia and cell junctions. Following lesion formation and cell loss, cells may be able to, or forced to, interact over larger distances possibly favouring the role of filopodia and TLSs. Additionally, the recruitment of migratory cells to sites of infection (382), such as immune cells, can increase the type of cell interactions. Immune cells, such as dendritic cells, are known to readily form TLSs and their recruitment to infection sites may increase the frequency of TLS mediated direct cell to cell spread of IAV material to these cells (383, 384). This could possibly aid in the function of these antigen presenting cells during the establishment of the adaptive immune response (383).

Another possible mechanism of immune evading infection spread that occurs independent of cell free virions is through the production of viral genome containing extracellular vesicles (EVs) (reviewed in (200)). Since this route of infection spread does not require close cell interactions, and involves the release of particles into the extracellular space, EVs should be considered separate from mechanisms of direct cell to cell spread. Nevertheless, the potential of EVs should be taken into consideration when measuring the direct cell to cell spread of IAV infection. Firstly, it is unlikely that EVs are restricted by neuraminidase inhibitors and could then contribute to microplaque formation. However, I showed in chapter 3 that infection was not transferred from collected supernatants supplemented with zanamivir, suggesting that EVs are not responsible for the spread of IAV infection in our experimental models. Secondly, EVs from IAV infected cells can deliver innate immune suppressing material that could enhance subsequent virus replication (385). For example, it was shown that the microRNA, miR-17-5p, was elevated in patients' bronchoalveolar lavage fluid and in EVs of IAV infected A549s (386). This microRNA was shown to then strongly downregulate the expression of the Mx1 antiviral protein, enhancing virus replication (386). Therefore, even if they are

not directly contributing to the transfer of IAV infection, EVs may alter the ability of cells to restrict IAV infection spread *in vitro* and *in vivo*.

6.3 TLSs and outcomes of infection

In chapter 4, I showed that IAVs trigger TLSs through virus-induced activation of caspases that function in the apoptotic pathway. Then in chapter 5 I found that uninfected cells can suppress apoptosis in contacted infected cells, which coincided with the observation that infected cells had a slight increase in mitochondrial exchange. This result in the context of known TLS bidirectional cargo exchange (230, 262), and the known function of mitochondria delivery via TLSs in suppressing PRRSV induced apoptosis (271), leads me to hypothesise a mechanism of negative feedback in TLS formation (Figure 6-1). I propose that IAV infection triggers the onset of apoptosis, that then triggers TLS formation (Figure 6-1 a). When this TLS connects a cell pair with an asymmetric infection, this then enables the trafficking of IAV genomes directly to the uninfected cell, whilst mitochondria is trafficked in the opposite direction to the infected cell (Figure 6-1 b). Apoptosis of the infected cell is then suppressed and virus replication prolonged (Figure 6-1 c).

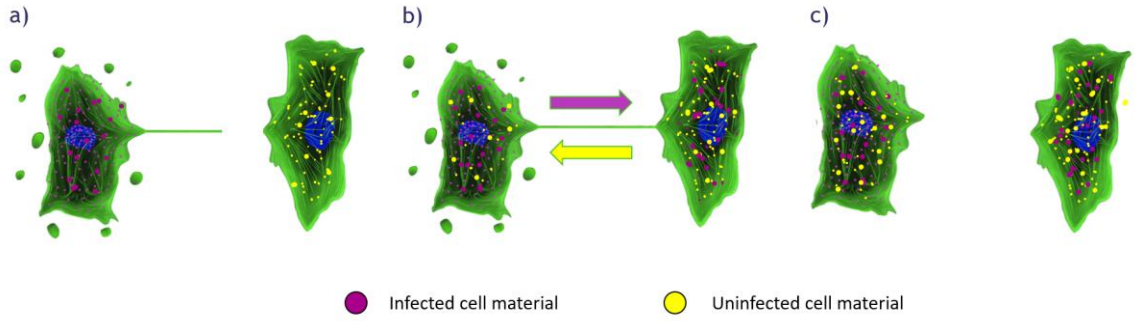

Figure 6-1: Hypothesised negative feedback of TLS induction by IAV triggered apoptosis. (a) IAV replication triggers apoptosis and TLS induction. (b) The TLS forms a connection with an uninfected cell and bidirectional trafficking through TLSs enables cytoplasmic IAV genome delivery to the connected uninfected cell, while cytoplasmic cargo (such as mitochondria) of the uninfected cell is trafficked in the opposite direction. (c) IAV replication occurs in both cells, with cargo of uninfected cell origin suppressing apoptosis within the initially infected cell. Suppression of apoptosis would remove the stimuli that induces TLS formation, and could also result in TLS retraction. In these drawings magenta punctae and arrow represent the direction of trafficked IAV infected cell material, e.g. the viral genome and yellow punctae and arrow represents cytoplasmic cargo trafficking, e.g. mitochondria. Additionally, green is used to represent F-actin and blue, the nucleus.

Since TLS induction requires apoptosis, and apoptosis could be suppressed by the function of TLSs, it is possible that TLS induction can be halted at least temporarily, i.e. negative feedback (Figure 6-1 c). Such a regulation could

provide insights into the process of TNT retraction, which as explained in section 1.4.1.1, remains poorly understood. Therefore, in addition to increased direct cell to cell spread of IAVs, a consequence of TLS trafficking could also be the prolonged survival of infected cells and virus replication which may also increase virion production. However, since caspases (such as caspase 3) are known to be important for both apoptosis and IAV propagation (340), the suppression of apoptosis (specifically by reducing the activation of caspases) suggests that delayed cell death may not also result in increased virus replication. Interestingly, when Ganti *et al*. added nocodazole to their HA-transcomplementing system, virus titres were increased at later infection time points (230). Nocodazole increases TLS formation (222), and could suggest that TLSs could increase virus titres. However, the role of apoptosis regulation in this is unknown and virion production was restricted to the HA expressing cells infected through direct cell to cell routes (230). Therefore, further investigation into how IAV apoptosis suppression by uninfected cells, possibly by TLSs, could influence virion production and cell free virion-mediated spread is required.

An important thing to consider when investigating possible negative feedback is that IAV infected cells do not survive indefinitely. Even if apoptosis of IAV infected cells is supressed by the function of induced TLSs, I show and discuss in chapter 4 that TLS induction was dependent on caspase activation in a manner that does not inhibit other relevant cell death pathways, such as pyroptosis and necroptosis. Therefore, even if apoptosis and TLS induction is suppressed, it does not guarantee that the cell will survive much longer to meaningfully prolong virus replication or enable the induction of TLSs again. Indeed research of IAV infected human bronchial epithelial cells has shown that apoptosis is activated earlier than pyroptosis, with a transition to the latter cell death pathway starting from 24 hours post infection and peaking at 48 hours (387). This study also found that IAV infection of these cells did not induce necroptosis (387). Other research with a dedicated focus on necroptosis during IAV infection showed that necroptosis becomes initiated when apoptosis signalling is absent or suppressed (352). Therefore, apoptosis can be considered to be the primary and earliest cell death response to IAV infection, with a transition to pyroptosis or necroptosis pathways following innate immune signalling or failed apoptotic pathways respectively (352, 387). In this way the suppression of apoptosis by TLS

trafficking may enable prolonged virus replication, but may also initiate a transition to alternative cell death pathways, meaning that cell death will no longer result in TLS induction or cell survival.

Exactly how mitochondrial exchange could be suppressing IAV apoptosis, and how this may influence IAV replication, are also interesting areas for future research. One possibility is via the fusion of uninfected and infected cell derived mitochondria. This could suppress apoptosis by restoring oxidative function, diluting pro-apoptotic signals, and stabilising membrane permeability, thereby preventing cytochrome C release (388-390). Such a mechanism could also have consequences for antiviral signalling as mitochondria contain mitochondrial antiviral signalling proteins (MAVS) that interfere with IAV replication via type 1 IFN production. To counteract this, IAV can encode for the viral protein PB1-F2 that localises to the inner mitochondrial membrane (391). PB1-F2 binds to the adaptor proteins of MAVS and in doing so prevents the production of IFN (392, 393). Therefore, one possible scenario involves the transfer of mitochondria from uninfected cells—capable of suppressing apoptosis—through fusion with the mitochondria of infected cells. The PB1-F2 within infected cell mitochondria could then also suppress antiviral signalling of the MAVS derived from the uninfected cell mitochondria. Such a scenario would reveal an interesting connection between the function of viral proteins modulating antiviral signalling pathways and the delivery of apoptosis suppressing cargo by TLSs, ultimately with the consequence of reduced host interference during virus replication.

Conversely, transferred TLS cargo may not always be proviral, or circumvented by innate immune antagonists. Given the range of cytoplasmic cargo trafficked through TLSs, it is plausible that antiviral proteins might be delivered to infected cells via these intercellular connections. Additionally, it is striking to note that the clearest evidence of TLS induction by IAVs comes from studies of high MOI infections (222, 230), which are also known to increase the occurrence of DVGs (394). As introduced in section 1.2.3.3, DVGs can interfere with the spread and replication of complete viral genomes. Currently, it is unknown if DVGs can also be trafficked through TLSs. However, given the common use of Rab11 in both trafficking genomes to virus budding sites and TLSs (129, 230, 315, 395), it is likely that DVGs are not excluded from the latter. Therefore, the transfer of DVGs via TLSs may reduce full length genome replication. Challenging

this suggestion is the aforementioned study by Ganti *et al.* which found an increase in fully infectious virus production when TLS formation was increased with nocodazole (222, 230). Nevertheless, the presence of DVGs and their ability to be trafficked through TLSs should be investigated alongside their consequence on co-trafficked full length genome replication.

As introduced in section 1.4.3, TNTs are not just relevant for the spread of infection but are also implicated in maintaining normal cellular processes and can contribute to a number of non-infectious diseases. Perhaps one of the most concerning examples of this is mitochondrial TNT trafficking causing cancer resistance to chemotherapeutic drugs (258, 396). The suggestion of enhanced mitochondrial exchange in IAV infected cells presented in chapter 5, could suggest that the risk of chemoresistance of these cells is elevated. Perhaps even more concerning is that in chapter 4, I found that the chemotherapeutic drug cisplatin promoted the TLS induction capabilities of IAVs. This may have implications for the development of chemoresistance via mitochondrial transfer, and may also increase the role of IAV direct cell to cell spread in patients undergoing cancer treatment. Interestingly, a case of a persistent IAV infection within a patient undergoing chemotherapy for malignant lymphoma was reported in 2016 (397). The patient was treated with zanamivir, but the virus developed resistance to this drug (397). Amongst factors such as a compromised immune response, an enhancement of IAV direct cell to cell spread in IAV persistence during chemotherapy, resulting in the acquisition of antiviral drug resistance mutations remains another possibility. Enhanced IAV direct cell to cell spread, coupled with a weakened immune response, could establish an opportune environment for IAV replication to continue at a scale that the selection of antiviral drug resistant mutants becomes increasingly likely.

6.4 Fundamental virology

6.4.1 Intracellular trafficking of viral genomes

As introduced in section 1.2.2, vRNPs are replicated within the nucleus and are then exported to the cytoplasm by traversing the nuclear pore complex. The accumulation of HA at the plasma membrane is known to trigger nuclear export via MAPK signalling (124). This is thought to regulate the timings of nuclear

export according to the assembly of virion structural components at budding sites. The involvement of MAPK signalling is an interesting link to-actin polymerisation that has been associated with TLS formation by SARS-CoV-2 (see Table 1-3). Therefore, it is possible that the triggering of IAV viral genome nuclear export can be regulated by the pathways that are also involved in actin polymerisation during TLS elongation. In a similar way to virion production, this could regulate nuclear export to coincide with the formation of structures that facilitate their intercellular spread. It is currently unknown if HA expression alone can trigger nuclear export and TLS formation via MAPK signalling. If so, this could have implications in studies of IAV direct cell to cell spread that use HA expressing cell lines. However, the lack of TLS induction even with robust viral replication and protein expression when apoptosis was inhibited (see chapter 4), suggests that HA accumulation alone is not responsible. A role of HA in TLS induction would then require this viral protein to function within the apoptotic pathway, and currently the molecular link between this protein and the activation of caspases during apoptosis onset is lacking.

An additional influence on IAV genome nuclear export follows the activation of caspases. Transmission electron microscopy data of IAV infected cells appeared to show an enlargement of the nuclear pore complex following the caspase mediated degradation of the Nup153 nucleoporin (398). Inhibition of caspase 3/7 caused NP to accumulate in the nucleus, with no cytoplasmic signal, suggesting that caspase activity supports the nuclear export of vRNPs (398). Once again, this is an interesting link between viral genome nuclear export and TLS induction, this time directly involving components of the apoptotic signalling pathway. However, in chapter 4, a dependency on caspase 3/7 activity for nuclear export and cytoplasmic NP detection was not found. By 16 hours post IAV infection, NP signal was mostly cytoplasmic in all infected cells, but only 35% of infected cells were positive for active caspase 3/7. Therefore, future work is required to better understand the role of apoptosis, specifically caspases, in vRNP nuclear export and how this could coincide with TLS induction and cytoplasmic genome trafficking.

As detailed in section 1.2.2, M1 coats vRNPs and recruits both NEP and Crm1 to mediate nuclear export. The coating of M1 covers the NLSs of NP, preventing the reuptake of exported assembled vRNP complexes back into the nucleus. To

initiate an infection in a new cell, M1 needs to be uncoated from the vRNPs. This is typically performed when virion cores are acidified within endosomes following receptor mediated endocytosis. In chapter 3 I confirm that mechanisms of IAV direct cell to cell spread within the microplaque assay does not require this acidification of endosomes associated with canonical virion entry pathways. How IAV vRNPs are uncoated to allow for nuclear import in a new cell is therefore an important question to address. A recent study by Larson *et al*. revealed interesting findings in the area of IAV vRNP uncoating. Through performing an analysis which correlated variations in gene expression across different cell lines with their susceptibility to IAV infection, combined with M1 immunofluorescence assays, they revealed that the host factor EPS8 was required for IAV M1 uncoating post fusion (399). Specifically, *EPS8* knock out cells had reduced viral gene expression and delayed nuclear import, emphasising its influence in supporting IAV replication (399). Acid bypass assays (enabling virion membrane fusion with the plasma membrane as opposed to endosomes) clearly showed that EPS8 performs its uncoating function post fusion (399). Exactly how EPS8 facilitates uncoating post fusion is not well understood and could require interactions with components of the virion (399). Therefore, it remains to be determined whether host factors like EPS8 can facilitate the uncoating of cytoplasmic IAV genomes delivered through mechanisms of direct cell to cell spread. Nevertheless, it remains an attractive possibility, in part because of the interesting connection with the actin bundling properties of EPS8 which has been shown to enable the formation of long TNTs (see 1.4.1).

6.4.2 Implications on the role of virion morphology and viral proteins during IAV direct cell to cell spread

In chapters 3 and 4 I investigated the role of IAV virion morphology in direct cell to cell spread. I found that the ability of an infection to directly spread from an individual cell to its neighbour was influenced by the infecting strain. However, the segment 7 reassortant viruses revealed that this difference was not because of the morphology of the virion. Furthermore, there was no difference in the scale of microplaques between these different viruses, suggesting that direct cell to cell spread is limited by certain host factors. Therefore, future work should investigate how differences other than morphology, such as subtype and replication kinetics, could confer a strain-dependent ability of direct cell to cell

spread. Additionally, the host and virological factors that limit and determine the scale of both spherical and filamentous IAV direct cell to cell spread should be investigated. The results presented in this thesis suggest that direct cell to cell spread is unlikely to cause significant areas of infection, with all viruses mostly forming microplaques limited to approximately 2 to 3 adjacent cells by 48 hours post infection.

Ultimately, the *in vitro* work presented in this thesis does not support the hypothesis that filamentous IAVs are selected for during natural infections due to an increase in direct cell to cell spread. Other work has found that filamentous viruses have increased rates and efficiency of fusion and entry in the presence of neutralising antibodies (162). Therefore, it is likely that the selection of filamentous IAVs is primarily due to the selective pressures of the immune response to extracellular virions. This reduced sensitivity of immune inactivation with filamentous virions is then more likely explained by the subsequent alterations of cell free virion interactions with recipient cells (162), as opposed to altering cell to cell interactions during virion formation. Nevertheless, with a possibility of cell culture influence on mechanisms of direct cell to cell spread (see chapter 4), an investigation using more relevant models would be required to definitively conclude that IAV strains with an ability to form filaments do not have an advantage during direct cell to cell spread.

As discussed in chapter 4, the discovery of a role of apoptosis in IAV direct cell to cell spread provides a helpful lens to view and investigate how IAVs perform direct cell to cell spread. The involvement of a number of IAV proteins in the regulation of apoptosis has been reported (summarised in Table 6-1). However, the differences in viral protein regulation of apoptosis between IAV subtypes and strains is not well characterised. Nevertheless, there is a precedence of differential apoptosis regulation between IAVs involving the NS1 protein. For example, the NS proteins of an H5N9 and H5N1 virus was shown to induce apoptosis within human bronchial epithelial cells, HeLa or MDCK cells (400, 401), whereas the NS proteins of an H6N6 virus was shown to suppress apoptosis in 293T cells (402). Whilst a cell type dependency could help to explain this, differences in the NS protein and their unique effect on apoptosis could also determine the strain specific frequency of IAV direct cell to cell spread that I observed with PR8 and Udorn strains.

Table 6-1: Viral proteins that regulate apoptosis.

Viral Protein	Effect on apoptosis	Apoptotic pathway	Mechanism	Ref.
M1	Promotes	Intrinsic	Binds to HSP70 and facilitates caspase activation.	(403)
M2	Promotes	N/A	Associates with the ATG5–Beclin-1 complex, disrupting autophagosome fusion and thereby indirectly promotes apoptosis.	(404)
NA	Promotes	Unknown	Unknown – requires NA activity	(405)
NP	Promotes	Intrinsic	Reduces the association of the antiapoptotic factor Clusterin with Bax.	(406)
NS1 (H5N9, H5N1)	Promotes	Extrinsic	Upregulates FasL mRNA expression.	(400)
NS1 (H6N6)	Supresses	Extrinsic (indirect)	Associates and prevents the pro-apoptotic function of Scribble.	(402)
PB1-F2	Promotes	Intrinsic	Localises to the mitochondrial membrane where it induces membrane permeabilisation and subsequent cytochrome c release	(84)

6.4.3 IAV tropism

As introduced in section 1.1.3.2, the susceptibility of host cells to IAV infection is typically determined by sialylated glycoconjugates on the cell surface that function as receptors. However, in chapter 3 I demonstrate that IAV direct cell to cell spread is independent of cell free virions that enter by receptor mediated endocytosis. Therefore, it is likely that cell susceptibility to IAV direct cell to

cell spread is separate from, and not determined by receptor binding. This then raises the question as to what cell types are infected by mechanisms of IAV direct cell to cell spread, and what determines this?

In mammals, most cells that are infected by IAVs are cells of the respiratory tract (407, 408). The sialic acid profiles of cells in the upper and lower respiratory tract are well characterised and compliments what is known about the HA receptor binding preferences of mammalian adapted IAVs (22, 407). However, reports of encephalitis in mammals infected with highly pathogenic H5Nx viruses (with a preference for the α2,3-linked sialic acid receptor) suggests that infection of mammals with these viruses is not limited to the respiratory tract, but can invade other areas such as the central nervous system (CNS), i.e. neuroinvasion (409). Sialic acid profiling in mammalian CNS cells remains limited, however, research of human CNS regions has revealed a high sialic acid content with both α2,6 – and α2,3- linked sialic acids represented (410). Studies of ferrets infected with IAVs that recognise either α2,3- or α2,6-linked sialic acids revealed that both viruses replicated within olfactory mucosa (411, 412). The olfactory mucosa is thought to be essential for neuroinvasion (413), and therefore this finding suggests that receptor binding is not the primary determinant of H5Nx ability to invade the CNS. How then H5Nx viruses are uniquely able to perform neuroinvasion is currently unknown, but the data suggests mechanisms independent of receptor binding. Interestingly, Pepe *et al.* showed that SARS-CoV-2 neuroinvasion could be facilitated by mechanisms of virus direct cell to cell spread (281). Specifically, non-permissive human neuronal cells were infected by SARS-CoV-2 only when cocultured with permissive, infected epithelial cells. This correlated with the observation that a variety of SARS-CoV-2 proteins are delivered to neuronal cells through TNT trafficking (281). Therefore, a possible mechanism of H5N1 neuroinvasion could be through TNTs connecting infected epithelial cells and neuronal cells. A role of TLSs in H5N1 intercellular spread is supported by Kongsomros *et al.* as they showed that H5N1 can trigger the induction of TLSs in MDCK cells (231). Future work should examine whether IAV infection induces the formation of TLSs that connect different cell types in coculture. Additionally, a comparison in direct cell to cell spread frequency between H5N1 and other IAVs should be performed, with a particular focus on the role of TLSs within. I hypothesise that H5Nx

viruses, associated with neuroinvasion, perform direct cell to cell spread more readily between heterotypic cell pairs, particularly via TLSs. The significant differences seen in direct cell to cell spread frequency between IAV strains in chapter 3 supports a strain-dependent effect required for this hypothesis to be true. However, I found that the differences in TLS induction between strains, whilst generally reflecting the differences in direct cell to cell spread frequency, was not significant.

6.5 IAV direct cell to cell spread in disease burden and management

Whilst evidence presented in chapter 3 suggests that IAV direct cell to cell spread is not responsible for the formation of large plaques that would otherwise be achieved by cell free virions, the role of IAV direct cell to cell spread in severe disease and outbreaks may be more nuanced but just as profound.

6.5.1 Virus evolution during coinfection

Perhaps the greatest risk posed by IAV direct cell to cell spread involves the risk associated with coinfection. In this section I consider how IAV direct cell to cell spread could function during cellular coinfection with different IAVs, as well as the common coinfection of a host with IAV and bacteria such as *Streptococcus pneumoniae*.

6.5.1.1 IAV coinfection and viral evolution

As introduced in section 1.1.2, pandemic strains of IAVs emerge through reassortment of gene segments proceeding cellular coinfection in a process referred to as antigenic shift. However, cellular coinfection is temporally regulated by the mechanisms of superinfection exclusion (see 1.2.3.3). It was found that the onset of IAV superinfection exclusion is as early as 3 hours post primary infection (163). Therefore, in order for reassortment to occur, secondary virus infection needs to occur within this narrow window of time. As introduced in section 1.3.2, one of the major potential benefits of direct cell to cell spread to the virus is that it can occur more quickly than cell free virion spread. An attractive way in which coinfection of a cell can then occur prior to superinfection exclusion onset is through initiating direct cell to cell spread. In

chapter 3 I presented and discussed the evidence that suggested that most IAV direct cell to cell spread, between confluent MDCKs, occurred by 8 to 10 hours post infection. Whilst the timings of this is after the onset of superinfection exclusion, it does occur prior to the timings in which cell free virion spread is reasonably expected to have been completed (virion release typically happens between 12 and 16 hours post infection). Together with the observation that up to 40% of IAV infected cells can spread infection to at least one neighbouring cell (see chapter 3), this suggests that direct cell to cell spread may account for a lot of the coinfection seen from *in vitro* experiments. One such experiment was performed by Sims *et al.*, where they assessed the extent of coinfection in the region between plaques that expanded into each other (163). By focusing on this region between interacting plaques, the involvement of direct cell to cell spread is likely relevant due to the ability of cells to interact with each other. They found that approximately 1% of infected cells were coinfected with differently labelled isogenic reporter IAVs, concluding that superinfection exclusion onset does significantly limit coinfection of cells as infected lesions expand from distinct foci (163). Since superinfection exclusion appeared to cause such a dramatic restriction, perhaps the 1% of coinfected cells was established by the more rapid, atypical routes of IAV intercellular spread. Future work should investigate the role of direct cell to cell spread in these coinfection events between expanding plaques by using similar drugs as those in chapter 4.

Since similar patterns of coinfection was then observed between expanded lesions *in vivo* (163), it is possible that the more rapid IAV direct cell to cell spread may facilitate coinfection more than cell free virions within infected hosts. If such a hypothesis is proven to be true, then perhaps mechanisms of IAV direct cell to cell spread may be responsible for reassortment events that generate novel strains of IAVs with pandemic capabilities.

Other consequences of coinfection (prior to superinfection exclusion onset) are also important to consider to fully understand the potential of IAV direct cell to cell spread. As introduced in section 1.2.2.3, many IAVs are semi-infectious, lacking one or more gene segments and require complementation to supply what was missing for an infectious particle to form. Therefore, direct cell to cell spread may enable the efficient delivery of these viral genomes, and in doing so may contribute to the enhancement of cell free virion-mediated spread. In this

way, an understanding of IAV direct cell to cell spread could be required to fully understand the within host and interhost spread of IAV infection.

Lastly, the consequence of direct cell to cell spread following coinfection of IAVs and other respiratory viruses is currently an unexplored area of research. It is possible that the induction of direct cell to cell spread by different viruses could be synergistic, expanding the frequency and diversity of direct cell to cell spread mechanisms. Coinfections of IAV and RSV have been shown to produce chimeric virions, harbouring the glycoproteins of both viruses (414). This is hypothesised to enable the delivery of IAV infection to the lower respiratory tract (abundant in α-2,3 linked sialic acids), that without the components of RSV, would be challenging for human adapted IAVs (414). This is an interesting example of how the presence of coinfecting viral proteins can enhance the spread of cell free IAVs. How diverse viral proteins within a coinfected cell could then also influence direct cell to cell spread of both viruses is an interesting prospect, especially given the role of viral proteins in establishing some routes of direct cell to cell spread (see 1.4.2.2). Currently, there is no evidence that RSV induces or use TNTs to mediate direct cell to cell spread, instead using filopodia (415). Therefore, the TNTs established by a coinfecting IAV may provide RSV with this opportunity. Alternatively, coinfection of respiratory viruses can cause interference to their replication (416), which may negatively effect their direct cell to cell spread. The relatively high frequency of respiratory virus coinfection (between 10 and 30% of respiratory infections, (417-419)) demands a dedicated effort to understand how virus coinfection positively or negatively influences the direct cell to cell spread of each virus.

6.5.1.2 Bacterial coinfection and direct cell to cell spread

As well as viral coinfection, coinfection of an IAV infected host with bacteria is also an important consideration. A leading cause of severe morbidity and mortality associated with seasonal influenza is due to pneumonia caused by bacterial coinfection (420). Therefore, how infection with these pathogens alter each other, and the host, is an important area of future research. This extends to the study of how bacterial coinfection alters the direct cell to cell spread of the virus. Interestingly, it was found that tuberculosis promotes the intercellular transmission of HIV-1 via enhancing TNT formation (421). This provides an

interesting link between bacterial coinfection and enhanced virus direct cell to cell spread that may extend to coinfections of different viruses and bacteria.

Additionally, the induction of TLSs by virus infection may also support the spread of bacteria. Bacteria have also been seen to exploit these intercellular connections for their within host spread (211). In this way, TLSs induced by IAV infection may exacerbate the disease caused by bacteria such as bacterial pneumonia. However, there is limited evidence that links TNT mediated spread of pneumonia causing bacterial species commonly found coinfecting with IAVs (see Table 6-2). This suggests that TNTs induced by IAVs may not be a significant contributor to the spread of bacteria responsible for causing pneumonia. Nevertheless, recent evidence has suggested that *Staphylococcus aureus* (a common bacteria that coinfects with IAV) biofilm spread is influenced by TLSs (422). In this case actin nanotube formation was linked to reduced biofilm spread (422). This emphasises the need to investigate how IAV induced TLSs may be positively or negatively influencing the spread of clinically relevant bacteria during coinfections.

Table 6-2: Evidence of TLS mediated spread of bacteria associated with IAV coinfection and/or pneumonia.

	Evidence of:			
Bacteria	**TLS spread**	**IAV coinfection**	**Pneumonia association**	**Ref**
Mycobacterium tuberculosis	Yes	Rarely	Yes	(423, 424)
Listeria monocytogenes	Yes	No	Rare	(425, 426)
Streptococcus pneumoniae	No	Yes	Yes	(427)
Staphylococcus aureus	Likely	Yes	Yes	(422, 427)

6.5.2 Therapeutic strategies

As introduced in section 1.1.3.3, the primary strategies used to reduce influenza disease burden is through the use of vaccines and antiviral drugs. The role of IAV direct cell to cell spread in the desired outcomes of these strategies could be interesting. For example, vaccines are designed to optimise the antibody response to the surface glycoproteins of the predicted seasonal IAV strains. Vaccines such as the Live Attenuated Influenza Vaccine (LAIV) are replication competent, and do so in the upper respiratory tract (428). LAIVs induce secretory IgA antibodies in the respiratory tract, and the replication inside nasal epithelial cells also activates both CD8+ and CD4+ T cells via MHC class I and II presentation respectively (429). Therefore, the replication of LAIVs triggers both humoral and cellular immunity. IAV direct cell to cell spread enables the continued replication of IAV in a new cell while evading the immune response (222, 223). Therefore, it may be important to assess the frequency by which LAIV strains perform direct cell to cell spread and determine how this may influence the strength of the immune response of these vaccines. Conversely, since these viruses are attenuated, direct cell to cell spread may be an efficient route of LAIV spread between epithelial cells whilst avoiding premature clearance of extracellular virions via mucociliary flow. This could enhance antigen distribution relevant for the activation of CD8 T cells and dendritic cells. IAV direct cell to cell spread may also localise virus replication to distinct zones in the mucosa which could enhance secretory IgA production through tissue resident dendritic cells (384, 430). A better understanding of the role IAV direct cell to cell spread following LAIV vaccination could then help provide insights into vaccine design and optimisation.

As also introduced in section 1.1.3.3, there are two classes of IAV antiviral drugs currently in use clinically: neuraminidase inhibitors and polymerase inhibitors. Resistance to neuraminidase inhibitors is a common problem, particularly with immunocompromised people (431). Neuraminidase inhibitors, as shown in chapters 3 and 4, do not prevent IAV direct cell to cell spread. On the other hand, it is reasonable to expect that polymerase inhibitors would inhibit both cell free virion and direct cell to cell spread. Given the uncertain role of direct cell to cell spread in IAV persistence and the potential emergence of adaptive

mutations—such as resistance to zanamivir (see 6.3)—polymerase inhibitors may offer a more favourable option for treating persistent infections than zanamivir.

In chapter 4, I show that apoptosis was required for IAV direct cell to cell spread between distant cells. A variety of drugs that inhibit apoptosis are used clinically for the treatment of a number of diseases including cancer and neurodegenerative disease (432). However, these drugs do not typically inhibit caspases, such as Z-VAD-fmk used in this thesis. Currently caspase inhibitors are limited to experimental models and are not yet widely used clinically (433). It remains to be seen whether other anti-apoptotic drugs, with a good clinical profile, inhibit IAV direct cell to cell spread. It should be noted that whilst the consequences of IAV direct cell to cell spread may be great, especially when it comes to reassortment (see 6.5.1.1), targeting apoptosis to inhibit direct cell to cell spread is unlikely to offer a benefit that would reasonably outweigh the risks associated with altering cell death regulating pathways, especially when effective antiviral drugs that target viral components are available.

6.6 Conclusion

Overall, this thesis set out to determine the efficiency and consequences of IAV direct cell to cell spread, with a view of how this could contribute to the within host spread of IAV infection. By focusing on the formation of TLSs, as a known mechanism of IAV direct cell to cell spread, I was able to uncover that TLSs form *in vivo* following IAV infection, and that IAVs induce TLSs by triggering apoptosis. From this, I was then able to show that apoptosis was required for IAV direct cell to cell spread between distant cells, and that TLS cargo includes mitochondria, which may regulate IAV induced apoptosis. The work of this thesis advances our understanding of how IAVs navigate the complex and hostile environment of its host to ensure its continued spread to neighbouring cells. Additionally, this work provides powerful insights that can be used as tools for future work that will better our understanding of the complex biology of virus interactions with their hosts, ultimately shaping the course of disease and IAV evolution. In this way, this work establishes an important link between virus induced alterations of a cell that determines individual cellular outcomes to infection, and the potential of IAVs to cause significant disease at a global scale.

References

1. Kilbourne ED. Taxonomy and Comparative Virology of the Influenza Viruses. In: Kilbourne ED, editor. Influenza. Boston, MA: Springer US; 1987. p. 25-32.
2. Hutchinson EC, Amorim MJ, Yamauchi Y. Understanding Influenza. In: Yamauchi Y, Amorim MJ, editors. Influenza Virus: Methods and Protocols. New York, NY: Springer US; 2025. p. 1-26.
3. Ferguson L, Olivier AK, Genova S, Epperson WB, Smith DR, Schneider L, et al. Pathogenesis of Influenza D Virus in Cattle. J Virol. 2016;90(12):5636-42.
4. Webster RG, Bean WJ, Gorman OT, Chambers TM, Kawaoka Y. Evolution and ecology of influenza A viruses. Microbiol Rev. 1992;56(1):152-79.
5. Barr IG, Subbarao K. Implications of the apparent extinction of B/Yamagata-lineage human influenza viruses. npj Vaccines. 2024;9(1):219.
6. Morens DM, Taubenberger JK. Historical thoughts on influenza viral ecosystems, or behold a pale horse, dead dogs, failing fowl, and sick swine. Influenza Other Respir Viruses. 2010;4(6):327-37.
7. Tong S, Zhu X, Li Y, Shi M, Zhang J, Bourgeois M, et al. New world bats harbor diverse influenza A viruses. PLoS Pathog. 2013;9(10):e1003657.
8. Caserta LC, Frye EA, Butt SL, Laverack M, Nooruzzaman M, Covaleda LM, et al. Spillover of highly pathogenic avian influenza H5N1 virus to dairy cattle. Nature. 2024;634(8034):669-76.
9. Harris A, Cardone G, Winkler DC, Heymann JB, Brecher M, White JM, Steven AC. Influenza virus pleiomorphy characterized by cryoelectron tomography. Proc Natl Acad Sci U S A. 2006;103(50):19123-7.
10. Zebedee SL, Lamb RA. Influenza A virus M2 protein: monoclonal antibody restriction of virus growth and detection of M2 in virions. J Virol. 1988;62(8):2762-72.
11. Carter T, Iqbal M. The Influenza A Virus Replication Cycle: A Comprehensive Review. Viruses. 2024;16(2).
12. Karakus U, Mena I, Kottur J, El Zahed SS, Seoane R, Yildiz S, et al. H19 influenza A virus exhibits species-specific MHC class II receptor usage. Cell Host Microbe. 2024;32(7):1089-102.e10.
13. Wu Y, Wu Y, Tefsen B, Shi Y, Gao GF. Bat-derived influenza-like viruses H17N10 and H18N11. Trends Microbiol. 2014;22(4):183-91.
14. Gerber M, Isel C, Moules V, Marquet R. Selective packaging of the influenza A genome and consequences for genetic reassortment. Trends Microbiol. 2014;22(8):446-55.
15. Centers for Disease C, Prevention. Types of Influenza Viruses. US Department of Health & Human Services. 2024.
16. Betakova T, Nermut MV, Hay AJ. The NB protein is an integral component of the membrane of influenza B virus. J Gen Virol. 1996;77 (Pt 11):2689-94.
17. Wang M, Veit M. Hemagglutinin-esterase-fusion (HEF) protein of influenza C virus. Protein & Cell. 2015;7(1):28-45.
18. Katayama M, Murakami S, Ishida H, Matsugo H, Sekine W, Ohira K, et al. Antigenic commonality and divergence of hemagglutinin-esterase-fusion protein among influenza D virus lineages revealed using epitope mapping. Journal of Virology. 2024;98(3):e01908-23.
19. Reddy T, Shorthouse D, Parton Daniel L, Jefferys E, Fowler Philip W, Chavent M, et al. Nothing to Sneeze At: A Dynamic and Integrative Computational Model of an Influenza A Virion. Structure. 2015;23(3):584-97.

20. Koopmans MPG, Barton Behravesh C, Cunningham AA, Adisasmito WB, Almuhairi S, Bilivogui P, et al. The panzootic spread of highly pathogenic avian influenza H5N1 sublineage 2.3.4.4b: a critical appraisal of One Health preparedness and prevention. The Lancet Infectious Diseases. 2024;24(12):e774-e81.
21. Ellis AM, Coyle J, Marshall KE. Serologic Evidence of Recent Infection with Highly Pathogenic Avian Influenza A(H5) Virus Among Dairy Workers — Michigan and Colorado, June–August 2024. MMWR Morbidity and Mortality Weekly Report. 2024;73:1004-9.
22. Long JS, Mistry B, Haslam SM, Barclay WS. Host and viral determinants of influenza A virus species specificity. Nature Reviews Microbiology. 2019;17(2):67-81.
23. Lee CY. Exploring Potential Intermediates in the Cross-Species Transmission of Influenza A Virus to Humans. Viruses. 2024;16(7).
24. Taubenberger JK, Kash JC. Influenza virus evolution, host adaptation, and pandemic formation. Cell Host Microbe. 2010;7(6):440-51.
25. Mostafa A, Abdelwhab E-S, Mettenleiter T, Pleschka S. Zoonotic Potential of Influenza A Viruses: A Comprehensive Overview. Viruses. 2018;10:497.
26. Perroncito E. Epizoozia tifoide nei gallinacei: Tip. e lit. Camilla e Bertolero; 1878.
27. Alexander DJ, Brown IH. History of highly pathogenic avian influenza. Rev Sci Tech. 2009;28(1):19-38.
28. Kandeil A, Patton C, Jones JC, Jeevan T, Harrington WN, Trifkovic S, et al. Rapid evolution of A(H5N1) influenza viruses after intercontinental spread to North America. Nature Communications. 2023;14(1):3082.
29. Banyard AC, Bennison A, Byrne AMP, Reid SM, Lynton-Jenkins JG, Mollett B, et al. Detection and spread of high pathogenicity avian influenza virus H5N1 in the Antarctic Region. Nat Commun. 2024;15(1):7433.
30. Pardo-Roa C, Nelson MI, Ariyama N, Aguayo C, Almonacid LI, Gonzalez-Reiche AS, et al. Cross-species and mammal-to-mammal transmission of clade 2.3.4.4b highly pathogenic avian influenza A/H5N1 with PB2 adaptations. Nature Communications. 2025;16(1):2232.
31. Lagan P, McKenna R, Baleed S, Hanna B, Barley J, McConnell S, et al. Highly pathogenic avian influenza A(H5N1) virus infection in foxes with PB2-M535I identified as a novel mammalian adaptation, Northern Ireland, July 2023. Euro Surveill. 2023;28(42).
32. Influenza CFC-cSTFoA, Wild B. Scientific Task Force on Avian Influenza and Wild Birds statement on H5N1 high pathogenicity avian influenza in wild birds - Unprecedented conservation impacts and urgent needs. 2023.
33. Plaza PI, Gamarra-Toledo V, Rodríguez Euguí J, Rosciano N, Lambertucci SA. Pacific and Atlantic sea lion mortality caused by highly pathogenic Avian Influenza A(H5N1) in South America. Travel Medicine and Infectious Disease. 2024;59:102712.
34. Garske T, Clarke P, Ghani AC. The Transmissibility of Highly Pathogenic Avian Influenza in Commercial Poultry in Industrialised Countries. PLOS ONE. 2007;2(4):e349.
35. Jahid MJ, Nolting JM. Dynamics of a Panzootic: Genomic Insights, Host Range, and Epidemiology of the Highly Pathogenic Avian Influenza A(H5N1) Clade 2.3.4.4b in the United States. Viruses. 2025;17(3):312.
36. Wu Z-Q, Zhang Y, Zhao N, Yu Z, Pan H, Chan T-C, et al. Comparative Epidemiology of Human Fatal Infections with Novel, High (H5N6 and H5N1) and Low (H7N9 and H9N2) Pathogenicity Avian Influenza A Viruses. International Journal of Environmental Research and Public Health. 2017;14(3):263.

37. Reperant LA, Kuiken T, Osterhaus ADME. Adaptive pathways of zoonotic influenza viruses: From exposure to establishment in humans. Vaccine. 2012;30(30):4419-34.
38. Waters K, Gao C, Ykema M, Han L, Voth L, Tao YJ, Wan X-F. Triple reassortment increases compatibility among viral ribonucleoprotein genes of contemporary avian and human influenza A viruses. PLOS Pathogens. 2021;17(10):e1009962.
39. Centers for Disease C, Prevention. 1918 Pandemic (H1N1 virus). Centers for Disease Control and Prevention. 2024.
40. Barro RJ, Ursúa JF, Weng J. The Coronavirus and the Great Influenza Pandemic: Lessons from the "Spanish Flu" for the Coronavirus's Potential Effects on Mortality and Economic Activity. National Bureau of Economic Research Working Paper Series. 2020;No. 26866.
41. Cheung PP, Rogozin IB, Choy KT, Ng HY, Peiris JS, Yen HL. Comparative mutational analyses of influenza A viruses. Rna. 2015;21(1):36-47.
42. Drake JW. Rates of spontaneous mutation among RNA viruses. Proc Natl Acad Sci U S A. 1993;90(9):4171-5.
43. Steinhauer DA, Holland JJ. Rapid evolution of RNA viruses. Annu Rev Microbiol. 1987;41:409-33.
44. Dou D, Revol R, Östbye H, Wang H, Daniels R. Influenza A Virus Cell Entry, Replication, Virion Assembly and Movement. Front Immunol. 2018;9:1581.
45. Bedford T, Suchard MA, Lemey P, Dudas G, Gregory V, Hay AJ, et al. Integrating influenza antigenic dynamics with molecular evolution. Elife. 2014;3:e01914.
46. World Health O. The Burden of Influenza. World Health Organization. 2023.
47. Klenk HD, Rott R, Orlich M, Blödorn J. Activation of influenza A viruses by trypsin treatment. Virology. 1975;68(2):426-39.
48. França MS, Brown JD. Influenza Pathobiology and Pathogenesis in Avian Species. In: Compans RW, Oldstone MBA, editors. Influenza Pathogenesis and Control - Volume I. Cham: Springer International Publishing; 2014. p. 221-42.
49. Jennelle CS, Carstensen M, Hildebrand EC, Cornicelli L, Wolf P, Grear DA, et al. Surveillance for Highly Pathogenic Avian Influenza Virus in Wild Birds during Outbreaks in Domestic Poultry, Minnesota, 2015. Emerg Infect Dis. 2016;22(7):1278-82.
50. Shinya K, Ebina M, Yamada S, Ono M, Kasai N, Kawaoka Y. Avian flu: influenza virus receptors in the human airway. Nature. 2006;440(7083):435-6.
51. Jia N, Barclay WS, Roberts K, Yen HL, Chan RW, Lam AK, et al. Glycomic characterization of respiratory tract tissues of ferrets: implications for its use in influenza virus infection studies. J Biol Chem. 2014;289(41):28489-504.
52. Singanayagam A, Zhou J, Elderfield RA, Frise R, Ashcroft J, Galiano M, et al. Characterising viable virus from air exhaled by H1N1 influenza-infected ferrets reveals the importance of haemagglutinin stability for airborne infectivity. PLoS Pathog. 2020;16(2):e1008362.
53. Cowling BJ, Ip DK, Fang VJ, Suntarattiwong P, Olsen SJ, Levy J, et al. Aerosol transmission is an important mode of influenza A virus spread. Nat Commun. 2013;4:1935.
54. Halwe NJ, Cool K, Breithaupt A, Schön J, Trujillo JD, Nooruzzaman M, et al. H5N1 clade 2.3.4.4b dynamics in experimentally infected calves and cows. Nature. 2025;637(8047):903-12.
55. Le Sage V, Campbell AJ, Reed DS, Duprex WP, Lakdawala SS. Persistence of Influenza H5N1 and H1N1 Viruses in Unpasteurized Milk on Milking Unit Surfaces. Emerg Infect Dis. 2024;30(8):1721-3.

56. Schafers J, Warren CJ, Yang J, Zhang J, Cole SJ, Cooper J, et al. Pasteurisation temperatures effectively inactivate influenza A viruses in milk. Nature Communications. 2025;16(1):1173.
57. Lowen AC, Mubareka S, Steel J, Palese P. Influenza virus transmission is dependent on relative humidity and temperature. PLoS Pathog. 2007;3(10):1470-6.
58. Yang W, Marr LC. Mechanisms by which ambient humidity may affect viruses in aerosols. Appl Environ Microbiol. 2012;78(19):6781-8.
59. Ng PS, Böhm R, Hartley-Tassell LE, Steen JA, Wang H, Lukowski SW, et al. Ferrets exclusively synthesize Neu5Ac and express naturally humanized influenza A virus receptors. Nat Commun. 2014;5:5750.
60. Suzuki Y, Ito T, Suzuki T, Holland RE, Jr., Chambers TM, Kiso M, et al. Sialic acid species as a determinant of the host range of influenza A viruses. J Virol. 2000;74(24):11825-31.
61. Rogers GN, Paulson JC. Receptor determinants of human and animal influenza virus isolates: differences in receptor specificity of the H3 hemagglutinin based on species of origin. Virology. 1983;127(2):361-73.
62. McAuley JL, Gilbertson BP, Trifkovic S, Brown LE, McKimm-Breschkin JL. Influenza Virus Neuraminidase Structure and Functions. Front Microbiol. 2019;10:39.
63. Iseli AN, Pohl MO, Glas I, Gaggioli E, Martínez-Barragán P, David SC, et al. The neuraminidase activity of influenza A virus determines the strain-specific sensitivity to neutralization by respiratory mucus. J Virol. 2023;97(10):e0127123.
64. Cohen M, Zhang XQ, Senaati HP, Chen HW, Varki NM, Schooley RT, Gagneux P. Influenza A penetrates host mucus by cleaving sialic acids with neuraminidase. Virol J. 2013;10:321.
65. Sher AC, Stacy MR, Reynolds SD, Chiang T. In vivo detection of pulmonary mucociliary clearance: present challenges and future directions. Eur Respir Rev. 2024;33(173).
66. Scholtissek C. Stability of infectious influenza A viruses at low pH and at elevated temperature. Vaccine. 1985;3(3):215-8.
67. Blumenkrantz D, Roberts KL, Shelton H, Lycett S, Barclay WS. The short stalk length of highly pathogenic avian influenza H5N1 virus neuraminidase limits transmission of pandemic H1N1 virus in ferrets. J Virol. 2013;87(19):10539-51.
68. Russell CJ, Hu M, Okda FA. Influenza Hemagglutinin Protein Stability, Activation, and Pandemic Risk. Trends Microbiol. 2018;26(10):841-53.
69. Hill EM, House T, Dhingra MS, Kalpravidh W, Morzaria S, Osmani MG, et al. The impact of surveillance and control on highly pathogenic avian influenza outbreaks in poultry in Dhaka division, Bangladesh. PLoS Comput Biol. 2018;14(9):e1006439.
70. World Health O. Recommended composition of influenza virus vaccines for use in the 2024–2025 northern hemisphere influenza season [WHO Meeting Report]. 2024 [updated 2024/02/23. Available from: https://www.who.int/publications/m/item/recommended-composition-of-influenza-virus-vaccines-for-use-in-the-2024-2025-northern-hemisphere-influenza-season.
71. Centers for Disease C, Prevention. Interim Guidance on the Use of Antiviral Drugs for Treatment of Human Infections with Avian Influenza A Viruses. Centers for Disease Control and Prevention. 2024.
72. Omoto S, Speranzini V, Hashimoto T, Noshi T, Yamaguchi H, Kawai M, et al. Characterization of influenza virus variants induced by treatment with the endonuclease inhibitor baloxavir marboxil. Sci Rep. 2018;8(1):9633.

73. Todd B, Tchesnokov E, Götte M. The active form of the influenza cap-snatching endonuclease inhibitor baloxavir marboxil is a tight binding inhibitor. Journal of Biological Chemistry. 2021;296:100486.
74. Agrawal U, Raju R, Udwadia ZF. Favipiravir: A new and emerging antiviral option in COVID-19. Med J Armed Forces India. 2020;76(4):370-6.
75. Dong G, Peng C, Luo J, Wang C, Han L, Wu B, et al. Adamantane-Resistant Influenza A Viruses in the World (1902–2013): Frequency and Distribution of M2 Gene Mutations. PLOS ONE. 2015;10(3):e0119115.
76. Eisfeld AJ, Neumann G, Kawaoka Y. At the centre: influenza A virus ribonucleoproteins. Nature Reviews Microbiology. 2015;13(1):28-41.
77. te Velthuis AJW, Grimes JM, Fodor E. Structural insights into RNA polymerases of negative-sense RNA viruses. Nature Reviews Microbiology. 2021;19(5):303-18.
78. Coloma R, Arranz R, de la Rosa-Trevín JM, Sorzano COS, Munier S, Carlero D, et al. Structural insights into influenza A virus ribonucleoproteins reveal a processive helical track as transcription mechanism. Nature Microbiology. 2020;5(5):727-34.
79. Pons MW, Schulze IT, Hirst GK. Isolation and characterization of the ribonucleoprotein of influenza virus. Virology. 1969;39(2):250-9.
80. Zhu Z, Fodor E, Keown JR. A structural understanding of influenza virus genome replication. Trends Microbiol. 2023;31(3):308-19.
81. Li X, Gu M, Zheng Q, Gao R, Liu X. Packaging signal of influenza A virus. Virol J. 2021;18(1):36.
82. Chauhan RP, Gordon ML. An overview of influenza A virus genes, protein functions, and replication cycle highlighting important updates. Virus Genes. 2022;58(4):255-69.
83. Pinto RM, Lycett S, Gaunt E, Digard P. Accessory Gene Products of Influenza A Virus. Cold Spring Harb Perspect Med. 2021;11(12).
84. Chen W, Calvo PA, Malide D, Gibbs J, Schubert U, Bacik I, et al. A novel influenza A virus mitochondrial protein that induces cell death. Nature Medicine. 2001;7(12):1306-12.
85. Chakrabarti AK, Pasricha G. An insight into the PB1F2 protein and its multifunctional role in enhancing the pathogenicity of the influenza A viruses. Virology. 2013;440(2):97-104.
86. Guilligay D, Tarendeau F, Resa-Infante P, Coloma R, Crepin T, Sehr P, et al. The structural basis for cap binding by influenza virus polymerase subunit PB2. Nat Struct Mol Biol. 2008;15(5):500-6.
87. Hara K, Schmidt FI, Crow M, Brownlee GG. Amino acid residues in the N-terminal region of the PA subunit of influenza A virus RNA polymerase play a critical role in protein stability, endonuclease activity, cap binding, and virion RNA promoter binding. J Virol. 2006;80(16):7789-98.
88. Hoffmann M, Pöhlmann S. Cell Entry of Influenza A Viruses: Sweet Talk between HA and Ca(V)1.2. Cell Host Microbe. 2018;23(6):697-9.
89. Ozawa M, Fujii K, Muramoto Y, Yamada S, Yamayoshi S, Takada A, et al. Contributions of two nuclear localization signals of influenza A virus nucleoprotein to viral replication. J Virol. 2007;81(1):30-41.
90. Yu M, Liu X, Cao S, Zhao Z, Zhang K, Xie Q, et al. Identification and characterization of three novel nuclear export signals in the influenza A virus nucleoprotein. J Virol. 2012;86(9):4970-80.
91. Peukes J, Xiong X, Erlendsson S, Qu K, Wan W, Calder LJ, et al. The native structure of the assembled matrix protein 1 of influenza A virus. Nature. 2020;587(7834):495-8.

92. Kordyukova LV, Shtykova EV, Baratova LA, Svergun DI, Batishchev OV. Matrix proteins of enveloped viruses: a case study of Influenza A virus M1 protein. J Biomol Struct Dyn. 2019;37(3):671-90.
93. Bourmakina SV, García-Sastre A. Reverse genetics studies on the filamentous morphology of influenza A virus. Journal of General Virology. 2003;84(3):517-27.
94. Cady SD, Luo W, Hu F, Hong M. Structure and function of the influenza A M2 proton channel. Biochemistry. 2009;48(31):7356-64.
95. Kim HJ, Jeong MS, Jang SB. Structure and Activities of the NS1 Influenza Protein and Progress in the Development of Small-Molecule Drugs. Int J Mol Sci. 2021;22(8).
96. Şenbaş Akyazi B, Pirinçal A, Kawaguchi A, Nagata K, Turan K. Interaction of influenza A virus NS2/NEP protein with the amino-terminal part of Nup214. Turk J Biol. 2020;44(2):82-92.
97. Reuther P, Giese S, Götz V, Kilb N, Mänz B, Brunotte L, Schwemmle M. Adaptive mutations in the nuclear export protein of human-derived H5N1 strains facilitate a polymerase activity-enhancing conformation. J Virol. 2014;88(1):263-71.
98. Lazarowitz SG, Choppin PW. Enhancement of the infectivity of influenza A and B viruses by proteolytic cleavage of the hemagglutinin polypeptide. Virology. 1975;68(2):440-54.
99. Böttcher E, Matrosovich T, Beyerle M, Klenk HD, Garten W, Matrosovich M. Proteolytic activation of influenza viruses by serine proteases TMPRSS2 and HAT from human airway epithelium. J Virol. 2006;80(19):9896-8.
100. Roy AM, Parker JS, Parrish CR, Whittaker GR. Early stages of influenza virus entry into Mv-1 lung cells: involvement of dynamin. Virology. 2000;267(1):17-28.
101. Chen C, Zhuang X. Epsin 1 is a cargo-specific adaptor for the clathrin-mediated endocytosis of the influenza virus. Proc Natl Acad Sci U S A. 2008;105(33):11790-5.
102. de Vries E, Tscherne DM, Wienholts MJ, Cobos-Jiménez V, Scholte F, García-Sastre A, et al. Dissection of the influenza A virus endocytic routes reveals macropinocytosis as an alternative entry pathway. PLoS Pathog. 2011;7(3):e1001329.
103. Bullough PA, Hughson FM, Skehel JJ, Wiley DC. Structure of influenza haemagglutinin at the pH of membrane fusion. Nature. 1994;371(6492):37-43.
104. White JM, Whittaker GR. Fusion of Enveloped Viruses in Endosomes. Traffic. 2016;17(6):593-614.
105. Martin K, Helenius A. Nuclear transport of influenza virus ribonucleoproteins: the viral matrix protein (M1) promotes export and inhibits import. Cell. 1991;67(1):117-30.
106. Martin K, Helenius A. Transport of incoming influenza virus nucleocapsids into the nucleus. J Virol. 1991;65(1):232-44.
107. Wu WW, Weaver LL, Panté N. Ultrastructural analysis of the nuclear localization sequences on influenza A ribonucleoprotein complexes. J Mol Biol. 2007;374(4):910-6.
108. Staller E, Barclay WS. Host Cell Factors That Interact with Influenza Virus Ribonucleoproteins. Cold Spring Harb Perspect Med. 2021;11(11).
109. Kutay U, Bischoff FR, Kostka S, Kraft R, Görlich D. Export of importin alpha from the nucleus is mediated by a specific nuclear transport factor. Cell. 1997;90(6):1061-71.

110. Plotch SJ, Bouloy M, Ulmanen I, Krug RM. A unique cap(m7GpppXm)-dependent influenza virion endonuclease cleaves capped RNAs to generate the primers that initiate viral RNA transcription. Cell. 1981;23(3):847-58.
111. Walker AP, Fodor E. Interplay between Influenza Virus and the Host RNA Polymerase II Transcriptional Machinery. Trends in Microbiology. 2019;27(5):398-407.
112. Dias A, Bouvier D, Crépin T, McCarthy AA, Hart DJ, Baudin F, et al. The cap-snatching endonuclease of influenza virus polymerase resides in the PA subunit. Nature. 2009;458(7240):914-8.
113. Poon LL, Pritlove DC, Fodor E, Brownlee GG. Direct evidence that the poly(A) tail of influenza A virus mRNA is synthesized by reiterative copying of a U track in the virion RNA template. J Virol. 1999;73(4):3473-6.
114. Wang W, Cui ZQ, Han H, Zhang ZP, Wei HP, Zhou YF, et al. Imaging and characterizing influenza A virus mRNA transport in living cells. Nucleic Acids Res. 2008;36(15):4913-28.
115. Cros JF, García-Sastre A, Palese P. An unconventional NLS is critical for the nuclear import of the influenza A virus nucleoprotein and ribonucleoprotein. Traffic. 2005;6(3):205-13.
116. Deng T, Engelhardt OG, Thomas B, Akoulitchev AV, Brownlee GG, Fodor E. Role of ran binding protein 5 in nuclear import and assembly of the influenza virus RNA polymerase complex. J Virol. 2006;80(24):11911-9.
117. Hutchinson EC, Orr OE, Man Liu S, Engelhardt OG, Fodor E. Characterization of the interaction between the influenza A virus polymerase subunit PB1 and the host nuclear import factor Ran-binding protein 5. J Gen Virol. 2011;92(Pt 8):1859-69.
118. Carrique L, Fan H, Walker AP, Keown JR, Sharps J, Staller E, et al. Host ANP32A mediates the assembly of the influenza virus replicase. Nature. 2020;587(7835):638-43.
119. Wang F, Sheppard CM, Mistry B, Staller E, Barclay WS, Grimes JM, et al. The C-terminal LCAR of host ANP32 proteins interacts with the influenza A virus nucleoprotein to promote the replication of the viral RNA genome. Nucleic Acids Res. 2022;50(10):5713-25.
120. Fan H, Walker AP, Carrique L, Keown JR, Serna Martin I, Karia D, et al. Structures of influenza A virus RNA polymerase offer insight into viral genome replication. Nature. 2019;573(7773):287-90.
121. Hutchinson EC, Charles PD, Hester SS, Thomas B, Trudgian D, Martínez-Alonso M, Fodor E. Conserved and host-specific features of influenza virion architecture. Nature Communications. 2014;5(1):4816.
122. Luczo JM, Spackman E. Molecular Evolution of the H5 and H7 Highly Pathogenic Avian Influenza Virus Haemagglutinin Cleavage Site Motif. Reviews in Medical Virology. 2025;35(1):e70012.
123. Zhirnov OP, Ikizler MR, Wright PF. Cleavage of influenza a virus hemagglutinin in human respiratory epithelium is cell associated and sensitive to exogenous antiproteases. J Virol. 2002;76(17):8682-9.
124. Marjuki H, Alam MI, Ehrhardt C, Wagner R, Planz O, Klenk HD, et al. Membrane accumulation of influenza A virus hemagglutinin triggers nuclear export of the viral genome via protein kinase Calpha-mediated activation of ERK signaling. J Biol Chem. 2006;281(24):16707-15.
125. Neumann G, Hughes MT, Kawaoka Y. Influenza A virus NS2 protein mediates vRNP nuclear export through NES-independent interaction with hCRM1. Embo j. 2000;19(24):6751-8.

126. Elton D, Simpson-Holley M, Archer K, Medcalf L, Hallam R, McCauley J, Digard P. Interaction of the influenza virus nucleoprotein with the cellular CRM1-mediated nuclear export pathway. J Virol. 2001;75(1):408-19.
127. O'Neill RE, Talon J, Palese P. The influenza virus NEP (NS2 protein) mediates the nuclear export of viral ribonucleoproteins. Embo j. 1998;17(1):288-96.
128. Petosa C, Schoehn G, Askjaer P, Bauer U, Moulin M, Steuerwald U, et al. Architecture of CRM1/Exportin1 suggests how cooperativity is achieved during formation of a nuclear export complex. Mol Cell. 2004;16(5):761-75.
129. Eisfeld AJ, Kawakami E, Watanabe T, Neumann G, Kawaoka Y. RAB11A Is Essential for Transport of the Influenza Virus Genome to the Plasma Membrane. Journal of Virology. 2011;85(13):6117-26.
130. Veler H, Fan H, Keown JR, Sharps J, Fournier M, Grimes JM, Fodor E. The C-Terminal Domains of the PB2 Subunit of the Influenza A Virus RNA Polymerase Directly Interact with Cellular GTPase Rab11a. J Virol. 2022;96(5):e0197921.
131. Kawaguchi A, Hirohama M, Harada Y, Osari S, Nagata K. Influenza Virus Induces Cholesterol-Enriched Endocytic Recycling Compartments for Budozone Formation via Cell Cycle-Independent Centrosome Maturation. PLoS Pathog. 2015;11(11):e1005284.
132. de Castro Martin IF, Fournier G, Sachse M, Pizarro-Cerda J, Risco C, Naffakh N. Influenza virus genome reaches the plasma membrane via a modified endoplasmic reticulum and Rab11-dependent vesicles. Nature Communications. 2017;8(1):1396.
133. Alenquer M, Vale-Costa S, Etibor TA, Ferreira F, Sousa AL, Amorim MJ. Influenza A virus ribonucleoproteins form liquid organelles at endoplasmic reticulum exit sites. Nat Commun. 2019;10(1):1629.
134. Vale-Costa S, Etibor TA, Brás D, Sousa AL, Ferreira M, Martins GG, et al. ATG9A regulates the dissociation of recycling endosomes from microtubules to form liquid influenza A virus inclusions. PLoS Biol. 2023;21(11):e3002290.
135. Schmitt AP, Lamb RA. Influenza virus assembly and budding at the viral budozone. Adv Virus Res. 2005;64:383-416.
136. Barman S, Nayak DP. Analysis of the transmembrane domain of influenza virus neuraminidase, a type II transmembrane glycoprotein, for apical sorting and raft association. J Virol. 2000;74(14):6538-45.
137. Zurcher T, Luo G, Palese P. Mutations at palmitylation sites of the influenza virus hemagglutinin affect virus formation. J Virol. 1994;68(9):5748-54.
138. Takeda M, Leser GP, Russell CJ, Lamb RA. Influenza virus hemagglutinin concentrates in lipid raft microdomains for efficient viral fusion. Proc Natl Acad Sci U S A. 2003;100(25):14610-7.
139. Rossman JS, Jing X, Leser GP, Lamb RA. Influenza virus M2 protein mediates ESCRT-independent membrane scission. Cell. 2010;142(6):902-13.
140. Ali A, Avalos RT, Ponimaskin E, Nayak DP. Influenza virus assembly: effect of influenza virus glycoproteins on the membrane association of M1 protein. J Virol. 2000;74(18):8709-19.
141. Jakob C, Paul-Stansilaus R, Schwemmle M, Marquet R, Bolte H. The influenza A virus genome packaging network — complex, flexible and yet unsolved. Nucleic Acids Research. 2022;50(16):9023-38.
142. Noton SL, Medcalf E, Fisher D, Mullin AE, Elton D, Digard P. Identification of the domains of the influenza A virus M1 matrix protein required for NP binding, oligomerization and incorporation into virions. J Gen Virol. 2007;88(Pt 8):2280-90.

143. Brooke CB, Ince WL, Wrammert J, Ahmed R, Wilson PC, Bennink JR, Yewdell JW. Most influenza a virions fail to express at least one essential viral protein. Journal of virology. 2013;87(6):3155-62.
144. Chen BJ, Leser GP, Morita E, Lamb RA. Influenza virus hemagglutinin and neuraminidase, but not the matrix protein, are required for assembly and budding of plasmid-derived virus-like particles. J Virol. 2007;81(13):7111-23.
145. Chlanda P, Schraidt O, Kummer S, Riches J, Oberwinkler H, Prinz S, et al. Structural Analysis of the Roles of Influenza A Virus Membrane-Associated Proteins in Assembly and Morphology. J Virol. 2015;89(17):8957-66.
146. Hilsch M, Goldenbogen B, Sieben C, Höfer CT, Rabe JP, Klipp E, et al. Influenza A matrix protein M1 multimerizes upon binding to lipid membranes. Biophys J. 2014;107(4):912-23.
147. Guarner J, Shieh WJ, Dawson J, Subbarao K, Shaw M, Ferebee T, et al. Immunohistochemical and in situ hybridization studies of influenza A virus infection in human lungs. Am J Clin Pathol. 2000;114(2):227-33.
148. Gallagher ME, Brooke CB, Ke R, Koelle K. Causes and Consequences of Spatial Within-Host Viral Spread. Viruses. 2018;10(11).
149. Pirillo C, Al Khalidi S, Sims A, Devlin R, Zhao H, Pinto R, et al. Cotransfer of antigen and contextual information harmonizes peripheral and lymph node conventional dendritic cell activation. Sci Immunol. 2023;8(85):eadg8249.
150. Ferreri LM, Seibert B, Caceres CJ, Patatanian K, Holmes KE, Gay LC, et al. Dispersal of influenza virus populations within the respiratory tract shapes their evolutionary potential. Proceedings of the National Academy of Sciences. 2025;122(4):e2419985122.
151. Zath GK, Thomas MM, Loveday EK, Bikos DA, Sanche S, Ke R, et al. Influenza A viral burst size from thousands of infected single cells using droplet quantitative PCR (dqPCR). PLOS Pathogens. 2024;20(7):e1012257.
152. Fukuyama S, Katsura H, Zhao D, Ozawa M, Ando T, Shoemaker JE, et al. Multi-spectral fluorescent reporter influenza viruses (Color-flu) as powerful tools for in vivo studies. Nat Commun. 2015;6:6600.
153. Hallatschek O, Nelson DR. Gene surfing in expanding populations. Theor Popul Biol. 2008;73(1):158-70.
154. McCrone JT, Woods RJ, Martin ET, Malosh RE, Monto AS, Lauring AS. Stochastic processes constrain the within and between host evolution of influenza virus. Elife. 2018;7.
155. Waters JM, Fraser CI, Hewitt GM. Founder takes all: density-dependent processes structure biodiversity. Trends Ecol Evol. 2013;28(2):78-85.
156. Mosley VM, Wyckoff RWG. Electron Micrography of the Virus of Influenza. Nature. 1946;157(3983):263-.
157. Vijayakrishnan S, Loney C, Jackson D, Suphamungmee W, Rixon FJ, Bhella D. Cryotomography of budding influenza A virus reveals filaments with diverse morphologies that mostly do not bear a genome at their distal end. PLoS pathogens. 2013;9(6):e1003413.
158. Dadonaite B, Vijayakrishnan S, Fodor E, Bhella D, Hutchinson EC. Filamentous influenza viruses. J Gen Virol. 2016;97(8):1755-64.
159. Seladi-Schulman J, Steel J, Lowen AC. Spherical influenza viruses have a fitness advantage in embryonated eggs, while filament-producing strains are selected in vivo. J Virol. 2013;87(24):13343-53.
160. Choppin PW, Murphy JS, Tamm I. Studies of two kinds of virus particles which comprise influenza A2 virus strains. III. Morphological characteristics: independence to morphological and functional traits. J Exp Med. 1960;112(5):945-52.

161. Chu CM, Dawson IM, Elford WJ. FILAMENTOUS FORMS ASSOCIATED WITH NEWLY ISOLATED INFLUENZA VIRUS. The Lancet. 1949;253(6554):602-3.
162. Li T, Li Z, Deans EE, Mittler E, Liu M, Chandran K, Ivanovic T. The shape of pleomorphic virions determines resistance to cell-entry pressure. Nature Microbiology. 2021;6(5):617-29.
163. Sims A, Tornaletti LB, Jasim S, Pirillo C, Devlin R, Hirst JC, et al. Superinfection exclusion creates spatially distinct influenza virus populations. PLoS Biol. 2023;21(2):e3001941.
164. Phipps KL, Ganti K, Jacobs NT, Lee CY, Carnaccini S, White MC, et al. Collective interactions augment influenza A virus replication in a host-dependent manner. Nat Microbiol. 2020;5(9):1158-69.
165. Marshall N, Priyamvada L, Ende Z, Steel J, Lowen AC. Influenza virus reassortment occurs with high frequency in the absence of segment mismatch. PLoS Pathog. 2013;9(6):e1003421.
166. Tao H, Li L, White MC, Steel J, Lowen AC. Influenza A Virus Coinfection through Transmission Can Support High Levels of Reassortment. J Virol. 2015;89(16):8453-61.
167. Wille M, Tolf C, Avril A, Latorre-Margalef N, Wallerström S, Olsen B, Waldenström J. Frequency and patterns of reassortment in natural influenza A virus infection in a reservoir host. Virology. 2013;443(1):150-60.
168. Ziegler CM, Botten JW. Defective Interfering Particles of Negative-Strand RNA Viruses. Trends in Microbiology. 2020;28(7):554-65.
169. Brennan JW, Sun Y. Defective viral genomes: advances in understanding their generation, function, and impact on infection outcomes. mBio. 2024;15(5).
170. Mendes M, Russell AB. Library-based analysis reveals segment and length dependent characteristics of defective influenza genomes. PLOS Pathogens. 2021;17(12):e1010125.
171. Rezelj VV, Levi LI, Vignuzzi M. The defective component of viral populations. Current Opinion in Virology. 2018;33:74-80.
172. Duprex WP, McQuaid S, Hangartner L, Billeter Martin A, Rima Bert K. Observation of Measles Virus Cell-to-Cell Spread in Astrocytoma Cells by Using a Green Fluorescent Protein-Expressing Recombinant Virus. Journal of Virology. 1999;73(11):9568-75.
173. Cifuentes-Muñoz N, Dutch RE, Cattaneo R. Direct cell-to-cell transmission of respiratory viruses: The fast lanes. PLoS Pathog. 2018;14(6):e1007015.
174. Takeuchi K, Miyajima N, Nagata N, Takeda M, Tashiro M. Wild-type measles virus induces large syncytium formation in primary human small airway epithelial cells by a SLAM(CD150)-independent mechanism. Virus Res. 2003;94(1):11-6.
175. Xie M. Virus-Induced Cell Fusion and Syncytia Formation. In: Kloc M, Uosef A, editors. Syncytia: Origin, Structure, and Functions. Cham: Springer International Publishing; 2024. p. 283-318.
176. Singh BK, Hornick AL, Krishnamurthy S, Locke AC, Mendoza CA, Mateo M, et al. The Nectin-4/Afadin Protein Complex and Intercellular Membrane Pores Contribute to Rapid Spread of Measles Virus in Primary Human Airway Epithelia. J Virol. 2015;89(14):7089-96.
177. Singh BK, Pfaller CK, Cattaneo R, Sinn PL. Measles Virus Ribonucleoprotein Complexes Rapidly Spread across Well-Differentiated Primary Human Airway Epithelial Cells along F-Actin Rings. mBio. 2019;10(6).
178. Mateo M, Generous A, Sinn PL, Cattaneo R. Connections matter--how viruses use cell–cell adhesion components. J Cell Sci. 2015;128(3):431-9.

179. Brimacombe CL, Grove J, Meredith LW, Hu K, Syder AJ, Flores MV, et al. Neutralizing antibody-resistant hepatitis C virus cell-to-cell transmission. J Virol. 2011;85(1):596-605.
180. Timpe JM, Stamataki Z, Jennings A, Hu K, Farquhar MJ, Harris HJ, et al. Hepatitis C virus cell-cell transmission in hepatoma cells in the presence of neutralizing antibodies. Hepatology. 2008;47(1):17-24.
181. Dingwell KS, Brunetti CR, Hendricks RL, Tang Q, Tang M, Rainbow AJ, Johnson DC. Herpes simplex virus glycoproteins E and I facilitate cell-to-cell spread in vivo and across junctions of cultured cells. J Virol. 1994;68(2):834-45.
182. Dingwell KS, Johnson DC. The herpes simplex virus gE-gI complex facilitates cell-to-cell spread and binds to components of cell junctions. J Virol. 1998;72(11):8933-42.
183. Garrod D, Chidgey M. Desmosome structure, composition and function. Biochimica et Biophysica Acta (BBA) - Biomembranes. 2008;1778(3):572-87.
184. Labudova M, Tomaskova J, Skultety L, Pastorek J, Pastorekova S. The nucleoprotein of lymphocytic choriomeningitis virus facilitates spread of persistent infection through stabilization of the keratin network. J Virol. 2009;83(16):7842-9.
185. Tishchenko A, Romero N, Van Waesberghe C, Delva JL, Vickman O, Smith GA, et al. Pseudorabies virus infection triggers pUL46-mediated phosphorylation of connexin-43 and closure of gap junctions to promote intercellular virus spread. PLOS Pathogens. 2025;21(1):e1012895.
186. Jolly C, Sattentau QJ. Retroviral spread by induction of virological synapses. Traffic. 2004;5(9):643-50.
187. Igakura T, Stinchcombe JC, Goon PK, Taylor GP, Weber JN, Griffiths GM, et al. Spread of HTLV-I between lymphocytes by virus-induced polarization of the cytoskeleton. Science. 2003;299(5613):1713-6.
188. McDonald D, Wu L, Bohks SM, KewalRamani VN, Unutmaz D, Hope TJ. Recruitment of HIV and its receptors to dendritic cell-T cell junctions. Science. 2003;300(5623):1295-7.
189. Hübner W, McNerney GP, Chen P, Dale BM, Gordon RE, Chuang FY, et al. Quantitative 3D video microscopy of HIV transfer across T cell virological synapses. Science. 2009;323(5922):1743-7.
190. Mattila PK, Lappalainen P. Filopodia: molecular architecture and cellular functions. Nat Rev Mol Cell Biol. 2008;9(6):446-54.
191. Disanza A, Bisi S, Winterhoff M, Milanesi F, Ushakov DS, Kast D, et al. CDC42 switches IRSp53 from inhibition of actin growth to elongation by clustering of VASP. Embo j. 2013;32(20):2735-50.
192. Kast DJ, Yang C, Disanza A, Boczkowska M, Madasu Y, Scita G, et al. Mechanism of IRSp53 inhibition and combinatorial activation by Cdc42 and downstream effectors. Nature Structural & Molecular Biology. 2014;21(4):413-22.
193. Henderson JM, Ljubojevic N, Belian S, Chaze T, Castaneda D, Battistella A, et al. Tunnelling nanotube formation is driven by Eps8/IRSp53-dependent linear actin polymerization. The EMBO Journal. 2023;42(24):e113761.
194. Sherer NM, Lehmann MJ, Jimenez-Soto LF, Horensavitz C, Pypaert M, Mothes W. Retroviruses can establish filopodial bridges for efficient cell-to-cell transmission. Nature cell biology. 2007;9(3):310-5.
195. Jouvenet N, Windsor M, Rietdorf J, Hawes P, Monaghan P, Way M, Wileman T. African swine fever virus induces filopodia-like projections at the plasma membrane. Cell Microbiol. 2006;8(11):1803-11.

196. Martinez MG, Kielian M. Intercellular Extensions Are Induced by the Alphavirus Structural Proteins and Mediate Virus Transmission. PLoS Pathog. 2016;12(12):e1006061.
197. Mullins RD, Heuser JA, Pollard TD. The interaction of Arp2/3 complex with actin: nucleation, high affinity pointed end capping, and formation of branching networks of filaments. Proc Natl Acad Sci U S A. 1998;95(11):6181-6.
198. Mellor H. The role of formins in filopodia formation. Biochimica et Biophysica Acta (BBA) - Molecular Cell Research. 2010;1803(2):191-200.
199. Stokes GV. High-voltage electron microscope study of the release of vaccinia virus from whole cells. J Virol. 1976;18(2):636-43.
200. Cifuentes-Munoz N, El Najjar F, Dutch RE. Viral cell-to-cell spread: Conventional and non-conventional ways. Adv Virus Res. 2020;108:85-125.
201. Doceul V, Hollinshead M, van der Linden L, Smith GL. Repulsion of superinfecting virions: a mechanism for rapid virus spread. Science. 2010;327(5967):873-6.
202. Rustom A, Saffrich R, Markovic I, Walther P, Gerdes H-H. Nanotubular highways for intercellular organelle transport. Science. 2004;303(5660):1007-10.
203. Vignais M-L, Caicedo A, Brondello J-M, Jorgensen C. Cell Connections by Tunneling Nanotubes: Effects of Mitochondrial Trafficking on Target Cell Metabolism, Homeostasis, and Response to Therapy. Stem Cells International. 2017;2017(1):6917941.
204. Tiwari V, Koganti R, Russell G, Sharma A, Shukla D. Role of Tunneling Nanotubes in Viral Infection, Neurodegenerative Disease, and Cancer. Front Immunol. 2021;12:680891.
205. Turos-Korgul L, Kolba MD, Chroscicki P, Zieminska A, Piwocka K. Tunneling Nanotubes Facilitate Intercellular Protein Transfer and Cell Networks Function. Front Cell Dev Biol. 2022;10:915117.
206. Okafo G, Prevedel L, Eugenin E. Tunneling nanotubes (TNT) mediate long-range gap junctional communication: Implications for HIV cell to cell spread. Sci Rep. 2017;7(1):16660.
207. Byford O, Shaw A, Tse HN, Moon-Walker A, Saphire E, Whelan S, et al. Lymphocytic choriomeningitis arenavirus utilises intercellular connections for cell to cell spread. Scientific Reports. 2024;14.
208. Gousset K, Marzo L, Commere PH, Zurzolo C. Myo10 is a key regulator of TNT formation in neuronal cells. J Cell Sci. 2013;126(Pt 19):4424-35.
209. Gurke S, Barroso JFV, Hodneland E, Bukoreshtliev NV, Schlicker O, Gerdes H-H. Tunneling nanotube (TNT)-like structures facilitate a constitutive, actomyosin-dependent exchange of endocytic organelles between normal rat kidney cells. Experimental Cell Research. 2008;314(20):3669-83.
210. Gerdes H-H, Bukoreshtliev NV, Barroso JFV. Tunneling nanotubes: A new route for the exchange of components between animal cells. FEBS Letters. 2007;581(11):2194-201.
211. Onfelt B, Nedvetzki S, Benninger RK, Purbhoo MA, Sowinski S, Hume AN, et al. Structurally distinct membrane nanotubes between human macrophages support long-distance vesicular traffic or surfing of bacteria. J Immunol. 2006;177(12):8476-83.
212. Eugenin EA, Gaskill PJ, Berman JW. Tunneling nanotubes (TNT) are induced by HIV-infection of macrophages: a potential mechanism for intercellular HIV trafficking. Cell Immunol. 2009;254(2):142-8.
213. Sowinski S, Jolly C, Berninghausen O, Purbhoo MA, Chauveau A, Köhler K, et al. Membrane nanotubes physically connect T cells over long distances presenting a novel route for HIV-1 transmission. Nature Cell Biology. 2008;10(2):211-9.

214. Boullé M, Müller TG, Dähling S, Ganga Y, Jackson L, Mahamed D, et al. HIV Cell-to-Cell Spread Results in Earlier Onset of Viral Gene Expression by Multiple Infections per Cell. PLoS Pathog. 2016;12(11):e1005964.
215. Chen P, Hübner W, Spinelli MA, Chen BK. Predominant mode of human immunodeficiency virus transfer between T cells is mediated by sustained Env-dependent neutralization-resistant virological synapses. J Virol. 2007;81(22):12582-95.
216. Kolodkin-Gal D, Hulot SL, Korioth-Schmitz B, Gombos RB, Zheng Y, Owuor J, et al. Efficiency of cell-free and cell-associated virus in mucosal transmission of human immunodeficiency virus type 1 and simian immunodeficiency virus. J Virol. 2013;87(24):13589-97.
217. Del Portillo A, Tripodi J, Najfeld V, Wodarz D, Levy DN, Chen BK. Multiploid inheritance of HIV-1 during cell-to-cell infection. J Virol. 2011;85(14):7169-76.
218. Sanjuán R, Thoulouze MI. Why viruses sometimes disperse in groups?(†). Virus Evol. 2019;5(1):vez014.
219. Sanjuán R. Collective Infectious Units in Viruses. Trends Microbiol. 2017;25(5):402-12.
220. Favoreel HW, Van Minnebruggen G, Adriaensen D, Nauwynck HJ. Cytoskeletal rearrangements and cell extensions induced by the US3 kinase of an alphaherpesvirus are associated with enhanced spread. Proc Natl Acad Sci U S A. 2005;102(25):8990-5.
221. El Najjar F, Cifuentes-Muñoz N, Chen J, Zhu H, Buchholz UJ, Moncman CL, Dutch RE. Human metapneumovirus Induces Reorganization of the Actin Cytoskeleton for Direct Cell-to-Cell Spread. PLOS Pathogens. 2016;12(9):e1005922.
222. Roberts KL, Manicassamy B, Lamb RA. Influenza A virus uses intercellular connections to spread to neighboring cells. J Virol. 2015;89(3):1537-49.
223. Kumar A, Kim JH, Ranjan P, Metcalfe MG, Cao W, Mishina M, et al. Influenza virus exploits tunneling nanotubes for cell-to-cell spread. Scientific Reports. 2017;7(1):40360.
224. Jolly C, Booth NJ, Neil SJ. Cell-cell spread of human immunodeficiency virus type 1 overcomes tetherin/BST-2-mediated restriction in T cells. J Virol. 2010;84(23):12185-99.
225. Richardson MW, Carroll RG, Stremlau M, Korokhov N, Humeau LM, Silvestri G, et al. Mode of transmission affects the sensitivity of human immunodeficiency virus type 1 to restriction by rhesus TRIM5alpha. J Virol. 2008;82(22):11117-28.
226. Zhong P, Agosto LM, Ilinskaya A, Dorjbal B, Truong R, Derse D, et al. Cell-to-cell transmission can overcome multiple donor and target cell barriers imposed on cell-free HIV. PLoS One. 2013;8(1):e53138.
227. Mori K, Haruyama T, Nagata K. Tamiflu-Resistant but HA-Mediated Cell-to-Cell Transmission through Apical Membranes of Cell-Associated Influenza Viruses. PloS one. 2011;6:e28178.
228. Sun X, Tse LV, Ferguson AD, Whittaker GR. Modifications to the Hemagglutinin Cleavage Site Control the Virulence of a Neurotropic H1N1 Influenza Virus. Journal of Virology. 2010;84(17):8683-90.
229. Pinto LH, Holsinger LJ, Lamb RA. Influenza virus M2 protein has ion channel activity. Cell. 1992;69(3):517-28.
230. Ganti K, Han J, Manicassamy B, Lowen AC. Rab11a mediates cell-cell spread and reassortment of influenza A virus genomes via tunneling nanotubes. PLoS Pathog. 2021;17(9):e1009321.
231. Kongsomros S, Manopwisedjaroen S, Chaopreecha J, Wang S-F, Borwornpinyo S, Thitithanyanont A. Rapid and Efficient Cell-to-Cell Transmission

of Avian Influenza H5N1 Virus in MDCK Cells Is Achieved by Trogocytosis. Pathogens. 2021;10(4):483.
232. Matejka N, Reindl J. Perspectives of cellular communication through tunneling nanotubes in cancer cells and the connection to radiation effects. Radiat Oncol. 2019;14(1):218.
233. Ljubojevic N, Henderson JM, Zurzolo C. The Ways of Actin: Why Tunneling Nanotubes Are Unique Cell Protrusions. Trends Cell Biol. 2021;31(2):130-42.
234. Sun X, Wang Y, Zhang J, Tu J, Wang XJ, Su XD, et al. Tunneling-nanotube direction determination in neurons and astrocytes. Cell Death Dis. 2012;3(12):e438.
235. Dagar S, Pathak D, Oza HV, Mylavarapu SVS. Tunneling nanotubes and related structures: molecular mechanisms of formation and function. Biochemical Journal. 2021;478(22):3977-98.
236. Vargas JY, Loria F, Wu YJ, Córdova G, Nonaka T, Bellow S, et al. The Wnt/Ca(2+) pathway is involved in interneuronal communication mediated by tunneling nanotubes. Embo j. 2019;38(23):e101230.
237. Abounit S, Zurzolo C. Wiring through tunneling nanotubes – from electrical signals to organelle transfer. Journal of Cell Science. 2012;125(5):1089-98.
238. Cordero Cervantes D, Zurzolo C. Peering into tunneling nanotubes—The path forward. The EMBO Journal. 2021;40(8):e105789.
239. Hase K, Kimura S, Takatsu H, Ohmae M, Kawano S, Kitamura H, et al. M-Sec promotes membrane nanotube formation by interacting with Ral and the exocyst complex. Nat Cell Biol. 2009;11(12):1427-32.
240. Delage E, Cervantes DC, Pénard E, Schmitt C, Syan S, Disanza A, et al. Differential identity of Filopodia and Tunneling Nanotubes revealed by the opposite functions of actin regulatory complexes. Scientific Reports. 2016;6(1):39632.
241. Jansens RJJ, Van den Broeck W, De Pelsmaeker S, Lamote JAS, Van Waesberghe C, Couck L, Favoreel HW. Pseudorabies Virus US3-Induced Tunneling Nanotubes Contain Stabilized Microtubules, Interact with Neighboring Cells via Cadherins, and Allow Intercellular Molecular Communication. J Virol. 2017;91(19).
242. Janke C, Bulinski JC. Post-translational regulation of the microtubule cytoskeleton: mechanisms and functions. Nat Rev Mol Cell Biol. 2011;12(12):773-86.
243. Osteikoetxea-Molnár A, Szabó-Meleg E, Tóth EA, Oszvald Á, Izsépi E, Kremlitzka M, et al. The growth determinants and transport properties of tunneling nanotube networks between B lymphocytes. Cell Mol Life Sci. 2016;73(23):4531-45.
244. Hanna SJ, McCoy-Simandle K, Miskolci V, Guo P, Cammer M, Hodgson L, Cox D. The Role of Rho-GTPases and actin polymerization during Macrophage Tunneling Nanotube Biogenesis. Scientific Reports. 2017;7(1):8547.
245. Sartori-Rupp A, Cordero Cervantes D, Pepe A, Gousset K, Delage E, Corroyer-Dulmont S, et al. Correlative cryo-electron microscopy reveals the structure of TNTs in neuronal cells. Nature Communications. 2019;10(1):342.
246. Sumi T, Matsumoto K, Takai Y, Nakamura T. Cofilin phosphorylation and actin cytoskeletal dynamics regulated by rho- and Cdc42-activated LIM-kinase 2. J Cell Biol. 1999;147(7):1519-32.
247. Ge J, Burnier L, Adamopoulou M, Kwa MQ, Schaks M, Rottner K, Brakebusch C. RhoA, Rac1, and Cdc42 differentially regulate αSMA and collagen I expression in mesenchymal stem cells. Journal of Biological Chemistry. 2018;293(24):9358-69.

248. Takenawa T, Suetsugu S. The WASP–WAVE protein network: connecting the membrane to the cytoskeleton. Nature Reviews Molecular Cell Biology. 2007;8(1):37-48.
249. Pergu R, Dagar S, Kumar H, Kumar R, Bhattacharya J, Mylavarapu SVS. The chaperone ERp29 is required for tunneling nanotube formation by stabilizing MSec. J Biol Chem. 2019;294(18):7177-93.
250. Dagar S, Pushpa K, Pathak D, Samaddar S, Saxena A, Banerjee S, Mylavarapu SVS. Nucleolin regulates 14-3-3ζ mRNA and promotes cofilin phosphorylation to induce tunneling nanotube formation. Faseb j. 2021;35(1):e21199.
251. Zhang H, Berg JS, Li Z, Wang Y, Lång P, Sousa AD, et al. Myosin-X provides a motor-based link between integrins and the cytoskeleton. Nature Cell Biology. 2004;6(6):523-31.
252. Lan M, Kojima T, Murata M, Osanai M, Takano K-i, Chiba H, Sawada N. Phosphorylation of ezrin enhances microvillus length via a p38 MAP-kinase pathway in an immortalized mouse hepatic cell line. Experimental Cell Research. 2006;312(2):111-20.
253. Baumgartner M, Sillman AL, Blackwood EM, Srivastava J, Madson N, Schilling JW, et al. The Nck-interacting kinase phosphorylates ERM proteins for formation of lamellipodium by growth factors. Proceedings of the National Academy of Sciences. 2006;103(36):13391-6.
254. Lin X, Wang W, Chang X, Chen C, Guo Z, Yu G, et al. ROS/mtROS promotes TNTs formation via the PI3K/AKT/mTOR pathway to protect against mitochondrial damages in glial cells induced by engineered nanomaterials. Particle and Fibre Toxicology. 2024;21(1):1.
255. Wang Y, Cui J, Sun X, Zhang Y. Tunneling-nanotube development in astrocytes depends on p53 activation. Cell Death Differ. 2011;18(4):732-42.
256. Andresen V, Wang X, Ghimire S, Omsland M, Gjertsen BT, Gerdes HH. Tunneling nanotube (TNT) formation is independent of p53 expression. Cell Death Differ. 2013;20(8):1124.
257. Desir S, Dickson EL, Vogel RI, Thayanithy V, Wong P, Teoh D, et al. Tunneling nanotube formation is stimulated by hypoxia in ovarian cancer cells. Oncotarget. 2016;7(28):43150-61.
258. Sarkari A, Lou E. Do tunneling nanotubes drive chemoresistance in solid tumors and other malignancies? Biochem Soc Trans. 2024;52(4):1757-64.
259. Omsland M, Andresen V, Gullaksen SE, Ayuda-Durán P, Popa M, Hovland R, et al. Tyrosine kinase inhibitors and interferon-α increase tunneling nanotube (TNT) formation and cell adhesion in chronic myeloid leukemia (CML) cell lines. Faseb j. 2020;34(3):3773-91.
260. Patheja P, Sahu K. Macrophage conditioned medium induced cellular network formation in MCF-7 cells through enhanced tunneling nanotube formation and tunneling nanotube mediated release of viable cytoplasmic fragments. Experimental Cell Research. 2017;355(2):182-93.
261. Melwani PK, Balla MMS, Bhamani A, Nandha SR, Checker R, Pandey BN. Macrophage-conditioned medium enhances tunneling nanotube formation in breast cancer cells via PKC, Src, NF-κB, and p38 MAPK signaling. Cell Signal. 2024:111274.
262. Lou E, Fujisawa S, Morozov A, Barlas A, Romin Y, Dogan Y, et al. Tunneling nanotubes provide a unique conduit for intercellular transfer of cellular contents in human malignant pleural mesothelioma. PLoS One. 2012;7(3):e33093.

263. Lou E, Zhai E, Sarkari A, Desir S, Wong P, Iizuka Y, et al. Cellular and Molecular Networking Within the Ecosystem of Cancer Cell Communication via Tunneling Nanotubes. Front Cell Dev Biol. 2018;6:95.
264. Liu K, Ji K, Guo L, Wu W, Lu H, Shan P, Yan C. Mesenchymal stem cells rescue injured endothelial cells in an in vitro ischemia-reperfusion model via tunneling nanotube like structure-mediated mitochondrial transfer. Microvasc Res. 2014;92:10-8.
265. Ady JW, Desir S, Thayanithy V, Vogel RI, Moreira AL, Downey RJ, et al. Intercellular communication in malignant pleural mesothelioma: properties of tunneling nanotubes. Front Physiol. 2014;5:400.
266. Desir S, O'Hare P, Vogel RI, Sperduto W, Sarkari A, Dickson EL, et al. Chemotherapy-Induced Tunneling Nanotubes Mediate Intercellular Drug Efflux in Pancreatic Cancer. Sci Rep. 2018;8(1):9484.
267. Kretschmer A, Zhang F, Somasekharan SP, Tse C, Leachman L, Gleave A, et al. Stress-induced tunneling nanotubes support treatment adaptation in prostate cancer. Scientific Reports. 2019;9(1):7826.
268. Kapoor D, Sharma P, Saini A, Azhar E, Elste J, Kohlmeir EK, et al. Tunneling Nanotubes: The Cables for Viral Spread and Beyond. Results Probl Cell Differ. 2024;73:375-417.
269. Jacob T, Broeke CVD, Waesberghe CV, Troys LV, Favoreel HW. Pseudorabies virus US3 triggers RhoA phosphorylation to reorganize the actin cytoskeleton. J Gen Virol. 2015;96(8):2328-35.
270. Michita RT, Tran LB, Bark SJ, Kumar D, Toner SA, Jose J, et al. Zika virus NS1 drives tunneling nanotube formation for mitochondrial transfer and stealth transmission in trophoblasts. Nature Communications. 2025;16(1):1803.
271. Guo R, Davis D, Fang Y. Intercellular transfer of mitochondria rescues virus-induced cell death but facilitates cell-to-cell spreading of porcine reproductive and respiratory syndrome virus. Virology. 2018;517:122-34.
272. Xu W, Santini PA, Sullivan JS, He B, Shan M, Ball SC, et al. HIV-1 evades virus-specific IgG2 and IgA responses by targeting systemic and intestinal B cells via long-range intercellular conduits. Nat Immunol. 2009;10(9):1008-17.
273. Mukerji J, Olivieri KC, Misra V, Agopian KA, Gabuzda D. Proteomic analysis of HIV-1 Nef cellular binding partners reveals a role for exocyst complex proteins in mediating enhancement of intercellular nanotube formation. Retrovirology. 2012;9:33.
274. Imle A, Abraham L, Tsopoulidis N, Hoflack B, Saksela K, Fackler OT. Association with PAK2 Enables Functional Interactions of Lentiviral Nef Proteins with the Exocyst Complex. mBio. 2015;6(5):e01309-15.
275. Uhl J, Gujarathi S, Waheed AA, Gordon A, Freed EO, Gousset K. Myosin-X is essential to the intercellular spread of HIV-1 Nef through tunneling nanotubes. J Cell Commun Signal. 2019;13(2):209-24.
276. Lotfi S, Nasser H, Noyori O, Hiyoshi M, Takeuchi H, Koyanagi Y, Suzu S. M-Sec facilitates intercellular transmission of HIV-1 through multiple mechanisms. Retrovirology. 2020;17(1):20.
277. Van Prooyen N, Gold H, Andresen V, Schwartz O, Jones K, Ruscetti F, et al. Human T-cell leukemia virus type 1 p8 protein increases cellular conduits and virus transmission. Proc Natl Acad Sci U S A. 2010;107(48):20738-43.
278. Omsland M, Pise-Masison C, Fujikawa D, Galli V, Fenizia C, Parks RW, et al. Inhibition of Tunneling Nanotube (TNT) Formation and Human T-cell Leukemia Virus Type 1 (HTLV-1) Transmission by Cytarabine. Scientific Reports. 2018;8(1):11118.

279. Li X, Zhao Y, Teng QY, Zhang XH, Xue J, Zhang GZ. Methyltransferase K-D-K-E motif influences the intercellular transmission of Newcastle disease virus. Virulence. 2023;14(1):2186336.
280. Bouhaddou M, Memon D, Meyer B, White KM, Rezelj VV, Correa Marrero M, et al. The Global Phosphorylation Landscape of SARS-CoV-2 Infection. Cell. 2020;182(3):685-712.e19.
281. Pepe A, Pietropaoli S, Vos M, Barba-Spaeth G, Zurzolo C. Tunneling nanotubes provide a route for SARS-CoV-2 spreading. Sci Adv. 2022;8(29):eabo0171.
282. Van den Broeke C, Radu M, Deruelle M, Nauwynck H, Hofmann C, Jaffer ZM, et al. Alphaherpesvirus US3-mediated reorganization of the actin cytoskeleton is mediated by group A p21-activated kinases. Proc Natl Acad Sci U S A. 2009;106(21):8707-12.
283. Jansens RJJ, Tishchenko A, Favoreel HW. Bridging the Gap: Virus Long-Distance Spread via Tunneling Nanotubes. J Virol. 2020;94(8).
284. Wang J, Shang KT, Ma QH, Dong ZY, Chen YH, Yao YF. Herpes Simplex Virus Type 1 Infection Induces the Formation of Tunneling Nanotubes. Microorganisms. 2023;11(8).
285. Panasiuk M, Rychłowski M, Derewońko N, Bieńkowska-Szewczyk K. Tunneling Nanotubes as a Novel Route of Cell-to-Cell Spread of Herpesviruses. Journal of Virology. 2018;92(10):10.1128/jvi.00090-18.
286. Ladelfa MF, Kotsias F, Del Médico Zajac MP, Van den Broeke C, Favoreel H, Romera SA, Calamante G. Effect of the US3 protein of bovine herpesvirus 5 on the actin cytoskeleton and apoptosis. Vet Microbiol. 2011;153(3-4):361-6.
287. Gill MB, Edgar R, May JS, Stevenson PG. A gamma-herpesvirus glycoprotein complex manipulates actin to promote viral spread. PLoS One. 2008;3(3):e1808.
288. May JS, Walker J, Colaco S, Stevenson PG. The murine gammaherpesvirus 68 ORF27 gene product contributes to intercellular viral spread. J Virol. 2005;79(8):5059-68.
289. Loesing JB, Di Fiore S, Ritter K, Fischer R, Kleines M. Epstein-Barr virus BDLF2-BMRF2 complex affects cellular morphology. J Gen Virol. 2009;90(Pt 6):1440-9.
290. Guo R, Katz BB, Tomich JM, Gallagher T, Fang Y. Porcine Reproductive and Respiratory Syndrome Virus Utilizes Nanotubes for Intercellular Spread. J Virol. 2016;90(10):5163-75.
291. Morales I, Carbajal MA, Bohn S, Holzer D, Kato SE, Greco FA, et al. The vaccinia virus F11L gene product facilitates cell detachment and promotes migration. Traffic. 2008;9(8):1283-98.
292. Valderrama F, Cordeiro JV, Schleich S, Frischknecht F, Way M. Vaccinia virus-induced cell motility requires F11L-mediated inhibition of RhoA signaling. Science. 2006;311(5759):377-81.
293. Xiao M, Xu N, Wang C, Pang DW, Zhang ZL. Dynamic monitoring of membrane nanotubes formation induced by vaccinia virus on a high throughput microfluidic chip. Sci Rep. 2017;7:44835.
294. Djurkovic MA, Leavitt CG, Arnett E, Kriachun V, Martínez-Sobrido L, Titone R, et al. Ebola Virus Uses Tunneling Nanotubes as an Alternate Route of Dissemination. J Infect Dis. 2023;228(Suppl 7):S522-s35.
295. Rostami J, Holmqvist S, Lindström V, Sigvardson J, Westermark GT, Ingelsson M, et al. Human Astrocytes Transfer Aggregated Alpha-Synuclein via Tunneling Nanotubes. The Journal of Neuroscience. 2017;37(49):11835.

296. Abounit S, Bousset L, Loria F, Zhu S, de Chaumont F, Pieri L, et al. Tunneling nanotubes spread fibrillar α-synuclein by intercellular trafficking of lysosomes. Embo j. 2016;35(19):2120-38.
297. Abounit S, Wu JW, Duff K, Victoria GS, Zurzolo C. Tunneling nanotubes: A possible highway in the spreading of tau and other prion-like proteins in neurodegenerative diseases. Prion. 2016;10(5):344-51.
298. Guan F, Wu X, Zhou J, Lin Y, He Y, Fan C, et al. Mitochondrial transfer in tunneling nanotubes—a new target for cancer therapy. Journal of Experimental & Clinical Cancer Research. 2024;43(1):147.
299. Chen M, Zhao D. Invisible Bridges: Unveiling the Role and Prospects of Tunneling Nanotubes in Cancer Therapy. Molecular Pharmaceutics. 2024;21(11):5413-29.
300. Resnik N, Levallet G, Errede M, Re F, Virgintino D. Editorial: Molecular profiles of tunneling nanotubes (TNTs) in human diseases-from 2D cultures to complex tissue. Frontiers in Cell and Developmental Biology. 2024;Volume 12 - 2024.
301. Zhu C, Shi Y, You J. Immune Cell Connection by Tunneling Nanotubes: The Impact of Intercellular Cross-Talk on the Immune Response and Its Therapeutic Applications. Molecular pharmaceutics. 2021;18.
302. Zaccard CR, Watkins SC, Kalinski P, Fecek RJ, Yates AL, Salter RD, et al. CD40L induces functional tunneling nanotube networks exclusively in dendritic cells programmed by mediators of type 1 immunity. J Immunol. 2015;194(3):1047-56.
303. Naphade S, Sharma J, Gaide Chevronnay HP, Shook MA, Yeagy BA, Rocca CJ, et al. Brief reports: Lysosomal cross-correction by hematopoietic stem cell-derived macrophages via tunneling nanotubes. Stem Cells. 2015;33(1):301-9.
304. Takara Bio Usa I. Easily deliver bright fluorescent proteins to your target cells [updated 2025/09/17. Available from: https://www.takarabio.com/learning-centers/gene-function/viral-transduction/lentivirus/lentiviral-particles-fluorescent.
305. Wit Ed, Spronken MIJ, Bestebroer TM, Rimmelzwaan GF, Osterhaus ADME, Fouchier RAM. Efficient generation and growth of influenza virus A/PR/8/34 from eight cDNA fragments. Virus Research. 2004;103(1):155-61.
306. Heaton N, Langlois R, Sachs D, Lim J, Palese P, Tenoever B. Long-term survival of influenza virus infected club cells drives immunopathology. The Journal of experimental medicine. 2014;211.
307. Fodor E, Devenish L, Engelhardt OG, Palese P, Brownlee GG, García-Sastre A. Rescue of influenza A virus from recombinant DNA. J Virol. 1999;73(11):9679-82.
308. Gaush CR, Smith TF. Replication and plaque assay of influenza virus in an established line of canine kidney cells. Appl Microbiol. 1968;16(4):588-94.
309. Sims A, Weir DJ, Cole SJ, Hutchinson E. SARS-CoV-2 cellular coinfection is limited by superinfection exclusion. Journal of Virology.0(0):e02077-24.
310. Hirst JC, Hutchinson EC. Single-particle measurements of filamentous influenza virions reveal damage induced by freezing. J Gen Virol. 2019;100(12):1631-40.
311. Zukauskas A, Merley A, Li D, Ang L-H, Sciuto TE, Salman S, et al. TM4SF1: a tetraspanin-like protein necessary for nanopodia formation and endothelial cell migration. Angiogenesis. 2011;14(3):345-54.
312. Schindelin J, Arganda-Carreras I, Frise E, Kaynig V, Longair M, Pietzsch T, et al. Fiji: an open-source platform for biological-image analysis. Nat Methods. 2012;9(7):676-82.

313. Nturibi E, Bhagwat AR, Coburn S, Myerburg MM, Lakdawala SS. Intracellular Colocalization of Influenza Viral RNA and Rab11A Is Dependent upon Microtubule Filaments. Journal of Virology. 2017;91(19):10.1128/jvi.01179-17.
314. Bhagwat AR, Le Sage V, Nturibi E, Kulej K, Jones J, Guo M, et al. Quantitative live cell imaging reveals influenza virus manipulation of Rab11A transport through reduced dynein association. Nature Communications. 2020;11(1):23.
315. Amorim MJ, Bruce EA, Read EKC, Foeglein Á, Mahen R, Stuart AD, Digard P. A Rab11- and Microtubule-Dependent Mechanism for Cytoplasmic Transport of Influenza A Virus Viral RNA. Journal of Virology. 2011;85(9):4143-56.
316. Trifkovic S, Gilbertson B, Fairmaid E, Cobbin J, Rockman S, Brown LE. Gene Segment Interactions Can Drive the Emergence of Dominant Yet Suboptimal Gene Constellations During Influenza Virus Reassortment. Front Microbiol. 2021;12:683152.
317. Guo J, Chen J, Li Y, Li Y, Deng G, Shi J, et al. SUMOylation of Matrix Protein M1 and Filamentous Morphology Collectively Contribute to the Replication and Virulence of Highly Pathogenic H5N1 Avian Influenza Viruses in Mammals. J Virol. 2022;96(4):e0163021.
318. Jalily PH, Eldstrom J, Miller SC, Kwan DC, Tai SS, Chou D, et al. Mechanisms of Action of Novel Influenza A/M2 Viroporin Inhibitors Derived from Hexamethylene Amiloride. Mol Pharmacol. 2016;90(2):80-95.
319. Cooper JA. Effects of cytochalasin and phalloidin on actin. J Cell Biol. 1987;105(4):1473-8.
320. Wong LL, Lam IP, Wong TY, Lai WL, Liu HF, Yeung LL, Ching YP. IPA-3 inhibits the growth of liver cancer cells by suppressing PAK1 and NF-κB activation. PLoS One. 2013;8(7):e68843.
321. Arnal I, Wade RH. How does taxol stabilize microtubules? Current Biology. 1995;5(8):900-8.
322. He Y, Xu K, Keiner B, Zhou J, Czudai V, Li T, et al. Influenza A Virus Replication Induces Cell Cycle Arrest in G₀/G₁ Phase. Journal of Virology. 2010;84(24):12832-40.
323. Jiang W, Wang Q, Chen S, Gao S, Song L, Liu P, Huang W. Influenza A virus NS1 induces G0/G1 cell cycle arrest by inhibiting the expression and activity of RhoA protein. J Virol. 2013;87(6):3039-52.
324. Stevenson BR, Begg DA. Concentration-dependent effects of cytochalasin D on tight junctions and actin filaments in MDCK epithelial cells. Journal of Cell Science. 1994;107(3):367-75.
325. Odenwald MA, Choi W, Buckley A, Shashikanth N, Joseph NE, Wang Y, et al. ZO-1 interactions with F-actin and occludin direct epithelial polarization and single lumen specification in 3D culture. Journal of Cell Science. 2017;130(1):243-59.
326. Okafo G, Prevedel L, Eugenin E. Tunneling nanotubes (TNT) mediate long-range gap junctional communication: Implications for HIV cell to cell spread. Scientific Reports. 2017;7(1):16660.
327. Peralta B, Gil-Carton D, Castaño-Díez D, Bertin A, Boulogne C, Oksanen HM, et al. Mechanism of Membranous Tunnelling Nanotube Formation in Viral Genome Delivery. PLOS Biology. 2013;11(9):e1001667.
328. Önfelt Br, Nedvetzki S, Benninger RKP, Purbhoo MA, Sowinski S, Hume AN, et al. Structurally Distinct Membrane Nanotubes between Human Macrophages Support Long-Distance Vesicular Traffic or Surfing of Bacteria1. The Journal of Immunology. 2006;177(12):8476-83.

329. Lai JC, Chan WW, Kien F, Nicholls JM, Peiris JS, Garcia JM. Formation of virus-like particles from human cell lines exclusively expressing influenza neuraminidase. J Gen Virol. 2010;91(Pt 9):2322-30.
330. Saletti D, Radzimanowski J, Effantin G, Midtvedt D, Mangenot S, Weissenhorn W, et al. The Matrix protein M1 from influenza C virus induces tubular membrane invaginations in an in vitro cell membrane model. Sci Rep. 2017;7:40801.
331. Simpson-Holley M, Ellis D, Fisher D, Elton D, McCauley J, Digard P. A Functional Link between the Actin Cytoskeleton and Lipid Rafts during Budding of Filamentous Influenza Virions. Virology. 2002;301(2):212-25.
332. Kumakura M, Kawaguchi A, Nagata K. Actin-myosin network is required for proper assembly of influenza virus particles. Virology. 2015;476:141-50.
333. Chinnery HR, Pearlman E, McMenamin PG. Cutting edge: Membrane nanotubes in vivo: a feature of MHC class II+ cells in the mouse cornea. J Immunol. 2008;180(9):5779-83.
334. Zhang J-Q, Takahashi A, Gu J-Y, Zhang X, Kyumoto-Nakamura Y, Kukita A, et al. In vitro and in vivo detection of tunneling nanotubes in normal and pathological osteoclastogenesis involving osteoclast fusion. Laboratory Investigation. 2021;101(12):1571-84.
335. Ady J, Thayanithy V, Mojica K, Wong P, Carson J, Rao P, et al. Tunneling nanotubes: an alternate route for propagation of the bystander effect following oncolytic viral infection. Molecular Therapy - Oncolytics. 2016;3:16029.
336. Antanavičiūtė I, Rysevaitė K, Liutkevičius V, Marandykina A, Rimkutė L, Sveikatienė R, et al. Long-distance communication between laryngeal carcinoma cells. PLoS One. 2014;9(6):e99196.
337. Thayanithy V, Dickson EL, Steer C, Subramanian S, Lou E. Tumor-stromal cross talk: direct cell-to-cell transfer of oncogenic microRNAs via tunneling nanotubes. Transl Res. 2014;164(5):359-65.
338. Seitz C, Frensing T, Höper D, Kochs G, Reichl U. High yields of influenza A virus in Madin–Darby canine kidney cells are promoted by an insufficient interferon-induced antiviral state. Journal of General Virology. 2010;91(7):1754-63.
339. Wang X, Gerdes HH. Transfer of mitochondria via tunneling nanotubes rescues apoptotic PC12 cells. Cell Death & Differentiation. 2015;22(7):1181-91.
340. Wurzer WJ, Planz O, Ehrhardt C, Giner M, Silberzahn T, Pleschka S, Ludwig S. Caspase 3 activation is essential for efficient influenza virus propagation. The EMBO Journal. 2003;22.
341. Liu B, Meng D, Wei T, Zhang S, Hu Y, Wang M. Apoptosis and pro-inflammatory cytokine response of mast cells induced by influenza A viruses. PLoS One. 2014;9(6):e100109.
342. Schwerdt G, Freudinger R, Schuster C, Weber F, Thews O, Gekle M. Cisplatin-Induced Apoptosis Is Enhanced by Hypoxia and by Inhibition of Mitochondria in Renal Collecting Duct Cells. Toxicological Sciences. 2005;85(1):735-42.
343. Muzumdar MD, Tasic B, Miyamichi K, Li L, Luo L. A global double-fluorescent Cre reporter mouse. genesis. 2007;45(9):593-605.
344. Bauer L, Rijsbergen LC, Leijten L, Benavides FF, Noack D, Lamers MM, et al. The pro-inflammatory response to influenza A virus infection is fueled by endothelial cells. Life Science Alliance. 2023;6(7):e202201837.
345. Breeze R, Turk M. Cellular structure, function and organization in the lower respiratory tract. Environmental Health Perspectives. 1984;55:3-24.
346. Ross MH, Pawlina W. Histology: A Text and Atlas. Philadelphia, PA: Wolters Kluwer Health; 2020. 118-9 p.

347. Uiprasertkul M, Kitphati R, Puthavathana P, Kriwong R, Kongchanagul A, Ungchusak K, et al. Apoptosis and pathogenesis of avian influenza A (H5N1) virus in humans. Emerg Infect Dis. 2007;13(5):708-12.
348. Yuan J, Ofengeim D. A guide to cell death pathways. Nature Reviews Molecular Cell Biology. 2024;25(5):379-95.
349. Wu Y, Zhang J, Yu S, Li Y, Zhu J, Zhang K, Zhang R. Cell pyroptosis in health and inflammatory diseases. Cell Death Discovery. 2022;8(1):191.
350. Hou J, Zhao R, Xia W, Chang CW, You Y, Hsu JM, et al. PD-L1-mediated gasdermin C expression switches apoptosis to pyroptosis in cancer cells and facilitates tumour necrosis. Nat Cell Biol. 2020;22(10):1264-75.
351. Hartmann BM, Albrecht RA, Zaslavsky E, Nudelman G, Pincas H, Marjanovic N, et al. Pandemic H1N1 influenza A viruses suppress immunogenic RIPK3-driven dendritic cell death. Nat Commun. 2017;8(1):1931.
352. Shubina M, Tummers B, Boyd DF, Zhang T, Yin C, Gautam A, et al. Necroptosis restricts influenza A virus as a stand-alone cell death mechanism. J Exp Med. 2020;217(11).
353. Mori I, Komatsu T, Takeuchi K, Nakakuki K, Sudo M, Kimura Y. In vivo induction of apoptosis by influenza virus. J Gen Virol. 1995;76 (Pt 11):2869-73.
354. Ito T, Kobayashi Y, Morita T, Horimoto T, Kawaoka Y. Virulent influenza A viruses induce apoptosis in chickens. Virus Res. 2002;84(1-2):27-35.
355. Wurzer WJ, Ehrhardt C, Pleschka S, Berberich-Siebelt F, Wolff T, Walczak H, et al. NF-kappaB-dependent induction of tumor necrosis factor-related apoptosis-inducing ligand (TRAIL) and Fas/FasL is crucial for efficient influenza virus propagation. J Biol Chem. 2004;279(30):30931-7.
356. Sun Y, Liu K. Mechanistic Insights into Influenza A Virus-Induced Cell Death and Emerging Treatment Strategies. Vet Sci. 2024;11(11).
357. Elmorsy EA, Saber S, Hamad RS, Abdel-Reheim MA, El-kott AF, AlShehri MA, et al. Advances in understanding cisplatin-induced toxicity: Molecular mechanisms and protective strategies. European Journal of Pharmaceutical Sciences. 2024;203:106939.
358. Zamarin D, García-Sastre A, Xiao X, Wang R, Palese P. Influenza virus PB1-F2 protein induces cell death through mitochondrial ANT3 and VDAC1. PLoS Pathog. 2005;1(1):e4.
359. Finnen RL, Roy BB, Zhang H, Banfield BW. Analysis of filamentous process induction and nuclear localization properties of the HSV-2 serine/threonine kinase Us3. Virology. 2010;397(1):23-33.
360. Wolf D, Witte V, Laffert B, Blume K, Stromer E, Trapp S, et al. HIV-1 Nef associated PAK and PI3-kinases stimulate Akt-independent Bad-phosphorylation to induce anti-apoptotic signals. Nat Med. 2001;7(11):1217-24.
361. Perfettini JL, Castedo M, Roumier T, Andreau K, Nardacci R, Piacentini M, Kroemer G. Mechanisms of apoptosis induction by the HIV-1 envelope. Cell Death Differ. 2005;12 Suppl 1:916-23.
362. Murata T, Goshima F, Yamauchi Y, Koshizuka T, Takakuwa H, Nishiyama Y. Herpes simplex virus type 2 US3 blocks apoptosis induced by sorbitol treatment. Microbes and Infection. 2002;4(7):707-12.
363. Geenen K, Favoreel HW, Olsen L, Enquist LW, Nauwynck HJ. The pseudorabies virus US3 protein kinase possesses anti-apoptotic activity that protects cells from apoptosis during infection and after treatment with sorbitol or staurosporine. Virology. 2005;331(1):144-50.
364. Dadonaite B, Gilbertson B, Knight ML, Trifkovic S, Rockman S, Laederach A, et al. The structure of the influenza A virus genome. Nature Microbiology. 2019;4(11):1781-9.

365. Julkunen I, Sareneva T, Pirhonen J, Ronni T, Melén K, Matikainen S. Molecular pathogenesis of influenza A virus infection and virus-induced regulation of cytokine gene expression. Cytokine & Growth Factor Reviews. 2001;12(2):171-80.
366. Short KR, Kroeze EJBV, Fouchier RAM, Kuiken T. Pathogenesis of influenza-induced acute respiratory distress syndrome. The Lancet Infectious Diseases. 2014;14(1):57-69.
367. Costers S, Lefebvre DJ, Delputte PL, Nauwynck HJ. Porcine reproductive and respiratory syndrome virus modulates apoptosis during replication in alveolar macrophages. Archives of Virology. 2008;153(8):1453-65.
368. Miller LC, Fox JM. Apoptosis and porcine reproductive and respiratory syndrome virus. Veterinary Immunology and Immunopathology. 2004;102(3):131-42.
369. Galluzzi L, Kepp O, Kroemer G. Mitochondria: master regulators of danger signalling. Nature Reviews Molecular Cell Biology. 2012;13(12):780-8.
370. Gant VA, Shakoor Z, Hamblin AS. A new method for measuring clustering in suspension between accessory cells and T lympocytes. Journal of Immunological Methods. 1992;156(2):179-89.
371. Wang QW, Kim JK. Cytokine Expression During the Early Response of A549 Cells to Infection with Influenza Virus, Alphacoronavirus and Betacoronavirus. American Journal of Biochemistry and Biotechnology. 2024;20(2).
372. Gomzikova MO, James V, Rizvanov AA. Mitochondria Donation by Mesenchymal Stem Cells: Current Understanding and Mitochondria Transplantation Strategies. Frontiers in Cell and Developmental Biology. 2021;Volume 9 - 2021.
373. Islam MN, Das SR, Emin MT, Wei M, Sun L, Westphalen K, et al. Mitochondrial transfer from bone-marrow-derived stromal cells to pulmonary alveoli protects against acute lung injury. Nat Med. 2012;18(5):759-65.
374. Morrison TJ, Jackson MV, Cunningham EK, Kissenpfennig A, McAuley DF, O'Kane CM, Krasnodembskaya AD. Mesenchymal Stromal Cells Modulate Macrophages in Clinically Relevant Lung Injury Models by Extracellular Vesicle Mitochondrial Transfer. Am J Respir Crit Care Med. 2017;196(10):1275-86.
375. Falchi AM, Sogos V, Saba F, Piras M, Congiu T, Piludu M. Astrocytes shed large membrane vesicles that contain mitochondria, lipid droplets and ATP. Histochem Cell Biol. 2013;139(2):221-31.
376. Li H, Yu H, Liu D, Liao P, Gao C, Zhou J, et al. Adenosine diphosphate released from stressed cells triggers mitochondrial transfer to achieve tissue homeostasis. PLOS Biology. 2024;22(8):e3002753.
377. Acquistapace A, Bru T, Lesault PF, Figeac F, Coudert AE, le Coz O, et al. Human mesenchymal stem cells reprogram adult cardiomyocytes toward a progenitor-like state through partial cell fusion and mitochondria transfer. Stem Cells. 2011;29(5):812-24.
378. Wada KI, Hosokawa K, Ito Y, Maeda M. Quantitative control of mitochondria transfer between live single cells using a microfluidic device. Biol Open. 2017;6(12):1960-5.
379. Zhang W, Lin X, Li Z-Y, Zhang L-J, Chen L, Sun Y-P, et al. Novel intercellular spread mode of respiratory syncytial virus contributes to neutralization escape. Antiviral Research. 2024;231:106023.
380. Zhang L, Peeples Mark E, Boucher Richard C, Collins Peter L, Pickles Raymond J. Respiratory Syncytial Virus Infection of Human Airway Epithelial Cells Is Polarized, Specific to Ciliated Cells, and without Obvious Cytopathology. Journal of Virology. 2002;76(11):5654-66.

381. Singh Brajesh K, Li N, Mark Anna C, Mateo M, Cattaneo R, Sinn Patrick L. Cell-to-Cell Contact and Nectin-4 Govern Spread of Measles Virus from Primary Human Myeloid Cells to Primary Human Airway Epithelial Cells. Journal of Virology. 2016;90(15):6808-17.
382. Reed SG, Ager A. Immune Responses to IAV Infection and the Roles of L-Selectin and ADAM17 in Lymphocyte Homing. Pathogens. 2022;11(2):150.
383. Marongiu L, Valache M, Facchini Fabio A, Granucci F. How dendritic cells sense and respond to viral infections. Clinical Science. 2021;135(19):2217-42.
384. Cabeza-Cabrerizo M, Minutti CM, da Costa MP, Cardoso A, Jenkins RP, Kulikauskaite J, et al. Recruitment of dendritic cell progenitors to foci of influenza A virus infection sustains immunity. Science Immunology. 2021;6(65):eabi9331.
385. Jiang Y, Cai X, Yao J, Guo H, Yin L, Leung W, Xu C. Role of Extracellular Vesicles in Influenza Virus Infection. Frontiers in Cellular and Infection Microbiology. 2020;Volume 10 - 2020.
386. Scheller N, Herold S, Kellner R, Bertrams W, Jung AL, Janga H, et al. Proviral MicroRNAs Detected in Extracellular Vesicles From Bronchoalveolar Lavage Fluid of Patients With Influenza Virus–Induced Acute Respiratory Distress Syndrome. The Journal of Infectious Diseases. 2018;219(4):540-3.
387. Lee S, Hirohama M, Noguchi M, Nagata K, Kawaguchi A. Influenza A Virus Infection Triggers Pyroptosis and Apoptosis of Respiratory Epithelial Cells through the Type I Interferon Signaling Pathway in a Mutually Exclusive Manner. Journal of Virology. 2018;92(14):10.1128/jvi.00396-18.
388. Youle RJ, van der Bliek AM. Mitochondrial fission, fusion, and stress. Science. 2012;337(6098):1062-5.
389. Sugioka R, Shimizu S, Tsujimoto Y. Fzo1, a protein involved in mitochondrial fusion, inhibits apoptosis. J Biol Chem. 2004;279(50):52726-34.
390. Perfettini J-L, Roumier T, Kroemer G. Mitochondrial fusion and fission in the control of apoptosis. Trends in Cell Biology. 2005;15(4):179-83.
391. Gibbs JS, Malide D, Hornung F, Bennink JR, Yewdell JW. The influenza A virus PB1-F2 protein targets the inner mitochondrial membrane via a predicted basic amphipathic helix that disrupts mitochondrial function. J Virol. 2003;77(13):7214-24.
392. Varga ZT, Ramos I, Hai R, Schmolke M, García-Sastre A, Fernandez-Sesma A, Palese P. The influenza virus protein PB1-F2 inhibits the induction of type I interferon at the level of the MAVS adaptor protein. PLoS Pathog. 2011;7(6):e1002067.
393. Varga Zsuzsanna T, Grant A, Manicassamy B, Palese P. Influenza Virus Protein PB1-F2 Inhibits the Induction of Type I Interferon by Binding to MAVS and Decreasing Mitochondrial Membrane Potential. Journal of Virology. 2012;86(16):8359-66.
394. von Magnus P. Incomplete Forms of Influenza Virus. In: Smith KM, Lauffer MA, editors. Advances in Virus Research. 2: Academic Press; 1954. p. 59-79.
395. Bruce EA, Digard P, Stuart AD. The Rab11 pathway is required for influenza A virus budding and filament formation. J Virol. 2010;84(12):5848-59.
396. Pasquier J, Guerrouahen BS, Al Thawadi H, Ghiabi P, Maleki M, Abu-Kaoud N, et al. Preferential transfer of mitochondria from endothelial to cancer cells through tunneling nanotubes modulates chemoresistance. J Transl Med. 2013;11:94.
397. Kawakami T, Hirabayashi Y, Kawakami F, Isobe R, Kaneko N, Mimura Y, et al. Persistent Infection of Drug-resistant Influenza A Virus during Chemotherapy for Malignant Lymphoma. Intern Med. 2016;55(13):1807-10.

398. Mühlbauer D, Dzieciolowski J, Hardt M, Hocke A, Schierhorn KL, Mostafa A, et al. Influenza virus-induced caspase-dependent enlargement of nuclear pores promotes nuclear export of viral ribonucleoprotein complexes. J Virol. 2015;89(11):6009-21.
399. Larson GP, Tran V, Yú S, Caì Y, Higgins CA, Smith DM, et al. EPS8 Facilitates Uncoating of Influenza A Virus. Cell Rep. 2019;29(8):2175-83.e4.
400. Lam WY, Tang JW, Yeung AC, Chiu LC, Sung JJ, Chan PK. Avian influenza virus A/HK/483/97(H5N1) NS1 protein induces apoptosis in human airway epithelial cells. J Virol. 2008;82(6):2741-51.
401. Schultz-Cherry S, Dybdahl-Sissoko N, Neumann G, Kawaoka Y, Hinshaw VS. Influenza virus ns1 protein induces apoptosis in cultured cells. J Virol. 2001;75(17):7875-81.
402. Liu H, Golebiewski L, Dow EC, Krug RM, Javier RT, Rice AP. The ESEV PDZ-binding motif of the avian influenza A virus NS1 protein protects infected cells from apoptosis by directly targeting Scribble. J Virol. 2010;84(21):11164-74.
403. Li G, Zhang J, Tong X, Liu W, Ye X. Heat shock protein 70 inhibits the activity of Influenza A virus ribonucleoprotein and blocks the replication of virus in vitro and in vivo. PLoS One. 2011;6(2):e16546.
404. Gannagé M, Dormann D, Albrecht R, Dengjel J, Torossi T, Rämer PC, et al. Matrix protein 2 of influenza A virus blocks autophagosome fusion with lysosomes. Cell Host Microbe. 2009;6(4):367-80.
405. Schultz-Cherry S, Hinshaw VS. Influenza virus neuraminidase activates latent transforming growth factor beta. J Virol. 1996;70(12):8624-9.
406. Tripathi S, Batra J, Cao W, Sharma K, Patel JR, Ranjan P, et al. Influenza A virus nucleoprotein induces apoptosis in human airway epithelial cells: implications of a novel interaction between nucleoprotein and host protein Clusterin. Cell Death & Disease. 2013;4(3):e562-e.
407. van Riel D, Munster VJ, de Wit E, Rimmelzwaan GF, Fouchier RA, Osterhaus AD, Kuiken T. Human and avian influenza viruses target different cells in the lower respiratory tract of humans and other mammals. Am J Pathol. 2007;171(4):1215-23.
408. Weinheimer VK, Becher A, Tönnies M, Holland G, Knepper J, Bauer TT, et al. Influenza A viruses target type II pneumocytes in the human lung. J Infect Dis. 2012;206(11):1685-94.
409. Mirolo M, Pohlmann A, Ahrens AK, Kühl B, Rubio-Garcìa A, Kramer K, et al. Highly pathogenic avian influenza A virus (HPAIV) H5N1 infection in two European grey seals (Halichoerus grypus) with encephalitis. Emerg Microbes Infect. 2023;12(2):e2257810.
410. Kim M, Yu JE, Lee J-H, Chang B-J, Song C-S, Lee B, et al. Comparative analyses of influenza virus receptor distribution in the human and mouse brains. Journal of Chemical Neuroanatomy. 2013;52:49-57.
411. Schrauwen Eefje JA, Herfst S, Leijten Lonneke M, van Run P, Bestebroer Theo M, Linster M, et al. The Multibasic Cleavage Site in H5N1 Virus Is Critical for Systemic Spread along the Olfactory and Hematogenous Routes in Ferrets. Journal of Virology. 2012;86(7):3975-84.
412. van Riel D, Leijten LM, Verdijk RM, GeurtsvanKessel C, van der Vries E, van Rossum AM, et al. Evidence for influenza virus CNS invasion along the olfactory route in an immunocompromised infant. J Infect Dis. 2014;210(3):419-23.
413. Bauer L, Benavides FFW, Veldhuis Kroeze EJB, de Wit E, van Riel D. The neuropathogenesis of highly pathogenic avian influenza H5Nx viruses in mammalian species including humans. Trends in Neurosciences. 2023;46(11):953-70.

414. Haney J, Vijayakrishnan S, Streetley J, Dee K, Goldfarb DM, Clarke M, et al. Coinfection by influenza A virus and respiratory syncytial virus produces hybrid virus particles. Nature Microbiology. 2022;7(11):1879-90.
415. Mehedi M, McCarty T, Martin SE, Le Nouën C, Buehler E, Chen Y-C, et al. Actin-Related Protein 2 (ARP2) and Virus-Induced Filopodia Facilitate Human Respiratory Syncytial Virus Spread. PLOS Pathogens. 2016;12(12):e1006062.
416. Dee K, Schultz V, Haney J, Bissett LA, Magill C, Murcia PR. Influenza A and Respiratory Syncytial Virus Trigger a Cellular Response That Blocks Severe Acute Respiratory Syndrome Virus 2 Infection in the Respiratory Tract. The Journal of Infectious Diseases. 2022;227(12):1396-406.
417. Zhang D, He Z, Xu L, Zhu X, Wu J, Wen W, et al. Epidemiology characteristics of respiratory viruses found in children and adults with respiratory tract infections in southern China. International Journal of Infectious Diseases. 2014;25:159-64.
418. Kim D, Quinn J, Pinsky B, Shah NH, Brown I. Rates of Co-infection Between SARS-CoV-2 and Other Respiratory Pathogens. Jama. 2020;323(20):2085-6.
419. Goka EA, Vallely PJ, Mutton KJ, Klapper PE. Single, dual and multiple respiratory virus infections and risk of hospitalization and mortality. Epidemiol Infect. 2015;143(1):37-47.
420. Bartley PS, Deshpande A, Yu PC, Klompas M, Haessler SD, Imrey PB, et al. Bacterial coinfection in influenza pneumonia: Rates, pathogens, and outcomes. Infect Control Hosp Epidemiol. 2022;43(2):212-7.
421. Souriant S, Balboa L, Dupont M, Pingris K, Kviatcovsky D, Cougoule C, et al. Tuberculosis Exacerbates HIV-1 Infection through IL-10/STAT3-Dependent Tunneling Nanotube Formation in Macrophages. Cell Reports. 2019;26(13):3586-99.e7.
422. Ahmed F, Urooj S, Ahmed A, et al. The Role of Nanotubes in Modulating Colony Spreading and Autolysis in Staphylococcus aureus Biofilms. Research Square. 2024.
423. Tan CK, Kao CL, Shih JY, Lee LN, Hung CC, Lai CC, et al. Coinfection with Mycobacterium tuberculosis and pandemic H1N1 influenza A virus in a patient with lung cancer. J Microbiol Immunol Infect. 2011;44(4):316-8.
424. Dupont M, Souriant S, Balboa L, Vu Manh TP, Pingris K, Rousset S, et al. Tuberculosis-associated IFN-I induces Siglec-1 on tunneling nanotubes and favors HIV-1 spread in macrophages. Elife. 2020;9.
425. Tilney LG, Portnoy DA. Actin filaments and the growth, movement, and spread of the intracellular bacterial parasite, Listeria monocytogenes. J Cell Biol. 1989;109(4 Pt 1):1597-608.
426. Koufakis T, Chatzopoulou M, Margaritis A, Tsiakalou M, Gabranis I. Pneumonia by Listeria monocytogenes: A Common Infection by an Uncommon Pathogen. Case Rep Infect Dis. 2015;2015:627073.
427. Joseph C, Togawa Y, Shindo N. Bacterial and viral infections associated with influenza. Influenza Other Respir Viruses. 2013;7 Suppl 2(Suppl 2):105-13.
428. Subbarao K. Live Attenuated Cold-Adapted Influenza Vaccines. Cold Spring Harb Perspect Med. 2021;11(9).
429. Mohn KG, Smith I, Sjursen H, Cox RJ. Immune responses after live attenuated influenza vaccination. Hum Vaccin Immunother. 2018;14(3):571-8.
430. Thwaites RS, Uruchurtu ASS, Negri VA, Cole ME, Singh N, Poshai N, et al. Early mucosal events promote distinct mucosal and systemic antibody responses to live attenuated influenza vaccine. Nature Communications. 2023;14(1):8053.

431. Shahani L, Ariza-Heredia EJ, Chemaly RF. Antiviral therapy for respiratory viral infections in immunocompromised patients. Expert Rev Anti Infect Ther. 2017;15(4):401-15.
432. Rossi E. Exploring Apoptotic Inhibitors: Mechanisms and Impact 2025 [updated 2025/09/16. Available from: https://integratingpulse.com/articles/exploring-apoptotic-inhibitors-mechanisms-impact.
433. Dhani S, Zhao Y, Zhivotovsky B. A long way to go: caspase inhibitors in clinical use. Cell Death Dis. 2021;12(10):949.